technische universität
dortmund

Arbeit zur Erlangung des akademischen Grades eines
Doktors der Naturwissenschaften

The Fermi-Hubbard model and its limiting cases as a testbed for techniques and phenomena

Philip Bleicker
geboren in Dortmund

2021

Technische Universität Dortmund
Lehrstuhl für Theoretische Physik I

1. Gutachter: **Prof. Dr. Götz S. Uhrig**
2. Gutachter: **Prof. Dr. Kai P. Schmidt**
Abgabedatum: **9. September 2021**

Version: 3B84FF7/777/15.11.2021

Abstract

Despite about six decades of research on the Fermi-Hubbard model (FHM), there is hardly any other model that holds a comparable fascination. The model has a conceptually simple structure and yet contains the essential ingredient of a solid: *interaction.* Precisely this interaction, however, opposes conclusive solutions of the FHM in equilibrium and non-equilibrium and imposes high demands on methodological approaches.

In the course of this work, we review the FHM and related models which can be derived from it, e.g. the t–J model or the Heisenberg model, discuss key topics of current research and use both well-known methods like CET and TPQS and new techniques like iEoM to contribute to the elucidation of some central questions. We begin with the analyses of equilibration and thermalisation in quenched closed quantum systems and confirm as well as extend previously made hypotheses. Furthermore, we challenge and falsify the assumption of a dynamical phase transition in one dimension. In a second step, we reduce the FHM to an effective t–J model, which is of particular interest in the context of high-temperature superconductivity, and consider the resulting charge carrier dynamics. Moreover, we confirm ideas on the quantitative predictability of the autocorrelation in dense spin systems. In the last step, we propose a novel theoretical approach based on iEoM for the systematic evaluation of Green's functions in reduced operator subspaces and motivate its applicability by means of an exemplary calculation.

Kurzfassung

Trotz mittlerweile etwa sechs Jahrzehnten Forschung am Fermi-Hubbard-Modell (FHM) geht von kaum einem anderen Modell eine vergleichbar hohe Faszination aus. Das Modell ist von konzeptionell einfacher Struktur und enthält dabei doch die wesentliche Grundzutat dessen, was Festkörper ausmacht: *Wechselwirkung.* Ebendiese Wechselwirkung ist es, die abschließenden Lösungen des FHM im Gleich- sowie Nichtgleichgewicht diametral entgegensteht und hohe Ansprüche an die verwendeten methodischen Zugänge stellt.

In dieser Arbeit wenden wir uns dem FHM sowie einigen hieraus ableitbaren Modellen zu, etwa dem t–J-Modell oder dem Heisenberg-Modell, diskutieren Kernfragen der aktuellen Forschung und nutzen bekannte Ansätze wie die CET oder TPQS sowie neue Techniken wie die iEoM, um zur Klärung einiger zentraler Fragestellungen beizutragen. Wir starten mit Analysen von Äquilibration und Thermalisierung in gequenchten von der Umgebung abgeschlossenen Quantensysteme und bestätigen und erweitern bisherige Annahmen. Ferner widerlegen wir die Vermutung eines dynamischen Phasenübergangs in einer Dimension. In einem zweiten Schritt reduzieren wir das FHM auf ein effektives t–J-Modell, das besonders im Kontext von Hochtemperatursupraleitung Beachtung findet, und betrachten hierin die Ladungsträgerdynamik. Darüber hinaus bestätigen wir Annahmen zur quantitativen Vorhersagbarkeit der Autokorrelation in dichten Spin-Systemen. Im letzten Schritt schlagen wir einen neuartigen theoretischen Ansatz mittels iEoM für die systematische Berechnung von Greenfunktionen in reduzierten Operator-Unterräumen vor und motivieren seine Anwendbarkeit im Rahmen einer exemplarischen Rechnung.

Contents

Publications

Partial results of the presented work have been published before as follows:

- P. Bleicker and G.S. Uhrig
  Strong quenches in the one-dimensional Fermi-Hubbard model (FHM).
  In: Phys. Rev. A **98**, 033602 (2018)
- P. Bleicker, J. Stolze and G.S. Uhrig
  Probing thermalization in quenched integrable and nonintegrable FHMs.
  In: Phys. Rev. A **102**, 013321 (2020)
- P. Bleicker, D.-B. Hering and G.S. Uhrig
  Charge gaps in magnetically disordered Mott insulators.
  Preprint: arXiv:2104.10158 (2021)
- T. Gräßer, P. Bleicker, D.-B. Hering, M. Yarmohammadi and G.S. Uhrig
  Dynamic mean-field theory for dense spin systems at infinite temperature.
  Preprint: arXiv:2107.07821 (2021), in press (Phys. Rev. Research)

Denjenigen Menschen hinter dieser Arbeit.
Meinen Eltern

1 Introduction

Each and every one of us deals with electricity on a daily basis. We charge our mobile phones, watch illuminated advertisements or simply switch on the ceiling light. You may even be reading this text digitally right now. We all take it for granted that electricity finds its way. Though, the exact materials used to transmit it from A to B are usually of at most secondary importance to us. And yet, it is worth to take a closer look.

We already know from school that some materials conduct electricity, whereas others are not conductive at all. Accordingly, we refer to the former ones as conductors and to the latter ones as insulators. But can every material be assigned exclusively to *one* of the two groups? At the latest since the conceptual introduction of the metal-insulator transition by Mott in 1949, this strict distinction is no longer feasible [1]. According to Mott, a material can turn from an insulator into a conductor by a reduction of its lattice constant, e.g. by applying external pressure [2]. Already decades earlier, Kamerlingh Onnes was able to show phenomenologically that there had to be a third group besides metals and insulators. Upon intense cooling of mercury, he found that below a transition temperature $T < T_\mathrm{c}$, it abruptly exhibited an immeasurably small electrical resistance. This change from a lossy to a perfect conductor was the birth of superconductivity [3]. Albeit widely unknown, the opposite case of a reduction of the conductivity on cooling also exists. For instance, vanadium dioxide (VO_2) shows a first-order metal-insulator transition near room temperature and, thus, becomes an insulator when cooled [4].

Explaining such observations often takes years or even decades. Nearly five decades passed before conventional superconductivity was explained by Bardeen, Cooper and Schrieffer using their famous BCS theory [5]. Similarly, it was not until a good ten years after the observation of the unusual properties of VO_2 that a first microscopic theory was proposed [6]. Unfortunately, often the same macroscopic effect can have completely different microscopic causes. When copper oxides with superconducting properties at high temperatures were discovered in 1986 [7], it became evident that conventional approaches by the BCS theory were not applicable, and even today, understanding all subtleties of the atomic processes and excitations in VO_2 is still the subject of ongoing research [8].

But what does it make so challenging to answer these questions? As unimpressive as this question may seem, it is actually a crucial one. Indeed, it is one of the main questions of condensed matter physics. The difficulty begins where constituents of the system are not independent of each other, but are strongly-correlated, i.e. influence each other in everything they do. Examples of this can be found in everyday life: changing seats in a crowded aeroplane or moving around inside the cabin is practically impossible without influencing other passengers. Electrons behave similarly in the periodically arranged Bravais lattice of atoms as they interact with each other and atomic cores via the Coulomb interaction. Since the dynamics of a physical system is determined by quantum mechanics [9] the Hilbert space grows exponentially with the number of particles, and since a typical solid has $\mathcal{O}(10^{23})$ particles, a numerical simulation – even with the fastest conventional computers – will probably never be a feasible option.

Therefore, simplified models are indispensable for an improved qualitative understanding of any physical system. In the context of this thesis, we are particularly concerned with the Fermi-Hubbard model (FHM) [10–12] as an archetypal model for a Mott metal-insulator transition. Nevertheless, the FHM is also remarkable for another reason. It is considered the simplest strongly-correlated model of interacting electrons in a solid. In this model, the actually long-range Coulomb interaction is reduced due to screening such that only electrons interact with each other that are in close proximity. The movement of itinerant electrons is represented by hopping from one lattice site to another. Despite its conceptual simplicity, the model is still a source of fascinating insights today [13, 14]. In the chapters to come, we discuss selected questions of the present research on the FHM and our contributions. We do so in three thematic blocks: quenching of the FHM and its effects, the dynamics of charge and spin degrees of freedom in the t–J model and the Heisenberg model as well as theoretical proposals for obtaining Green's functions in operator subspaces. But what is it that renders these topics so relevant and, above all, what has triggered the renewed interest in research on the FHM in the recent past?

During many decades, research on the FHM was mostly of theoretical nature. For experiments, there was a major obstacle: the reduction of a realistic physical solid to a set of electrons in an ideal lattice influenced by only two effective parameters, the strength of the interaction and the hopping, does not correspond to reality. Microscopically small systems are hard to decouple from their environment and the precise tuning of two well-defined parameters is challenging. Moreover, real solids never have perfect lattices. Instead, they are full of impurities or defects, i.e. influences that are not included in the FHM. Finding an ideal experimental setting for the FHM was therefore nearly impossible for a long time. In short, the model was actually *too* simple for a complex world.

In a pioneering theoretical work in 1998, Jaksch et al. [15] proposed to lock particles into optical lattices. An optical lattice is a periodic potential of intersected laser beams where the lattice constant is of the order of the wavelength of the laser beam [16]. Typically, the periodic potential is generated as standing waves by two counterpropagating beams. The atoms themselves are cooled down to sufficiently low temperatures and then loaded into the lattice [17]. The optical lattice controls the ratio of the two FHM parameters. Thus, depending on the strength of the potential of the optical lattice, either a tight-binding system [18] or a system of completely localised electrons is created. In case of exceptionally strong on-site interaction, the electrons become completely immobile and only their spin degrees of freedom determine the dynamics of the system. Even this scenario is potentially controllable through precise adjustment of the intensity, frequency and polarisation of the laser beam [19]. Already a few years after the theoretical introduction of optical lattices by Jaksch and his colleagues, the first realisation of the idea was achieved [20]. Since then, the interest in optical lattices has continued unabated and has led to an almost innumerable number of contributions, see e.g. Ref. [21] for an insightful review.

And yet, optical lattices do not only offer a clean setting for the decoupling of a fixed lattice from the environment. Indeed, it is now also possible to change the lattice itself at any point in time which provides a clean way of reproducibly driving a system out of equilibrium. The effects induced by abrupt changes in optical lattices are also referred to as quenches and are described extensively in section 5.2. The curiosity in the resulting non-equilibrium physics is anything but purely academic. Systems far from equilibrium can exhibit unusual transport properties [22] or even show superconducting features when stimulated, e.g. by light [23–26]. A profound understanding of systems in non-equilibrium can, therefore, contribute significantly to the discovery of new phases of matter and consequently, for instance, to the energy-efficient use of resources in the future. Nevertheless, it is not only the properties of a solid in non-equilibrium that are remarkable. Likewise, there are still questions about the return of a system to equilibrium following an excitation. To put it vividly, the question is whether a system whose past is completely known and whose future can be unambiguously determined from the past can forget its past fully during its time-evolution. If it can, it is said to thermalise [27]. As we see in section 5.3, it is typically far from being clear whether arbitrary systems thermalise, and if so, under what specific conditions they do. Moreover, selected observables of the system, e.g. the jump at the Fermi surface, may exhibit characteristically distinct behaviour depending on the strength of the quench, cf. section 5.4.

Another cause of fascination in strongly-correlated quantum systems remains the fact that even supposedly simple questions are hard to answer. If a certain particle moves without any significant external constraints, it performs a so-called random walk. While this situation is easy to describe for classical particles, the quantum mechanical equivalent poses a substantially tougher problem. For instance, it turns out that quantum interference can significantly change the results of the quantum mechanical random walk compared to its classical counterpart [28]. This is mainly explained by the fact that the quantum mechanical path of a particle from a starting point A to an endpoint B is not simply a direct connection of the two points but a superposition of *all* available paths that can be chosen between these two points [29]. Consequently, they all interfere differently with each other. This phenomenon becomes particularly problematic for charge carriers in high-temperature superconductors, often described by a t–J model and, thus, the FHM in the limit of strong interaction. If holes move in disordered random spin backgrounds, they displace spins along their path in every step, effectively destroying the original environment [30]. We analyse hole motion and its effects in section 6.2.

In light of all these ongoing problems, unresolved issues and experimental challenges in dealing with quantum mechanical systems, the legitimate question may arise whether quantum mechanical systems are not per se too sensitive for real-world applications. In particular, the typically insufficient decoupling of quantum mechanical systems from their environment is a frequently encountered difficulty in the practical realisation of theoretical concepts. More recently, however, it has increasingly been seen as an opportunity: if quantum mechanical systems respond so sensitively to all possible external excitations, no matter how weak, ought they not to be excellent sensors? In fact, it turned out in various experiments that quantum sensors can have a high quality and broad practical applicability [31]. Among the systems already successfully used are diamonds with nitrogen vacancies (NVs). Their NV centres are excellent probes, e.g. in magnetometry [32]. Nevertheless, even with optimal production of the NV centres, unpaired spin ensembles emerge at the surface [33]. A theoretically reliable description of these ensembles is important to improve the coherence and, thus, the applicability of the NV centres. We turn to these kinds of dense spin ensembles in section 6.3.

This thesis addresses some exemplary aspects from the plethora of fascinating topics of the FHM. In this context, we will repeatedly revisit the aspect of modelling physical systems throughout the course of the entire work. We will notice that it may be necessary to partly simplify the FHM or to adapt it for different problems, and we will see what influence topology and the dimensionality of the system may have on the FHM. We begin with a mathematical description of the FHM in chapter 2, where we discuss its many applications to questions of non-equilibrium physics, high-temperature superconductivity, magnetism in insulators and Kondo physics in detail. In each case, we give a brief overview of the relevant current state of research. In chapters 3 and 4, we discuss the theoretical methods used or enhanced in the framework of this thesis. In particular, we review different possibilities to reliably determine time-dependent observables in strongly-correlated systems in chapter 3. Moreover, we outline ways to optimise their computational efficiency. In chapter 4, we address the question of how the thermal behaviour of systems can be adequately determined. In the two-part chapter 5 we are concerned with quantum quenches. At first, we discuss key issues of the fundamental questions regarding equilibration and thermalisation after interaction quenches. For this purpose, we resort to the FHM on both lattices with periodic boundary conditions and to the FHM on fully arbitrary topologies including so-called infinite-range graphs. Then, we deal with the highly debated occurrence or absence of a dynamical phase transition, i.e. a significant change in the behaviour of the jump at the Fermi surface, in the quenched, integrable one-dimensional FHM. In chapter 6, we employ a slight modification of the FHM, the so-called t–J model, and study the motion of a hole in a disordered spin background. Here, we use an effective generalised version of the t–J model to account for both charge and spin degrees of freedom in a reliable manner and compute the corresponding excitation spectra by means of numerically determined Green's functions. Thereafter, we freeze the charge degrees of freedom of the t–J model which leads us to the Heisenberg model. For this model, we heavily increase the coordination number z to systematically analyse the limit $z \to \infty$. This limit is revelant, for example, in dense surface spin ensembles. The respective information conservation of the initial spin polarisation is described via the associated autocorrelation function. By performing an extrapolation in the system size, we examine whether dynamical mean-field theories might be applicable to spin systems as long as they are dense, i.e. consisting of many mutually connected constituents. In chapter 7, we describe a novel theoretical method to obtain Green's functions in reduced operator subspaces. Eventually, we motivate possible applications to the single impurity Anderson model, i.e. the FHM in the boundary case of infinite dimension, e.g. to efficiently compute and characterise the Kondo physics inherent in the model. The key findings of this work as well as further suggestions for upcoming research are summarised and discussed at length in the concluding chapter 8.

2 Fermi-Hubbard model and its limiting cases

The Fermi-Hubbard model (FHM) describes strongly correlated electrons in a lattice. It has been proposed independently by Hubbard [10], Kanamori [11] and Gutzwiller [12] and was consequently used to describe general condensed-matter systems with narrow energy bands, metal-insulator transitions, itinerant ferromagnetism and high-temperature superconductors. It is a specialised version of the more general Pariser-Parr-Pople model being prominent in quantum chemistry and outlined about ten years ealier [34, 35]. While the Pariser-Parr-Pople model also includes Coulomb intersite interactions [36] the mutual interactions in the Hubbard model are assumed to be confined to particles on the same lattice site. This fully screened on-site interaction renders the FHM one of the simplest models possible for describing interacting fermions in a solid.

In spite of this remarkable conceptual simplicity, the FHM is impressive in two ways: on the one hand, it is capable of explaining a whole range of physical phenomena in solids, and on the other hand, it has remained closed to complete solutions for decades. Only in very few and special cases the FHM is solvable at all.

In the following chapter, we will first discuss the actual model and its characteristic properties, and then present models related to the FHM. These derived models cover special physical cases in a form much easier to handle while at the same time maintaining the fundamental physical features. It turns out, for example, that the FHM in second-order perturbation theory is well-suited to describe high-temperature superconductivity in a certain class of materials. Moreover, the FHM can be mapped onto the Heisenberg model in the case of half-filling or results – in the limiting case of infinitely large dimensions or coordination numbers – in a model with which a magnetic impurity in metals can be described. This makes the FHM suitable for the description of Kondo-like phenomena.

In the course of this thesis all models presented in the following, i.e. both the complete FHM as well as its simplified limiting cases, will be analysed. For the respective physical applications, the model which best describes the physical situation at hand will be chosen.

2.1 Fermi-Hubbard model

2.1.1 Real space representation

The complete FHM consists of two contributions which are the single particle term H_0 and the two-particle interaction term H_{int}. While H_0 describes the hopping of tightly bound electrons through a lattice the interaction part mimics a highly oversimplified fully local Coulomb interaction due to screening. Here and in the following, $f_{i\sigma}^{\dagger}$ and $f_{i\sigma}$ describe creation and annihilation operators for creating or annihilating a particle of spin σ at the lattice site i at position $\mathbf{r}_i$ and $\widehat{n}_{i\sigma} = f_{i\sigma}^{\dagger} f_{i\sigma}$ denotes the occupancy number operator. The one-particle basis used for this purpose consists of Wannier functions [9, 37] which are a complete set of orthogonal functions. Taking only one band into consideration and denoting the hopping elements[1] between adjacent sites with J_{ij} and the on-site interaction with U_i leads to the full Fermi-Hubbard Hamiltonian $H = H_0 + H_{\mathrm{int}}$ with

$$H_0 = -\sum_{\langle i,j\rangle,\sigma} J_{ij} f^{\dagger}_{i\sigma} f_{j\sigma}, \tag{2.1a}$$

$$H_{\mathrm{int}} = \sum_{i\sigma} U_i \widehat{n}_{i\uparrow} \widehat{n}_{i\downarrow}. \tag{2.1b}$$

In spite of its seemingly simple nature, merely the one-dimensional FHM as shown in figure 2.1 and the FHM in infinitely many dimensions can be solved exactly. But even for these two limiting cases the approaches themselves have nothing in common. While the one-dimensional model fulfils the Yang-Baxter conditions [38, 39] and is solved by resorting to a Bethe ansatz in the form of Lieb-Wu equations [14, 40] the model of infinitely many dimensions is solved by a dynamical mean-field theory (DMFT) approach and, therefore, mapped onto a self-consistent single impurity Anderson model (SIAM) which yields the same local Green functions under specific conditions [41]. We take another look at the SIAM in more detail in section 2.4.

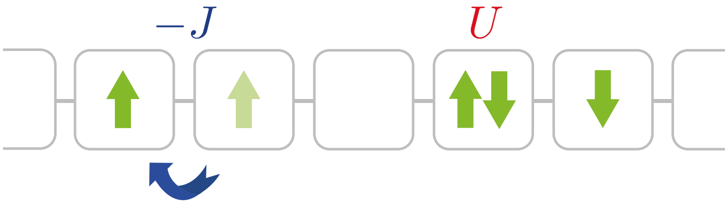

Figure 2.1: Illustration of the one-dimensional Fermi-Hubbard model in real space with constant hopping $J_{ij} = J$ and on-site interaction $U_i = U$ taken from Ref. [42].

Like many models in solid state physics the FHM is a local quantum many-body system with interactions of finite range. Such systems can always be decomposed [27] into a sum of individual h_i acting on a finite number of sites only, i.e. the Hamiltonian can be described by the sum

$$H = \sum_i h_i. \tag{2.2}$$

Comparable systems for which the decomposition (2.2) is possible are, e.g. spin lattice systems, bosonic or fermionic lattice systems, models with short range interactions or even long range interactions with polynomially decaying strengths.

It is worth to reconsider the fact that one specific site has a finite number of interaction partners only. This implies that each lattice or cluster can be described by means of a graph $G = (V, E)$ whose vertices V label and contain information about sites and whose

---

[1] Contrary to other conventions, the abbreviation J_{ij} is chosen here and in the following for the hopping matrix elements instead of t_{ij}. We choose this notation intentionally in order to avoid possible confusion of the hopping matrix elements with the time t.

edges E connect interacting vertices. We revisit this very aspect in more detail in the context of exactly solving many-body quantum systems in section 3.1.1.

2.1.2 Momentum space representation

While the most general form of the FHM, cf. equation (2.1), for non-vanishing hopping and interaction strengths, i.e. $J_{ij} \neq 0$ and $U_i \neq 0$, lacks an analytical solution for arbitrary dimensions the opposite case of vanishing on-site interactions can be solved in a simpler way for translationally invariant lattices. Since the underlying Fourier transform motivates a vivid and easily accessible representation of the so-called Fermi sea state – the ground state of H_0 – the respective ansatz will be given here for illustrative purposes.

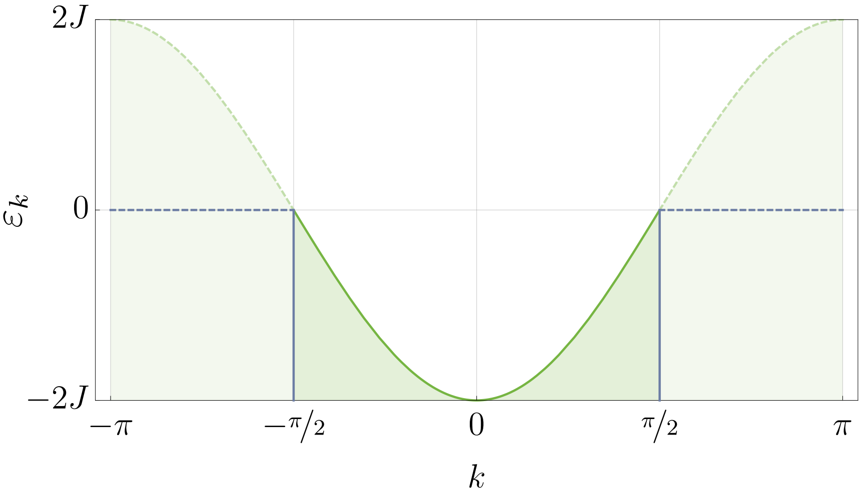

Figure 2.2: Dispersion relation ε_k as given in (2.5) for the one-dimensional Fermi-Hubbard model over the first Brillouin zone at half-filling. The momentum of the highest occupied state is denoted by solid blue lines, the Fermi energy ε_F by dashed blue lines. Occupied states are shown in dark-green, unoccupied states in pale-green. Figure reprinted from Ref. [43].

Since $H(U=0) = H_0$ holds with H_0 being an effective one-particle problem of an electron in a lattice-periodic potential with discrete translational symmetry, the Bloch theorem [44] ensures that an energy eigenbasis of Bloch functions exists. The corresponding transformation for a crystal of N unit cells is performed by a Fourier transform of the Wannier creation and annihilation operators using

$$f^\dagger_{\mathbf{k}\sigma} = \frac{1}{\sqrt{N}} \sum_j f^\dagger_{j\sigma} e^{i\mathbf{k}\mathbf{r}_j} \tag{2.3}$$

and the Hermitian conjugate, respectively. Inserting equation (2.3) into (2.1) leads to the Fermi-Hubbard Hamiltonian in the eigenbasis of the one-particle part H_0. Therefore, the momentum space representation of the real space Hamiltonian (2.1) is given by

$$H_0 = \sum_{\mathbf{k}\sigma} \varepsilon_{\mathbf{k}} f^\dagger_{\mathbf{k}\sigma} f_{\mathbf{k}\sigma}, \tag{2.4a}$$

$$H_{\text{int}} = \frac{U}{N} \sum_{\mathbf{k}\mathbf{k}'\mathbf{q}} f^\dagger_{\mathbf{k}+\mathbf{q}\uparrow} f^\dagger_{\mathbf{k}'-\mathbf{q}\downarrow} f_{\mathbf{k}'\downarrow} f_{\mathbf{k}\uparrow}. \tag{2.4b}$$

Then, the dispersion relation in the case of a hypercubic d-dimensional lattice reads

$$\varepsilon_{\mathbf{k}} := -2J \sum_{i=1}^{d} \cos\left(\mathbf{k}\mathbf{r}_i\right). \tag{2.5}$$

It is depicted in figure 2.2 for the one-dimensional model, i.e. $d = 1$, at half-filling. Now, the intuitive approach towards constructing the Fermi sea as the ground state of H_0 is easy to perform. Starting by filling the energetically lowest lying state at the energy $\varepsilon_0 = -2J$ and gradually inserting further particles into the system in the order of increasing energy up to a threshold given by the Fermi energy ε_{F} leads to the state of minimum overall energy for a fixed total number of particles.

Once the local repulsion is turned on the electrons are scattered by the non-diagonal contribution (2.4b) while conserving the total (lattice) momentum $\mathbf{k}+\mathbf{k}' = \mathbf{k}+\mathbf{q}+\mathbf{k}'-\mathbf{q}$ due to the discrete translational invariance of the underlying model. In this case, the underlying dynamics of the model changes fundamentally and previous one-particle approaches have to be replaced by much more advanced techniques to gain insight into the physical processes and the behaviour of observables in the model. We discuss such approaches especially in chapter 3 for time-dependent observables and in chapter 4 for the respective thermodynamic properties.

2.1.3 Symmetries and model properties

One of the most trivial and yet most important properties of the Hamiltonian (2.1) is its conservation of the number of particles N_σ of spin σ due to $\left[H, \widehat{N}_\sigma\right] = 0$ with

$$\widehat{N}_\sigma = \sum_i \widehat{n}_{i\sigma} \tag{2.6}$$

and, therefore, also its conservation of the total particle number $N = N_\uparrow + N_\downarrow$. This stems from the $U(1)$ symmetry which can be proven by inserting the transformation

$$f^\dagger_{j\sigma} \to f^\dagger_{j\sigma} \exp\left(i\alpha\right) \tag{2.7}$$

as well as its Hermitian conjugate for the creation and annihilation operators. Here, α denotes an arbitrary global phase. Moreover, the model possesses a spin-flip symmetry $\sigma \to -\sigma$ as part of its $SU(2)$ symmetry.

The latter one results in the fact that the Hamiltonian commutes individually with all global spin operators of the form

$$S^\alpha = \frac{1}{2}\sum_{i,ab} f^\dagger_{ia}(\sigma^\alpha)^a_b f_{ib} \qquad \forall\, \alpha \in \{x,y,z\} \quad \text{with} \quad a,b \in \{\uparrow,\downarrow\} \tag{2.8}$$

where i labels the sites, a and b denote the possible spin combinations and σ^α is given by the respective Pauli matrix

$$\sigma^x = \begin{pmatrix} 0 & 1 \\ 1 & 0 \end{pmatrix}, \qquad \sigma^y = \begin{pmatrix} 0 & -i \\ i & 0 \end{pmatrix} \qquad \text{or} \qquad \sigma^z = \begin{pmatrix} 1 & 0 \\ 0 & -1 \end{pmatrix}. \tag{2.9}$$

As a result, this renders the following quantities good, i.e. conserved, quantum numbers

$$[H, S^\alpha] = \left[H, \mathbf{S}^2\right] = 0. \tag{2.10}$$

Further highly non-trivial conserved quantities can be deduced for special cases such as the partly U-dependent integrals of motion of the one-dimensional model [14] or, more generally, the particle-hole symmetry in the case of half-filling on a bipartite lattice.

As we will be often working in situations where the latter symmetry is preserved a brief motivation [45] shall be given in the following. First, we consider a bipartite lattice, i.e. a lattice whose vertices can be separated into two independent sets of vertices V_1 and V_2 such that every edge connects vertices of both sets but no edge connects vertices within the very same set V_i. Second, we perform the particle-hole transformation

$$f^\dagger_{i\sigma} \to f_{i\sigma}, \qquad f_{i\sigma} \to f^\dagger_{i\sigma} \tag{2.11}$$

which changes the role of particles and holes and thus modifies the occupancy number operator of a given site to become

$$\widehat{n}_{i\sigma} = f^\dagger_{i\sigma} f_{i\sigma} \to f_{i\sigma} f^\dagger_{i\sigma} = 1 - \widehat{n}_{i\sigma}. \tag{2.12}$$

Obviously, equation (2.12) can only be invariant for half-filling which is a strong hint at the central prerequisite for particle-hole symmetry in the FHM. We verify this assumption by negating the creation operators on only one of the two sublattices V_2 using

$$f^\dagger_{i\sigma} \to -f^\dagger_{i\sigma} \text{ if } i \in V_2 \tag{2.13}$$

and, thus, transforming the Hamiltonian to become $H \to H + U(|\Lambda| - N)$ where Λ denotes the set of lattice vertices and $|\Lambda|$ gives the number of sites. In the case of exact half-filling the number of sites equals the number of particles in the lattice. This is the reason why the Fermi-Hubbard Hamiltonian is invariant under a particle-hole transformation in this specific situation.

2.2 Generalised t–J model

2.2.1 Copper oxides and superconductivity

In view of the striking ease with which we analysed and analytically solved the limiting case of a non-correlated system, i.e. a system with $U = 0$, in section 2.1.2, the question arises as to whether the limiting case of strong correlation, i.e. $J/U \ll 1$, can be dealt with just as easily. When answering this we will concentrate on the case of half-filling.

The introduction of a not negligible on-site interaction U leads to the situation that electrons as charge carriers can no longer move completely freely. Their movement is restricted in particular by the effort not to realise the undesirable case of a double occupancy (DO) of the same lattice site. This trend of energetically highly unfavourable states can also be seen when looking at the local density of states $\rho(E)$ of the Hubbard model in the limiting case of strong interaction: It splits into two parts, the lower and the upper Hubbard band (LHB and UHB), cf. figure 2.3.

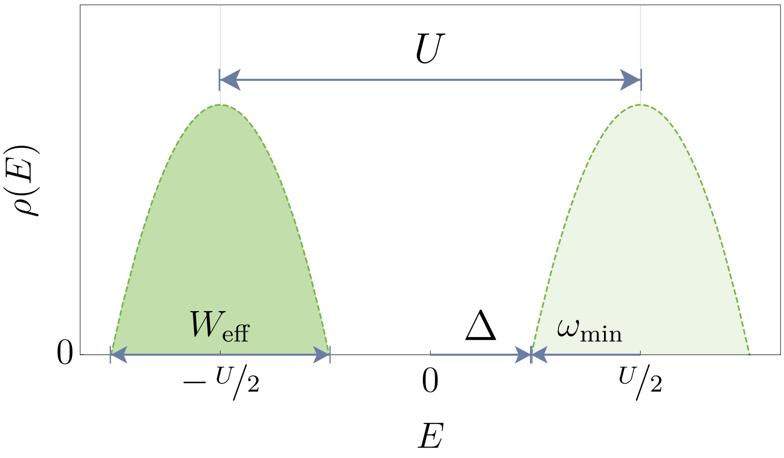

Figure 2.3: At half-filling and for $J/U \ll 1$, the local density of states $\rho(E)$ splits into the LHB and the UHB with each band having the effective bandwidth W_{eff}. Exactly at half-filling the LHB is completely filled while the UHB is empty. Thus, charge excitations have a minimum excitation energy of the spectrum gap Δ [46].

To introduce charge carrier excitations into the half-filled system with the Fermi energy ε_{F} lying in between the LHB and the UHB, at least the energy amount Δ, the so-called Mott gap, must be applied to overcome the excitation gap in the spectrum. The resulting excitations take the form of double occupancies (DOs) by electrons or holes. The ground state of this strongly correlated system is an insulator. In this state the electrons are spatially fixed and only their magnetic moments undergo mutual (exchange) interactions. For this reason, it is energetically advantageous for the localised electrons to have the singlet state of antiparallel aligned spins.

If one leaves the exactly half-filled state and thus allows deviations in the occupancy number of the lattice, from a physical point of view the movement of DOs in an antiferromagnetic background is studied. However, why is this scenario relevant at all?

Even though already discussed in 1970 [47], the great interest in the Hubbard model in the limiting case of strong interaction exists especially since the discovery of high-temperature superconductivity in the copper oxide $\mathrm{La}_{2-x}\mathrm{Ba}_x\mathrm{CuO}_4$ in 1986 by Bednorz and Müller [7] with the then highest ever measured transition temperature of a superconductor of only 30 K. Since then, the family of copper oxides has more and more become the focus of research - in the constant hope of superconductivity at room temperature. Although, in the meantime, much higher transition temperatures almost close to room temperature could be realised, see e.g. Ref. [48], the corresponding physical materials mostly suffer from one problem: They only become superconducting at very high pressure.

It continues to be a challenge to establish superconductivity at room temperature. The highest temperatures currently achievable for superconductivity without additional external pressure are in the range of $T \approx 133\,\mathrm{K}$ [49]. An applicability in typical scenarios of day-to-day life is thus impossible and further research therefore inevitable. For these studies the family of copper oxides is still an important candidate with regard to the realisation of high-temperature superconductivity and with it in particular one physical model, the generalised t–J model as a limiting case of the FHM with strong interaction. A detailed discussion and derivation of the t–J model can be found in section 2.2.2.

Unfortunately, even with the t–J model as a simplified version of the FHM the theoretical description of the motion of a DO in an antiferromagnetic background remains highly demanding [13, 50]. Despite various efforts, for example by resorting to self-consistent Born approximations [51], cumulant [52] or spin-wave [53] expansions, perturbative approaches [54] or limited functional spaces [55], it has not yet been possible to develop satisfactory theoretical tools to describe the dynamics of such systems in equilibrium or, lately, even away from equilibrium [56]. For instance, it has been shown that highly non-trivial quantum effects occur when holes move in a perfectly ordered antiferromagnet: one hole can destroy the ordered background, whereas a second hole can restore it [57]. Consequently, both holes perceive the existence of each other. Thereby, an effective attraction between the two holes is created. Such effects naturally prohibit the treatment of the problem with effective one-particle methods, which in turn creates a variety of methodical problems. Moreover, the fundamental mechanism of charge carrier interaction via the environment is very reminiscent of the explanation by Bardeen, Cooper and Schrieffer (BCS) for conventional superconductivity at low temperatures [5] proposed as early as 1957. Here, two electrons can interact via lattice deformations, quantised by phonons, and form so-called Cooper pairs. These Cooper pairs can then move through the surrounding crystal lattice without collision or energy dissipation.

With this conceptual similarity of the mechanisms, the question naturally arises why the theoretical description for conventional BCS superconductivity cannot simply be adapted to the high-temperature superconductivity domain. The BCS explanation for superconductivity is a mean-field approach, which is justified in particular by the fact that the average distance between the two constituents of a Cooper pair, the correlation length ξ, is far greater than the average distance between Cooper pairs. As a result, the Cooper pairs mix and it is justified to consider the resulting average effects of all

BCS quasiparticles. This is not the case with high-temperature superconductivity in copper oxides as they consist of several distinct CuO_2 layers with two different correlation lengths, cf. especially Ref. [58]. The correlation length $\xi_\perp$ is measured perpendicular to the CuO_2 planes, the correlation length $\xi_{||}$ parallel to the planes. While $\xi_\perp$ is significantly smaller than the distance between the planes, even $\xi_{||}$ is only a few lattice constants in size. The small correlation length $\xi_\perp$ causes Cooper pairs of different planes to mutually interact with a very small probability. The electronic states and, thus, the actual high-temperature superconductivity in copper oxides are therefore effectively a two-dimensional phenomenon. The second correlation length $\xi_{||}$ is slightly larger but still small compared to the average free distance of the charge carriers. Correspondingly, the Cooper pairs, which are not strongly spread out, hardly mix and a mean-field approach is not justified. This is a consequence of the fact that mean-field approaches are more suitable in higher dimensions $d > 2$.

It is reasonable now to assume that at least the treatment of a freely moving hole in a *disordered* background is possible with classical one-particle methods. After all, in this case there is no order at all that could cause attractive effects. But even that is not possible. It was shown that the one-particle gap $1/2 \cdot (W - U)$ with W being the bandwidth of the system is only reproduced in the limit $U \to \infty$ and for movements with self-retracing paths, for example in one dimension [59–61]. Once the interaction U changes only slightly towards a finite value, however, the situation is altered significantly. Accordingly, the prediction at which critical U_c the band gap in the density of states $\rho(E)$ opens up becomes much more complicated. For the infinite-dimensional case at finite U there are a great number of analyses with consistent qualitative and slightly differing quantitative results [62–65].

Since in the one-dimensional case an exact analytical approach is available with the Bethe ansatz [14], for this case reliable reference results can be obtained, for example for benchmarking numerical or approximate methods. The completely disordered spin background here corresponds illustratively to a case where $J \ll T \ll U \approx W$. This means that the temperature T is high compared to the typical energy scale of spins J, but small compared to the Hubbard interaction U. The spin background is therefore obviously hot and all spins are essentially disordered. For the charge carrier excitations, however, the situation is different. Here, the system behaves as if it had a temperature of $T \approx 0$. The few excitations in the system are therefore exclusively formed by DOs. Only these determine the dynamics significantly. The critical minimal interaction for the emergence of a band gap in the disordered one-dimensional model was determined to be $U_\mathrm{c} = \sqrt{3}/2 \cdot W$ [66].

In summary, it can be said that the calculation of dynamical structure properties in cases other than the one-dimensional case still poses significant challenges for the theoretical methods and that, in particular, the two-dimensional t–J model is of outstanding importance due to its explanatory character for high-temperature superconductivity in copper oxides. The ability to understand and predict the movement of DO charge carriers in the generalised t–J model can hardly be overestimated in its importance.

2.2.2 Analytic derivation for strong interactions

There are many different ways of analytically motivating and deducing the t–J model, see for instance the derivations in Refs. [67, 68]. One of the most elegant and shortest ways relies on second-order perturbation theory. The energy corrections of the insulating ground state and the charge carrier dynamics of a freely moving hole are then derived by means of a projection of the Fermi-Hubbard Hamiltonian (2.1) onto a reduced subspace such that the resulting effective Hamiltonian operates on states without any sites being occupied by two electrons at once. In order to separate these double occupancies by electrons from double occupancies by holes, i.e. unoccupied lattice sites, we introduce in the following an additional notation for double occupancies exclusively formed by electrons (eDO). This expression is thus to be separated from the previous abbreviation DO for any double occupancy. It is of importance to keep in mind that the t–J model prohibits eDOs exclusively.

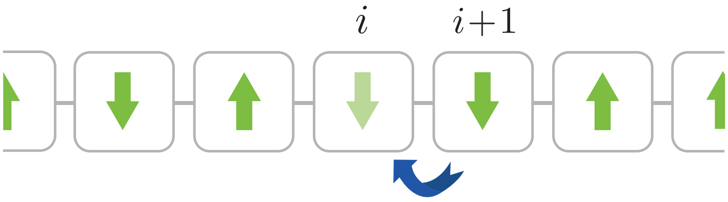

Figure 2.4: Illustration of the one-dimensional t–J model in real space. The system contains an additional hole, e.g. added via doping, which moves in the direction of the arrow, i.e. from $i+1$ to i. The movement of the parallely moving electron takes place in opposite direction and thus from i to $i+1$.

The following derivation is a highly abbreviated and partly modified version of Refs. [14, 59], of which the latter one is based in particular on Refs. [69, 70]. In order to be able to use perturbation theory successfully, it is necessary to identify a sufficiently small perturbation parameter in the very first step. For this, we assume that $J_{ij} \ll U_i = U$ holds and, thus, that the hopping H_0 described by (2.1a) is a small perturbation to the unperturbed Hamiltonian H_{int} as given in (2.1b). Since H_{int} implies a strong localisation of the particle at the individual lattice sites it is advisable to resort to the tight-binding representation of the model, cf. section 2.1.1.

Before we start with the actual derivation, it is helpful to consider the influence of the interaction term H_{int} on the structure of the Hilbert space $\mathcal{H}$. For this we first consider the operator

$$\widehat{D} := H_{\text{int}}/U = \sum_i \widehat{n}_{i\uparrow}\widehat{n}_{i\downarrow}. \tag{2.14}$$

Here, the operator $\widehat{n}_{i\uparrow}\widehat{n}_{i\downarrow}$ measures whether the site i is occupied by two electrons, so that $\widehat{D}$ calculates the sum of all eDOs for a given state. Its eigenvalues are therefore $D \in \{0, \ldots, N\}$, since a minimum of zero and a maximum of all lattice sites can have an eDO. Just like H_{int} also $\widehat{D}$ is block diagonal in the chosen basis. This fact implies that the underlying Hilbert space

$$\mathcal{H} = \mathcal{H}_0 \oplus \ldots \mathcal{H}_N \tag{2.15}$$

splits into different independent subspaces $\mathcal{H}_i$ with exactly i eDOs each. The projectors onto these subspaces $\mathcal{H}_i$ with a fixed number of eDOs are called P_i in the following.

Since the ground states of the Mott insulator cannot have any eDOs, these states are fully located in the corresponding subspace $\mathcal{H}_0$ with the respective projector

$$P_0 = \prod_i \left(1 - \widehat{n}_{i\uparrow}\widehat{n}_{i\downarrow}\right). \tag{2.16}$$

Since a product is zero exactly when at least one of its factors vanishes, the operator P_0 applied to a many-particle state ensures that only states without a single eDO remain. Note that the projector P_0 in its explicit form (2.16) has no effect on states with double occupancies caused by holes. So if a given lattice site i is unoccupied, the application of P_0 to this site results in the neutral element with respect to multiplication, i.e. a one. Thus, charge carrier dynamics of holes added to the system, e.g. by means of doping, is maintained after an application of P_0 as can be seen in figure 2.4.

The typical generalised t–J model does not leave the respective subspace $\mathcal{H}_0$, i.e. the associated Hamiltonian only links states with each other in which there is at most one electron on each lattice site. With this motivation in mind, the second-order perturbation theory for the rescaled Hamiltonian

$$H/U = \widehat{D} + \lambda H_0 \tag{2.17}$$

may be performed in the parameter $\lambda = {}^1\!/_U$ as done in Ref. [14] resulting in an expression for the individual subspace contributions to the unperturbed energies E_n as

$$\left[P_n H_0 P_n + \lambda \sum_{m\neq n} \frac{P_n H_0 P_m H_0 P_n}{E_n - E_m}\right] |\psi\rangle = \frac{E - E_n}{\lambda}\, |\psi\rangle \tag{2.18}$$

when applied to an arbitrary state $|\psi\rangle$. The expression (2.18) is merely a slightly generalised version of conventional second-order perturbation theory, as it appears in various textbooks for energy corrections in degenerate subspaces, cf. in particular Ref. [71]. Since we are especially focused on corrections of energy and dynamics in the Hilbert space without a single eDO, we set $n = 0$ and $E_0 = 0$ in (2.18) and get the conventional representation of the generalised t–J model [14, 59, 72] after some basic commutations and rearrangements as

$$H_{t-J} = P_0 \left[H^{(2)}_{t-J} + H^{(3)}_{t-J}\right] P_0 \tag{2.19a}$$

$$H^{(2)}_{t-J} = \sum_{jk\sigma} J_{jk} f^\dagger_{j\sigma} f_{k\sigma} + \sum_{jk} \frac{2|J_{jk}|^2}{U} \left(\mathbf{S}_j \mathbf{S}_k - \frac{\widehat{n}_j \widehat{n}_k}{4}\right) \tag{2.19b}$$

$$H^{(3)}_{t-J} = \frac{1}{U} \sum_{\substack{j\neq k\neq l\neq j\\ \sigma\sigma'}} J_{jk} J_{kl} \left(f^\dagger_{j\sigma} \boldsymbol{\sigma}_{\sigma\sigma'} f_{l\sigma'} \mathbf{S}_k - \frac{1}{2} f^\dagger_{j\sigma} f_{l\sigma} \widehat{n}_k\right) \tag{2.19c}$$

with the spin operators $\mathbf{S}_i$, the vector of the Pauli matrices $\boldsymbol{\sigma} = (\sigma^x, \sigma^y, \sigma^z)^T$ and the occupancy number operator $\widehat{n}_i = \widehat{n}_{i\uparrow} + \widehat{n}_{i\downarrow}$. The superscripts in (2.19) describe the number of lattice sites involved in the processes being considered by the respective Hamiltonian. Since H_{t-J} does not contain any contributions which create or annihilate particles the whole t–J model conserves the total number of particles in the system, i.e.

$$\left[H_{t-J}, \widehat{N}\right] = 0. \tag{2.20}$$

Furthermore, the Hamiltonian (2.19) has an effect on $\mathcal{H}_0$ only due to its projectors P_0. The first sum of the t–J model in equation (2.19b) describes normal hopping, the second sum represents the exchange interaction of the spins localised at the individual lattice sites and the third sum (2.19c) reflects processes that describe correlated hopping over exactly three lattice sites. In particular, this correlated hopping is often omitted in the consideration of the model. The name t–J model comes from the fact that – in conventional naming of the hopping matrix elements by t_{ij} and omitting the three-place contributions – the essential contributions of the model are given by hopping as well as by the exchange interaction of the spins. The exchange interaction, i.e. the parameter before the spin-spin interaction, is often referred to as J.

2.3 Heisenberg model

In 1928, Heisenberg drew parallels between the nature of ferromagnetism and that of the helium atom in a phenomenological way, postulating that ferromagnetism, too, must be caused by a kind of exchange interaction [73]. Since its first description, the Heisenberg model has been used countless times, particularly to describe ferro-, antiferro- and ferrimagnetism in insulators. The Heisenberg model does not capture magnetic properties of metallic materials with moving electrons. The reason for this becomes obvious when considering the t–J model once again – this time in the limit of half-filling. Since the complete t–J model according to equation (2.20) does not change the total number of particles in the system and, furthermore, eDOs are not allowed, the t–J model can be significantly simplified for half-filling. If exactly N electrons have to be distributed over N lattice sites without creating a single eDO, the only allowed configuration is the one with one electron per lattice site. Thus, the eigenstates of the Hamiltonian H_{t-J} in the half-filled system consist of completely spatially fixed spins. Due to the fact that in such case hopping processes – no matter whether simple or correlated hopping across three lattice sites – are impossible, the t–J model is reduced to pure spin-spin interaction as

$$H_{t-J}^{\mathrm{HF}} = \sum_{jk} \frac{2|J_{jk}|^2}{U} \left(\mathbf{S}_j \mathbf{S}_k - \frac{1}{4}\right). \tag{2.21}$$

Since the last summand in equation (2.21) only makes an absolute energy correction, it can be neglected when considering the dynamics of the model. In this case, however, the resulting model is nothing other than the Heisenberg model

$$H_H = \widetilde{J} \sum_{\langle i,j \rangle} \mathbf{S}_i \mathbf{S}_j \tag{2.22}$$

provided that the interaction is restricted to nearest neighbours, which results in an elimination of one of the sums and, thus, in a global factor of 2, and provided that the quotient of hopping elements $J := J_{ij}$ and the repulsive Hubbard interaction strength U is identified as the exchange interaction

$$\widetilde{J} = \frac{4J^2}{U}. \tag{2.23}$$

Further extensions of the Heisenberg model are feasible and can easily be carried out. For instance, next-nearest neighbour interactions can be included in a similar manner.

Being essentially a scalar product of two spin operators $\mathbf{S}_i$, the Heisenberg model is completely invariant to rotations and any arbitrary direction in space can be selected as the quantisation direction of the spins. Without limitation of the generality we choose the z-axis as quantisation direction in the following. A depiction of the Heisenberg model in such a quantisation direction can be found in figure 2.5. There are many different variants of the Heisenberg model. For example, the isotropy of the model (2.22) can be broken by adding an external magnetic field or by using different exchange interaction strengths $\widetilde{J}_i$ for the different directions in space (as in the well-known XXZ model). As such modifications of the model do not play a role in the following work, they will not be discussed in more detail. Moreover, mappings are possible by transformations, e.g. by a Jordan-Wigner transformation to spinless fermions in the case of one-dimensional chains with periodic boundary conditions or also by a transformation to permutation operators in the case of only two possible spin orientations, i.e. $s = 1/2$. The latter case is particularly helpful for computationally analysing the Heisenberg model and its effect on states of an occupancy number basis and will be used at a later stage.

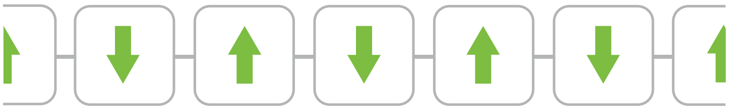

Figure 2.5: Illustration of the one-dimensional Heisenberg model in real space. The system consists of fixed spins which interact via exchange coupling with each other. No hopping processes of particles can take place.

To see the motivation for this reformulation, we first replace the scalar product in equation (2.22) with an equivalent expression using the spin ladder operators

$$S^{\pm} = S^x \pm i S^y \tag{2.24}$$

which can be shown to obey to the following commutation and anticommutation relations

$$\left\{S^+, S^-\right\} = 1, \tag{2.25a}$$

$$\left[S^+, S^-\right] = 2S^z \tag{2.25b}$$

and act on a spin state $|\sigma\rangle$ by either changing its orientation or extinguishing it

$$S^- S^+ |{\downarrow}\rangle = S^- |{\uparrow}\rangle = |{\downarrow}\rangle \tag{2.26a}$$

$$S^+ |{\uparrow}\rangle = S^- |{\downarrow}\rangle = 0. \tag{2.26b}$$

By using (2.24) the respective Heisenberg Hamiltonian in spin ladder operators reads

$$H_H = \frac{\widetilde{J}}{2} \sum_{\langle i,j \rangle} \left(S_i^+ S_j^- + S_i^- S_j^+ + 2S_i^z S_j^z \right). \tag{2.27}$$

The general structure in (2.27) implies that, on the one hand, there is a swapping of the orientations of the spins at the sites i and j, and on the other hand, there is a measuring process that does not change the state because S^z is included in the complete set of commutating observables of the basis. This observation suggests the substitution of all spin operators by permutation operators P_{ij}. Such a permutation operator P_{ij} exchanges the spin information[2] at lattice site i with that at site j. Consequently, the general structure of the new Hamiltonian is

$$H_H^{(c)} = \frac{\widetilde{J}}{2} \sum_{\langle i,j \rangle} (P_{ij} + c) \text{ with } c \in \mathbb{R} \tag{2.28}$$

with an additive constant c to be determined. Obviously, as this constant is only an absolute shift of energies, it is of no further interest for the dynamics of the system. Nevertheless, we want to derive it exactly in the following and prove the equivalence of the permutation operators and the spin operators for an $s = 1/2$ Heisenberg model simultaneously. Here, we choose $\widetilde{J} = 1$ for the sake of brevity.

The two representations are exactly identical if and only if the effect of the operators on the states is the same. As there are only two lattice sites involved and on each of them two spin orientations are possible, there are four cases in which the effects have to be identical. We start with the case of identical spin orientations, where the spin ladder operators cannot have any effects, so that

$$H_H |\sigma\sigma\rangle = S_i^z S_j^z |\sigma\sigma\rangle = \frac{1}{4} |\sigma\sigma\rangle \tag{2.29}$$

---

[2] Please note that a substitution of the spin operators $\mathbf{S}_i \mathbf{S}_j$ by the permutation operator P_{ij} is naturally also possible in the case of the original t–J model in (2.19b). However, especially in the general t–J model, which also permits the presence of holes, there is a subtle aspect to be considered: The phrase *spin* information is to be taken literally. The permutation operator P_{ij} exclusively exchanges the spin at lattice site i with that at site j, it does not act on unoccupied sites and thus, above all, does not exchange a spin with a hole.

holds. The effect of the permutation operator on these states follows analogously

$$H_H^{(c)} \left|\sigma\sigma\right\rangle = \frac{1}{2} \left(P_{ij} + c\right) \left|\sigma\sigma\right\rangle = \frac{1}{2}(1 + c) \left|\sigma\sigma\right\rangle \tag{2.30}$$

so that the constant $c = -{}^1\!/_2$ can be determined. We proceed in the same way for states of mixed orientation, where $\overline{\sigma}$ symbolises the opposite orientation to σ. This leads to

$$H_H \left|\sigma\overline{\sigma}\right\rangle = \frac{1}{2} \left|\overline{\sigma}\sigma\right\rangle - \frac{1}{4} \left|\sigma\overline{\sigma}\right\rangle \tag{2.31}$$

for the effect of the Heisenberg Hamiltonian and to

$$H_H^{(c)} \left|\sigma\overline{\sigma}\right\rangle = \frac{1}{2} \left|\overline{\sigma}\sigma\right\rangle + \frac{c}{2} \left|\sigma\overline{\sigma}\right\rangle \tag{2.32}$$

for the effect of the Hamiltonian using the permutation representation. Again, we see that $H_H = H_H^{-1/2}$ holds. In the course of this work, we will use the alternative representation (2.28) of the Heisenberg model due to its computational simplicity.

2.4 Single impurity Anderson model

The single impurity Anderson model (SIAM) was introduced in 1966, cf. Ref. [74], to describe a system in which a single magnetic impurity is embedded in a group of otherwise conductive electrons of a host metal. Analogous to the foundations explained in section 2.1.2, the metal is best described in a momentum basis, whereas the impurity is a purely local phenomenon. Rigorously mathematically, however, the impurity breaks the strict translational symmetry. Thus, we can still consider the metal electrons phenomenologically as quasiparticles rather spread out over real space, yet we are no longer able to assign conserved momenta to these levels. Instead, we number the different energy levels in the bath, i.e. the metal surrounding the impurity, in ascending order. Here, the indices k do not represent a momentum, but an energy level in the basis with respect to which the Hamiltonian of the bath is diagonal. While the electrons of the bath perceive no interaction with each other, the impurity has energy levels dependent on its local occupancy number. It is modelled by two-particle interaction. The coupling of the impurity to the surrounding bath occurs via hopping processes in which an electron hops from the bath to the impurity or away from it.

Due to the general structure of many similar and interaction-free energy levels as well as the one position distinguished by the impurity and being coupled via hybridisation to the bath, it is by now common to represent and discuss the SIAM in a star-shaped topology. As shown in figure 2.6, in this topology the impurity is given by the central location and all bath electrons are connected to it via the different hybridisation strengths V_k. The undeniable advantage of such schematic modelling is that the SIAM by its design is not only able to describe impurities in metals, but can describe any system in which a single dedicated level is connected to many similar levels. As a result, the focus of research on the SIAM has also shifted slightly in the meantime and is more focused on quantum dots

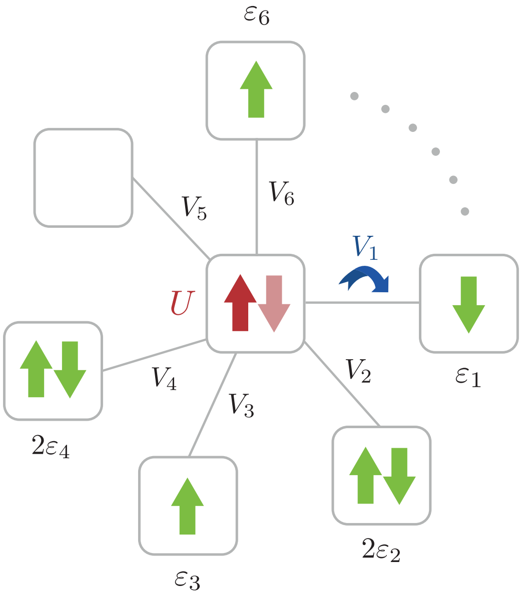

Figure 2.6: Illustration of the single impurity Anderson model with star-shaped topology. For demonstration purposes only the first six of the n_b bath levels and the central impurity site are shown. Only at the impurity site there is an interaction, bath levels cannot interact with each other. All bath levels are coupled to the central site via the hybridisation strengths V_k.

as well as research on electronics [75–77] making the SIAM the archetypal model for the treatment of quantum information storage and nanoelectronics.

From a purely theoretic perspective the SIAM describes a system in which only a single level has a true Hubbard interaction. For the sake of simplicity, this level will be referred to as zero below. Consequently, only at this zeroth level a real two-particle interaction exists. All other levels of the bath show the typical behaviour of itinerant electrons, i.e. the electrons of the bath are fully mobile without any restriction. These bath levels are coupled to the impurity via the hybridisation strengths V_k. In second quantisation and when using $f^\dagger_\sigma$ as a creation operator for a particle with spin σ at the impurity level and $c^\dagger_{k\sigma}$ for one with spin σ at the bath level k the model consists of the following contributions

$$H_{\text{SIAM}} = H_{\text{Imp}} + H_{\text{Bath}} + H_{\text{Hyb}} \tag{2.33a}$$

$$H_{\text{Imp}} = \varepsilon_0 \sum_\sigma f^\dagger_\sigma f_\sigma + U \widehat{n}_\uparrow \widehat{n}_\downarrow \tag{2.33b}$$

$$H_{\text{Bath}} = \sum_{k\sigma} \varepsilon_k c^\dagger_{k\sigma} c_{k\sigma} \tag{2.33c}$$

$$H_{\text{Hyb}} = \sum_{k\sigma} \left(V_k f^\dagger_\sigma c_{k\sigma} + \text{h.c.} \right) . \tag{2.33d}$$

The three previously motivated features can also be found here: H_{Imp} acts exclusively on the impurity and has a kinetic contribution and an interaction term, H_{Bath} solely describes the free electrons of the bath and H_{Hyb} couples the impurity to the bath. All fundamental dynamic processes of the SIAM are exemplified in figure 2.6. At the six illustrated energy levels of the bath any constellations consistent with the Pauli principle can be found, while merely the local energies ε_k are affected. Levels can be completely empty, such as level $k=5$, filled by one particle ($k=3$ and $k=6$) or even be completely filled ($k=2$ and $k=4$). For an exchange process between the impurity and any bath level the parameter V_k denotes the transition amplitude ($k=1$).

Considerably later than its phenomenologically motivated introduction in 1966, the emergence of DMFT allowed for another view on the SIAM. It could be proven mathematically rigorously that the SIAM is just another limiting case of the FHM – the limiting case of infinitely high coordination number z. It was first shown in 1989 that this limiting case of infinite dimensions $d \to \infty$ for hypercubic lattices with a resulting infinite coordination number $z \to \infty$ is a reasonable limit of the FHM with non-trivial physics [78]. In analogy to the ideas of statistical mechanics, such a limit cannot be obtained without rescaling the system parameters. While the interaction U does not require a rescaling at all, the hopping elements $J_{ij} = J$ have to be adjusted as the dimension increases. The initial motivation for this observation was the density of states in the case of vanishing interaction which follows by the central limit theorem [79] as

$$\rho(E) = \frac{1}{2J\sqrt{\pi d}} \exp\left(-\frac{E^2}{4dJ^2}\right). \tag{2.34}$$

To keep $\rho(E)$ finite at all times, the hopping element must be rescaled according to $J \to {}^{J}\!/\!\sqrt{2d}$. The examination of the model within this limit is not just a feasibility study. It was shown that the limit $d \to \infty$ is, on the one hand, able to provide robust results reproducing characteristic properties for three-dimensional materials, and on the other hand, that the analysis of the infinite-dimensional case is much easier than the case of finite dimensions. But why is this limit any simpler now?

To understand the dynamics of physical systems, it is mostly sufficient to be able to describe the average behaviour of one or two characteristic particles [80]. For this purpose, one often resorts to Green's functions or propagators $G(\mathbf{k}, \omega)$, which provide a convenient access to dynamic quantities. Such Green's functions are calculated from diagrammatic perturbation theory, e.g. via the Dyson equation

$$G(\mathbf{k}, \omega) = \frac{1}{G_0^{-1}(\mathbf{k}, \omega) - \Sigma(\mathbf{k}, \omega)} \tag{2.35}$$

with the self-energy $\Sigma(\mathbf{k}, \omega)$ and the non-interacting propagator $G_0(\mathbf{k}, \omega)$ of a free particle. The propagator of the free particle is easy to calculate, the complete determination of the self-energy – especially in case of strongly correlated systems – is arbitrarily complicated. In systems of infinitely large dimension, however, the self-energy Σ is independent of any momenta [81]. Thus, the Dyson equation is simplified significantly and the required interacting single-electron Green's function is only frequency-dependent. Conversely, this means that all processes that can contribute to the self-energy at all are completely local in real space. Unfortunately, this knowledge of a completely local self-energy alone does not automatically help. Nonetheless, with the SIAM one can find a model that has exactly the same self-energy as the FHM for $d \to \infty$ but is much easier to solve [82].

It is this systematic mapping of the FHM in infinite dimensions to the SIAM that provides a method for gaining insights into the FHM that would otherwise hardly be possible. In practice, this mapping of the FHM to a SIAM is often used especially in self-consistency calculations, in which a gradually increasing accuracy is achieved by repeated iteration of the Dyson equation for the last obtained result of the self-energy.

And yet, even solving the simplified SIAM is not easy. The many energy scales present in the model, as well as the fact that conventional perturbation theory approaches do not converge, make the numerical treatment of the SIAM a veritable challenge. Here, the energy scales emerging in the process comprise the (nearly) continuum of the bath energies to which the impurity can couple as an interacting system. This may lead to infrared divergences and the occurrence of the Kondo problem [83]. Many approaches exist from more conventional ones such as exact diagonalisation (ED) [84], density matrix renormalization group (DMRG) [85] or Bethe ansatz techniques [86] to highly specialised ones such as adapted quantum Monte Carlo (QMC) [87] approaches, but all suffer from different shortcomings. Be it that they only work for small systems (ED), that they are limited to one-dimensional systems (DMRG) or that analytical continuations of the imaginary-valued quantities to the real axis are ill-conditioned (QMC).

In particular, one method has turned out as the de facto way to treat the low-energy dynamics of the SIAM: the numerical renormalisation group (NRG), see e.g. Ref. [83] for an instructive review. Albeit approved and promising, a problem arises when several impurity sites are to be considered instead of one as the effort of NRG increases exponentially with the number of impurities in the system. The associated exponential decrease in accuracy can be partially remedied by a so-called z-averaging [88]. The fundamental principle behind this is to average over several calculations, each with a slightly different discretisation, in order to obtain an improved approximation of the continuum limit. Moreover, it is fairly difficult to resolve sharp spectral features of the high-energy spectrum using NRG due to its logarithmic discretisation. By now, first successful strategies towards this goal have been established by using dynamic DMRG [89, 90]. Considering the fact that especially abrupt changes of a system, such as those occurring due to quenching[3], generate short-term dynamics that take place on all time and thus energy scales, a non-existing access to the high-energy excitations of a system limits the applicability of a method to equilibrium. Even though systematic extensions of NRG to non-equilibrium situations exist under certain conditions [91, 92], at least one central facet still remains a major concern of NRG: The massive numerical complexity when extending the model or adding additional impurities.

In the context of this work, we adopt a semi-analytical method that addresses such shortcomings and is both numerically and analytically tractable with reasonable effort.

---

[3] For a dedicated discussion of the terminology as well as the problems and central issues arising in the context of quenching, see particularly chapter 5.

3 Approaches to operator dynamics

A central task in the analysis of solids is the determination of the time-dependent properties of the system. Such properties are generally described by physical observables O, i.e. quantities that can actually be measured for the system in experiments. If a system starts at the beginning of the measurement, i.e. at time $t = 0$, in the known state $|\psi(t{=}0)\rangle$, the time-evolution of the observable O is described by

$$O(t) = \langle\psi(t)|O|\psi(t)\rangle\,, \tag{3.1}$$

where $|\psi(t)\rangle$ evolves unitarily from the given initial state and the Schrödinger equation

$$i\frac{\partial}{\partial t}\,|\psi(t)\rangle = H\,|\psi(t)\rangle\,. \tag{3.2}$$

Here and henceforth, we constantly resort to natural units for simplicity, i.e. we set $\hbar = 1$. Specifically, for systems in non-equilibrium states, the calculation of such properties is highly demanding. But even for moderately large systems in equilibrium, it can be exceedingly challenging to capture the dynamics of the system due to the exponential growth of the Hilbert space with the number of system's constituents.

If we stick to the Schrödinger picture, the primary objective is to determine the time-evolution of the state $|\psi(t)\rangle$. For a Hamiltonian that does not explicitly depend on time, the stationary Schrödinger equation holds. The corresponding time-evolution operator reads

$$U(t) = \exp\left(-iHt\right) \tag{3.3}$$

and can be used to express the full time-evolution of an initial state by means of

$$|\psi(t)\rangle = U(t)\,|\psi(t{=}0)\rangle\,. \tag{3.4}$$

As simple as the phrasing of the actual algebraic problem is, as complex and sometimes sophisticated is the algorithmic implementation. It is not only the exponential growth of the Hilbert space that is problematic, the actual handling of quantum mechanical states in a computer also poses difficulties. In order to be able to represent a state or an operator, a problem-adapted and efficient basis is required. Here, *problem-adapted* means that the structural design of the basis states should be as close as possible to the physical reality of the problem, and *efficient* means that the representation should be chosen in such a way that computer resources are optimally utilised.

In this chapter we present various methods to deal with the above mentioned tasks. In order to do so, we start with basic ideas on the transformation of physical states and measurable quantities into mathematical representations in section 3.1.1 and derive the Hamiltonian governing the dynamics in the chosen representation in section 3.1.2. With this Hamiltonian, we discuss a naive approach to obtaining the operator dynamics as well as its respective limitations in section 3.2. Thereafter, we discuss a highly efficient numerically exact alternative to this naive method in section 3.3 and finally we turn to approximate, but extremely fast ways of determining the time-evolution (3.1) in section 3.4.

3.1 Exact approaches

3.1.1 Organising the Hilbert space

Henceforth, O shall denote a linear operator defined on a given Hilbert space $\mathcal{H}$ with dimension $d := \dim(\mathcal{H})$ and $\mathbf{O} \in \mathbb{C}^{d\times d}$ shall be the corresponding Hermitian matrix representing O in $\mathcal{H}$ with respect to a chosen basis. For the sake of brevity, we will drop the formal notation of $\mathbf{O}$ for a representation of the linear operator O altogether and use the latter symbol for both the matrix and the operator interchangeably. The respective context will clarify what is referred to.

In the FHM as stated in equation (2.1), a single lattice site may be either occupied by two electrons of different spin each $|\uparrow\downarrow\rangle$, by one electron of arbitrary spin orientation which reads $|\uparrow\rangle$ or $|\downarrow\rangle$ or it may not be occupied at all as in the state $|\circ\rangle$.[1] In order to organise the Hilbert space it is necessary to introduce particular conventions to properly account for the fermionic algebra. The following way of labelling and dealing with sites and states is by far not the only one but has proven to be especially handy and fast when dealing with large amounts of data as in the case of even moderately sized systems. Since this issue of exponentially growing Hilbert space sizes stems from physical restrictions there is no general remedy for it. Nevertheless, the typical system sizes can be heavily enlarged by exploiting physical properties and symmetries of the FHM like particle conservation which we will use in the following.

Figure 3.1: Graph representation of a system with $N = 2$ sites and arbitrary but fixed vertex labelling.

We start by modelling the topology of a given finite site cluster as described in section 2.1.1, i.e. by means of a graph. Thus, the site cluster is described by the undirected graph $G = (V, E)$ consisting of consecutively labeled vertices (sites) V each having information about its local repulsion U_i and edges (hopping matrix elements) E. The most natural representation of an undirected graph G is by means of its adjacency matrix $A(G)$. The adjacency matrix of a finite site cluster of size N is a square matrix of size $N \times N$ whose matrix elements $a_{ij} := J_{ij}$ denote the hopping elements for a hopping between the sites i and j. Since in our model $J_{ij} = J_{ji} \in \mathbb{R}$ holds, the matrix $A(G)$ is symmetric. An example for a system with $N = 2$ sites is depicted in figure 3.1, while the adjacency matrix of this graph for $J_{ij} = J$ is shown in figure 3.2. The respective labelling of the

---

[1] For reasons of simplicity, we exclusively concentrate on the FHM in the examples provided in this chapter. However, all the techniques discussed here are also applicable, with slight modifications, to the other models discussed in chapter 2.

different cluster sites is arbitrary but has to be chosen once and kept constant thereafter.

In order to transfer the resulting Hamiltonian of the system to an easily applicable matrix form an operator basis has to be chosen. A very first naive attempt for establishing a basis is to apply all physically possible combinations of elementary fermionic creation operators $f^\dagger_{i\sigma}$ to the many-particle vacuum state $|0\rangle$. Doing so creates all existing states of the respective Hilbert space and will eventually lead to basis states of the exemplary pictorial and algebraic form given by

$$A(G) = \begin{pmatrix} 0 & J \\ J & 0 \end{pmatrix}$$

Figure 3.2: Adjacency matrix of the cluster depicted in figure 3.1 for $J_{ij} = J$.

$$\left|\uparrow_{N-1},\dots,\downarrow\uparrow_2,\circ_1,\uparrow_0\right\rangle := f^\dagger_{N-1\uparrow}\cdots f^\dagger_{2\downarrow}f^\dagger_{2\uparrow}f^\dagger_{0\uparrow}\left|0\right\rangle . \tag{3.5}$$

It is necessary to implement an unambiguous and efficient book keeping of the states on the right-hand side of (3.5) when implementing them on modern computers. Resulting from the fermionic algebra phase factors arise in these cases due to

$$\left\{f^\dagger_\alpha, f^\dagger_\beta\right\} = 0. \tag{3.6}$$

This becomes problematic in cases of inconsistent ordering of operators. Moreover, this approach does not take any symmetries of the model into account rendering the basis larger than actually needed.

According to section 2.1.3, the FHM possesses no spin-flip terms and the total number of particles N_σ of spin σ is a conserved quantity. Consequently, the dynamics of the system is confined to a subspace of the overall Hilbert space $\mathcal{H}$ with $\dim(\mathcal{H}) = 4^N$. Since the particle number conservation is equal to a conserved total spin S^z, the basis of states can be chosen such that the Hamiltonian of the system will be of block-diagonal structure where each block has a well-defined spin S^z as given by equation (2.8) and (2.9) with

$$S^z = \frac{1}{2}\sum_i \left(\widehat{n}_{i\uparrow} - \widehat{n}_{\downarrow}\right) \overset{(2.6)}{=} \frac{1}{2}\left(\widehat{N}_\uparrow - \widehat{N}_\downarrow\right) = \text{const.} \tag{3.7}$$

Consequently, the subspace of the Hilbert space in which the dynamics take place consists of all states with fixed numbers N_σ. This is equal to independently distributing $N_\downarrow$ and $N_\uparrow$ particles over the lattice of size N leading to a total number of

$$M := \underbrace{\binom{N}{N_\downarrow}}_{m_\downarrow} \cdot \underbrace{\binom{N}{N_\uparrow}}_{m_\uparrow} \tag{3.8}$$

basis states to be used which is considerably smaller than the initial $\dim(\mathcal{H})$.

Then, we need to find a representation in which both spin species can be treated independently from each other while in each spin sector the total number of fermions is conserved. We achieve this by resorting to occupancy number states of the form

$$\left|n_{N-1},\dots,n_0\right\rangle_\sigma := \left(f^\dagger_{N-1\sigma}\right)^{n_{N-1}}\left(f^\dagger_{N-2\sigma}\right)^{n_{N-2}}\cdots\left(f^\dagger_{0\sigma}\right)^{n_0}\left|0\right\rangle \tag{3.9}$$

where exactly $n_i \in \{0,1\}$ spin σ particles are located at the site labeled with i and $\sum_i n_i = N_\sigma$ holds. A more detailed explanation of the theoretical background of these Fock basis states will be given in appendix A.2. For now, it is fully sufficient to know about their semantic structure. Note that (3.9) also implies that the lattice sites are consecutively identified in ascending order from right to left in the chosen representation.

The resulting tensor product states have to incorporate both spins and read

$$|n_{N-1}, ..., n_0\rangle_\downarrow \otimes |n_{N-1}, ..., n_0\rangle_\uparrow \tag{3.10}$$

for a lattice of N sites. The most effective way to map this structure onto a fast and storage-effective scheme is by resorting to twofold Lin tables [93]. The possible practical usages of Lin tables are wide-ranging. They can be used whenever the quantum mechanical states of a system can be divided into two non-overlapping subsets. The partition in the context of the FHM into two different non-interacting spin orientations is obvious. Nevertheless, Lin tables can also be used in cases where the topology of a lattice is bipartite. This implies that the lattice can be divided into two distinct subsets, for example by alternately colouring a two-dimensional rectangular lattice like a chessboard in two colours. All lattice sites of one colour then form one of the two sets.

In the case of the FHM we start by concatenating both spin species and reading the full state as a bit string. This leads to a bit pattern of the form $I = I_\downarrow I_\uparrow$ where each I_σ can simultaneously be seen as an array of bits $I_\sigma[i] \in \{0,1\}$ and as the binary representation for an integer value

$$I_\sigma = \sum_{i=0}^{N-1} I_\sigma[i] \cdot 2^i. \tag{3.11}$$

For consistency, we apply the concept of equation (3.9) for the enumeration of lattice sites to the integer representation I as well. Hence, the least significant bit $I_\sigma[0]$ at the first position counted from right to left in the bit pattern denotes the occupation of the lattice site of the index $i = 0$. In other words, the value of $I_\sigma[0]$ corresponds to the value n_0 of the spin σ subspace state given in (3.9). The overall state is characterised by an integer value as well. This follows from

$$I = 2^N I_\downarrow + I_\uparrow. \tag{3.12}$$

For example, if the system shown in figure 3.1 consisted of two different lattice sites, one conceivable state would be the half-filled one

$$\left|\downarrow_1, \uparrow_0\right\rangle. \tag{3.13}$$

In this state, two particles of different spin orientation are distributed over the two available lattice sites. On site $i = 0$ there is a spin ↑ and on site $i = 1$ there is a spin ↓. According to the previous considerations, the bit representation of the state (3.13) follows according to

$$|10\rangle_\downarrow |01\rangle_\uparrow \equiv 1001_2 = 9 = I. \tag{3.14}$$

Thereby, each spin σ subspace state comprises the full number of lattice sites, in this case two. In the spin subspace for $\downarrow$ the most significant bit is set because a particle of this spin orientation sits on site $i = 1$, whereas in the spin subspace for $\uparrow$ the least significant bit is set to symbolise a particle with spin $\uparrow$ on lattice site $i = 0$.

What might have been subtle when constructing states and identifying them with bit patterns is the fact that we actually introduced two important conventions with equations (3.9) and (3.10). These allow for an unambiguous mapping from the fermionic algebra – consisting of elementary fermionic creation and annihilation operators eventually applied to the vacuum state $|0\rangle$ – to the actual states. These conventions are

(1) indices increase from right to left within the respective spin species, e.g. $f^\dagger_{1\uparrow} f^\dagger_{0\uparrow}$,

(2) $\uparrow$ before $\downarrow$, i.e. $\left\{f^\dagger_{i\downarrow}\right\} \left\{f^\dagger_{i\uparrow}\right\} |0\rangle$, where the operators having a spin of $\uparrow$ are applied first to the vacuum state.

The advantage of this storage scheme is easy to see. We do not need to maintain one large table of size M with all states, but we are able to work with two tables of noticeably smaller sizes m_σ instead. Identifying states is done by using their table indices $J = J(I)$ with respect to the overall table of basis states later on. To reconstruct this index of interest J for a particular binary state I we resort to the separated bit patterns of both spins, $I_\downarrow$ and $I_\uparrow$, find each one in the respective table leading to $J_\downarrow$ and $J_\uparrow$, respectively, and reconstruct the total table index by

$$J = J_\downarrow \cdot m_\uparrow + J_\uparrow. \tag{3.15}$$

The power of this method is twofold. At first, at no point the whole table of all M states has to be stored. This leads to a huge decrease in memory while simultaneously speeding up the look-up times for the individual J_σ. Secondly, since the states in both tables can be arranged in ascending integer order, i.e.

$$J(I^{(i)}) < J(I^{(j)}) \quad \Leftrightarrow \quad I^{(i)} < I^{(j)} \tag{3.16}$$

for blocks of constant S^z, the lists are sorted. This makes it feasible to look for the bit patterns I_σ within the tables using asymptotically faster searching algorithms.[2]

Example

We derive the two necessary Lin tables for the easiest system possible, the $N = 2$ sites case depicted in figure 3.1, by making use of the formerly discussed ansatz. More detailed explanations including in-depth examples are to be found, e.g. in Refs. [94–96]. For ease of understanding, table 3.1 gives an overview over all the states of the Hilbert space in both algebraic and binary representation. We explicitly emphasise that this representation is

---

[2] With no inherent structure in the data of length n the estimate to find an element is given by $\mathcal{O}(n)$ since half the data set has to be traversed on average. In the case of sorted lists an algorithm like *binary search* is able to find an element asymptotically faster in $\mathcal{O}(\log n)$.

not equal to the actual Lin tables and that the Lin tables do not necessitate the storage of a complete basis at any time, but – on the contrary – only require the storage of two significantly smaller tables.

Table 3.1: All binary basis states with their bit patterns I_σ and table indices J_σ for a system of $N = 2$ sites and two particles. The full pattern $\mathbf{I}$ as well as the full table index $\mathbf{J}$ are marked bold for better readability. The different spin sectors S^z stem from conservation of the individual N_σ.

Total spin	State	Bit pattern	$I_\downarrow$	$I_\uparrow$	**I**	$J_\downarrow$	$J_\uparrow$	$m_\downarrow$	$m_\uparrow$	**J**
$S^z = 1$	$\|00\rangle_\downarrow \|11\rangle_\uparrow$	0011_2	0	3	3	0	0	1	1	0
$S^z = 0$	$\|01\rangle_\downarrow \|01\rangle_\uparrow$	0101_2	1	1	5	0	0	2	2	0
...	$\|01\rangle_\downarrow \|10\rangle_\uparrow$	0110_2	1	2	6	0	1	...	...	1
	$\|10\rangle_\downarrow \|01\rangle_\uparrow$	1001_2	2	1	9	1	0			2
	$\|10\rangle_\downarrow \|10\rangle_\uparrow$	1010_2	2	2	10	1	1			3
$S^z = -1$	$\|11\rangle_\downarrow \|00\rangle_\uparrow$	1100_2	3	0	12	0	0	1	1	0

Presuming that our system is half-filled meaning exactly two particles of up to now unspecified spin orientation are distributed over the lattice of $N = 2$ sites, there are three different possibilities to do so. The system can possess two spins of the same spin orientation with either ↑ or ↓ ($S^z = 1$ or $S^z = -1$) or it can be filled with two particles of opposite spin ($S^z = 0$). Distributing two particles of the very same spin leads to $m_\sigma = 1$ possible configuration due to the Pauli exclusion principle. For exactly one spin σ particle in the case of vanishing total spin there are $m_\sigma = 2$ different possibilities. Ordering the bit patterns in increasing integer order leads to the states shown in table 3.1 where the respective indices J unambiguously label the state in the sector of conserved S^z.

Table 3.2: Lin table for $N = 2$ sites and $S^z = 0$.

State	Bit pattern	I_σ	J_σ
$\|01\rangle_\sigma$	01_2	1	0
$\|10\rangle_\sigma$	10_2	2	1

Assuming in this example that the initial state $|\psi(t{=}0)\rangle$ of the time-evolution (3.4) has a spin of $S^z = 0$, there are only $m_\sigma = 2$ possible configurations for each spin subspace. Only these two actually need to be stored in a Lin table. Thus, we create two different Lin tables of the general structure of table 3.2. In each Lin table, it is sufficient to exclusively store the integer information I_σ and the local label J_σ and to retrieve all remaining information from it. Further columns are only given for didactic purposes. Any handling of quantum mechanical states now requires knowing the total index J of a state with respect to the full Hilbert space. To determine J for an arbitrary state, such as the state

$$|s\rangle := |10\rangle_\downarrow |01\rangle_\uparrow , \tag{3.17}$$

the state is split into its two distinct spin components. Each spin component is then searched for in the available Lin table 3.2 so that, for example, $J_\downarrow = 1$ and $J_\uparrow = 0$ are determined. By knowing the number of entries $m_\sigma = 2$ of each Lin table, J as defined in (3.15) can be calculated. In our example, this results in $J = 1 \cdot 2 + 0 = 2$ which is consistent with the index $J = 2$ for the state $|s\rangle$ that could be obtained from table 3.1.

Given an arbitrary physical state we are now able to construct the corresponding bit pattern I and from this the index J of the state by means of a significantly faster and memory-saving procedure compared to the use of the complete table 3.1. By memory-saving we mean that instead of the naively allocated amount of memory $\mathcal{O}(m_\downarrow m_\uparrow)$ for all states of the system under use of Lin tables, only $\mathcal{O}(m_\downarrow + m_\uparrow)$ of memory is needed.

In this minimal example, there is only a saving of access time, but no saving of memory. Here, two tables with two entries each had to be saved instead of one table with four entries. The effect becomes more obvious in larger systems: If, for example, one had $m_\sigma = 10$ states in each spin sector and, thus, $M = 10 \times 10 = 100$ states in the entire Hilbert space, one would have to store a single table with 100 entries. With Lin tables, however, only two tables with 10 entries each need to be stored.

3.1.2 Creating the Hamiltonian

With the basis which has been chosen and discussed in section 3.1.1, it is possible to obtain the matrix representation of the Fermi-Hubbard Hamiltonian. This task is equal to determining the matrix elements

$$\left\langle I' \middle| H \middle| I \right\rangle \quad \Leftrightarrow \quad \left\langle J'(I') \middle| H \middle| J(I) \right\rangle =: h(J', J). \tag{3.18}$$

For the hopping part H_0 of the Fermi-Hubbard Hamiltonian (2.1) we need to identify which basis states $|I\rangle$ and $|I'\rangle$ are connected by hopping processes. These allowed hopping processes are defined by the adjacency matrix elements a_{ij}. In the event that two states are connected by a permitted hopping process from site i to site j, i.e. $a_{ij} \neq 0$, the corresponding matrix element of the Hamiltonian reads

$$h(J', J) = (-1)^{p+1} a_{ij} \tag{3.19}$$

where p is the number of hops over occupied sites between the sites i and j with respect to the representation (3.9). Such permitted processes can be derived by iterating over all states $|I\rangle$ of the Hilbert space and constructing for each state all possible states $|I'\rangle$ that emerge from the state $|I\rangle$ by exchanging the information on exactly one occupied and one unoccupied site provided that these sites are connected in the adjacency matrix. More formally put, the conservation of N_σ requires that the Hamming weight[3] $\delta(\cdot)$ of the actually different parts of both basis states $|I\rangle$ and $|I'\rangle$ amounts to $\delta\left(\overline{I}\right) = 2$. This actual difference is given by a logical XOR operation as

$$\overline{I} = I \oplus I'. \tag{3.20}$$

Furthermore, the topology of the cluster imposes that hopping processes only take place between sites that are connected via non-vanishing adjacency matrix elements.

---

[3] On a modern CPU the Hamming weight of a binary string can be measured in a fast way due to the fact that the embedded instruction set offers commands for that purpose, e.g. *popcount*.

In order to derive the fermionic phase factor and, thus, p in (3.19) we identify the two positions $i > j$ that are set in the binary pattern $\overline{I}$ and construct a binary mask

$$M_{ij} = \underbrace{0\dots\overbrace{0}^{i}}_{N-i}\underbrace{1\dots1}_{i-j-1}\underbrace{\overbrace{0}^{j}\dots0}_{j+1} \tag{3.21}$$

for measuring the occupied sites in between. Then, the number of swaps with other fermionic creation operators can be deduced by the Hamming weight of the conjunction

$$p = \delta\left(I \wedge M_{ij}\right) = \delta\left(I' \wedge M_{ij}\right). \tag{3.22}$$

The interaction part H_{int} is even easier because it is diagonal in the chosen real space basis and does not couple off-diagonal basis states. Using $n_{i\sigma}^{J}$ to denote the occupancy number of the spin σ particle at site i of the basis state indexed with label J it reads

$$h(J,J) = \sum_{i=0}^{N-1} U_i n_{i\uparrow}^{J} n_{i\downarrow}^{J}. \tag{3.23}$$

This is equal to a logical AND operation of both spin patterns $I_\downarrow$ and $I_\uparrow$ according to

$$\widetilde{I} = I_\downarrow \wedge I_\uparrow \tag{3.24}$$

and summing up the set bits, i.e. the sites at which double occupancies occur, weighted by their on-site interactions as

$$h(J,J) = \sum_{i=0}^{N-1} \widetilde{I}[i] \cdot U_i. \tag{3.25}$$

Example (cont'd)

We revisit the example of section 3.1.1 to calculate the Hamiltonian for the non-trivial $S^z = 0$ block. For the sake of simplicity, we assume $U_i = U$ and $J_{ij} = J$.

There are eight allowed hopping processes of which we only need to examine four in detail for symmetry reasons. Starting from the state $I = 5$, cf. table 3.1, it is possible for an electron of spin ↑ to hop which results in the state $I = 6$. Likewise, a hopping of a spin ↓ is possible leading to the state $I = 9$. In a similar manner the states $I = 6$ and $I = 9$ can become $I = 10$. For the hopping part of the Hamiltonian we, thus, receive

$$\langle 6|H_0|5\rangle = \langle 9|H_0|5\rangle = \langle 10|H_0|6\rangle = \langle 10|H_0|9\rangle = (-1)^{p+1} a_{ij}. \tag{3.26}$$

As all of these hoppings can be performed back and forth, i.e. from site i to j but also from j to i, four more processes stemming from symmetry are possible. Due to the fact that in all aforementioned cases our binary mask M_{ij} given by (3.21) vanishes, the Hamming weight in equation (3.22) vanishes as well resulting in a global $p = 0$. This can be easily understood from the fact that in between the two neighbouring sites of our example no further particles can be present.

There are only the two states $I = 5$ and $I = 10$ that lead to non-vanishing results in equation (3.24). As a result, the interaction part is determined by

$$\langle 5|H_{\text{int}}|5\rangle = \langle 10|H_{\text{int}}|10\rangle = U. \tag{3.27}$$

Taking both the hopping and the interaction part into account the matrix representation of the Hamiltonian in the subspace of a constant $S^z = 0$ can be calculated. Here, the states are sequentially numbered in ascending I according to table 3.1 which leads to

$$H = \begin{pmatrix} U & -J & -J & 0 \\ -J & 0 & 0 & -J \\ -J & 0 & 0 & -J \\ 0 & -J & -J & U \end{pmatrix}. \tag{3.28}$$

Even though the overall scale might be larger in practical problems studied throughout this thesis the concepts explained in this section make up the foundation for understanding the techniques and methods to come.

3.2 Exact diagonalisation

To yield the actual time-evolution (3.4) with the Hamiltonian H just determined, the most natural approach is a complete diagonalisation providing the eigenvalues and -vectors of the system. We call a basis of vectors $\{\mathbf{v}_1, ..., \mathbf{v}_d\}$ eigenbasis of the matrix O if the condition

$$O\mathbf{v} = \lambda\mathbf{v} \tag{3.29}$$

is met. The factors $\{\lambda_1, ..., \lambda_d\}$ of the linear transformation are called eigenvalues.

A special case of an operator is the Hamiltonian itself, i.e. $O = H$. Since the Hamiltonian is the operator of energy the $|i\rangle$ usually go by the name (energy) eigenstates whereas the eigenvalues E_i are referred to as eigenenergies. In Dirac notation equation (3.29) reads

$$H\,|i\rangle = E_i\,|i\rangle\,. \tag{3.30}$$

Obtaining the complete set of eigenstates and eigenenergies is called full diagonalisation. Then, the time-propagation (3.4) of a quantum state $|\psi(t)\rangle$ from its initial value $|\psi_0\rangle := |\psi(t{=}0)\rangle$ can be performed using the projector onto energy eigenstates as

$$|\psi(t)\rangle = \sum_n e^{-iE_n t}\,|n\rangle\,\langle n|\psi_0\rangle\,. \tag{3.31}$$

Due to the fact that in the Schrödinger picture all information is contained in the states the equation (3.31) is sufficient to describe the system. In other words, once $|\psi(t)\rangle$ is calculated all physical quantities are within reach and can easily be obtained for arbitrary times t. Especially the quantity $O(t)$ as in equation (3.1) can be derived by means of

$$\begin{aligned} O(t) &= \langle\psi(t)|O|\psi(t)\rangle && \text{(3.32a)} \\ &= \sum_{mn} \langle m|O|n\rangle \underbrace{\langle n|\psi_0\rangle}_{=:\,\alpha_n} \underbrace{\langle\psi_0|m\rangle}_{=:\,\alpha_m^*} e^{-i(E_n-E_m)t} && \text{(3.32b)} \\ &= \sum_{mn} \alpha_n\alpha_m^* \langle m|O|n\rangle\, e^{-i(E_n-E_m)t}. && \text{(3.32c)} \end{aligned}$$

Essentially, with equations (3.31) and (3.32) all the tools one needs to compute the time-evolution of observables are at hand. So why would there be a real necessity to employ more complicated or sophisticated methods instead of relying on exact diagonalisation (ED)? The reason lies mainly in the effort of the complete diagonalisation of a matrix H as required by (3.30). The asymptotic time complexity of a complete diagonalisation of a $d \times d$ matrix is of the order of $\mathcal{O}\left(d^3\right)$. As the dimension d of the Hilbert space itself grows exponentially with the number of system constituents, i.e. in the FHM with the number of lattice sites N, the effort for the complete diagonalisation quickly exceeds all feasibility limits. Fortunately, on the one hand, in practical situations mostly no simulation of $O(t)$ is required for arbitrarily large times $t \to \infty$, on the other hand, not all energy eigenstates $|i\rangle$ contribute equally to the time-evolution for moderately large simulation times t. By a smart representative sampling of $N_\mathrm{c} \ll d$ states $|\phi_n\rangle$ and the simulation of the system in the subspace $\operatorname{span}\left(|\phi_0\rangle, ..., |\phi_{N_\mathrm{c}-1}\rangle\right)$ spanned by these states, it is commonly possible to capture the dynamics with sufficient accuracy. This is the key idea of the technique described in the next section.

3.3 Chebyshev expansion

In order to derive the basic ideas of the Chebyshev expansion technique (CET) we start from the most general ansatz of expanding an arbitrary function $f(x)$ using Chebyshev polynomials. By employing this method on the rescaled time-evolution operator as given in (3.3), we will be able to compute arbitrary time-dependent expectation values $O(t)$, cf. equation (3.4), with controllable accuracy. The principles of the expansion of a function by means of a complete set of orthogonal functions as presented in this section will also play a central role in the calculation of thermal expectation values. This topic will be discussed in chapter 4. The following section is partly based on Refs. [97, 98].

3.3.1 Expanding in orthogonal polynomials

We start by considering the closed interval $I = [-1; 1]$ and two arbitrary complex-valued functions $f, g\colon I \to \mathbb{C}$ of which the former function is to be expanded in terms of a given set of orthogonal polynomials $p_n(x)$ fulfilling the relation

$$\langle p_n|p_m\rangle = \mathcal{N}_n^{-1}\delta_{n,m} \text{ with a norm } \mathcal{N}_n = \langle p_n|p_n\rangle^{-1}. \qquad (3.33)$$

Furthermore, we define a weighted scalar product between the two functions $f(x)$ and $g(x)$ with a positive weight function $w_j\colon I \to \mathbb{R}^+$ according to

$$\langle f|g\rangle_j := \int_{-1}^{1} w_j(x) f^*(x) g(x)\,\mathrm{d}x\,. \tag{3.34}$$

When needed, the subscript j is used to denote the weight function in use. The most general form of the expansion of $f(x)$ in terms of orthogonal polynomials reads

$$f(x) = \sum_{n=0}^{\infty} \alpha_n p_n(x) \text{ with } \alpha_n = \mathcal{N}_n \langle p_n|f\rangle\,. \tag{3.35}$$

While basically every set of orthogonal functions could be used for the expansion in equation (3.35) it turns out that there is a special set of polynomials that converges particularly fast, distributes errors uniformly on its support and whose basis only grows linearly in the maximum simulation time $t_{\max}$ [99]. These are the Chebyshev polynomials $T_n(x)$ of first kind [100]. They are defined explicitly using trigonometric functions

$$T_n(x) = \begin{cases} \cos\left(n \arccos(x)\right) & x \in I \\ \cosh\left(n \operatorname{arccosh}(x)\right) & \text{otherwise} \end{cases} \tag{3.36}$$

or in an iterative fashion using the following recursion relation

$$T_0(x) = 1, \quad T_1(x) = x \tag{3.37a}$$

$$T_{n+1}(x) = 2xT_n(x) - T_{n-1}(x). \tag{3.37b}$$

The polynomials $T_n(x)$ are mutually orthogonal with respect to the scalar product in equation (3.34) and the weight function $w_1(x) = \left(\pi\sqrt{1-x^2}\right)^{-1}$ due to

$$\langle T_n|T_m\rangle_1 = \frac{\pi}{2-\delta_{n,0}}\delta_{n,m}. \tag{3.38}$$

As the last property of interest we examine the finite Fourier transform of the weighted Chebyshev polynomials $T_n(x)$ over the closed interval I, cf. Ref. [101], which is related to the Bessel functions of first kind $J_n(x)$ by

$$J_n(t) = \frac{(-i)^n}{\pi} \int_{-1}^{1} \frac{e^{izt} T_n(z)}{\sqrt{1-z^2}}\,\mathrm{d}z\,. \tag{3.39}$$

Inserting equation (3.36) into (3.35) and using the corresponding scalar product $\langle\cdot|\cdot\rangle_1$ leads to the expansion of the given function in terms of Chebyshev polynomials

$$f(x) = \lambda_0 + 2\sum_{n=1}^{\infty} \lambda_n T_n(x) \tag{3.40a}$$

$$\lambda_n = \langle f|T_n\rangle_1 = \int_{-1}^{1} \frac{f^*(x) T_n(x)}{\pi\sqrt{1-x^2}}\,\mathrm{d}x\,. \tag{3.40b}$$

The expansion coefficients λ_n of the function $f(x)$ are often referred to as moments. It can sometimes become problematic to integrate over $w_1(x)$ due to its singularities at $x = \pm 1$ when calculating these moments. As a remedy for these cases, we define the new orthogonal basis set

$$W_n(x) = w_1(x) T_n(x) \tag{3.41}$$

and a scalar product $\langle \cdot | \cdot \rangle_2$ with a weight function $w_2(x) = \pi\sqrt{1 - x^2}$. The expansion in terms of the new basis set reads

$$f(x) = \frac{1}{\pi\sqrt{1-x^2}} \left(\mu_0 + 2 \sum_{n=1}^{\infty} \mu_n T_n(x) \right) \tag{3.42a}$$

$$\mu_n = \langle f | W_n \rangle_2 = \int_{-1}^{1} f^*(x) T_n(x) \, \mathrm{d}x \, . \tag{3.42b}$$

In the context of the Chebyshev expansion technique in section 3.3.3, we use in particular the expansion (3.40), while for the calculation of thermal expectation values in section 4.1.2 equation (3.42) will prove useful.

3.3.2 Generalising the applicability

Strictly speaking, the equations (3.40) and (3.42) may only be used for scalar functions defined on the interval I. All quantities we are going to derive in the following are directly dependent on the energy spectrum $\{E'\}$ of a given Hamiltonian or on the Hamiltonian H' itself. This means we always deal with functions of type $f(E')$ or $f(H')$. In order to be able to handle these with the help of CET, we have to map the spectrum of H' onto the interval I.

Transforming the Hamiltonian

Given the extremal eigenvalues E'_{min} and E'_{max} of H', the linear transformation

$$H' \to H = \frac{H' - b}{a} \qquad \Longrightarrow \qquad E' \to E = \frac{E' - b}{a} \tag{3.43}$$

is sufficient to yield a dimensionless Hamiltonian H with a spectrum of eigenvalues in the required interval I. This ensures the applicability of the Chebyshev expansion technique. The offset or scaling factors of the linear transformation are given by

$$a = {}^1\!/\!_2 \left(E'_{\mathrm{max}} - E'_{\mathrm{min}} \right) \tag{3.44a}$$

$$b = {}^1\!/\!_2 \left(E'_{\mathrm{max}} + E'_{\mathrm{min}} \right) . \tag{3.44b}$$

Obviously, in order to perform the linear transformation (3.43) knowledge of at least a part of the spectrum is required. Since a full diagonalisation is not feasible a different approach has to be taken.

Triangle inequality

It would be detrimental to the method if the evaluation of the extremal eigenvalues $E'_{\min}$ and $E'_{\max}$ in the context of the transformation (3.43) took more time than the execution of the actual time-evolution. In this respect, we are looking for a method that determines the approximations $\eta_{\min}$ and $\eta_{\max}$ to the extremal eigenvalues quickly and in a memory-saving way. It is not necessary to have an extremely exact approximation as long as the actual energy spectrum of the Hamiltonian fully lies in the energy interval spanned by the approximation, i.e.

$$\eta_{\min} < E'_{\min} \text{ and } E'_{\max} < \eta_{\max}. \tag{3.45}$$

The accomplishment of this task becomes even easier if we keep in mind that in fact we only need an upper bound $\xi \geq \lambda_{\max}$ to the eigenvalue $\lambda_{\max} = \lambda_{\max}(H)$ with the largest absolute value. For then it follows that

$$\eta_{\min} = -|\xi| \text{ and } \eta_{\max} = |\xi| \tag{3.46}$$

holds as a general approximation. There are many different approaches towards gaining an approximation of $\lambda_{\max}$, e.g. by means of techniques starting from a randomly chosen vector $\mathbf{s}$ and operating on the iteratively constructed F-dimensional Krylov subspace

$$\mathcal{K}^F(\mathbf{s}) = \operatorname{span}\left(\mathbf{s},\, H\mathbf{s},\, H^2\mathbf{s}, \ldots,\, H^{F-1}\mathbf{s}\right) \tag{3.47}$$

like the power method [102], the Arnoldi algorithm [103] or – in the case of Hermitian matrices – the Lanczos iteration [104]. In our practical application of these methods to the FHM, it turned out that the numerically most stable and consequently most reliable approach for obtaining an upper bound ξ can be performed by resorting to the extended triangle inequality

$$\|A + B + C\| \leq \|A\| + \|B\| + \|C\|. \tag{3.48}$$

Since we are dealing with matrices, the spectral norm is a natural choice to be used in equation (3.48). It is defined according to

$$\|A\| := \|A\|_2 = \sqrt{\lambda_{\max}\left(A^\dagger A\right)} \tag{3.49}$$

which is merely the absolute value of $\lambda_{\max}(A)$ in the case of a Hermitian matrix $A = A^\dagger$. Thus, the right-hand side of equation (3.48) can be read as the desired quantity ξ for a decomposition of the Fermi-Hubbard Hamiltonian (2.1) into the two hopping parts of both spin species, i.e. $H_\uparrow$ and $H_\downarrow$, and the interaction part H_{int}.[4] In order to obtain the final approximation to the largest absolute eigenvalue, the right-hand side of equation (3.48) must be evaluated by means of the diagonalisation of the two hopping matrices H_σ and

---

[4] An short review of computational improvements, the decomposition of the hopping part into the two distinct spin species and the practical implications and advantages can be found in appendix A.1.

the identification of the largest absolute eigenvalue of H_{int}.[5] The latter is bounded by the sum over all on-site interaction strengths.

3.3.3 Application to time-dependent observables

Initially introduced by Tal-Ezer and Kosloff [99] to yield the time-evolution of physical observables, the Chebyshev expansion technique (CET) is by now a widely used method for a variety of purposes: Be it the determination of eigenvalues of Hermitian matrices within a specified range [105], the calculation of the one-electron density matrix by expanding the Fermi-Dirac distribution [106], the computation of spectral functions in one-dimensional models with short-range interactions [107] or the analysis of spin-noise spectra of the anisotropic central spin model [108]. There are even various applications of approaches based on CET to the Hubbard model [109, 110].

The time-evolution operator as matrix exponential

To find a suitable approximation to the result of equation (3.1) we start by considering the time-propagation of a quantum state (3.4) using the unitary time-evolution operator $U = e^{-iH't}$. By applying the linear transformation (3.43) to U we obtain the function

$$f(H) = e^{-iaHt}e^{-ibt} \tag{3.50}$$

which can be directly expanded using the techniques outlined in section 3.3.1. Here it is advantageous and, thus, advisable to start from equation (3.40) by determining

$$\begin{aligned} \lambda_n &= e^{-ibt} \int_{-1}^{1} \frac{e^{iazt}\, T_n(z)}{\pi\sqrt{1-z^2}}\, \mathrm{d}z && \text{(3.51a)} \\ &\overset{(3.39)}{=} i^n e^{-ibt} J_n(at). && \text{(3.51b)} \end{aligned}$$

Inserting equation (3.51b) into (3.40a) provides the time-evolution operator U in terms of Chebyshev polynomials as

$$\begin{aligned} U &= \sum_{n=0}^{\infty} \alpha_n(t) T_n(H) && \text{(3.52a)} \\ \alpha_n(t) &= (2 - \delta_{n,0}) i^n e^{-ibt} J_n(at). && \text{(3.52b)} \end{aligned}$$

An intriguing property of (3.52) is the fact that the actual time-evolution and the effect of the Hamiltonian are completely separated from each other. The time-dependence

---

[5] The attentive reader may wonder why two explicit diagonalisations are performed given the fact that we tried to avoid a full diagonalisation at all costs up to now. The reason is to be found in the overall dimension $\binom{N}{N_\sigma}$ of the two effective one-particle problems H_σ. This dimension is significantly smaller than the overall Hilbert space dimension leading to low computational costs. A second source of irritation may be the fact that while H_σ are matrices of small dimensions H_{int} evidently is not. Fortunately, in a real space representation the interaction is diagonal such that the identification of the largest absolute eigenvalue can be performed in linear time.

is contained only in the $\alpha_n(t)$, the effect of the Hamiltonian is contained only in the Chebyshev polynomials $T_n(H)$.[6] Resorting to (3.37) permits us to compute the time-evolution of a given initial quantum state $|\psi_0\rangle$ easily by means of an iterative scheme

$$|\psi(t)\rangle = U\,|\psi_0\rangle = \sum_{n=0}^{\infty} \alpha_n(t)\, \underbrace{T_n(H)\,|\psi_0\rangle}_{=:\,|\phi_n\rangle}\,. \tag{3.53}$$

Since a treatment of the infinite series is computationally not possible, a cut-off value of $N_\mathrm{c} < \infty$ must be introduced for practical usability. The basis of the expansion $|\phi_n\rangle, n \in \{0, \dots, N_\mathrm{c}-1\}$, can be determined iteratively by

$$|\phi_0\rangle = |\psi_0\rangle\,, \quad |\phi_1\rangle = H\,|\phi_0\rangle \tag{3.54a}$$

$$|\phi_{n+1}\rangle = 2H\,|\phi_n\rangle - |\phi_{n-1}\rangle\,. \tag{3.54b}$$

If (3.53) is to be calculated in an iterative manner in large systems, it is not a requirement to keep all the N_c states of the Chebyshev basis in the memory at once – the states that are necessary for the next iteration step (3.54b) as well as the temporary result vector to sum $|\psi(t)\rangle$ are sufficient. Hence, the only truly limiting factor of a CET in large Hilbert spaces is the ability to store this minimal set of states.

Estimating the accuracy

In order to keep the number N_c of basis states as small as possible it is worthwhile to estimate the error for a truncation of (3.52) after a finite number of elements precisely. Since the asymptotic behaviour of the time-dependent prefactors is determined by the Bessel functions of the first kind $J_n(z)$, their asymptotic behaviour for $n \to \infty$ and fixed $z \neq 0$ is of interest. This is provided, e.g. in Ref. [111, Eq. 10.19.1], as

$$J_n(z) \propto \frac{1}{\sqrt{2\pi n}} \left(\frac{z \cdot e}{2n}\right)^n. \tag{3.55}$$

The higher the order n the longer it takes the Bessel function $J_n(t)$ to have a noticeable impact on the result as can be seen in figure 3.3a. While the Bessel function $J_0(t)$ is notably different from zero for arbitrarily small times, the Bessel functions of higher order make significant contributions for considerably larger times only. This in turn means that the coefficients (3.52b) for a fixed time t' above a certain order $n \propto N_\mathrm{c}$ can no longer make a contribution to the time dynamics that exceeds the order of magnitude ϵ. Thus, this upper bound ϵ to the error of the first contribution not taken into account when truncating with a cut-off value of N_c can be provided as

$$\epsilon \geq \left(\frac{at \cdot e}{2N_\mathrm{c}}\right)^{N_\mathrm{c}}. \tag{3.56}$$

---

[6] While the easily computable time-dependence of a quantum state is the most notable benefit of CET it is by far not the only one. Especially two further advantages are worth mentioning: Since H only occurs applied to a state merely the effect of H needs to be known, not H itself. This renders two options possible: The first is the obvious advantage not to store H. The second is that the resulting on-the-fly reconstruction of H is a perfect starting point for highly parallelised matrix-vector-multiplications.

Evidently, the error ϵ is not only related to N_c but also depends directly on the maximum time t_max up to which results should be calculated as well as the parameter a which equals half the width of the energy spectrum as defined in (3.44a). This has two implications: A too rough overestimation of the bandwidth of the energy spectrum and, thus, of a leads to an unnecessarily large basis. Furthermore, the basis size N_c only has to increase linearly with the desired maximum simulation time t_max.

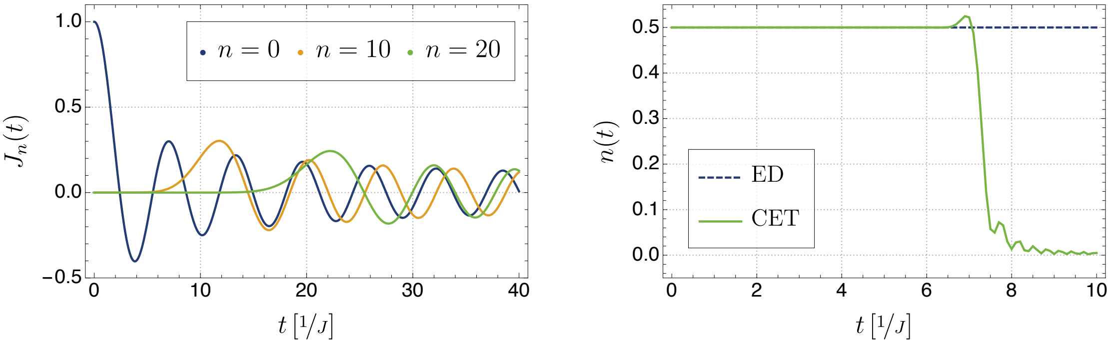

(a) Different Bessel functions of the first kind $J_n(t)$ which determine the asymptotic behaviour of the expanded time-evolution operator (3.53) according to (3.52b).

(b) Comparison of the result of exact diagonalisation (ED) and of Chebyshev expansion technique (CET) for $N = 8$, half-filling and ${}^U\!/_J = 3$. The analytical result equals $n(t) = 0.5$.

Figure 3.3: Components and error of a Chebyshev expansion

In order to get an impression of the implications of the choice of ϵ, we look at a practical example. For a half-filled one-dimensional FHM with $N = 8$ sites and periodic boundary conditions as well as a local interaction strength ${}^U\!/_J = 3$ we simulate the local particle density $n(t) := \langle \widehat{n}_{i\sigma}(t) \rangle$ at site i for a particle with spin σ using both ED and CET. Due to the translational symmetry, the chosen lattice site does not matter. The corresponding results can be found in figure 3.3b. The analytically determined reference result for the observable is hereby a time-independent and constant average filling of $n(t) = 0.5$. To emphasise the key differences between the two techniques, we deliberately choose the cut-off value N_c for the CET such that an accuracy better than $\epsilon = 10^{-3}$ is guaranteed for all times $t \leq 5\,[{}^1\!/_J]$. While the results of the ED for arbitrarily large times t completely correspond to the analytical reference, there are significant deviations starting at about $t = 6\,[{}^1\!/_J]$ in the case of the CET. The explanation for this lies in the fact that an ED describes the dynamics in the entire Hilbert space and, thus, yields proper results for arbitrarily long simulations, cf. (3.32). In the case of the CET, however, the subspace of the Hilbert space is chosen from the very beginning in such a way that it is adequate to capture the dynamics up to the chosen maximum time only. Results of a CET above this maximum simulation time are therefore in no way meaningful, as the computed values above $t > 6\,[{}^1\!/_J]$ impressively prove. However, keeping this restriction in mind, CET provides a robust and highly efficient way to study the dynamics of even moderately large systems, which would be impossible using ED.

3.4 Iterated equations of motion

Despite the fact that the CET presented in section 3.3 offers innumerable advantages, it is and remains an exclusively numerical procedure. Occasionally, this has the disadvantage that analytical *a priori* statements about the system are infeasible. For example, within the framework of CET, long-time averages can only be determined by simulating a system up to finite times t and subsequently averaging over it. True long-time averages for $t \to \infty$ are therefore clearly out of reach. An even more striking shortcoming of CET relates to the fact that the basis vectors (3.54) to be stored comprise the full dimension of the Hilbert space and scale exponentially with the system size. Such problems are not inherent to the semi-analytical iterated equations of motion (iEoM) method based on the Heisenberg equation of motion and described in this section.

3.4.1 Heisenberg picture

Whilst in the Schrödinger picture employed so far all information about the time-dependence of the quantum mechanical system is completely contained in the states $|\psi(t)\rangle$, in the Heisenberg picture the operators themselves carry this information. In order to emphasise the contrast between these two pictures, we temporarily use corresponding indices attached to the operators in the following. A unitary transformation between both pictures is given by

$$A_{\mathrm{H}}(t) = U_{\mathrm{S}}^{\dagger}(t) A_{\mathrm{S}}(t) U_{\mathrm{S}}(t), \tag{3.57}$$

whereby unitarity is reflected by the property of the time-evolution operator that

$$U_{\mathrm{S}}^{\dagger}(t) = U_{\mathrm{S}}^{-1}(t) = U_{\mathrm{S}}(-t). \tag{3.58}$$

The time-evolution of an operator $A_{\mathrm{H}}(t)$ in the Heisenberg picture can be derived from an operator $A_{\mathrm{S}}(t)$ with possibly present explicit time-dependence in the Schrödinger picture by means of

$$\begin{aligned}\frac{\mathrm{d}}{\mathrm{d}t} A_{\mathrm{H}}(t) &= \frac{\mathrm{d}}{\mathrm{d}t}\left(U_{\mathrm{S}}^{\dagger}(t)\right) A_{\mathrm{S}}(t) U_{\mathrm{S}}(t) + U_{\mathrm{S}}^{\dagger}(t) \frac{\partial A_{\mathrm{S}}(t)}{\partial t} U_{\mathrm{S}}(t) \\ &\quad + U_{\mathrm{S}}^{\dagger}(t) A_{\mathrm{S}}(t) \frac{\mathrm{d}}{\mathrm{d}t}\left(U_{\mathrm{S}}(t)\right) &\text{(3.59a)} \\ &= i[H_{\mathrm{H}}(t), A_{\mathrm{H}}(t)] + U_{\mathrm{S}}^{\dagger}(t) \frac{\partial A_{\mathrm{S}}(t)}{\partial t} U_{\mathrm{S}}(t). &\text{(3.59b)}\end{aligned}$$

As before, we use natural units. Given that all the operators considered in this thesis do not exhibit an explicit time-dependence in the Schrödinger picture, i.e. $A_{\mathrm{S}}(t) = A_{\mathrm{S}}$, the Heisenberg equation of motion (3.59b) can be transformed into its simplified form

$$\frac{\mathrm{d}}{\mathrm{d}t} A_{\mathrm{H}}(t) = i[H_{\mathrm{H}}(t), A_{\mathrm{H}}(t)] = i\mathcal{L}(A_{\mathrm{H}}(t)), \tag{3.60}$$

which will be used from now on. In order to be able to write down the repeated commutations of an operator with the Hamiltonian of the system in a streamlined way, the Liouville superoperator $\mathcal{L}(.) := [H_{\mathrm{H}}(t), .]$ was introduced here. Furthermore, the fact that all subsequent operators possess no explicit time-dependence in the Schrödinger picture allows us to simplify the notation a bit further. Instead of the cumbersome notation for the two pictures by means of indices, we specify that operators with time-dependence belong to the Heisenberg picture, while those without time-dependence belong to the Schrödinger picture.

A special case of (3.60) worth mentioning arises when the Hamiltonian of the total system is time-independent. In this case the system is conservative and in particular the relation $H_{\mathrm{H}} = H_{\mathrm{S}} = H$ holds.

3.4.2 Operator expansion

One of the fundamental ideas of the iEoM approach [42, 112–116] is to calculate the time-dependence of any operator $A(t)$ with the help of (3.60) by writing the operator as a linear combination

$$A(t) = \sum_i h_i(t) A_i. \tag{3.61}$$

The occurring Schrödinger picture operators $\{A_i\}$ have to be linearly independent to form a basis in the space of operators and only the complex-valued prefactors $h_i(t)$ carry the time-dependence. Substituting equation (3.61) into (3.60) yields

$$\frac{\mathrm{d}}{\mathrm{d}t} A(t) = i\mathcal{L}(A(t)) \tag{3.62a}$$

$$= i \sum_i h_i(t) \mathcal{L}(A_i)\,. \tag{3.62b}$$

The result of applying the Liouville superoperator to a basis operator A_i yields a linear combination of the form

$$\mathcal{L}(A_i) = \sum_j M_{ji} A_j \tag{3.63}$$

which simultaneously defines the Liouvillian matrix M, sometimes also called the dynamic matrix. By combining all time-dependent prefactors $h_i(t)$ into a single vector $\mathbf{h}(t)$, the dynamics of a system can be described entirely by

$$\frac{\mathrm{d}}{\mathrm{d}t} \mathbf{h}(t) = iM\mathbf{h}(t). \tag{3.64}$$

As straightforward as the characterisation of the dynamics by means of (3.64) seems at first, as difficult is it to assess the consequences of insufficient approximations. Building on the basic ideas of Kalthoff et al. [116] we pointed out the specific implications in Ref. [42]. We will briefly discuss the core aspects presented in both works in the following.

From a purely mathematical point of view, due to (3.3) all solutions $\mathbf{h}(t)$ of (3.64) are superpositions of oscillatory solutions. The oscillation frequencies of the solutions are given by differences of the eigenenergies of the system. Thus, relaxation processes or dephasing arise naturally in open quantum systems. This characteristic physics does not change, of course, by a switch to the Heisenberg picture. If, however, an insufficient approximation is made, it may happen that the dynamic matrix has complex eigenvalues $z \in \mathbb{C}$. If the matrix itself is real-valued, the eigenvalues occur in pairs as $z_\pm = R \pm iI$ with real part R and imaginary part I. Consequently, exponential divergences arise in the progress of time. However, even if the eigenvalues remain entirely real, the matrix might not be fully diagonalisable but of Jordan normal form. In this case, divergences of power law type would arise. Only if it is ensured that the matrix can be diagonalised and has exclusively real eigenvalues, such divergences can be excluded with certainty.

A sufficient, though not necessary, condition to guarantee this is that the dynamic matrix is Hermitian [116], i.e. $M = M^\dagger$. Then, the matrix has always real eigenvalues λ_j of the same geometric and algebraic multiplicity and a solution of (3.64) is provided by

$$\mathbf{h}(t) = \sum_{j=1}^{f} \alpha_j e^{i\lambda_j t} \mathbf{v}_j. \tag{3.65}$$

Here, the $\mathbf{v}_j$ denote the eigenvectors of the dynamic matrix and the α_j include the initial conditions imposed on the system. Unquestionably, the structure of (3.65) ensures that all solutions are composed solely of superpositions of oscillatory contributions.

By choosing the basis operators A_i orthogonal with respect to an arbitrary scalar product $(\cdot|\cdot)$, which implies

$$(A_i|A_j) = \delta_{ij}, \tag{3.66}$$

the matrix elements of the dynamical matrix M may be written in the form

$$M_{ji} = (A_j|\mathcal{L}(A_i)). \tag{3.67}$$

For a completely arbitrary scalar product, however, hermiticity of M is not guaranteed. Therefore, the selection of such a scalar product is decisive. A suitable choice is, for example, the Frobenius scalar product

$$(A|B) := \mathcal{N}\,\mathrm{Tr}\Big(A^\dagger B\Big) \text{ with } \mathcal{N} := \frac{1}{\mathrm{Tr}(\mathbb{1})} \tag{3.68}$$

as initially proposed in Ref. [116]. Since the trace is invariant under cyclic permutations we can ensure the self-adjointness of $\mathcal{L}(\cdot)$ and thus the hermiticity of M, i.e.

$$\begin{aligned} M_{ji} &= \mathcal{N}\,\mathrm{Tr}\Big(A_j^\dagger (HA_i - A_i H)\Big) && \text{(3.69a)} \\ &= (A_i|\mathcal{L}(A_j))^* && \text{(3.69b)} \\ &= M_{ij}^*. && \text{(3.69c)} \end{aligned}$$

We highlight the fact that the scalar product (3.68) requires the local Hilbert space of the system to be finite. Such a space is given for all spin systems, fermionic systems as for instance the FHM, or models with a combination of spin and fermionic degrees of freedom. Bosonic systems with their infinite-dimensional Hilbert spaces, in contrast, cannot be captured with the scalar product.

As indicated at the beginning, the iEoM are not only capable of describing the actual real-time dynamics of a system, but they also enable a semi-analytical determination of true long-time averages

$$A_\infty := \lim_{t\to\infty} \frac{1}{t} \int_0^t \mathrm{d}t' \left\langle A(t') \right\rangle . \tag{3.70}$$

The basic idea is that the long-time dynamics (3.70) is completely determined by the initial conditions of the system. Typically, the observables $A(t)$ are products of fermionic creation or annihilation operators. For simplicity, here we resort to an exemplary product of exactly one creation and one annihilation operator. For each of these operators, the dynamics can be determined with the help of (3.61). Then, one decomposes their individual initial vectors $\mathbf{h}(0)$ into the oscillatory eigenmodes (3.65) of the system and eliminates all contributions that cannot participate in the long-time dynamics by using

$$\lim_{t\to\infty} \frac{1}{t} \int_0^t \mathrm{d}t' h_m^*(t') h_n(t') \tag{3.71a}$$

$$= \sum_{i,j} \overline{v}_{i,m}^* \overline{v}_{j,n} \underbrace{\lim_{t\to\infty} \frac{1}{t} \int_0^t \mathrm{d}t' e^{i(\lambda_j - \lambda_i)t'}}_{=\delta_{\lambda_i,\lambda_j}} \tag{3.71b}$$

$$= \sum_{\substack{i,j \\ \lambda_i = \lambda_j}} \overline{v}_{i,m}^* \overline{v}_{j,n} . \tag{3.71c}$$

Thus, one obtains statements about the genuine $t \to \infty$ behaviour of a physical system. We have published a very comprehensive explanation of this method together with its application to the one-dimensional FHM in Ref. [42]. For the full analytical derivation and results, we refer the reader to that paper.

3.4.3 On the concept of unitarity

A common misunderstanding concerning the terminology of a unitary time-evolution is that there are actually two, not entirely synonymous, meanings of this term – depending on whether one speaks of unitary time-evolution of *states* or of *operators*. We explicitly point out this fact in Ref. [42] and recap the most important aspects here.

We will start with the prevailing textbook understanding, i.e. unitarity on the level of *states*. Thereby, any solution $U(t)$ of the differential equation

$$i \frac{\mathrm{d}}{\mathrm{d}t} U(t) = H(t) U(t) \tag{3.72}$$

implies simultaneously that the scalar product of any two states $|a(t)\rangle$ and $|b(t)\rangle$ is invariant because of (3.58) for all times resulting in

$$\langle a(t)|b(t)\rangle = \langle a(0)|U^\dagger(t)U(t)|b(0)\rangle \tag{3.73a}$$

$$= \langle a(0)|b(0)\rangle . \tag{3.73b}$$

In contrast, unitarity on the level of *operators* is a much weaker criterion and merely implies that the scalar product of two operators remains constant, i.e.

$$(A(t)|B(t)) = (A(0)|B(0))\,. \tag{3.74}$$

This, in turn, is easier to ensure. Formally, every time-evolution of the form

$$A(t) = \mathcal{U}A \tag{3.75}$$

with an operator $\mathcal{U} = \mathcal{U}(t)$, for which $\mathcal{U}^\dagger = \mathcal{U}^{-1}$ holds, satisfies the condition of operator unitarity. The formal requirements regarding $\mathcal{U}$ are, thus, more modest than those for a full mapping from the Schrödinger to the Heisenberg picture as given in equation (3.57). Only if we impose the special form

$$\mathcal{U}A := U^\dagger A U \tag{3.76}$$

which places further constraints on $\mathcal{U}$ and, thus, on unitarity on the operator level, operator unitarity also implies time-invariant scalar products of states as in equation (3.73).

What does this difference mean in a practical application? It means, in particular, that although the actual dynamics of an observable is assured to consist exclusively of oscillating terms, conserved quantities of the system do not necessarily remain constant in time in a truncated operator basis. We were able to impressively substantiate this fact in connection with the calculation of the time-dependent local particle density $n(t)$ in the translationally invariant one-dimensional FHM. While the analytical result tells us that there is a constant particle density

$$n(t) = \text{const} \tag{3.77}$$

equal to the filling, cf. section 3.3.3, deviations from this reference value were detectable in the iEoM calculations [42]. There, we were also able to show that this implication does not necessarily represent a disadvantage. We could use the proper non-dependence on time of a conserved quantity as a sensitive test for the accuracy of different truncation schemes used when constructing the operator basis.

It is tempting to believe that a method like iEoM, which cannot guarantee unitarity of states, can only inadequately simulate physical systems, if at all. Nevertheless, such deviations do not always have to occur and mainly depend on the observables to be considered and the truncation scheme. For example, we were able to obtain highly accurate results for the (non-local) jump at the Fermi surface with a comparatively small basis for the one-dimensional FHM. These results were in complete agreement with numerically substantially more demanding calculations like those of a DMFT approach [117]. For further details and an in-depth discussion of the results regarding energy scales and dynamical phase transitions within the one-dimensional FHM as obtained by means of the iEoM method, the reader is referred to section 5.4 and Ref. [42].

The characteristic difference between the iEoM approach and other methods is that the iEoM approach is hardly subject to any practical obstacles and can easily be used to calculate the time-evolution for arbitrarily long periods of time as well as arbitrary lattices.

4 Approaches to thermal expectation values

While the calculation of time-dependent observables as discussed in chapter 3 provides insight into the dynamics of a system at a fixed time t, it is sometimes of similar interest to be able to make predictions about its thermal behaviour. This behaviour is characterised by the so-called thermal expectation values $\langle O\rangle_{\text{th}}$. These are the mean values that observables O of the system adopt when the system is in complete thermal equilibrium. Whether such a thermal equilibrium occurs, and if so to what extent, is still a highly debated question in theoretical physics [27]. A dedicated discussion of the reasons and implications of the question and our contribution to the debate can be found in chapter 5. For the moment, we simply assume that the system to be considered is in the state of thermal equilibrium after a sufficiently long relaxation period.

In this case, the system is described best by its canonical ensemble and only the effective inverse temperature $\beta := {}^1\!/_T$ of the system determines its thermal properties. Here, each quantum mechanical eigenstate $|i\rangle$ with corresponding energy E_i of the system is weighted by its probability of occurrence, i.e. its Boltzmann factor $e^{-\beta E_i}$, leading to

$$\langle O\rangle_{\text{th}} = \frac{1}{Zd}\operatorname{Tr}\left(Oe^{-\beta H}\right) \tag{4.1a}$$

$$= \frac{1}{Zd}\sum_{i=0}^{d-1}\langle i|O|i\rangle\, e^{-\beta E_i}. \tag{4.1b}$$

In this context, the scalar Z denotes the partition function counting all weighted states

$$Z = \frac{1}{d}\operatorname{Tr}\left(e^{-\beta H}\right) = \frac{1}{d}\sum_{i=0}^{d-1} e^{-\beta E_i}. \tag{4.2}$$

Contrary to the usual convention, a normalisation by means of $d := \dim(\mathcal{H})$ is used here to achieve a more stable numerical integration of (4.1) and (4.2) in section 4.1.

A complete diagonalisation as described in section 3.2 would be the apparently most direct path to a solution, but once again this approach is in practice simply impossible due to the enormous numerical effort. So what are the possibilities to fathom the thermal behaviour (4.1) with alternative approaches? In the following, we present two different approaches to answer this question and evaluate them, especially with regard to their numerical stability and simplicity of implementation in our actual applications.

4.1 Kernel polynomial method

The most intuitive approach to determining thermal expectation values is obviously to fall back on the already existing toolsets and, thus, on conceptual ideas of the Chebyshev expansion, cf. section 3.3. A prominent example of such an approach is the Kernel polynomial method (KPM). Such methods have a long history and have suffered for a long time from problems related to finite temperatures $\beta > 0$. Subsequent concepts of this section are partly based on Ref. [118].

For the successful application of a Chebyshev expansion a function is required in the first step, analogous to (3.50), that we may expand on the closed interval $I = [-1; 1]$ using moments μ_n. In the following, we always assume that a suitable rescaling of the system, comparable to that used in (3.43), has already taken place. In concrete terms, this means that all observables and functions calculated here are defined on I only. A subsequent rescaling to the actual physical result domain is therefore necessary, for example, if a comparison is to be made with experimental results. When we refer to a *rescaled* density of states in subsequent calculations the respective quantity on I is meant.

In order to obtain functions to be expanded we rewrite our two target quantities (4.1) and (4.2) into a continuous form. Thereby, the canonical partition function becomes

$$Z = \int_{-1}^{1} \rho(E) e^{-\beta E} \, \mathrm{d}E \tag{4.3}$$

and the desired thermal expectation value may be rewritten in an analogous way as

$$\langle O \rangle_{\mathrm{th}} = \frac{1}{Z} \int_{-1}^{1} o(E) e^{-\beta E} \, \mathrm{d}E \,. \tag{4.4}$$

The actual task now lies in finding reasonably good approximations of the rescaled density of states $\rho(E)$ as well as of the observable density $o(E)$ given by

$$\rho(E) = \frac{1}{d} \sum_{i=0}^{d-1} \delta(E - E_i) \tag{4.5a}$$

$$o(E) = \frac{1}{d} \sum_{i=0}^{d-1} \langle i | O | i \rangle \, \delta(E - E_i). \tag{4.5b}$$

Unfortunately, an analytical derivation of the expansion coefficients with a precise error estimate as we did in equations (3.51b), (3.52b) and (3.56) is not always feasible. Likewise, even if an analytical approach is possible it might lead nowhere. As an instructive example, consider the density of states (4.5a) which – inserted into equation (3.42b) – leads to moments involving the complete energy spectrum by

$$\mu_n = \frac{1}{d} \sum_{i=0}^{d-1} T_n(E_i) = \frac{1}{d} \sum_{i=0}^{d-1} \langle i | T_n(H) | i \rangle \,. \tag{4.6}$$

Such a complete spectrum, however, can only be determined by a complete diagonalisation. Since this is not feasible, equation (4.6) is not of any practical use. In practice, the situation is actually even worse. Imagine that we were given the full spectrum E_i and all we had to do was to evaluate (4.6) to insert it into (3.42a). Contrary to the expansion of the time-evolution operator U, it is not easily possible for us here to truncate the infinite series in a controlled manner after a finite number of contributions, so we would in theory have to compute an infinite number of moments μ_n. Needless to say, for practical reasons we do not have such an option. But what happens if we uncontrollably truncate the series after a finite number of summands?

The most urgent issue when truncating an infinite series such as (3.42a) after a finite number of contributions are Gibbs oscillations, cf. Ref. [111, § 6.16(i)]. This means that in the vicinity of points where the initial function possesses discontinuities or singularities highly oscillating fluctuations occur. This does not only lead to an unsatisfactory approximation of $f(x)$ but also to the more severe impossibility to numerically integrate the approximated function afterwards with a high precision which is a key ingredient to the determination of thermal quantities such as (4.3) or (4.4). Furthermore, note that the Boltzmann weight disproportionately penalises the smallest numerical errors in the low-energy region of the spectrum upon integration.

For these reasons, on the one hand, we have to find a procedure in which Gibbs oscillations can be suppressed sufficiently and, on the other hand, moments μ_n may be computed even if they contain traces $\mathrm{Tr}(A) := \sum_{i=0}^{d-1} \langle i|A|i\rangle$ involving the full spectrum as, for example, in equation (4.6). We address these issues in the following two sections.

4.1.1 Convolution with a kernel

In order to obtain a first impression of the nature and extent of Gibbs oscillations, we turn to the concrete example of a two-dimensional free electron gas with (piecewise) constant density of states, i.e.

$$\rho_{\mathrm{2D}} \propto \theta(E). \tag{4.7}$$

This density has a discontinuity at $E = 0$ and, thus, inevitably leads to Gibbs oscillations. If one naively approximates the underlying step function by truncating the infinite series (3.42a) after $N < \infty$ contributions, one sees a strong overshoot especially in the discontinuity region. Right before and after, oscillations that diminish with distance from the discontinuity appear, cf. naive truncation in figure 4.1.

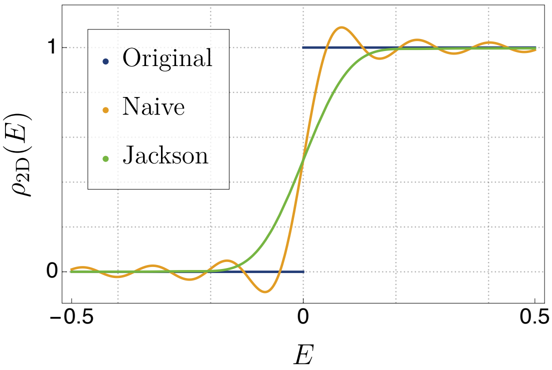

Figure 4.1: Piecewise constant density of states ρ_{2D} being first approximated by the naive approach of a simple truncation and second by truncation and convolution with the Jackson kernel. Here, we truncate after $N = 39$ contributions.

To avoid a highly oscillating resulting function when the Chebyshev expansion is performed up to a maximum degree of N polynomials, we use an integral kernel

$$K_N(x, y) = g_0 W_0(x) W_0(y) + 2 \sum_{n=1}^{N-1} g_n W_n(x) W_n(y). \tag{4.8}$$

In this case, the functions $W_n(x)$ represent a set of basis functions modified according to equation (3.41). Using (4.8) is sometimes referred to as convolution in the literature. Written in a less formal way, this convolution is equal to a rescaling of the moments $\mu_n \to g_n\mu_n$ such that the approximate function (3.42a) becomes

$$f_{\mathrm{KPM}}(x) = \langle K_N(x,y)|f(y)\rangle_2 = \frac{1}{\pi\sqrt{1-x^2}}\left(g_0\mu_0 + 2\sum_{n=1}^{N-1} g_n\mu_n T_n(x)\right). \tag{4.9}$$

The crucial aspect when resorting to (4.9) is the question how to optimally choose the rescaling factors g_n. The simplest choice in this context is the so-called Dirichlet kernel. A convolution of the approximated function with this kernel leads to $g_i = 1\,\forall\, i$ and, thus, effectively to an unmodified truncation. The result of this convolution is consequently inadequate and less desirable as seen for the naive truncation in figure 4.1. Among many possibilities of choosing a kernel, one stands out in particular. The Jackson kernel [119, 120] has proven to be the optimal choice for many practical applications. We present its central motivation and schematic derivation here briefly and, for this purpose, resort to the extensive calculations carried out by Weiße et. al [118]. Readers who are interested in the detailed derivation of a variety of different kernels as well as in their individual convergence properties are recommended to consult this source for further information.

A uniform convergence of the approximated function $f_{\mathrm{KPM}}(x)$ towards the original function $f(x)$ for an increasing number of polynomials is a highly preferable property that allows us to make various reliable assertions about the approximated function, such as its continuity or integrability. Uniform convergence is achieved if the kernel fulfils the following conditions requiring that

(1) the kernel has to be positive, i.e. $K_N(x,y) > 0 \;\forall\; x,y \in I$,

(2) the kernel is normalised, i.e. $g_0 = 1$,

(3) the second coefficient obeys $g_1 \xrightarrow{N\to\infty} 1$.

In order to prove the positivity (1) of the kernel $K_N(x,y)$ the strictly positive function

$$p(\phi) = \left|\sum_{v=0}^{N-1} a_v e^{iv\phi}\right| = g_0 + 2\sum_{v=1}^{N-1} g_n \cos(n\phi) \;\text{ with }\; g_n := \sum_{v=0}^{N-1-n} a_v a_{v+n} \tag{4.10}$$

is used where $a_v \in \mathbb{R}$ are arbitrary coefficients. Since $p(\phi)$ is positive, the following expression is positive in the interval I as well

$$\frac{1}{2}\left[p(\arccos(x) + \arccos(y)) - p\left(\arccos(x) - \arccos(y)\right)\right] > 0\,\forall\, x,y \in I. \tag{4.11}$$

Subsequently, it is possible to rewrite the expression on the left-hand side of (4.11) into the form $K_N(x,y)$ defined in (4.8), which yields $K_N(x,y) > 0 \;\forall\; x,y \in I$ as required. This can be achieved by inserting $\phi = \arccos(x)$ as well as using the identity (3.36) for the

Chebyshev polynomials and rescaling the polynomials with the positive weight function $w_1(x)$ as defined in section 3.3.1.

Here, the fulfilment of positivity explicitly places no requirements on the general structure of the real-valued coefficients a_v. This freedom of choice makes it possible to select the a_v as optimally as possible in the sense that the broadening achieved by the kernel for arbitrary functions $f(x)$ is as small as feasible. Abrupt changes of the function, i.e. sharp features, should thereby remain as distinct as they can be. To optimise this broadening and preserve pronounced features, we minimise the expression

$$Q := \iint_I (x-y)^2 K_N(x,y)\,\mathrm{d}x\,\mathrm{d}y \tag{4.12}$$

which in fact reduces the squared width of the peak at $x = y$ under convolution. One then replaces $x \to T_1(x)$ and $y \to T_1(y)$ in equation (4.12) and uses the orthogonality of the Chebyshev polynomials (3.38) in connection with Lagrange multipliers. The latter ones are resorted to since the condition (2) of a normalised kernel with $g_0 = 1$ has to be fulfilled. Undergoing all these steps, cf. Ref. [121], leads to the Jackson coefficients

$$g_n = \frac{(N-n+1)\cos\left({}^{\pi n}/_{N+1}\right) + \sin\left({}^{\pi n}/_{N+1}\right)\cot\left({}^{\pi}/_{N+1}\right)}{N+1}. \tag{4.13}$$

The effect of convolution with the Jackson kernel (4.13) is significant and has the great advantage, especially in comparison to naive truncation, that oscillatory artefacts are almost completely dodged, cf. figure 4.1. This, however, comes at a cost. The unavoidable broadening of the original function due to the convolution becomes evident in the less pronounced slope of the convolved function in comparison to the original and naively approximated function.

4.1.2 Stochastic evaluation of traces

In order to enhance an approximation by means of a convolution with a kernel, it must be calculated in the first place. This is particularly difficult if the function to be approximated requires the full spectrum E_i as in (4.5). Since $\rho(E)$ emerges from $o(E)$ for $O = \mathbb{1}$, we will concentrate on the approximation of the observable density $o(E)$ only. All moments (3.42b) appearing in this case may be written as

$$\begin{aligned} \mu_n &= \int_{-1}^{1} o(E) T_n(E)\,\mathrm{d}E && \text{(4.14a)} \\ &= \frac{1}{d}\sum_{i=0}^{d-1} \langle i|O|i\rangle\, T_n(E_i) && \text{(4.14b)} \\ &= \frac{1}{d}\operatorname{Tr}\left(O T_n(H)\right). && \text{(4.14c)} \end{aligned}$$

The trace arising here cannot be calculated exactly, even for moderately large systems. But can we eventually approximate this trace and, if so, to what quality? To answer this question, we fall back on ideas for stochastic trace evaluation initially proposed by Skilling [122] and generalised and applied to physical quantities by Silver et al. [123] as well as by Drabold et al. [124]. The main idea of this technique is to average over a small subset of $R \ll d$ randomly chosen quantum states instead of using all d states spanning the Hilbert space. In order to be able to easily distinguish between the full trace $\mathrm{Tr}(A)$ of a given operator A and the trace estimate, we define the latter one by means of

$$\mathrm{tr}\,(A) := \frac{1}{R} \sum_{r=0}^{R-1} \langle r|A|r\rangle \,. \tag{4.15}$$

Here, each of the R quantum states is completely random and does not need to coincide in any way with any meaningful state of the system, such as an eigenstate of the Hamiltonian. The states are constructed using arbitrary orthogonal basis states $|i\rangle$ by

$$|r\rangle = \sum_{i=0}^{d-1} \xi_{ri}\,|i\rangle \tag{4.16}$$

with complex coefficients $\xi_{ri} \in \mathbb{C}$ that stem from a probability distribution which fulfils

$$\langle\!\langle \xi_{ri} \rangle\!\rangle = 0, \quad \langle\!\langle \xi_{ri}\xi_{r'j} \rangle\!\rangle = 0, \quad \langle\!\langle \xi_{ri}^{*}\xi_{r'j} \rangle\!\rangle = \delta_{rr'}\delta_{ij}. \tag{4.17}$$

In this context, the notation $\langle\!\langle \cdot \rangle\!\rangle$ means the statistical average. It is evident that the relation $\langle\!\langle \mathrm{tr}\,(A) \rangle\!\rangle = \mathrm{Tr}\,(A)$ will hold if we construct only sufficiently many states $|r\rangle$ and average over them according to equation (4.15). That is, the mean value of the approximated trace will be equal to the trace over the entire Hilbert space. The apparent point here is: How quickly do the two results approach each other and how many random states must actually be drawn in order to provide a sufficiently good approximation? To answer this question the variance of the approximation comes in handy.

For a given Hermitian operator A, the variance as calculated in Ref. [118] reads

$$\sigma^2 = \langle\!\langle \mathrm{tr}\,(A)^2 \rangle\!\rangle - \langle\!\langle \mathrm{tr}\,(A) \rangle\!\rangle^2 = \frac{1}{R}\left(\mathrm{Tr}\big(A^2\big) + \Big(\langle\!\langle |\xi_{ri}|^4 \rangle\!\rangle - 2\Big)\sum_{i=0}^{d-1} A_{ii}^2\right) \tag{4.18}$$

where $A_{ij} = \langle i|A|j\rangle$ denotes the matrix elements. It is possible to eliminate the rightmost part of equation (4.18) by drawing both the real and the imaginary part of the coefficients $\xi_{ri} = a + ib$ independently from a Gaussian distribution with an expectation value of $\mu = 0$ and a variance of $\sigma^2 = 1/2$ due to its statistical average given by

$$\langle\!\langle |\xi_{ri}|^4 \rangle\!\rangle = \langle\!\langle a^4 + 2a^2b^2 + b^4 \rangle\!\rangle \tag{4.19a}$$

$$= \frac{2}{\sqrt{\pi}} \int_{\mathbb{R}} x^4 e^{-x^2}\,\mathrm{d}x + 2 \cdot \left(\frac{1}{\sqrt{\pi}} \int_{\mathbb{R}} x^2 e^{-x^2}\,\mathrm{d}x\right)^2 \tag{4.19b}$$

$$= \frac{6}{4} + \frac{2}{4} = 2. \tag{4.19c}$$

This, in turn, leads to a variance being independent of the chosen basis. Traces depend linearly on the dimension d of the Hilbert size implying that $\mathrm{tr}(A) \in \mathcal{O}(d)$. Consequently, the relative error σ_{rel} of a stochastically evaluated trace is of the order

$$\sigma_{\mathrm{rel}} = \frac{\sigma}{\mathrm{tr}(A)} \propto \frac{\sqrt{{}^{d}/_{R}}}{d} = \frac{1}{\sqrt{Rd}}. \tag{4.20}$$

When looking at equation (4.20), it becomes clear why the approximation of traces is a highly promising concept for realistic cases of medium to large systems. The reason for this lies in particular in the behaviour $\sigma_{\mathrm{rel}} \propto d^{-1/2}$ which has an implication that seems counterintuitive: For a constant number of drawn states R, the approximation error becomes smaller with increasing Hilbert space dimension. Analogously, it can be stated that as the dimension of the Hilbert space increases, fewer and fewer states are required for an approximation of a specified quality.

For a better understanding of this effect, we turn to an application for the half-filled, one-dimensional FHM. As the number of particles is conserved in this model, the effective Hilbert space is significantly reduced in accordance with (3.8). In the following, we denote the dimension of this effective Hilbert space by d'. For a relative error of $\sigma_{\mathrm{rel}} < 10^{-3}$, which is conventional in practice, the necessary amount of random states R for different lattice sizes N is listed in table 4.1.

Table 4.1: Number of random states R for a relative trace error below 10^{-3} with lattice size N and effective Hilbert space dimension d'.

N	d' $[10^5]$	R
8	0.05	205
10	0.64	16
12	8.54	2
14	117.79	1

For a lattice size of $N = 8$ only $R = 205$ randomly drawn states are necessary. This corresponds approximately to 4 % of the effective Hilbert space. This effect becomes even more pronounced with increasing lattice size or Hilbert space dimension. Already for $N = 14$ states, only one single random state $|r\rangle$ has to be drawn in order to approximate a given trace with the help of (4.15) in sufficient accuracy.

4.1.3 Low-temperature issues

As described in the context of thermal expectation values (4.1), a system in thermal equilibrium can be characterised solely by its inverse temperature $\beta := {}^{1}/_{T}$. In the case of a low temperature, i.e. $T \ll J$, the resulting inverse temperature becomes noticeably large with $\beta_{\mathrm{eff}} \gg {}^{1}/_{J}$. In interacting systems, this leads to a large Boltzmann weight in equation (4.4) for the lowest part of the energy spectrum E_i which then heavily amplifies even small numerical errors in this domain. Since common computational systems use floating-point algebra, minor numerical inaccuracies are inevitable and – once amplified by large Boltzmann weights – may spoil numerical results completely. Note that this issue is of fundamental character and cannot be solved by trivial means such as the mere increase of the number of expansion moments μ_n. We return to this issue and its possibly serious implications in the comparison of KPM with an alternative method in section 4.3.

It is worthwhile to emphasise that this problem does not persist in the case of non-interacting fermionic particles since in this case all energies of the many-particle system can be separated into isolated contributions from effective one-particle subsystems. This leads to an average occupancy of one of the levels which is given by the Fermi-Dirac distribution. This distribution converges to a step function in the limit of $\beta \to \infty$ and, thus, does not cause any numerical shortcomings.

The only promising way to address the problem of large Boltzmann weights in strongly correlated systems when using KPM is to exclude the low-energy region of the spectrum in all calculations. Nevertheless, as this region is highly relevant, especially for weakly excited systems, it cannot simply be omitted, but must be treated with an alternative procedure. This is precisely the approach proposed by Weiße et al. [118]. They suggest to overcome the obstacles in the interacting regime by combining iterative approaches and the kernel polynomial method. This way, the ground state and the $m-1$ energetically lowest excitations of the systems are treated in an exact manner while the remainder of the spectrum is calculated using the kernel polynomial expansion. The respective decomposition of (4.4) reads

$$\langle O \rangle_{\mathrm{th}} = \frac{1}{Zd} \sum_{i=0}^{m-1} \langle i|O|i\rangle \, e^{-\beta E_i} + \frac{1}{Z} \int_{-1}^{1} o(E) e^{-\beta E} \, \mathrm{d}E \tag{4.21}$$

where the partition function Z is decomposed likewise and i counts the eigenstates of the systems in energetically increasing order. Since the new moments μ_n used for KPM must not capture the full Hilbert space, we project out the subspace that was treated exactly, e.g. by resorting to the Lanczos algorithm, using the projection operator

$$P = \mathbb{1} - \sum_{i=0}^{m-1} |i\rangle\langle i| \, . \tag{4.22}$$

For the part of the spectrum that does not contain the low-energy excitations, the Boltzmann weight is no longer a noteworthy problem. This fraction can thus be treated normally with KPM on the reduced Hilbert space. For this purpose the new moments of the functional expansion are slightly altered to become

$$\mu_n = \frac{1}{d} \operatorname{Tr}\left(POT_n(H)\right) . \tag{4.23}$$

Analogously, the modified moments for the expansion of the partition function Z follow from equation (4.23) by setting the observable O to unity.

4.2 Quantum typicality

For a better understanding of the principle behind the concept to come, it is suggested to first reconsider the approximation of traces in section 4.1.2. In this framework, a few random states have sufficed to reproduce and capture the behaviour of a significantly larger Hilbert space with adequate accuracy. The phenomenon underlying this observation is commonly called quantum typicality and states that the expectation values of characteristic pure states are equal to the expectation values of the statistical ensemble, see for example Refs. [125, 126]. Its key aspect is the tremendously high level of entanglement between the subsystem and the environment coupled to that system. We come back to this aspect and our own contributions to the topic in detail in section 5.3 and first focus on the consequences of this observation.

4.2.1 Thermal pure quantum states

When we examine equation (4.15) again, it becomes clear that the approximated trace $\mathrm{tr}(A)$ corresponds to the searched thermal expectation value (4.1) for infinitely high temperatures T. In other words, we notice that the relation

$$\lim_{T\to\infty} \langle A\rangle_{\mathrm{th}} = \mathrm{tr}(A) \tag{4.24}$$

holds. This observation is intuitively easy to accept because the states used for the approximation have been drawn completely uniformly in the context of (4.16) as well as (4.17). Nevertheless, this just means that every pure state of the Hilbert space is considered equally probable and the system is completely disordered. A disordered canonical ensemble is characterised by a density matrix $\rho \propto \mathbb{1}$ and $T \to \infty$. Thus, in order to be able to calculate thermal expectation values for finite temperatures T, not all states may be regarded as equivalent any more. The previously completely randomly drawn states must, loosely speaking, be cooled down to inverse temperatures $\beta > 0$.

To find out what form these cooled-down characteristic states $|\beta\rangle$ have, we decompose the application of the Boltzmann weight to the normalised state $|r\rangle$ into two contributions using the invariance of the trace under cyclic permutation. This results in

$$\begin{aligned}
\mathrm{Tr}\left(Oe^{-\beta H}\right) &= \mathrm{Tr}\left(e^{-\beta H/2} O e^{-\beta H/2}\right) && (4.25\mathrm{a})\\
&= d\,\overline{\langle r|e^{-\beta H/2} O e^{-\beta H/2}|r\rangle} && (4.25\mathrm{b})\\
&\overset{(*)}{=} d\,\overline{\langle \beta|O|\beta\rangle} && (4.25\mathrm{c})
\end{aligned}$$

when using the overbar to denote the arithmetic mean over a set of different normalised states $\{|r\rangle\}$ and identifying

$$|\beta\rangle := e^{-\beta H/2}\,|r\rangle\,. \tag{4.26}$$

The states $|\beta\rangle$ are commonly named thermal pure quantum states (TPQS) and were suggested by Sugiura and Shimizu [127]. As long as the set $\{|r\rangle\}$ is the full basis of the d-dimensional Hilbert space, then the equality denoted by the asterisk in (4.25c) is given. However, if only a smaller subset of $R \ll d$ randomly drawn normalised states is used, i.e. if the trace is approximated analogously to section 4.1.2, the same considerations regarding the relative error described by (4.20) apply and the error follows to $\sigma_{\mathrm{rel}} \propto {}^{1}/\sqrt{Rd}$. In order to obtain the thermal expectation value we identify the partition sum as

$$Z = d\overline{\langle \beta|\beta\rangle}. \tag{4.27}$$

Inserting the partition sum Z and equation (4.25) into (4.1a) eventually yields

$$\langle O\rangle_{\text{th}} = \frac{\overline{\langle\beta|O|\beta\rangle}}{\overline{\langle\beta|\beta\rangle}}. \tag{4.28}$$

Especially in high-dimensional Hilbert spaces, typically only few or even a single state $|\beta\rangle$ are sufficient to calculate the expectation values of the system in thermal equilibrium.

It is to be noted that quantum typicality is not only limited to static quantities in thermal equilibrium. It has been shown that the dynamics of observables and, thus, the equilibration behaviour of systems can also be simulated with representatively drawn states. For example, the autocorrelation function of the spin current in the Heisenberg model can be derived from only a single state that is to be propagated [128]. As quantum typicality will be used throughout this work exclusively for approaches to thermal expectation values, we will not discuss applications to dynamical quantities any further. For the interested reader, Ref. [129] is recommended for a methodological review.

The primary advantage of resorting to TPQS is its conceptual simplicity, both in terms of implementation effort and the directness of the method. In contrast to the approach via KPM, for TPQS no auxiliary quantities such as functions to be expanded have to be calculated and no numerically potentially demanding or even unstable integrations have to be carried out. Yet all these advantages are only given if it is possible to calculate the matrix exponential of TPQS in a time-saving and efficient way. An especially efficient way, which was put forward in Ref. [130], is by resorting to the Lanczos algorithm [104].

4.2.2 Lanczos algorithm and matrix exponentials

One of the main issues in applying the matrix exponential $\exp\left(-{}^{\beta H}/_{2}\right)$ to the randomly drawn state $|r\rangle$ in (4.26) is the necessity to know the eigenbasis of H to calculate its corresponding exponential. We circumvent this problem by constructing an s-dimensional Krylov space $\mathcal{K}^s$ with $s \ll d$ as a small subspace of the full d-dimensional Hilbert space.

For this purpose, we transform the state $|r\rangle$ into a coefficient vector $\mathbf{r}$ as well as the Hamiltonian into a matrix H with respect to a chosen basis. The special form or configuration of this basis is not of importance in this case [129]. In fact, any suitable basis can be chosen which is optimal for the problem. This is insofar remarkable as with the eigenstate thermalisation hypothesis a very similar, but not identical statement is available. It states that the expectation value $A_{ii} = \langle i|A|i\rangle$ of a local observable A in an eigenstate $|i\rangle$ of a non-integrable Hamiltonian is practically indistinguishable from the expectation value $\langle A\rangle_{\text{mc}}$ of the equivalent microcanonical ensemble at the same energy in realistically large systems [131], i.e.

$$A_{ii} = \langle A\rangle_{\text{mc}} \tag{4.29}$$

holds. Similarly, a single pure state $|i\rangle$ is enough to capture an ensemble of many different states sufficiently well. In contrast to (4.26), however, there are clear requirements for the structure of the state $|i\rangle$ in (4.29): It must be an eigenstate of H. This condition is not imposed on the states in the framework of quantum typicality. Only their randomness given by (4.16) and a sufficiently large dimension of the Hilbert space are necessary. As Heitmann et al. [129] motivate, this means in particular that quantum typicality is also applicable in cases where the eigenstate thermalisation hypothesis breaks down. This, according to the authors, is because (4.16) is invariant under unitary transformations and thus, in particular, a transformation is permitted that changes the formerly arbitrary but orthogonal basis states $|i\rangle$ into eigenstates of the Hamiltonian. Then, however, $|r\rangle$ would be a superposition of eigenstates and the prerequisites of the eigenstate thermalisation hypothesis would no longer be given. Nevertheless, the applicability of quantum typicality is still given. Obviously, the freedom of choice of the basis also includes the possibility of exploiting symmetries of the system in the construction of basis states. Without explicitly stating this fact, we have already made use of it in the context of table 4.1, where we employed particle number conservation to reduce the size of the effective Hilbert space.

After choosing a basis, the actual matrix exponential has to be calculated. For this purpose, we use the Lanczos algorithm [104], whose following description is taken from Ref. [43] and slightly adapted for an easy applicability to TPQS according to the ideas presented in Ref. [130]. In order to calculate the matrix exponential we start from the random vector $\mathbf{r}$ drawn according to (4.16) and repeatedly apply the Hamiltonian in its matrix form H. This procedure creates the underlying Krylov space

$$\mathcal{K}^s(\mathbf{r}) = \operatorname{span}\left(\mathbf{r},\, H\mathbf{r},\, H^2\mathbf{r}, \ldots,\, H^{s-1}\mathbf{r}\right) \tag{4.30}$$

in which the evaluation of the matrix exponential takes place.[1] This iterative process [132] begins with the normalised initial vector

$$\mathbf{b}_1 = \frac{\mathbf{r}}{\|\mathbf{r}\|} \tag{4.31a}$$

as the first basis vector of $\mathcal{K}^s$. All further vectors $\mathbf{r}_j$ of the Krylov space are constructed to be mutually orthogonal using

$$\gamma_j = \mathbf{b}_j^\dagger H \mathbf{b}_j \tag{4.31b}$$

$$\mathbf{r}_j = H\mathbf{b}_j - \gamma_j \mathbf{b}_j - \beta_{j-1}\mathbf{b}_{j-1} \tag{4.31c}$$

$$\beta_j = \begin{cases} \|\mathbf{r}_j\| & \text{if } j \geq 1 \\ 0 & \text{otherwise.} \end{cases} \tag{4.31d}$$

In each step, the resulting basis vector is finally normalised according to

$$\mathbf{b}_{j+1} = \frac{\mathbf{r}_j}{\|\mathbf{r}_j\|}. \tag{4.31e}$$

Thus, the Lanczos algorithm (4.31) leads to a new basis of orthonormal basis vectors $\mathbf{b}_j, j \in \{1, \ldots, s\}$, which are created in the course of the iterative process and fulfil

$$\mathbf{b}_i^\dagger \mathbf{b}_j = \delta_{ij}. \tag{4.32}$$

---

[1] In most cases, relatively small dimensions s are sufficient to reproduce results of the full Hamiltonian. Since an exact diagonalisation has an asymptotic complexity which is cubic in the matrix dimension the time to find the eigensystem of eigenvalues and eigenvectors of the Krylov space representation H_s is $\mathcal{O}\left(s^3\right)$ and thus significantly less than $\mathcal{O}\left(d^3\right)$ for a diagonalisation of H.

Here, the notation $\mathbf{b}_i^\dagger$ denotes the conjugate transpose of the vector $\mathbf{b}_i$. The Hamiltonian H has now been significantly reduced regarding its dimension and can be expressed in its new basis $\{\mathbf{b}_i\}$ leading to the real-valued symmetric tridiagonal matrix

$$H_s = \begin{pmatrix} \gamma_1 & \beta_1 & 0 & \cdots & 0 & 0 \\ \beta_1 & \gamma_2 & \beta_2 & \cdots & 0 & 0 \\ 0 & \beta_2 & \gamma_3 & & 0 & 0 \\ \vdots & \vdots & & \ddots & & \vdots \\ 0 & 0 & 0 & & \gamma_{s-1} & \beta_{s-1} \\ 0 & 0 & 0 & \cdots & \beta_{s-1} & \gamma_s \end{pmatrix}. \tag{4.33}$$

To calculate the numerator of equation (4.28), we average over as many different realisations of $\langle\beta|O|\beta\rangle$ as necessary for the desired accuracy. The computation of one of these realisations involves the usage of the Krylov basis vectors $\mathbf{b}_i$ created in the iterative process. Let B_s be the matrix whose columns are given by these Krylov basis vectors, i.e.

$$B_s = (\mathbf{b}_1 \mid \cdots \mid \mathbf{b}_s)\,. \tag{4.34}$$

Then, the approximate correspondence for the full Hamiltonian H in the s-th step reads

$$H \approx B_s H_s B_s^\dagger. \tag{4.35}$$

Inserting this approximation (4.35) into the numerator of equation (4.28) leads to

$$\begin{aligned} \langle\beta|O|\beta\rangle &= \langle r|e^{-\frac{\beta}{2}H} O e^{-\frac{\beta}{2}H}|r\rangle && (4.36a) \\ &\approx \mathbf{r}^\dagger B_s e^{-\frac{\beta}{2}H_s} B_s^\dagger O B_s e^{-\frac{\beta}{2}H_s} B_s^\dagger \mathbf{r} && (4.36b) \\ &= \mathbf{e}_1^\dagger e^{-\frac{\beta}{2}H_s} B_s^\dagger O B_s e^{-\frac{\beta}{2}H_s} \mathbf{e}_1. && (4.36c) \end{aligned}$$

Here, the unit vector into the first direction of the Krylov space basis

$$\mathbf{e}_1 = (1, 0, \cdots, 0)^T \tag{4.37}$$

stems from the orthogonality of the different basis vectors according to (4.32). Note that H_s is not in its diagonal form but tridiagonal instead. Exactly diagonalising this tridiagonal matrix, e.g. by means of QR decompositions, is easily feasible and fast due to the reduced Krylov space dimension as it is analysed in-depth in footnote 1 on page 55.

The denominator $\langle\beta|\beta\rangle$ and, thus, the partition sum Z follows directly from equation (4.36) by setting O to unity.

4.3 Method comparison

In view of the two very different approaches to the thermal behaviour of systems, the question arises almost instantaneously which procedure is to be preferred for which application. In our work on the relaxation behaviour of quenched systems, see section 5.3

or Ref. [133], both methods were implemented on highly parallel cluster systems. In the following, we use the resulting opportunity for a dedicated comparison of both methods to work out the strengths and weaknesses of the methods on the basis of an illustrative concrete example. For this purpose, we simulate the thermal expectation value of the double occupancy d_i at the lattice site i for the one-dimensional FHM with $N = 10$ lattice sites, periodic boundary conditions, half-filling and an on-site interaction strength of $U/J = 3$. The overall Hilbert space dimension of this model equals roughly $6.4 \cdot 10^4$. To get an idea of the expected results, we qualitatively estimate the two limiting cases $\beta = 0$ as well as $\beta \to \infty$. A central role in this estimation is played by the Boltzmann weight shown in figure 4.2 for different fixed values of β.

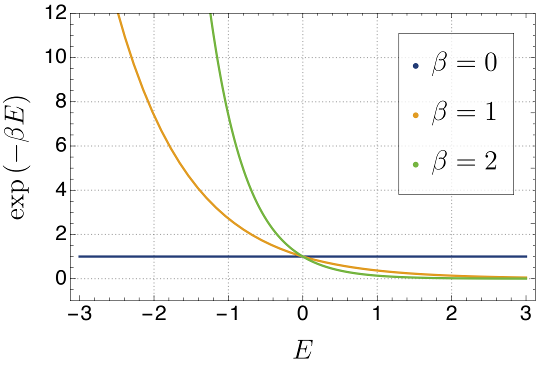

Figure 4.2: Boltzmann weight $\exp(-\beta E)$ for three fixed values of β as a function of the energy E. Solely for infinitely high temperature T, i.e. $\beta = 0$, the energy eigenstates $|i\rangle$ of the Hamiltonian are equally weighted. For all other $\beta > 0$, only the lowest-energy part of the spectrum has a significant contribution.

For the first case $\beta = 0$, all states are equally weighted in the trace calculation, so that the limiting value of the thermal expectation value (4.1a) can simply be calculated by means of a combinatorial approach: For half-filling, i.e. a fixed number $N_\sigma = N/2$ of spins of orientation σ, exactly one of four possible scenarios on each lattice site i results in a double occupancy (DO). Since all scenarios are equally likely, $d_i(\beta = 0) = 1/4$ holds.

For the case $\beta \to \infty$, a combinatorial *a priori* estimation is not possible without knowledge concerning the spectrum. This is, in particular, due to the fact that the Boltzmann weight generates a strong imbalance already for minimally larger $\beta > 0$: eigenstates $|i\rangle$ of the Hamiltonian contribute much more to the thermal expectation value if they are of low energy. The lower the actual effective temperature T of the system becomes, the less high-energy states contribute to the thermal behaviour. In the extreme case $\beta \to \infty$, the trace is dominated by a few low-energy excitations of the system, if not exclusively by the ground state of the system only. In particular, we thus expect an asymptotic convergence to a fixed value for this edge case. Given the large relative importance of low-energy excitations for $\beta \to \infty$, it can already be concluded that a method must be particularly accurate in this range of the spectrum in order to capture the behaviour at low temperatures T correctly.

After these general considerations we take a look at the concrete use case of the one-dimensional FHM. As a start, we resort to the unmodified KPM approach according to equation (4.4). The respective results are depicted in figure 4.3a. For the high temperature range, i.e. $\beta = 0$, the results agree with the combinatorial ones. For an increasing number k of moments μ_n a gradual decrease of the predictions of the thermal expectation value in the range $\beta \sim 0.5/J$ can be observed. For even larger $\beta > 0.7/J$, the KPM results asymptotically approach the same value, which is of the order of $d_i(\beta{=}0) = {}^1\!/_4$. This is physically remarkable insofar as only low-lying excitations or the ground state should be of importance in this range. However, for an interaction ${}^U\!/_J \gg 1$, the ground state of the FHM has to be a state that avoids energetically unfavourable DOs if possible. As a result, the probability of encountering DOs should subsequently be reduced significantly. The KPM results, however, suggest that DOs in the ground state are approximately as likely as for the completely disordered case $\beta = 0$. In order to examine this prediction, the comparison with an exact method is a logical next step.

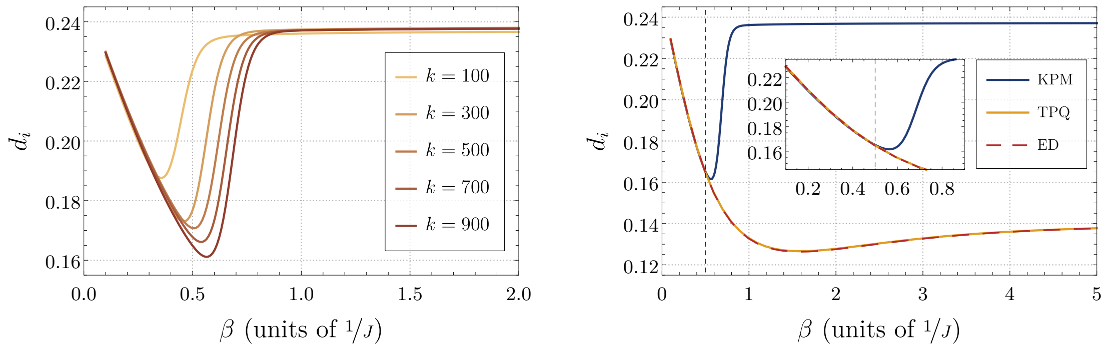

(a) Thermal expectation value of the double occupancy calculated with KPM and k expansion moments. A higher number of moments improves the accuracy but does not change the qualitative behaviour for $\beta > 0.7/J$.

(b) Comparison of results from both KPM ($k = 900$) and TPQS (Krylov space dimension $d = 50$) with an exact diagonalisation (ED). KPM (unlike TPQS) results show notable deviations from ED for increasing β.

Figure 4.3: High temperature behaviour for half-filled FHM with ${}^U\!/_J = 3$ [133]

If the same scenario is simulated using ED, a completely different picture emerges, cf. figure 4.3b. Although the results are consistent with the KPM results for the range $\beta < 0.5/J$, there are noticeably different results for increasing β. In contrast to the prediction of KPM, significantly fewer DOs occur in reality already at $\beta > 0.5/J$. This probability of the occurrence of DOs decreases successively until the minimum of $d_i^{\min} \approx 0.125$ sets in at about $\beta \approx 1.5/J$. For even larger β, a slight increase in the expected number of DOs can be observed until in the range of $\beta \approx 4/J$ and higher, there is an asymptotic convergence to an edge value of about $d_i(\beta \to \infty) = 0.14$. This actual limit is nearly 60 % below the prediction of KPM. This diminished value is highly plausible and in line with the previously motivated expectations.

The qualitatively as well as quantitatively erroneous behaviour of the KPM results is easily explained by the shortcomings in the range of low temperatures of the unmodified KPM used here, cf. section 4.1.3. As a remedy, two solutions in particular may be considered: Since the KPM requires a very high accuracy of the observable density in the range of low energies for the proper approximation of the low-temperature behaviour, a piecewise approximation of the densities with particularly many moments in the range of low energies is possible. This approach bears similarity to importance sampling. However, figure 4.3a shows that this approach is costly and yields only very small gains in accuracy.

Provided that the actual qualitative behaviour of ED could be reproduced at all by more moments and numerical artefacts would not make convergence infeasible, then an enormous number of additional moments would be necessary with significantly increased computational effort. This is no option.

The only way to correct the shortcomings of KPM is to treat the low-energy excitations with other methods and then analyse the remaining spectrum with KPM as described in section 4.1.3 and particularly by equation (4.21). That this concept is highly promising has been shown in a dedicated analysis of an XXZ model on a square lattice [118]. Here, it was proven that for a lattice of 4×4 sites an exact treatment of only $m \leq 9$ of these low-energy excitations is sufficient to capture the general physics on the level of comparable ED results. This makes it possible to choose a moderately sized m in (4.21) and treat the lowest part of the spectrum using Arnoldi procedures [103].

The final method available to us is the TPQS approach as described in section 4.2.1. The corresponding results are shown in figure 4.3b. Clearly, all TPQS results are fully in accordance with those results obtained by ED. In particular, this means that the low-temperature physics is also correctly captured. Again, the asymptotic value for $\beta \to \infty$ clearly confirms less frequently occurring DOs. The results of the TPQS calculation are identical to ED results for comparatively small Krylov space dimensions ($d = 50$) even for larger $\beta \sim 10/J$ (not shown here). Admittedly, a word of caution is necessary with respect to choosing the required Krylov space dimensions. Since the one-dimensional model with periodic boundary conditions at hand possesses a translational symmetry[2], the momentum is a conserved quantity. As with any conserved quantity, this allows for a partition of the original Hilbert space into closed subspaces of smaller dimensions. Therefore, the required Krylov space dimension to achieve the desired accuracy decreases. On the contrary, systems with fewer symmetries may demand a higher dimension to produce satisfactory approximations.

When comparing the different methods with each other, three aspects have to be noted in particular: First, pure KPM calculations without spectrum decompositions do not provide adequate results for low temperature physics. Second, already for medium to high temperatures, here above $T \geq 2J$ as can be seen in the inset of figure 4.3b, the physics is captured fully by pure KPM calculations. Third, TPQS results are able to reproduce ED results with moderate effort and without special modifications for all temperatures.

In view of the fact that a thorough implementation of the Lanczos algorithm is already available in our setup of TPQS, it is a straightforward exercise to use KPM with spectrum decompositions for the calculation of thermal expectation values. Nevertheless, given the fact that TPQS are very tolerant against accumulated numerical errors, easy to deal with and that they can be used regardless of the specific temperature β, all further computations will be performed using TPQS and we will refrain from following the route of enhancing KPM by spectrum decompositions any further.

---

[2] In strongly correlated systems there are further conservation laws besides translational symmetry such as charge conservation, conservation of the total spin S^z or point group symmetry which allow for a reduction of the total Hilbert space. An instructive example on how the translational symmetry helps to reduce the number of basis states of the full FHM by constructing Bloch states of well-defined momentum can be found in Ref. [134].

5 Quenches in the Fermi-Hubbard model

Employing the techniques discussed in chapters 3 and 4, a systematic approach to the dynamics as well as to the thermal behaviour of physical systems is feasible. In this chapter, we use these techniques to gain insights into one of the most fascinating and promising areas of research in solid state physics - the field of non-equilibrium physics. Here, the model under consideration is the full FHM as described in section 2.1.1, either on a one-dimensional chain or on arbitrary lattice topology.

The chapter reproduced herein is an enhanced and partially modified and/or restructured full reprint of our original publications in Refs. [42, 133] that are subject to copyright by the American Physical Society in 2018 and 2020, respectively.

5.1 Introduction

Systems far away from thermal equilibrium give rise to fascinating properties and, thus, have been a source of inspiration for finding both highly non-linear material characteristics and studying the evolution of strong correlations. Unfortunately, most of these studies had to remain gedankenexperiments for a long time with no feasible experimental realisation. In recent years, however, the research in non-equilibrium physics gained steam mainly due to remarkable experimental progress which rendered a dedicated preparation and observation of non-equilibrium phenomena possible.

The creation and precise tuning of optical lattices to confine ultra-cold atomic gases [135–137] form the basis for experimentally analysing former purely theoretical Hamiltonians [20, 138]. Moreover, femtosecond spectroscopy and pump-probe experiments allow one to gain insight into the evolution of ultrafast correlations in solid state physics [139–141]. Various invasive and non-invasive imaging processes have been proposed to perform in-depth studies of quantum states. For this purpose, the use of Bragg spectroscopy and time-of-flight experiments [142], *in situ* techniques with fluorescence [143], matter-wave scattering [144, 145], optical cavities [146], or Dicke superradiance [147] is possible.

A suitable method to prepare a system out of equilibrium in order to study the ensuing dynamics is to quench the system, i.e. to change its parameters abruptly. This approach has been used very frequently, e.g. in one-dimensional Bose-Hubbard systems for quenches across quantum phase transitions both theoretically [148] and experimentally [149] or to observe propagations of thermal correlations by coherently splitting a one-dimensional Bose gas into two separate parts [150]. Given that a quantum quench is a straightforward setting for the analysis of non-equilibrium phenomena, we resort to this method of exciting a system in the following. The quenching protocol which we apply to drive a system out of equilibrium is described in more detail in section 5.2.1.

Systems outside of equilibrium often show completely new characteristics, which can be indications of new, still unexplored physics or system mechanisms. Especially for practical applications, it is mandatory to understand how and whereto excited systems relax. Possible observable phenomena in the relaxation of systems are equilibration and thermalisation. Although these phenomena appear similar at first glance, they are not identical. We discuss the corresponding differences in the sections 5.2.2 and 5.2.3. Particularly finite closed quantum systems have time-reversal invariant and recurrent time-evolutions which consequently already make the meaningful definition of the term equilibration a challenge. But even if that succeeds, fundamental conceptual issues remain to be clarified [27]: How do equilibration and thermalisation occur in closed quantum systems? Which properties of the systems and of the quenches influence these processes? And also if equilibration and thermalisation exist under certain circumstances, they are far from doing so under all of them. In particular, this motivates another question: In which situations could thermalisation be weakened or break down [151, 152]?

In addition to these questions about the physical nature of closed quantum systems, there are entirely new practical implications: The groundbreaking experimental progress induces an urgent demand for corresponding theoretical methods to simulate non-equilibrium phenomena in an adequate way. Systems away from equilibrium are usually in highly excited states so that the occurring processes are spread over wide scales of energy and hence of time. For this reason, common predictions from equilibrium physics are often not applicable. The hugely varying time scales can be illustrated, e.g. by the relaxation times of doublons, i.e. the excitations caused by DOs, in Mott insulators which are shown to be different from intrinsic equilibrium time scales of the system by orders of magnitude [153]. Especially the enormous number of excitations in the system makes the theoretical description in terms of a few dressed quasi-particles [80] insufficient.

In view of the high level of research interest, there are a large number of approaches that have dealt with the description of non-equilibrium physics by now. Unfortunately, many methods are either not universally applicable or computationally very demanding. For example, only very few special systems allow for analytic treatments [154–156]. ED, as described in section 3.2, is very flexible, but limited in the maximum size of the system [157]. Non-equilibrium DMFT [117, 158] or perturbative expansions in the inverse coordination number [159, 160] work both best for infinite or large dimensions. The time-dependent DMRG [161] is most powerful in one dimension and simulations by QMC [162, 163] rely on detailed balance so that they are inherently designed for equilibrium configurations. Variational Gutzwiller approaches [164, 165] provide an analytical approach which captures quantum fluctuations only partly, variational QMC is a very powerful technique, but computationally very expensive [166]. Continuous unitary transformations (CUTs) have so far been employed in leading order in U only [167–169]. Thus, despite undoubtedly great progress in the description of non-equilibrium systems, the need for universal and fast methods remains.

After thorough definitions of all terms describing the fundamental concepts in section 5.2, we discuss our contributions to the two basic questions raised by non-equilibrium physics motivated above. In section 5.3, we analyse the universality of a generalised concept of equilibration and the impact of integrability on equilibration and thermalisation, respectively, and in section 5.4, we propose and apply a conceptually new, polynomial and thus efficient approach to non-equilibrium physics of larger systems by means of the iEoM method.

5.2 Fundamental concepts

5.2.1 Quenching

Consider a system of temperature $T = 0$ which is initially prepared in an arbitrary pure or mixed state given by a density operator

$$\rho = \sum_i p_i \, |i\rangle\langle i| \, . \tag{5.1}$$

In the statistical ensemble described by (5.1) each pure state $|i\rangle$ occurs with a probability of p_i. Evidently, at each time the total probability is conserved and thus the sum over all weights has to fulfil

$$\sum_i p_i = 1. \tag{5.2}$$

In the special case of a pure state all but one p_i vanish which results in a density operator being idempotent, i.e. $\rho = \rho^2$. Moreover, the time-evolution of the density operator is given by the von Neumann equation

$$\frac{\partial \rho}{\partial t} = i[\rho, H]. \tag{5.3}$$

As done before, we resort to natural units. Obviously, a non-trivial time-evolution of the density operator in (5.3) can only emerge if the condition $[\rho, H] \neq 0$ holds. Otherwise the density operator is stationary, i.e. $\rho(t) = \rho(0)$, and, hence, the system is in equilibrium.

To induce such a non-trivial time-evolution and excite the system, we use a global parameter quench, in which we quickly change a global system parameter. In the context of the FHM, this quench is executed by preparing the system in an eigenstate of H_0 and then resorting to the quench protocol

$$H_\mathrm{Q}(t) = H_0 + \Theta(t) H_\mathrm{int} \tag{5.4}$$

where $\Theta(t)$ is the Heaviside function. Without limiting generality, in the following we use the Fermi sea $|\mathrm{FS}\rangle$ as the respective eigenstate of H_0.

Due to the fact that the arbitrary lattices we examine are not necessarily translationally invariant and the momentum $\mathbf{k}$ is, therefore, not a conserved quantity we cannot resort to the momentum space representation (2.4) when constructing the initial state $|\mathrm{FS}\rangle$. Nevertheless, even for this rather general case one can proceed analogously to section 2.1.2. Provided that the lattice is given by an undirected graph G and its adjacency matrix by $A(G)$, as described in section 3.1.1, it is sufficient to diagonalise the one-particle Hamiltonian

$$h_0 := -A(G) \tag{5.5}$$

in order to obtain the Fermi sea. Let $|\nu\sigma\rangle$ be the eigenstates of h_0, i.e. let them fulfil the eigenvalue equation

$$h_0 \, |\nu\sigma\rangle = \epsilon_\nu \, |\nu\sigma\rangle \, . \tag{5.6}$$

Then, the Fermi sea is constructed by gradually filling the states $|\nu\sigma\rangle$ in order of increasing eigenenergies ϵ_ν according to

$$|\mathrm{FS}\rangle := \prod_{(\nu,\sigma)\,\in\, I} f^\dagger_{\nu\sigma} \, |0\rangle \, . \tag{5.7}$$

Here, the index set I is chosen in a way that the condition $\epsilon_\nu < \epsilon_\mathrm{F}$ with ϵ_F being the Fermi energy is fulfilled for all occupied eigenstates of h_0. In the case of an m-fold degeneracy, we consider a mixed state using all m Fermi seas in (5.1) with a probability of $p_i = {}^1\!/_m$. When studying observables in real space, it can be advantageous to construct the Fermi sea in a real space representation instead of using the eigenbasis of H_0 as in equation (5.7). Further details and practical examples for this can be found in appendix A.2.

But what exactly happens to the system when it is quenched? To answer this, let us simplify the scenario (5.1) slightly and assume a pure state $|\psi_0\rangle$ as the initial state of the system. Moreover, we assume that $|\psi_0\rangle$ is the ground state of H_0. Then, its time-evolution before the quench is trivial since it is an eigenstate of H_0. After the quench, i.e. for times $t > 0$, however, its time-evolution is governed by H_Q and reads

$$|\psi(t)\rangle = e^{-iH_Q t} \, |\psi_0\rangle = \sum_n \alpha_n e^{-iE_n t} \, |\Psi_n\rangle \tag{5.8}$$

with $|\Psi_n\rangle$ as the eigenstates with energy E_n of the final Hamiltonian H_Q as given in equation (5.4) and $\alpha_n = \langle \Psi_n | \psi_0 \rangle$. Although (5.8) is in fact simply a textbook decomposition of the dynamics into the eigenstates of H_Q, the implications are huge: the new dynamics suddenly take place in the entire subspace of $\mathrm{span}\left(|\Psi_n\rangle\right)$ for which $\alpha_n \neq 0$ holds. The total energy of the system is changed according to

$$\Delta E = \langle \psi_0 | H_Q | \psi_0 \rangle - \langle \psi_0 | H_0 | \psi_0 \rangle \tag{5.9}$$

and $|\psi_0\rangle$ is no longer the ground state of the new Hamiltonian H_Q, but constitutes a highly excited state. Consequently, the system is no longer in equilibrium and allows the study of a plethora of effects such as equilibration and thermalisation.

Even though the technique (5.4) of globally quenching a system is widely used [154–156, 167, 170, 171] it is not the only possibility to suddenly change fundamental properties of a quantum system. Aside from the instant modification of one unique global parameter a variety of ways for driving a system out of equilibrium locally exists. Particularly worth mentioning here are, for example, the immediate change of the overall system geometry [172] or the concatenation of two possibly different subsystems to become one [173, 174].

Example: Local observable

In order to gather a sense of the practical consequences of a quench in addition to the analytical perspective (5.8), let us consider the double occupancy operator

$$\widehat{d}_i = \widehat{n}_{i\uparrow}\widehat{n}_{i\downarrow} \tag{5.10}$$

of site i. This observable is of particular importance in the FHM in view of the fact that the interaction part (2.1b) can also be written as

$$H_{\text{int}} = \sum_i U_i \widehat{d}_i. \tag{5.11}$$

For simplicity of notation, we abbreviate the time-dependent expectation value (3.1) or thermal expectation value (4.1) of the double occupancy operator by $d_i(t)$ or d_i hereafter.

The enormous effects of a global quench, i.e. how strongly the local double occupancy depends on the activation of the on-site interaction $U > 0$, can easily be motivated by a gedankenexperiment: In a half-filled one-dimensional chain with periodic boundary conditions (PBC), the electrons are maximally delocalised according to section 2.1.2 for $U = 0$ and can thus move freely along the chain without constraints. We therefore speak of itinerant electrons, the material is a conductor. In the different limiting case $U \to \infty$, however, the interaction part (5.11) penalises each single double occupancy. The electrons occupy one lattice site each and consequently become immobile. The material under consideration is now an insulator. The resulting high sensitivity of the double occupancy operator to quenching in the FHM makes it an excellent litmus test for investigating the resulting non-equilibrium dynamics.

5.2.2 Equilibration

By equilibration of a quantum system we denote the process that time-dependent observables $\langle A(t)\rangle$ eventually relax for $t \to \infty$ to an average value

$$\overline{A} = \mathrm{Tr}(A\omega) \tag{5.12}$$

where the density operator of the system is averaged over very long time intervals by

$$\omega := \overline{\rho(t)}. \tag{5.13}$$

Equilibration is considered a generic phenomenon in quantum systems [175–178]. But finite quantum systems with a finite-dimensional Hilbert space are special in a rigorous sense because they display a discrete and finite set of eigenvalues. Hence, the temporal evolution of an arbitrary quantum state and thereby of its expectation values is governed by frequencies corresponding to these eigenvalues or more precisely to the differences between these eigenvalues. For a finite set of eigenvalues one has a finite set of possible frequencies so that an oscillatory evolution is induced (except if one starts by accident from an eigenstate). Rigorously, no equilibration towards $\overline{A}$ can occur which seems to indicate that only infinite systems can display equilibration. While this conclusion is correct in the strict sense, it does not reflect the range of observable phenomena. Due to the exponential increase of the dimensionality of the Hilbert space with system sizes that are still finite, not too large systems reflect the behaviour of their infinite counterparts. But there are fluctuations around the long-time averages $\overline{A}$ and their strength and dependence on the system size constitute an important issue which we will address below.

For studying equilibration one conventionally starts by partitioning a given closed quantum system into a small subsystem and a considerably larger bath

$$\mathcal{H} = \mathcal{H}_S \otimes \mathcal{H}_B \text{ with } d_S \ll d_B \tag{5.14}$$

where $d_n := \dim \mathcal{H}_n$. In line with most of the present literature, we assume that this partitioning is done in real space. Certain aspects may carry over to other representations as well. Measurements are supposed to take place on the smaller subsystem which can be taken as small as a single site if the measurement of local, on-site observables is considered. Equilibration means that the chosen subsystem S resides in a state described by the partial density matrix

$$\rho_S(t) = \mathrm{Tr}_B\, \rho(t) \tag{5.15}$$

which is close to its time-averaged state for all times, at least after a sufficiently long initial period of relaxation. In this context, the notation Tr_B denotes a trace over the subsystem B only. We denote the respective time-averaged state by

$$\omega_S = \overline{\rho_S(t)}. \tag{5.16}$$

For initial product states, i.e. states with separable contributions of system and bath,

$$|\psi\rangle_{SB} = |\psi\rangle_S \otimes |\psi\rangle_B \tag{5.17}$$

it has been proven rigorously by Linden et al. [179] that the trace distance for two Hermitian operators as given by

$$D(t) = \frac{1}{2}\,\mathrm{Tr}\left(\sqrt{(\rho_S(t) - \omega_S)^2}\right) \tag{5.18}$$

between the density matrix $\rho_S(t)$ and its long-time average ω_S is bounded by

$$\overline{D(t)} \leq \frac{1}{2}\sqrt{\frac{d_S}{d_{\text{eff}}(\omega_B)}} \leq \frac{1}{2}\sqrt{\frac{d_S^2}{d_{\text{eff}}(\omega)}}. \tag{5.19}$$

Here and in similar studies [175–177, 180, 181], the relevant quantity has proven to be the effective dimension

$$d_{\text{eff}}(\omega) := 1/\,\mathrm{Tr}\left(\omega^2\right) \tag{5.20}$$

of the time-averaged state $\omega = \overline{\rho(t)}$. The effective dimension is formally given by

$$d_{\text{eff}}(\omega) = \left(\sum_n (\mathrm{Tr}\,(P_n\rho(0)))^2\right)^{-1} \tag{5.21}$$

where we use the projector P_n onto the eigenspace of energy E_n and the initial state is given by $\rho(0)$ [176, 180]. If this effective dimension is sufficiently large the above inequality implies that the small subsystem equilibrates in the sense that the expectation values in the subsystem deviate from their long-time average little and very rarely. It is reasonable to presume that the effective dimension in realistic cases of interacting Hamiltonians is very large due to exponentially many energy eigenstates contributing to quenched states, even if these states display only small energy uncertainties [179, 182].

The physical motivation for the phenomenon of equilibration in a subsystem is intuitively accessible. Equilibration means that information encoded in the initial state of the subsystem is lost. Since rigorously the unitary evolution of the whole quantum system does not allow for information loss, the loss must occur to the bath, i.e. to the remainder of the system. This is favored if the quantum dynamics allows to reach the whole Hilbert space or a substantial part of it. This, in turn, requires a high effective dimension.

Even though highly plausible, it remains unclear whether the assumption of a sufficiently large effective dimension holds for all physically realistic configurations. What is more, the evaluation of the quantity $d_{\text{eff}}(\omega)$ requires an *a priori* complete exact diagonalisation and, thus, highly limits the applicability of the bound (5.19) in practical situations.

Recent research has reformulated the effective dimension in terms of the Rényi entanglement entropy. This reformulation does not imply an improved calculability [177]. In addition, however, an upper bound for the Rényi entanglement entropy was derived which predicts a linear increase of the entropy with system size N, implying an exponential growth of the effective dimension with N. The prefactor of N in these estimates remains yet unknown. Furthermore, the mathematical considerations implying

$$\ln(d_{\text{eff}}) \propto N, \tag{5.22}$$

as put forward in Ref. [177], consider product states of system and bath as initial states. The open issue remains whether the situation changes fundamentally if the system is quenched starting from other types of initial states than those of equation (5.17).

To address this question we will investigate another generic, but non-product initial state. We prepare the system initially in a state which is highly entangled with respect to the chosen real space partitioning, namely the Fermi sea (5.7). This means that there are no pure states of both subsystems S and B individually since $|\text{FS}\rangle$ cannot be split into a product state of a state of S and B, respectively. By doing so we intentionally violate one of the main conditions conventionally assumed to hold in the process of equilibration. We want to study whether equilibration still occurs in this more generic setting. Subsequently, the system will be subject to a quench to drive it out of equilibrium in a well-defined and reproducible manner. We further discuss the results of this novel approach of using non-product initial states in section 5.3.1.

5.2.3 Thermalisation

When referring to thermalisation a specific form of equilibration is meant. If the average value $\overline{A}$ equals the thermal value A_{th} which results from statistical ensemble theory thermalisation has taken place. For further details on thermal averages and their computation see chapter 4. In short, thermal expectation values are defined by

$$A_{\mathrm{th}} = \mathrm{Tr}(A\rho_{\mathrm{can}}) \tag{5.23}$$

where the canonical density matrix at inverse temperature $\beta = {}^{1}\!/_{T}$ in natural units reads

$$\rho_{\mathrm{can}} = \frac{1}{Z} e^{-\beta H}. \tag{5.24}$$

The most intriguing aspect about thermalising systems is that the expectation values $\overline{A} = A_{\mathrm{th}}$ only depend on an effective inverse temperature β_{eff} resulting from the overall energy $E = \langle H \rangle$ according to

$$E = -\frac{\mathrm{d}}{\mathrm{d}\beta} \ln(Z(\beta)) \bigg|_{\beta=\beta_{\mathrm{eff}}}. \tag{5.25}$$

In other words, it appears that the system has lost its memory about the initial state at $t = 0$ except for its energy content. Of course, this cannot be true if one had access to all conceivable observables of a system. Then, it would be easy to see that this access provided complete knowledge about the temporal evolution of the initial state without any loss of information. Hence, equilibration and thermalisation can only occur for observables measured on a small subsystem of the total quantum system. Typically, observables acting only on a very few adjacent sites are considered. In the FHM, in particular the double occupancy operator (5.10) is a sensible choice due to its high local confinement. The local support of this observable, i.e. the subsystem S in the language of equilibration, is only one lattice site in size.

The essential question is: Do all systems exhibit thermalisation? Is thermalisation therefore a similarly generic phenomenon as equilibration? To answer this question, one must first understand what can prevent thermalisation. Conserved quantities C_i in integrable models restrict the dynamics similar to the energy in the canonical ensemble. Obviously, the expectation values of the C_i are constant in time and do not change from their initial values. Thus, they cannot relax to any thermal value. Hence, thermalisation is claimed to be a specific property of non-integrable systems [183–185].

In our subsequent analyses of the occurrence or absence of thermalisation, it is therefore appropriate to reflect this insight. Accordingly, we consider two different classes of systems: Integrable and non-integrable ones. As an example for the inherent constraints of the dynamics of an integrable system, we resort to the FHM on a finite PBC chain [14, 40] with nearest-neighbour hoppings $J_{ij} = J$ and on-site Hubbard repulsions $U_i = U$. Most of the integrals of motion, but not all of them, are functionally dependent on the ratio ${}^{J}\!/_{U}$ [186, 187]. As realisations of non-integrable systems we consider connected clusters of arbitrary topology. In the design of these clusters, we try to avoid any form of symmetry. In order to accomplish this, we select finite clusters without any PBC and with individually different hopping elements J_{ij} and on-site repulsions U_i. The corresponding J_{ij} and U_i are chosen randomly in a uniform manner within a one-percent range around the respective parameters J and U of the integrable one-dimensional chain with which we compare the arbitrary clusters. Since the exact shape of the clusters is not of interest for the analysis, we refer the interested reader to appendix B for an overview over all considered clusters.

Independent of integrability, any number of integrals of motion C_i restricts equilibration. Instead of the thermal density matrix in the canonical ensemble it is straightforward to derive that the maximisation of the entropy of a density matrix for given, fixed expectation values $\langle C_i \rangle$ of the respective conserved quantities C_i leads to a generalisation of (5.24) called the generalised Gibbs ensemble (GGE) [184, 188]

$$\rho_{\text{GGE}} = \frac{1}{Z} e^{-\sum_i \lambda_i C_i}, \tag{5.26}$$

where the λ_i are Lagrange multipliers which are determined by the condition

$$\langle C_i \rangle_{\text{GGE}} = \langle C_i \rangle_{\text{initial}}. \tag{5.27}$$

We emphasise that this result does not require the conserved quantities to commute pairwise, i.e. $[C_i, C_j] = 0$ is not a necessary condition. This is so because the entropy to be maximised is given by a trace which allows for cyclic permutations after derivation so that the sequence of operators can always be chosen such that C_i stands in front of (or after) the density matrix. In literature, the GGE for non-commuting integrals of motion is sometimes called non-Abelian thermal state [189, 190]. In any case, a system with conserved quantities may show generalised thermalisation to the GGE in (5.26) while its thermalisation to the canonical ensemble (5.24) is only possible if this ensemble fulfils the conditions (5.27) accidentally.

For the scope of the results of section 5.3 it is of importance to stress the key idea here once again: Non-integrable generic clusters, which are not restricted by any conserved quantities other than the overall energy, are expected to show signs of thermalisation while integrable ones are expected not to do so. Using the numerically exact CET approach, which is discussed in further detail in the context of section 3.3, we investigate this expectation for the one-band FHM. In particular, we discuss the results for the globally quenched FHM on clusters of various topologies, study the influence of the cluster properties on the general relaxation behaviour and work out the thermalisation behaviour of different systems.

5.3 Equilibration and thermalisation

5.3.1 Results on equilibration

As outlined in section 5.2.2, analytic arguments for equilibration have been brought forward for the case of initial product states of system and bath [177]. In order to extend evidence for equilibration beyond this special situation, we focus on the Fermi sea $|\text{FS}\rangle$ as a generic non-product state in real space representation. The initial non-equilibrium is generated by an interaction quench according to (5.4).

In the highly excited state ensuing from the global parameter quench, we examine the tendency of the finite clusters to equilibrate by simulating the time-dynamics of proper local observables which are measurable in the subsystem S. To study this phenomenon in detail we consider the two types of clusters motivated in section 5.2.3, i.e.

(i) integrable ones with PBC and a constant ratio U/J,

(ii) generic clusters with an arbitrary topology.

A complete overview of the used finite-size clusters is given in appendix B. Henceforth, the corresponding labels (a), (b), ..., (n) ascribed to the individual topologies will be used for identifying a particular cluster. In order to avoid any undesired symmetries in the generic clusters, we additionally slightly randomise the parameters of the model such as the hopping strengths $J_{ij} = J_{ji}$ by drawing their values with uniform probability from the respective intervals $[J - p \cdot J;\ J + p \cdot J]$ with $p = 0.01$. The same applies to the on-site interactions U_i as well, i.e. they are drawn from the corresponding interval $[U - p \cdot U;\ U + p \cdot U]$. Note that the randomisation is deliberately chosen weak in order to avoid any many-body localisation [191]. The only purpose of randomisation is to avoid the influence of accidental symmetries. In the integrable clusters no randomisation is performed because it would spoil the integrability of the model.

As a meaningful local observable which incorporates two-particle interaction we choose the double occupancy (5.10). Consequently, the subsystem S consists of site i only. For the calculation of the time-dependence we resort to CET as given in equation (3.53).

Results of the time-dependence in the integrable cluster with a lattice size of $N = 12$ as well as in the non-integrable cluster (l) of the same size are shown in figure 5.1 for half-filling and $U = 3J$. The results described below are always collected for this intermediate quench of strength $U = 3J$. If other quenching strengths are used, for example to check whether observed phenomena are also preserved in the weak or strong quenching regime, these are stated explicitly. For $U = 3J$, we clearly see signs of the expected fluctuations around an average value in figure 5.1. Nevertheless, there is no tendency to converge to a constant stationary value, cf. section 5.2.2. Even on longer time scales which are not shown here no constant stationary value is approached. This comes as no surprise and is a direct result of the finite system size.

Interestingly, there seem to be qualitative differences between the integrable and the generic cluster. The time series of the integrable cluster shows fluctuations which are of the same magnitude for all times. In contrast, the time series of the generic cluster first shows larger fluctuations which subsequently diminish to some extent. This observation, however, certainly needs to be substantiated further quantitatively.

To do so we need to determine the long-time averages of the fluctuating quantities. These values are the best guesses on finite clusters for stationary values after relaxation. Certainly, an analytical calculation of these long-time averages after relaxation is feasible via the method of stationary phases, cf. equation (3.70), but this would require an ED and consequently a complete diagonalisation of the Hamiltonian matrix. Consequently, such a procedure is neither applicable nor efficient. Accordingly, we proceed differently. Since at the beginning there are various transient effects, see figure 5.1, it is not trivial

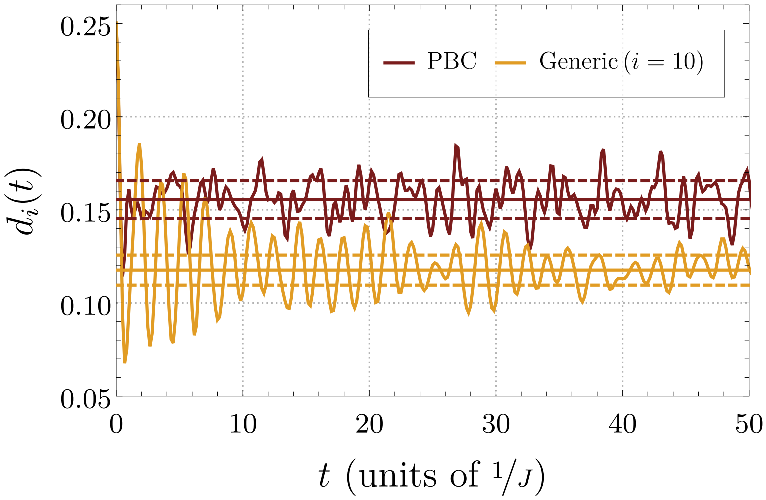

Figure 5.1: Time-evolution of the double occupancy on the integrable periodic FHM chain (PBC) after an interaction quench of $U = 3J$ and on the non-integrable (Generic) cluster of $N = 12$ sites at half-filling. For the non-integrable case, site $i = 10$ of cluster (l) is depicted and a one percent randomisation around the average $U \approx 3J$ is chosen. Solid lines denote the average values (5.28), dashed lines the average plus and minus the standard deviation σ_i, both calculated at $\tau = 0.6$ [133].

to compute the long-time averages reliably. We account for this obstacle by introducing an averaging according to

$$\overline{d}(\tau) := \frac{1}{t_{\text{max}} - t_{\text{min}}} \int_{t_{\text{min}}}^{t_{\text{max}}} \mathrm{d}t \, d(t) \tag{5.28}$$

with $\tau := t_{\text{min}}/t_{\text{max}} \in [0;1]$ for fixed values of t_{max}. By tuning τ and, thus, the minimum starting time from which the averaging is performed we are able to eliminate the influence of initial transient effects on the dynamics. If not noted otherwise, all numerical CET calculations are performed up to a maximum simulation time $t_{\text{max}} = 100/J$.

Exemplary results for all sites of the non-integrable, half-filled $N = 12$ cluster (l) are shown in figure 5.2. As can be seen, some weak initial transients are visible up to the range of $\tau \leq 0.2$. During this initial time span we consider the data not fully converged yet, cf. especially the data for sites $i = 6$ or $i = 8$. Nevertheless, after these initial transients, the averaged data converges to an almost constant value. Only if τ is chosen too large, i.e. too close to unity, large fluctuations appear. The reason is that the averaged time span becomes too small so that the fluctuations do not cancel sufficiently anymore, cf. the range $\tau \gtrapprox 0.8$ in figure 5.2. In conclusion, avoiding the initial transient effects as well as the final fluctuations can be achieved by reading off $\overline{d}_i$ for medium values of τ, i.e. around $\tau \approx 0.5$ to $\tau \approx 0.6$.

In all checked cases of various lattice sizes N and both integrable and non-integrable topology the determination of the time-averaged value according to (5.28) is possible since no significant variations occur in the range of $\tau \approx 0.5$ to $\tau \approx 0.6$. Thus, all following

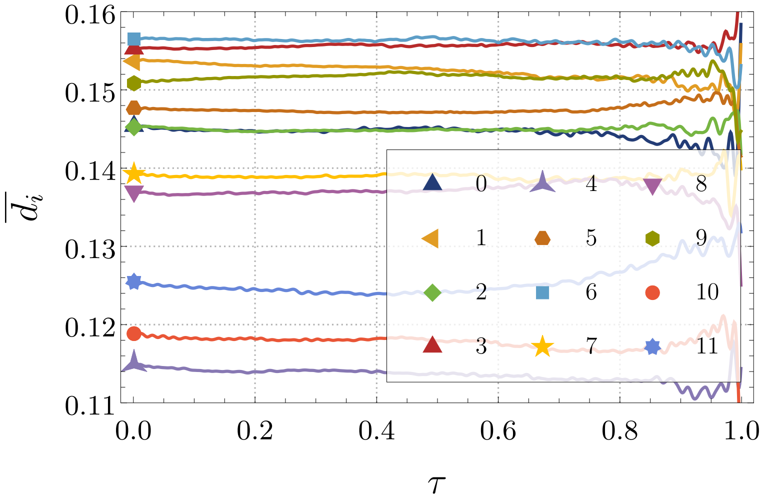

Figure 5.2: Averages of the double occupancy of cluster (I) at the sites i determined according to (5.28). A tendency of the dynamics to converge towards an essentially constant value around $\tau \approx 0.5$ to $\tau \approx 0.6$ is discernible for all sites [133].

calculations are performed for a constant $\tau = 0.6$. This way, we obtain a suitable approximation of the stationary value of an observable $\overline{A}$ as discussed in section 5.2.2. We refer to these time-averages $\overline{d}_i$ both in the study of equilibration and thermalisation for describing the respective final relaxation values.

For a better visual orientation, figure 5.1 shows the long-time averages (solid lines) and the standard deviations around them (dashed lines), both calculated at $\tau = 0.6$. The initial dynamics differ qualitatively between the two cases considered. The generic model shows longer-lasting transients after the quench. Nevertheless, the long-time fluctuations show roughly the same amount of spread. This observation leads to the hypothesis that fluctuations show no pronounced dependence on the integrability of the model. We will substantiate this conjecture in the following by a detailed analysis of the global standard deviation of the system.

The fluctuations present in the dynamics of the system around the time-averaged values $\overline{d}_i$ of the double occupancies are quantified by their individual variances σ_i^2. They are a measure for how well the (finite) system stays close to the time average $\overline{d}_i$. A fully equilibrating system would show vanishing fluctuations since it would fulfil

$$\lim_{t\to\infty} d_i(t) = \overline{d}_i \tag{5.29}$$

so that $\sigma_i^2 = 0$ if the latter is determined for long, ideally infinite, time ranges. Practically, we use (5.28) also for the determination of the σ_i^2. We are not aware of analytic *a priori* predictions of the values of σ_i^2 in the physical situation we are considering, namely a highly entangled initial state in real space. Applying a scheme similar to (5.19) for an observable O leads to an upper bound to its variance [176] given by

$$\sigma_O^2 \leq \frac{\Delta(O)^2}{4d_{\text{eff}}(\omega)} \leq \frac{\|O\|^2}{d_{\text{eff}}(\omega)} \tag{5.30}$$

with $\|O\|$ being the largest absolute eigenvalue of the Hermitian operator O and

$$\Delta(O) = 2 \min_{c\in\mathbb{C}} \|O - c\mathbb{1}\|. \tag{5.31}$$

Unfortunately, these upper bounds (5.30) still require the cumbersome calculation of the effective dimension $d_{\text{eff}}(\omega)$ as main ingredient which can neither be predicted without a complete diagonalisation nor estimated except for initial product states of system and bath. Consequently, it is not readily assessable how the variance of the double occupancy behaves in this particular scenario. Hence, our main motivation here is to study to which extent the considered systems equilibrate after the quench.

In order not to discuss each site in a cluster separately we define the global variance as the arithmetic mean of all variances σ_i^2 of the individual lattice sites by

$$\sigma^2 = \frac{1}{N}\sum_{i=1}^{N} \sigma_i^2. \tag{5.32}$$

This quantity provides a good measure for the degree of equilibration. If it vanishes it indicates equilibration, at least on average. Figure 5.3 depicts the global standard deviation σ as defined by (5.32). For the generic, non-integrable cluster, the values for σ^2 are averaged additionally over all clusters of the same size N, cf. appendix B. For example, all generic clusters of $N = 12$ sites are those labeled by (l)-(n). The plotted error bars indicate the average spread between the maximum and minimum standard deviation for each of the different clusters contributing to each data point for a specific cluster size N, i.e. half the error bar of the generic data set amounts to ${}^1\!/\!{}_2(\sigma_{\text{max}} - \sigma_{\text{min}})$.

The first remarkable observation is that the standard deviations of the integrable and the non-integrable clusters are very similar for the same cluster size. One could have expected that the fluctuations in the integrable systems are larger because there is less accessible Hilbert space due to the large number of conserved quantities. But this does not seem to be the case. Furthermore, one could think that the similarity of the integrable and non-integrable fluctuations in figure 5.3 is at odds with the time series shown in figure 5.1 where the generic fluctuations are larger shortly after the quench. But for longer times this is no longer true and it is for these longer times that the quantity σ is determined, e.g. the evaluation at $\tau = 0.6$ for $t_{\text{max}} = 100/J$ implies that σ is computed for the time interval $[60/J, 100/J]$. In figure 5.1, the dashed lines and their mutual distance illustrate that the fluctuations of both systems are comparable in size.

A common challenge in the simulation of finitely large systems is to obtain statements about realistic lattice sizes as they occur in typical solids. We tackle this issue by extrapolating the data to the thermodynamic limit. To do so, we compare two kinds of fits. The first one is linear in the inverse lattice size, i.e. $\sigma = a + {}^b\!/\!{}_N$, and the second

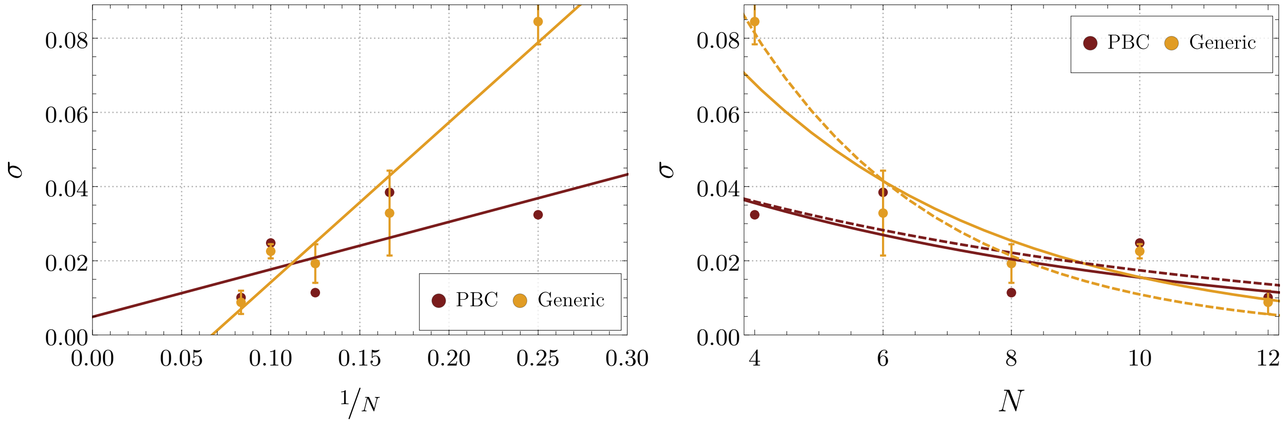

(a) A linear least-square fit to the numerical data of the form $\sigma = a_0 + {}^{b_0}/_{N}$ is inserted using solid lines.

(b) Two least-square fits are displayed using either $\ln(\sigma) = \ln(a_1) - b_1 N$ (solid lines) or $\sigma = a_2 \exp(-b_2 N)$ (dashed lines).

Figure 5.3: Global standard deviation σ depending on the (inverse) lattice size N (${}^{1}/_{N}$). The quantity σ is derived from (5.32) and describes fluctuations of the double occupancies $d_i(t)$ around their individual average values $\overline{d}_i$. Results for integrable (PBC) and non-integrable (Generic) clusters and different fits are shown [133].

one is exponential in the lattice size, i.e. $\sigma = a \exp(-bN)$. The linear fit is shown in figure 5.3a and the corresponding exponential fit is shown in figure 5.3b. Note that the exponential fit is carried out in two ways of least-square fits by means of

(i) σ being fitted with $a \exp(-bN)$,

(ii) $\ln(\sigma)$ being fitted with $\ln(a) - bN$.

The difference between both seemingly equal approaches lies in the fact that a least-squares algorithm which is computed for σ or $\ln(\sigma)$ leads to different weights. The first procedure is depicted using dashed lines and keeps the fit close to the data points at larger values of σ since they have a strong numerical influence while the second procedure is denoted by solid lines and focuses on the data points at smaller values. This is the reason for two slightly differing fits for the same overall scaling in figure 5.3b.

When considering the numerical results shown in figure 5.3 in detail, we find that our data is consistent with the exponential scaling predicted by Wilming et al. [177]. Nevertheless, it is appropriate to state that the numerical data does not necessarily require an exponential dependency of the global standard deviation σ on the lattice size N and thus does not provide fully compelling evidence for the exponential scaling. As a result, further research on this issue is certainly desirable and called for.

One aspect, however, is quite evident. Both data sets and all fits regardless of the implied form of scaling indicate a vanishing global variance for $N \to \infty$, especially if the notoriously small system of $N = 4$ is excluded from the fits (not shown here). This provides numerical evidence for the fact that equilibration takes place in all systems of increasing system sizes. In other words, equilibration appears to be a generic scenario independent of the property of integrability. We emphasise here that there is not even a discernible trend in the variances of the integrable and non-integrable systems. Depending on the lattice size N, sometimes the one, sometimes the other kind of system shows a slightly larger variance on average, while the orders of magnitude of the variances are identical in each case. This leads us to postulate that equilibration is an even more generic property than currently proven as it is neither limited by a highly entangled initial state nor by constants of motion present in integrable systems.

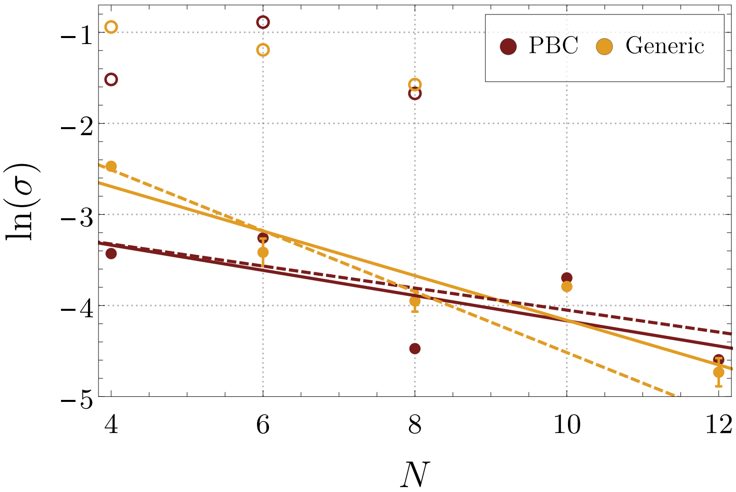

Figure 5.4: Comparison of the actual global standard deviations σ (filled symbols) to the upper bounds (open symbols) given by equation (5.33) on logarithmic scale. The same fits and parameters as in figure 5.3b are shown; they appear here as straight lines [133].

In view of the exponential scaling behaviour of the global variance that is to be assumed, it is appropriate to choose a logarithmic representation for the further analyses. We refer to the raw data from figure 5.3b again in figure 5.4, this time with a logarithmic representation of the global variances. The exponential fits already used in figure 5.3b appear accordingly as straight lines in figure 5.4.

An additional question that naturally arises is the relevance of the upper bound in equation (5.30). Is this upper bound sharp and thus meaningful? In order to shed some light on this question, we have to obtain the upper bound and therefore perform a concrete calculation of the rather artificial quantity of the effective dimension $d_{\text{eff}}(\omega)$. One way to do this would be to resort to approximate techniques such as the Lanczos algorithm, cf. section 4.2.2 for details or Ref. [192] for another example in the context of the FHM. Nevertheless, since a possibly too small Krylov space dimension can cause systematic errors in the determination of the upper bound (5.30), we refrain from a corresponding procedure at this point and choose a fully exact approach by means of ED.

This, however, requires a complete diagonalisation of the system including a determination of the eigenstates, which has been mostly avoided so far. In this context, it

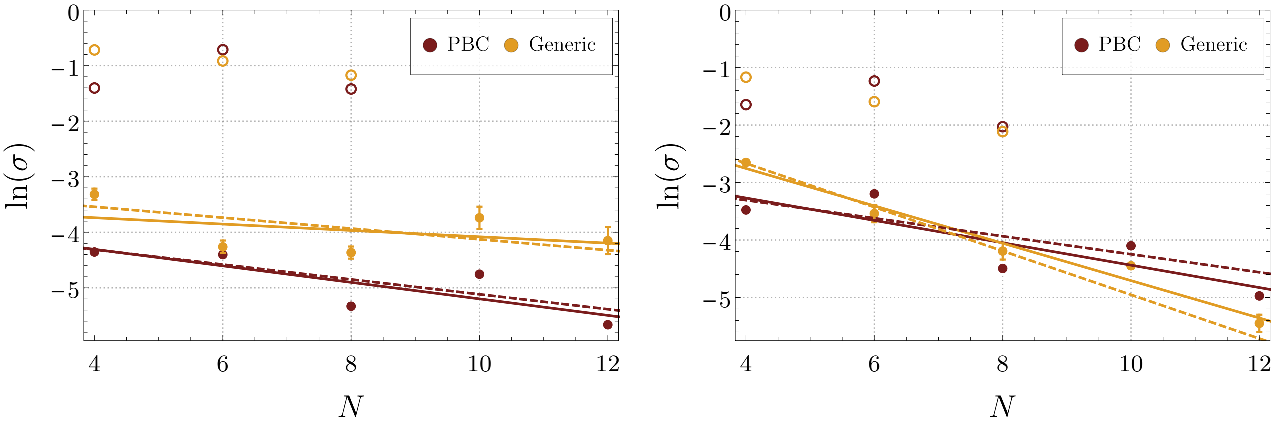

(a) $U = 1J$

(b) $U = 6J$

Figure 5.5: Results for σ as derived from (5.32). The results are calculated in the same manner as in figure 5.4 except for $U = 1J$ or $U = 6J$ instead of $U = 3J$. In full accordance with figure 5.4 fluctuations are becoming exponentially smaller with increasing cluster size N. Upper bounds (5.33) are computed by complete exact diagonalisation and shown using open symbols. The bounds are indeed well above the actual data, but they are clearly not tight [133].

is worthwhile to consider the restrictions of using the ED approach for non-integrable, highly non-symmetric clusters: the usage of ED on strongly correlated lattice systems usually exploits symmetries of the underlying lattice to generate so-called symmetry adapted basis states [193]. This is no longer an option here since our goal in constructing the generic clusters was to avoid any symmetry as far as possible. Thus, a reduction of the overall Hilbert space by means of symmetries is infeasible. In contrast, we have to resort to a purely unenhanced ED without any optimisations other than those described in section 3.1.1, e.g. in the context of particle conservation.

For the respective system sizes that are accessible to such an ED, we additionally determine the effective dimensions and the respective upper bounds (5.30) to variance and standard deviation. In this context, we resort to the tightest upper bound for the double occupancies, i.e. $O = d_i$ and $c = 1/2$ in (5.31), leading to the upper bound

$$\sigma_i \leq \frac{1}{2} d_{\text{eff}}(\omega)^{-\frac{1}{2}}. \tag{5.33}$$

The required effective dimension is computed assuming the absence of any degeneracy so that the following relation holds

$$\frac{1}{d_{\text{eff}}(\omega)} = \sum_{n,j} \left(p_j |\langle n|\psi_j\rangle|^2 \right)^2. \tag{5.34}$$

Here, the initial state may be given as mixture $\rho(0) = \sum_j p_j \, |\psi_j\rangle\langle\psi_j|$, as motivated in the context of (5.1), and $|n\rangle$ shall denote the eigenstates of H. The resulting upper bounds are displayed in figure 5.4 by open symbols in the same colour as the time-averaged standard deviations. It is evident that the mathematically rigorous upper bounds are not particularly tight for the actually occurring fluctuations. Note the logarithmic axis representation. There are almost two orders of magnitude between upper bounds and the actual variances in some cases. We conclude from this that the upper bound (5.33), at least in this concrete application scenario, does not yet take into account all physically relevant processes in a meaningful weighting.

Analogous to the results presented in figure 5.4 for quenches of strength $U = 3J$, we also test the hypothesis of equilibration independent of integrability in the weak and strong quench regimes, i.e. for $U = 1J$ and $U = 6J$, respectively. The corresponding results can be found in figure 5.5. In the case of $U = 1J$ as well as in the case of $U = 6J$, completely analogous results can be seen: for none of the cases a significant dependence on integrability can be detected, the variance visibly goes towards zero with increasing lattice size N. In all cases, the upper bounds (5.33) are not very tight.

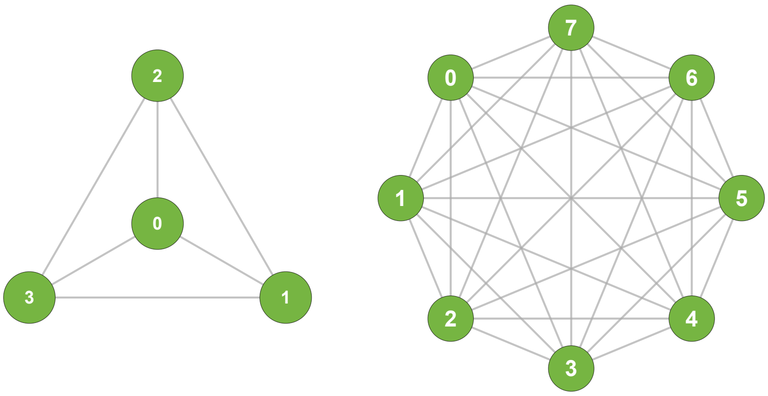

Figure 5.6: Infinite-range clusters G_c for $N = 4$ and $N = 8$ with a maximum number of hoppings possible, also called complete graphs. For each of the N sites the coordination number is $z = N - 1$ leading to a total of $K = {}^1\!/_2 N(N-1)$ hopping links or bonds, respectively [133].

When discussing fluctuations the coordination number z is relevant. In the clusters considered so far, it is $z = 2$ for the PBC chain and has a mean value of $\overline{z} = 2.45$ for the generic clusters. Hence, these numbers do not vary much. Yet, it is to be expected that systems with large coordination numbers display smaller fluctuations. At least in equilibrium, it is common lore that mean-field approaches work much better in higher dimensions and for larger coordination numbers because the relative relevance of the individual fluctuations is lower. The same presumption is a plausible working hypothesis out-of-equilibrium. We put this hypothesis to a test below.

Our assumption of decreasing fluctuations with increasing connectivity, i.e. more possible hopping processes, can be tested in various ways. Typically, the limiting case of a maximum coordination number z is constructed by an increase of the lattice dimension $d \to \infty$ in analytical calculations. Here, we go for another route that is rendered possible by the finite clusters at hand. It is reached by linking each site in a cluster with every other site implying $z = N - 1$. Then, we extrapolate these results by $z \to \infty$. The resulting clusters G_c are called infinite-range clusters in physics and complete graphs in mathematics. Each of them has

$$K = \frac{1}{2} N(N-1) \tag{5.35}$$

bonds in total. The respective adjacency matrix of such a cluster G_c reads

$$A(G_c) = J_N - \mathbb{1}_N \tag{5.36}$$

where J_N denotes the $N \times N$ all-ones-matrix and $\mathbb{1}_N$ stands for the identity matrix. We subtract the latter one to exclude local terms corresponding to hops from site i to i. We point out that in infinite-range clusters without any randomisation the system has an enormously high level of symmetry and that the initial Fermi sea is thus highly degenerate leading to $\rho^2 \ll \rho$. Due to this inherent self-averaging the fluctuations in fully symmetric clusters G_c with the same J on each bond and the same U at each site are strongly suppressed. These results are not shown here since they merely stem from symmetry. Consequently, this is not what we want to study.

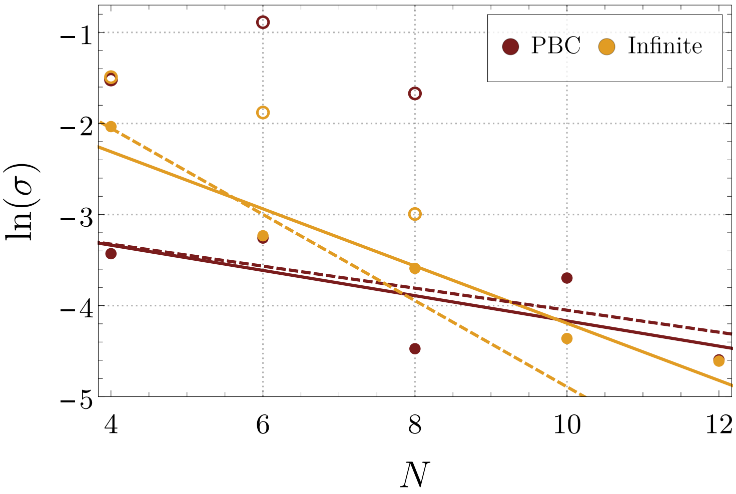

Figure 5.7: Global standard deviations σ of integrable chains with $z = 2$ (PBC) and of infinite-range clusters G_c with $z = N - 1$ and a one-percent randomisation. Results, fits and bounds are to be compared with figure 5.4. The amount of fluctuations depends on the number of bonds and decreases upon increasing coordination number so that the infinite-range clusters display only small fluctuations in the limit $N \to \infty$ relative to the fluctuations in the PBC clusters [133].

Instead, we again slightly randomise the hoppings J_{ij} and the interactions U_i by 1 %. This is exactly what we did for the generic clusters allowing for a study of the direct influence of large coordination numbers z without being distracted by a large number of symmetries as we would when using infinite-range clusters G_c without randomisation.

An example of two infinite-range clusters G_c with $N = 4$ and $N = 8$, respectively, is given in figure 5.6. Note that each lattice site is connected to every other lattice site and only self-hops which are not present in the FHM are forbidden. We use such clusters G_c to compute the time-averaged double occupancies $\overline{d}_i$ and, subsequently, the global standard deviations σ for a quench of strengths $U = 3J$ as before for (non-)integrable models in figure 5.4. No averaging over various clusters is conducted. The results are displayed in figure 5.7 and compared to the ones for integrable chains. Again, we include the upper bounds for σ_i determined by (5.33) by means of open symbols for small systems. A clear difference of the thermodynamic behaviour, i.e. for $N \to \infty$, can be noticed. In PBC systems with a small coordination number, the extrapolated fluctuations are noticeably larger than in the infinite-range clusters G_c. The standard deviations in the infinite-range clusters have a much steeper slope for increasing N rendering fluctuations less important for larger complete graphs than for long PBC chains. This clearly supports the hypothesis that a larger connectivity favors smaller fluctuations. Hence, as a rule of thumb we expect that systems with larger coordination number equilibrate better than those with smaller coordination number. We stress that this finding does not necessarily imply that the equilibration occurs faster, i.e. on a shorter time scale. In view of the used CET approach the issue of time scales is beyond the scope of this analysis since the reliable determination of equilibration time scales is numerically very challenging.

5.3.2 Results on thermalisation

In the previous section 5.3.1, we noted no substantial influence of integrability on the degree of equilibration. In both cases of PBC and of the generic clusters the results indicated a stationary, equilibrated state in the thermodynamic limit. Moreover, the fluctuations due to the finite size of the studied clusters are comparable for the same system sizes. While equilibration thus seems to be a general characteristic, the legitimate question arises whether the same applies to thermalisation. To answer this question we compare the equilibrated, time-averaged double occupancies $\overline{d}_i$ with the thermal predictions $\langle d_i \rangle_{\text{th}}$ where the latter ones are computed for the canonical statistical ensemble at the same energy as the quenched system. The key question will be: Are they equal?

In order not to be distracted by accidental effects at particular sites i we define the global deviation from the thermalised values by means of

$$\Delta_{\text{therm}} := \frac{1}{N} \sum_{i=1}^{N} \left| \overline{d}_i - \langle d_i \rangle_{\text{th}} \right| \tag{5.37}$$

for integrable (PBC) and non-integrable (generic) clusters of size N. The thermal predictions $\langle d_i \rangle_{\text{th}}$ are calculated using TPQ states as described in section 4.2.1. Since each site i of a given cluster contributes to (5.37) this definition accommodates for the highly differing individual topologies in a systematic way. A system showing perfect thermalisation is characterised by a vanishing deviation $\Delta_{\text{therm}} = 0$.

Since we are dealing with closed quantum systems the total energy is conserved. This allows us to determine the effective temperature of the quenched system easily. Knowing the corresponding inverse temperature β is necessary to compute the thermal expectation value of the cluster since this temperature defines the statistical density matrix ρ_{can} of the canonical ensemble as described by (5.24). The initial state of the system, cf. equation (5.7), defines this effective temperature. It has an overall energy

$$E = \langle \text{FS}|H|\text{FS}\rangle \tag{5.38}$$

which translates into an effective inverse temperature according to equation (5.25).

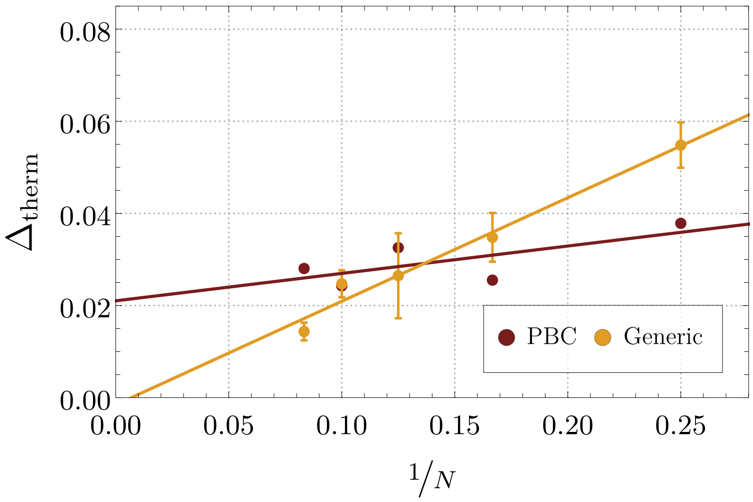

Figure 5.8: Global deviation of the time-averages $\overline{d_i}$ from the thermal predictions $\langle d_i \rangle_{\text{th}}$ at the effective temperature for $U = 3J$. This deviation Δ_{therm} is shown in dependence on the inverse cluster size $^1/_N$. For the generic clusters the shown values are averaged over various clusters of the same size and the error bar indicates the spread within this set of clusters. The lines represent linear regressions to the data [133].

In figure 5.8, the different global deviations for an intermediate quench of the strength $U = 3J$ are plotted against the inverse cluster sizes $^1/_N$ for the various topologies. Error bars again account for the spread of the values between the differently shaped clusters of the same overall lattice size N in the generic, non-integrable cases. In order to analyse the data, a linear fit $\Delta_{\text{therm}} = {}^A/_N + B$ is performed and included in the plot for both data sets. In accordance with previous studies [185, 188, 194–198] and with our expectations, clear trends can be read off. The generic, non-integrable clusters display a vanishing deviation Δ_{therm} in the limit $N \to \infty$. This is a definite indication that theses clusters thermalise. In contrast, the integrable chains show only a slight decrease of the global deviation which is not consistent with a vanishing value for $N \to \infty$. The persisting finite value of $\Delta_{\text{therm}} > 0$ even for extrapolated infinitely large systems is a strong sign for equilibration of the integrable chains towards a *non-thermal* state. This must be attributed to the restricted dynamics in a subspace of the overall Hilbert space due to the large number of constants of motion.

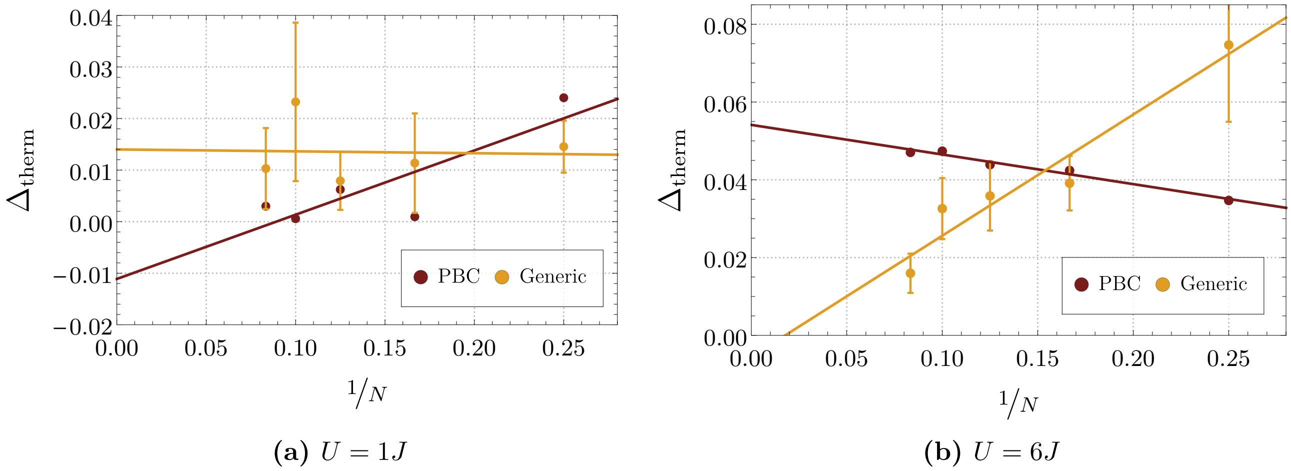

(a) $U = 1J$ **(b)** $U = 6J$

Figure 5.9: Results for the global deviation Δ_{therm}. The results are calculated in the same manner as in figure 5.8 except for $U = 1J$ and $U = 6J$ instead of $U = 3J$. While the results for $U = 6J$ agree qualitatively with the ones shown in figure 5.8, the results for $U = 1J$ show no clear tendency of thermalisation or the absence thereof. This can be ascribed to the very small energy deposited in the system whose results can be visible on larger time scales only [133].

It is worthwhile to keep in mind that perfectly thermalising systems, e.g. the non-integrable generic clusters in the former example, lose all knowledge about their initial states $\rho(0)$ to the larger baths. Furthermore, consider that we use a quench to divert a system from its previous ground state $|\psi_0\rangle$. Such a quench deposits energy in the system according to (5.9). This energy is reflected in the new dynamics of the system after the quench by equation (5.8). If the difference between the state excited by the quench and the previous ground state of the unexcited system is small, mainly (but not exclusively) states $|\Psi_n\rangle$ with lower energies E_n participate in the dynamics. Low energies naturally translate into low-frequency contributions to the dynamics, so that significant changes in the system take place on substantially longer time scales. Thus, two borderline cases come to ones mind here. First, one may ask whether a system which is only *weakly* perturbed, i.e. which is quenched to $U \lessapprox J$, is kept from thermalising – at least on the time scales considered here. So, does a weak quench allow to retain memory about $\rho(0)$? Second, one can wonder whether systems which are quenched even stronger than with $U = 3J$ support the hypothesis that integrability is the key ingredient, and thus also show thermalisation. The corresponding results for the weak quench regime $U = 1J$ are to be found in figure 5.9a and results for a comparatively strong quench of $U = 6J$ are depicted in the respective figure 5.9b.

Here, we notice that the situation is slightly different for the thermalisation behaviour characterised by the global deviation Δ_{therm} between actual results and thermal predictions in both cases. The predictions regarding thermalisation with a vanishing $\Delta_{\text{therm}} \to 0$ in the thermodynamic limit hold when the quenching strength is reasonably large, cf. figure 5.9b. In situations, however, where the quench is weak – which is the case when hopping strength J and interaction U are equal at $U = 1J$ – the system is only weakly perturbed. As stated above, the amount of energy deposited in the system is relatively small and it is plausible that the effects induced by the lower amount of quench energy make themselves felt only on larger time scales.

Parallel to the energy deposited in the system, there is another factor that gains importance with a reduced strength of the quench: the topology and, thus, ultimately also the system size N is of relevance. For $U \lessapprox J$, the hopping part H_0 of the Hamiltonian is no longer a small perturbation of H_{int}, but a significant contribution influencing the dynamics. Consequently, larger spatial scales would be required to fully analyse $U = 1J$ quenches. While the CET computations can be performed for longer times with reasonable effort, increasing only linearly in time, it is extremely tedious, if not impossible, to tackle larger systems because of their exponentially larger Hilbert spaces. It is worth mentioning in this context that the average spread of Δ_{therm} among the generic clusters is much larger for $U = 1J$ in figure 5.9a than in the other cases $U = 3J$ and $U = 6J$ in figure 5.8 and figure 5.9b, respectively. This fact emphasises the noticeably higher influence of the varying topology of the generic clusters for a particular system size N for weak quenches. Obviously, for weak interaction quenches the kinetic part of the Hamiltonian comprising the hoppings remains important. It is this part which defines the topology while for the local interaction any set of N sites behaves the same.

Thus, we state that while in the domain of intermediate and strong quenches the relation between integrability and an absence of thermalisation is quantitatively confirmed, weak quenches require further in-depth research due to the conceptual difficulties.

5.3.3 Summary

Using the numerically exact CET method as well as the TPQS approach we computed results for equilibration and thermalisation of arbitrarily shaped finite-size clusters of the quenched FHM. The chosen initial state is the Fermi sea which is highly entangled in real space. The double occupancy is the local quantity of which the non-trivial quantum dynamics is studied after the interaction quenches.

We showed that even for the Fermi sea as a quantum state that is extremely far from a product state in real space the property of equilibration towards a stationary state is a generic feature regardless of topology or integrability in the thermodynamic limit, i.e. for infinite system sizes $N \to \infty$. The fluctuations present in finite systems are of comparable magnitude for various topologies and do not show a strong influence of integrability.

In addition, we studied infinite-range graphs G_c which represent systems with a maximum coordination number for a given system size. We showed that the fluctuations in these graphs become significantly smaller for $N \to \infty$ than those in graphs of a smaller coordination number $z = 2$. We stress that in infinite-range graphs the coordination number increases with the system size as $z = N - 1$. This corroborates the expectation that fluctuations are less important for a higher connectivity of the cluster. This paradigm is well established in equilibrium and the evidences found indicate that it holds true as well in non-equilibrium situations.

Concerning thermalisation, we confirmed the expectations established in the literature that it depends decisively on the extent that integrals of motion exist. The integrable chains studied do not show thermalisation and stay away from the thermal canonical ensemble. In contrast, the generic clusters clearly display thermalisation.

Obviously, many issues in the field of equilibration and thermalisation still require intensive investigation. Our data showed that there are clear signs of transient behaviour briefly after the quench before the long-time averages and variances emerge. For conceptual and practical purposes it is highly desirable to understand this transient behaviour better, for instance by determining or at least estimating the relevant time scales. Knowledge of the relevant time scales in turn will help to compute long-time averages and stationary values with high accuracy. Finally, passing from quenches to more general forms of time-dependences of closed or open quantum systems represents a vast field of research and continues to be a source of inspiration.

5.4 Dynamical phase transition

5.4.1 Overview

In the previous section, we discussed questions of equilibration and thermalisation on very long time scales. In this section, we turn to the relaxation dynamics of the system on short to medium time scales. That is, so far we aimed to better understand phenomena for which physical observables with the smallest possible local support were advantageous. In other words, we split the system into the smallest possible subsystem S and the largest possible bath B in terms of (5.14). This local limitation of an observable is no longer necessary here and sometimes even undesirable, because it can restrict insights into the entire system. Consequently, an opposite approach is appropriate here. The subsequent choice must fall on an observable that adequately covers the entire real-space system and has a large support or – even better – is fully non-local. All following calculations are performed for the FHM on one-dimensional PBC chains.

Example (cont'd): Non-local observables

One such non-local observable of the one-dimensional FHM is the momentum distribution. It counts how many particles of a certain momentum k and spin σ are present on average at a given time t. For this purpose, the momentum space representation motivated in section 2.1.2 and in particular the corresponding creation and annihilation operators are used. The momentum distribution thus follows as

$$n_{k\sigma}(t) := \left\langle f^{\dagger}_{k\sigma}(t) f_{k\sigma}(t) \right\rangle . \tag{5.39}$$

For an unperturbed, half-filled system in the ground state, the momentum distribution is the Fermi-Dirac distribution at temperature $T = 0$, where all states k up to the Fermi wave vector k_{F} are occupied and all others are unoccupied. In particular, a sharp discontinuity occurs at k_{F} itself. This discontinuity is commonly referred to as jump at the Fermi surface and is defined by

$$\Delta n(t) := \lim_{k \to k_\mathrm{F}^-} n_{k\sigma}(t) - \lim_{k \to k_\mathrm{F}^+} n_{k\sigma}(t). \tag{5.40}$$

The mutual dependence of momentum distribution and jump is shown in figure 5.10 for times $t > 0$ after a quench. It can be seen that the distribution is no longer a Fermi-Dirac distribution, but instead levels at momenta $k > k_\mathrm{F}$ are partly occupied, while levels at momenta $k < k_\mathrm{F}$ have reduced in occupation. As a consequence, the jump loses its height. The discontinuity is still present for a short time after the quench, but it is usually smaller than in the undisturbed system.

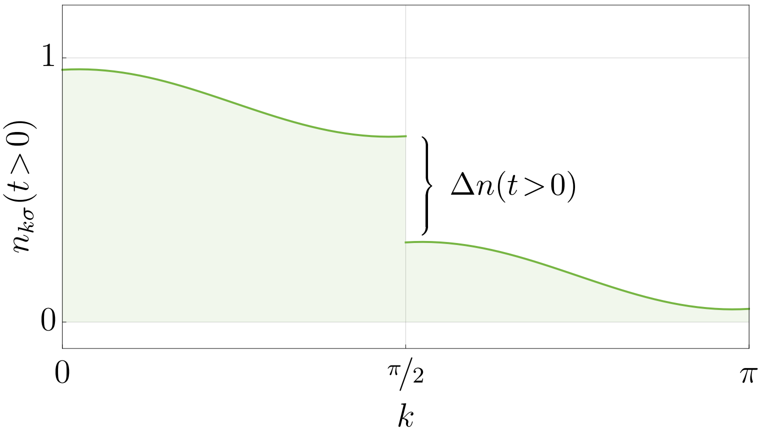

Figure 5.10: The momentum distribution [43] for times $t > 0$ after a quench of the form (5.4). It noticeably differs from the initial Fermi-Dirac distribution at temperature $T = 0$. The jump $\Delta n(t)$ decreases due to momentum conserving scattering processes which transfer particles to formerly unoccupied momenta.

Typically, both the momentum distribution and the jump at the Fermi surface are strongly influenced in their qualitative behaviour by external quenching [113–115, 117, 158, 199]. Furthermore, only a momentum distribution with vanishing jump $\Delta n(t) = 0$ can be thermal in the sense of section 5.2.3: Since a quench transfers energy into the (closed) quantum system, the effective temperature is $T > 0$. For $T \neq 0$, however, the corresponding Fermi-Dirac distribution would no longer show a discontinuity and $\Delta n(t) = 0$ would have to hold. Conversely, this means that a momentum distribution with a non-vanishing jump for $T > 0$ cannot represent a thermalised state. An instructive comparison of the thermal momentum distribution and the actual relaxed momentum distribution based on DMFT can be found, for example, in Ref. [158].

For the jump $\Delta n(t)$, previous studies [113, 117, 164, 165] have consistently predicted a remarkable behaviour: Depending on the strength of a quench, there are two clearly distinguishable behaviours, which are separated by a dynamical phase transition at a critical strength U_c. For weak quenches, i.e. $U \ll U_\mathrm{c}$, the jump changes little and oscillates slightly. This phenomenon is commonly referred to as wiggling. For stronger quenches $U \gg U_\mathrm{c}$, however, a qualitatively completely different behaviour occurs. In this case, the jump disappears almost completely in the course of time, only to increase again almost to its initial level. Typically, this phenomenon is called collapse-and-revival in the literature, cf. for example Ref. [158].

It should be noted, however, that previous studies on this topic were methodologically limited. For instance, results could only be calculated for infinite dimension [117], for very small time spans [113] or they were based on variational approaches, which have to neglect quantum fluctuations for the most part [164, 165]. Consequently, an in-depth investigation of this predicted dynamical phase transition with novel, less constrained methods is desirable. This is the subject of the following sections.[1]

5.4.2 Obtaining the jump $\Delta n(t)$

The jump at the Fermi surface $\Delta n(t)$ is a discontinuity in reciprocal space and, thus, places particularly high demands on methodological approaches. On the one hand, a method used must be able to adequately consider long-range processes in real space, and on the other hand, the system in real space has to be as large as possible. These requirements make the use of CET basically impossible. Instead, we resort to the iEoM described in section 3.4, an approximative method that permits a systematic consideration of processes relevant for the dynamics. In the following, we discuss its specific application to the jump at the Fermi surface and present the corresponding results.

Since the jump is a rescaled Heaviside-like discontinuity, only terms proportional to $1/r$ can contribute to it, i.e. terms with the longest range in real space. These contributions are those due to single-particle excitations *relative* to the Fermi sea [112, 113]. To extract these terms we proceed by normal-ordering all contributions which are present in the dynamics of the fermionic creation operator by

$$f^\dagger_{i\uparrow}(t) = \underbrace{\sum_m^N H_m^{(i)*}(t) :f^\dagger_{m\uparrow}:}_{\substack{\text{single-particle}\\ \text{excitations}}} + :\left[P^\dagger \left(P^\dagger H^\dagger\right)\right]_i: + \dots \,. \tag{5.41}$$

Here, only the first term relates to single-particle excitations and thus matters for the jump Δn. In this notation a particle is inserted at the lattice site i at time $t = 0$ and $:A:$ denotes the normal-ordering of the operator A with respect to the Fermi sea. Once the one-particle prefactors $H_n(t)$ are determined, the jump $\Delta n(t)$ can be computed either by

$$\Delta n(t) = \sum_{m,n}^N H_m^{(0)*}(t) H_n^{(0)}(t) e^{ik_\mathrm{F}(m-n)} \tag{5.42}$$

---

[1] Statement on the work carried out within the scope of this dissertation: The contents discussed in section 5.4 are a systematic continuation of earlier work results from the master's thesis, listed in the bibliography as Ref. [43]. Contents already discussed there are only reproduced where absolutely necessary for understanding.

or by first computing the complete Fourier series [112–114] as given by

$$H_k^{(0)}(t) = \sum_n H_n^{(0)}(t) \exp(-ikn) \tag{5.43}$$

and then taking the square of its absolute value leading to the jump by means of

$$\Delta n(t) = \left| H_k^{(0)}(t) \right|^2 . \tag{5.44}$$

We emphasise here that this method is a highly efficient approach since only the differential equation system (3.64) has to be solved for the determination of all real-space contributions $H_n^{(0)}(t)$. The number of contributions of this differential equation system depends on the size of the chosen operator basis and is typically polynomial in the lattice size N. In particular, compared to a Hilbert space size that increases exponentially with N in the case of CET, much larger systems can thus be treated with iEoM. All calculations discussed below are carried out for $N = 40$ at half-filling, which is far beyond the feasibility limits of a CET approach.

5.4.3 Operator basis

The choice of a problem-adapted orthonormal operator basis (ONOB) for the linear combination (3.63) is a central aspect of any iEoM calculation. To understand what influences the choice of a proper ONOB, we turn to the basic processes affecting the dynamics in the one-dimensional FHM. Each operator A_i of the chosen basis may consist of a product of many elementary fermionic creation or annihilation operators and will be called operator monomial in the following. Moreover, all monomials are orthonormal with respect to the Frobenius scalar product (3.68).

For an arbitrary scenario with $0 < {}^{J}\!/_{U} < \infty$, each application of the Liouville operator, i.e. each commutation with H in (3.60), creates new operator monomials which were not yet in the considered ONOB. In the following, all time-dependent prefactors are omitted for brevity and the set of lattice sites in real space where an operator monomial has a non-trivial effect is called its corresponding cluster. In general, the hopping part H_0 moves operators through the lattice and the interaction part H_{int} generates monomials with increasing numbers of operators. Consequently, no finite ONOB can be closed under iterated commutation with both H_0 and H_{int}. Thus, the number of sites involved proliferates upon commutation, i.e. the clusters continuously grow.

Nevertheless, not all operators contribute to the dynamics to the same extent depending on the parameter regime. Exemplarily, for the limit of strong on-site repulsion, i.e. ${}^{J}\!/_{U} \ll 1$, hopping represents a small perturbation and plays a minor role since nearly local processes dominate the time-evolution of the system. Henceforth, we focus on this particular regime and refrain from including physically strongly suppressed operators in the ONOB. This means that monomials generated by many hopping processes are neglected and an effective operator subspace is used onto which the true dynamics is projected. Similar approaches have been used successfully in former studies, e.g. for calculating resolvents by modified Mori-Zwanzig equations [70].

To construct a suitable ONOB we start by applying both H_0 and H_{int} to the initial fermionic creation operator $f^\dagger_{i\uparrow}$ by means of

$$\mathcal{L}_0\left(f^\dagger_{i\uparrow}\right) \propto f^\dagger_{i\pm1\uparrow} \tag{5.45a}$$

$$\mathcal{L}_{\text{int}}\left(f^\dagger_{i\uparrow}\right) \propto f^\dagger_{i\uparrow} f^\dagger_{i\downarrow} f_{i\downarrow}. \tag{5.45b}$$

Thereafter, we orthonormalise all newly created operators. Eventually, this leads to

$$w^\dagger_1(i) = \sqrt{2} f^\dagger_{i\uparrow} \tag{5.46a}$$

$$w^\dagger_2(i,j,k) = \left(\sqrt{2}\right)^3 f^\dagger_{i\uparrow}\left(f^\dagger_{j\downarrow} f_{k\downarrow} - \frac{1}{2}\delta_{jk}\right) \tag{5.46b}$$

with $N^3 + N$ (and thus only polynomially many) operators in total. All operators of the set (5.46) are invariant under repeated applications of $\mathcal{L}_0(\cdot)$. Already the two operator families of (5.46) allow for the same level of description which was reached perturbatively by continuous unitary transformations before [167, 168]. But since we aim at a description of strong interaction quenches where the local terms dominate we extend the basis (5.46) slightly and close it under repeated applications of $\mathcal{L}_{\text{int}}(\cdot)$ leading to seven additional monomials by

$$w^\dagger_3(i,j,k) = \left(\sqrt{2}\right)^5 f^\dagger_{i\uparrow}\left(\widehat{n}_{i\downarrow} - \frac{1}{2}\right)\left(f^\dagger_{j\downarrow} f_{k\downarrow} - \frac{1}{2}\delta_{jk}\right) \tag{5.47a}$$

$$w^\dagger_4(i,j,k) = \left(\sqrt{2}\right)^5 f^\dagger_{i\uparrow} f^\dagger_{j\downarrow}\left(\widehat{n}_{j\uparrow} - \frac{1}{2}\right) f_{k\downarrow} \tag{5.47b}$$

$$w^\dagger_5(i,j,k) = \left(\sqrt{2}\right)^5 f^\dagger_{i\uparrow} f^\dagger_{j\downarrow} f_{k\downarrow}\left(\widehat{n}_{k\uparrow} - \frac{1}{2}\right) \tag{5.47c}$$

$$w^\dagger_6(i,j,k) = \left(\sqrt{2}\right)^7 f^\dagger_{i\uparrow}\left(\widehat{n}_{i\downarrow} - \frac{1}{2}\right) f^\dagger_{j\downarrow}\left(\widehat{n}_{j\uparrow} - \frac{1}{2}\right) f_{k\downarrow} \tag{5.47d}$$

$$w^\dagger_7(i,j,k) = \left(\sqrt{2}\right)^7 f^\dagger_{i\uparrow}\left(\widehat{n}_{i\downarrow} - \frac{1}{2}\right) f^\dagger_{j\downarrow} f_{k\downarrow}\left(\widehat{n}_{k\uparrow} - \frac{1}{2}\right) \tag{5.47e}$$

$$w^\dagger_8(i,j,k) = \left(\sqrt{2}\right)^7 f^\dagger_{i\uparrow} f^\dagger_{j\downarrow}\left(\widehat{n}_{j\uparrow} - \frac{1}{2}\right) f_{k\downarrow}\left(\widehat{n}_{k\uparrow} - \frac{1}{2}\right) \tag{5.47f}$$

$$w^\dagger_9(i,j,k) = \left(\sqrt{2}\right)^9 f^\dagger_{i\uparrow}\left(\widehat{n}_{i\downarrow} - \frac{1}{2}\right) f^\dagger_{j\downarrow}\left(\widehat{n}_{j\uparrow} - \frac{1}{2}\right) f_{k\downarrow}\left(\widehat{n}_{k\uparrow} - \frac{1}{2}\right). \tag{5.47g}$$

Here, restrictions regarding the site indices i, j and k apply. All operators of (5.47) exist for three distinct indices $i \neq j \neq k$, $i \neq k$. Moreover, the operator family $w^\dagger_3(i,j,k)$ also exists for the case where only i is distinct from the other two indices. The same applies to $w^\dagger_4(i,j,k)$ for the index j and $w^\dagger_5(i,j,k)$ for the index k. The complete basis consisting of (5.46) and (5.47) is well suited for strong quenches where hopping can be seen as a pertubation. Furthermore, it is exact for monomials up to order $({}^{J}\!/\!{}_{U})^2$. This stems from the fact that the monomials comprise up to three sites and, starting from a single sites, clusters of three sites require at least two hopping processes.

A rather subtle problem when choosing such an operator basis for calculating the jump at the Fermi surface lies in the fact that this basis does not consist exclusively of single-particle excitations. Each monomial of the basis (5.46) and (5.47) also contains two-particle excitations as well as even higher excitations. A transformation is possible by means of

$$H_n^{(0)}(t) = \sum_j t_{nj} h_j^{(0)}(t) \tag{5.48}$$

where $h_j^{(0)}(t)$ is the time-dependent prefactor of the operator A_j and $t_{nj} \in \mathbb{C}$ quantifies to which extent the normal-ordering of the operator A_j contributes to the single-particle operator $f_{n\sigma} = {:}f_{n\sigma}{:}$. For further details we refer the interested reader to Ref. [42].

5.4.4 Results on the dynamical phase transition

To get a first impression of the procedure described in the previous section as well as an overview about the dynamics at the Fermi surface, we turn to the jump $\Delta n(t)$ itself for varying quenches prior to a dedicated analysis of a possibly occurring dynamical phase transition. It is worthwhile to note that the jump is not accessible in a direct calculation on finite lattices because the one-sided limits in equation (5.40) cannot be computed then. Thus, we use the detour via the one-particle contributions $H_n(t)$ in connection with equation (5.42) in all subsequent calculations.

Earlier studies based on iEoM but without the Frobenius scalar product (3.68) were limited to very short time spans due to the resulting exponentially increasing or decreasing contributions in the dynamics. Nevertheless, a comparison with these data provides a good benchmark for our method. The respective comparison is shown in figure 5.11. Here, our results which resort to the scalar product are shown using solid lines whereas former analyses not using it [113–115, 200] are depicted by means of dashed lines. The benchmark data (dashed lines) is highly accurate where it is converged, i.e. for short time spans only. The time range shown and used for comparison is adapted accordingly. We emphasise that the time range is restricted for benchmark reasons only and that the Frobenius scalar product provides results on much longer time scales with merely oscillatory dynamics.

On detailed examination of the results two striking phenomena are to be observed. First, for all interaction strengths the zeros of each curve agree very well for both methods. This can be seen as a first indication of a general physical process that determines the overall dynamics for strong quenches. More precisely, the pronounced oscillations of the jump correspond to Rabi oscillations, well-known from two-level systems. The physical interpretation is straightforward. In the limit ${}^{J}\!/_{U} \to 0$, the FHM is mainly governed by local processes which induce Rabi oscillations between singly and doubly occupied sites with periods according to

$$T = \frac{2\pi}{U} \tag{5.49}$$

because their energy difference is U, cf. Refs. [113–115]. This is analogous to spin precession around the z-axis if initially the spin points along a transversal direction

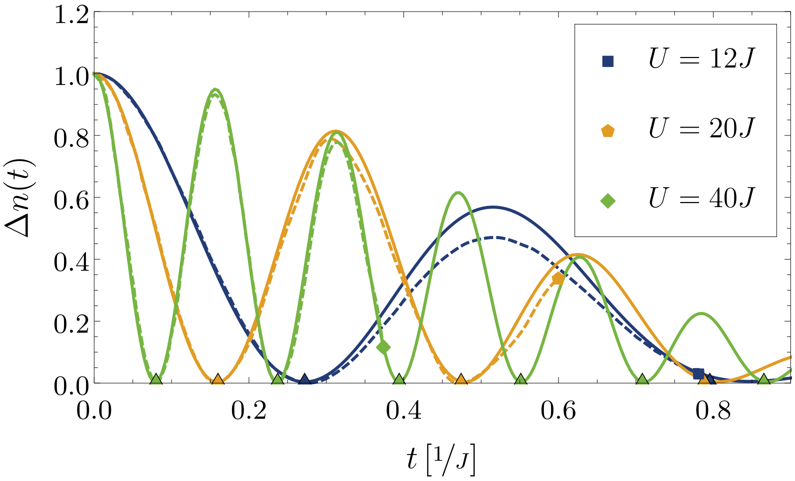

Figure 5.11: Comparison of results [42] obtained using the Frobenius scalar product (solid lines) and results calculated for normal-ordered operators without scalar product [114, 200] (dashed lines). The latter results are calculated in a highly accurate approach, but are only converged up to short times. The respective maximum times are given by the three different plot symbols. Triangles at the x-axis mark predictions for zeros of the curve based on the Rabi oscillations (5.49).

in the xy-plane. When quenching, the initial state is a superposition of the two local possibilities of singly and doubly occupied sites. Note that at half-filling both, single occupation and double occupation, are two-fold degenerate: Single occupation due to the two spin states and double occupation because the completely empty site acts like a site doubly occupied with holes. In the considered regime of quenches to intermediate and strong interaction strengths, we see that the estimate by means of Rabi oscillation periods (5.49) for the observed oscillations matches the zeros very well, cf. the triangular symbols at the bottom axis. The first symbol is put at the first zero of the computed curves and the following symbols are placed at multiples of the Rabi oscillation period T.

Second, the amplitudes of the jump for both approaches nearly coincide for strong interaction quenches, i.e. $U \geq 20J$. This observation indicates that our scalar product method yields highly accurate results especially in the limit of strong quenches providing the advantages that

(i) the operator basis to be considered, though large, is much smaller in the present approach than in the previous approach;

(ii) the present approach is able to capture noticeably longer time spans so that it renders more extensive studies possible.

While the data already suggest a high precision of the iEoM method employing the Frobenius scalar product, they do not yet answer the question of the occurrence of a dynamical phase transition in the form presented here. Especially isolating weaker low-frequency parts of the oscillation is highly demanding if not impossible in an approach in the time domain as in figure 5.11. We address this problem by a systematic analysis of the entire frequency components contained in the jump. To analyse the relevant frequencies in the evolution of the Fermi jump systematically we use a Fourier analysis. Obviously, a straightforward approach is not initially feasible here. An unmodified Fourier analysis is hampered by the discontinuous onset at the time $t = 0$ where the signal starts. As we have already seen in the context of section 4.1.1, abruptly starting or stopping signal components will lead to Gibbs phenomena and, thus, make a systematic analysis difficult. As a remedy for the analysis, we therefore choose a slightly modified approach. Since we want to focus only on the frequency content we resort to a fast Fourier transform of the symmetrised signal $\Delta n(t) + \Delta n(-t)$. This signal is additionally smoothed by means of a low-pass Gaussian filter in order to remove any possibly occurring numerical artefacts.

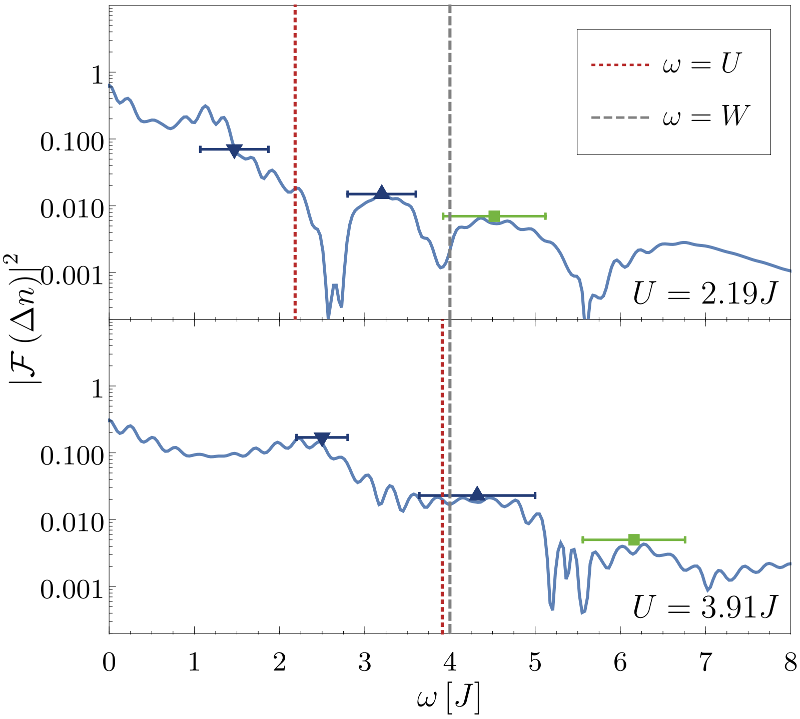

Figure 5.12: Spectra as obtained by Fourier transform of the time-dependent symmetrised Fermi jump for weaker interaction quenches. The symbols with error bars indicate spectral features which we read off [42].

The figures 5.12 to 5.14 display the squares of the absolute values of the resulting spectra for various quenches in logarithmic plots. The value of the quenching strength is indicated in the lower right corner of the panels. The coloured symbols with error bars show the frequencies which we read off. Mostly, they are used to indicate peaks, in some cases, however, they denote shoulders. An example for a shoulder can be seen in the low-frequency feature in the upper panel of figure 5.12. We chose to read off this feature because at even smaller interaction only the shoulder can be identified reliably.

Note that different symbols are chosen to display different spectral structures. Upon increasing U, the high-frequency feature shown using a green square shifts to higher and higher values, but becomes less and less significant. Beyond a certain value of U it does not appear anymore, cf. figures 5.13 and 5.14. In parallel, a low-frequency feature appears which was not discernible before. We denote this low-frequency feature by the red hexagons in figures 5.13 and 5.14.

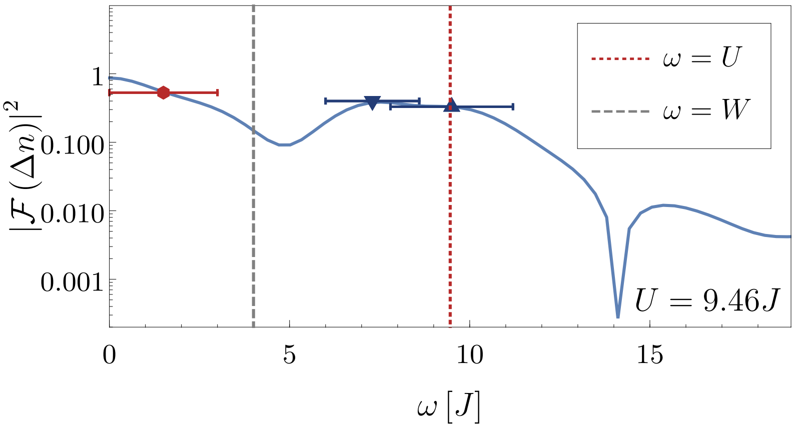

Figure 5.13: Exemplary spectrum for intermediate interaction quenches. The same caption as in figure 5.12 applies [42].

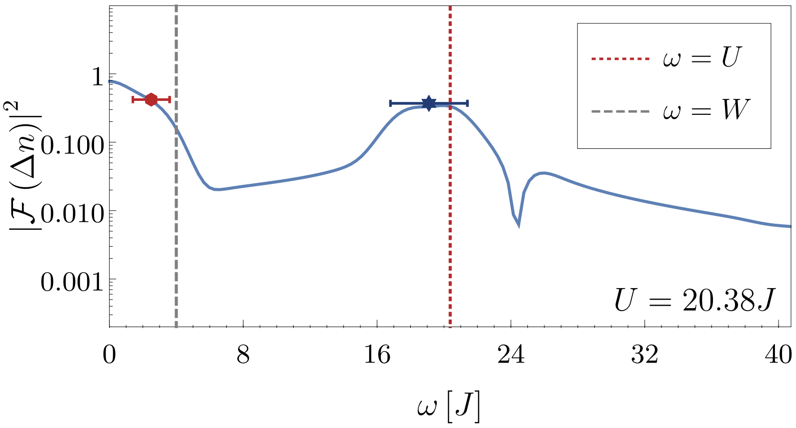

Figure 5.14: Exemplary spectrum for strong interaction quenches. The same caption as in figure 5.12 applies [42].

Comparing the figure 5.13 and the figure 5.14, it appears as if the two peaks indicated by blue triangles, which are still discernible in figure 5.13, were merged in figure 5.14. Consequently, we denote the new combined feature by a single symbol formed from both triangles. The vertical dashed lines are a means to identify the two typical energies of the system, namely the bandwidth W (grey) and the interaction strength U (red) for orientation and comparison with the identified spectral features. It appears as if both of them showed up in the spectral features. This means that pronounced spectral features occur at frequencies which are close to both W and U. The same energy scales have also been identified in previous studies, cf. for example Ref. [113], but always individually limited to one regime. For weak quenches, only spectral features in the bandwidth range were identified, for strong quenches only those in the on-site interaction range. Our data, however, indicate that both energy scales are present in all regimes.

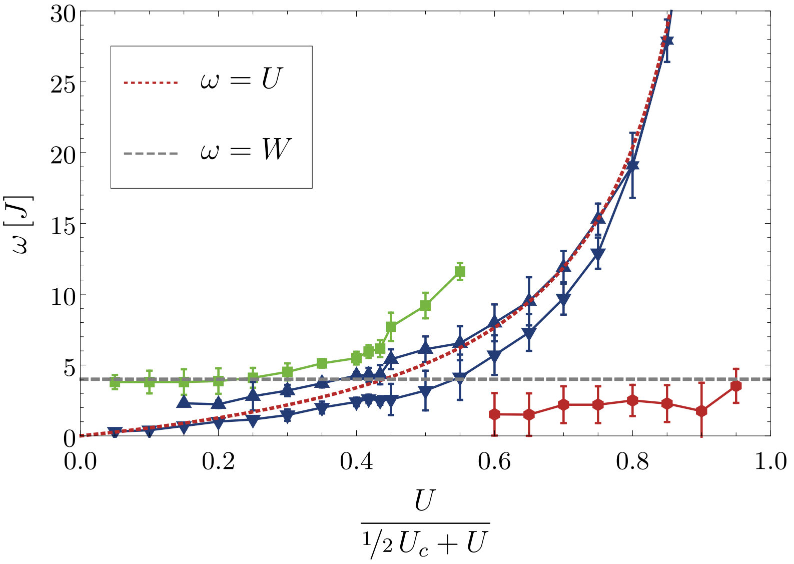

Figure 5.15: Frequencies of the most important spectral features in the spectra of $\Delta n(t)$ plotted as functions of the interaction strength. The latter is given in a compactified form with $U_c = -8E_{\text{kin}}/N$ where $E_{\text{kin}}/N = -W/\pi$ is the kinetic energy per site of the half-filled non-interacting system. This permits to show the full range from $U = 0$ to $U = \infty$. The error bars are determined approximately by the half-widths at half maximum of the peaks. The frequency of local Rabi oscillations and the bandwidth are depicted for comparison as dashed lines [42].

We analysed many more spectra than the four shown here explicitly. The derived data of all spectral features is compiled in figure 5.15. In total, we identified four relevant features. For weak quenches, one feature is clearly given by the bandwidth W as shown by the green curve in figure 5.15. Besides this feature, there are two features located at frequencies above and below the local Rabi frequency U (blue curves). The lower frequency curve almost coincides with U for weak quenches. We stress that the features for weak quenches must be regarded with some caution because the choice of the ONOB is specifically designed for the regime of strong quenches.

For strong quenches, a low-frequency feature occurs as depicted by the red curve. It does not coincide quantitatively with the bandwidth W, but it is close to it within a factor of two. Given the difficulty to extract the proper frequency for the low-frequency feature, see especially figures 5.13 and 5.14, the quantitative deviations are not surprising. The high-frequency feature clearly matches the local Rabi frequency U almost quantitatively. As motivated before, the two spectral features above and below U merge for larger U, at least they can no longer be detected separately, cf. figure 5.14.

The intermediate parameter region $U \approx U_c/2$ in figure 5.15 is of particular interest since in all previous analyses [113, 117, 164, 165] it seemed as if there were two qualitatively distinct regimes for weak and for strong quenches, separated by a sharp dynamical phase transition. The results in figure 5.15 at least question this interpretation. We recall that the iEoM approach used here allows for an analysis on considerably longer time scales and with essentially more substantial contributions to the dynamics. In contrast to former studies, the respective results in figure 5.15 point towards a crossover. Indeed, different spectral features dominate for weak and strong quenches. But there is no sharp, singular transition between these two regimes as pointed out in the previous studies. Instead, the weight of the different spectral features shifts so that W is more relevant for weak quenches while U dominates for strong quenches. Thus, the prediction of a dynamical phase transition deserves a further in-depth investigation.

Although the integrability of the one-dimensional FHM was not a prerequisite for the application of the iEoM approach and was not used at any time, it can limit the dynamics. We have seen one example of this in the context of thermalisation in section 5.3.2. As a result, the situation in higher dimensions, for instance in $d = 2$, might be also of interest.

5.4.5 Summary

With the results presented in section 5.4, progress has been made in the analysis of the relaxation behaviour of the one-dimensional FHM on short to medium time scales. Here, the integrability of the model was not used at any stage.

Using a modified iEoM approach, we computed the dynamics of the time-evolution of the discontinuity of the momentum distribution, namely the Fermi jump. We used the Heisenberg picture with a truncated basis and continuously preserved operator unitarity. Using these techniques, we studied interaction quenches from the non-interacting Fermi sea to a finite interaction strength U. In doing so we conceived an ONOB that describes all possible physical processes which can occur on up to three lattice sites and that is designed to capture the limit of strong interactions and small hopping. This ONOB is exact up to order $(J/U)^2$. The accuracy of it was tested by a comparison to highly accurate reference results. For large values of U the agreement is especially good.

For stronger quenches the jump shows pronounced oscillations which correspond to Rabi oscillations, well-known from two-level systems. They are reminiscent of the collapse-and-revival scenario in bosonic systems [20] and they were observed before in the one-, two- and infinite-dimensional FHM [113, 115, 117]. A systematic frequency analysis of the jump showed that two important energies dominate: the bandwidth W and the interaction strength U. Interestingly, we do not find a singular dynamical phase transition as function of the quenched interaction, but a smooth crossover. Spectral features gain and lose weight, but they do not pop up or vanish suddenly. This is in contrast to previous interpretations. This progress has become possible due to the significantly longer accessible times thanks to the conceptual progress.

6 Excitations and dynamics in the t–J model

In this chapter, we address the limiting case of the FHM in the presence of strong interaction, the so-called t–J model. For a physical motivation and the theoretical derivation of this model the reader is referred to section 2.2. Here, we focus primarily on two situations, which allow us to study the respective charge and spin degrees of freedom. First, we consider the motion of a hole in a disordered spin background for the analysis of the charge carrier dynamics. Second, we resort to strict half-filling such that all charge degrees of freedom in the resulting Heisenberg model are frozen out, cf. section 2.3. This way, the mere spin dynamics can be analysed. In this context, we consider systems on one-dimensional chains, two-dimensional square lattices or on infinite-range graphs.

The chapter reproduced herein is an enhanced and partially revised and/or restructured reprint of Refs. [46, 201]. These works may be or become subject to copyright. The studies on which these two works are based are the results of different collaborations.[1]

6.1 Introduction

Strongly correlated fermionic systems and, in particular, Mott-Hubbard physics continue to represent a great challenge for theoretical treatments in spite of many decades of research [13]. Even apparently rather simple physical questions cannot be answered in a straightforward manner. A prominent example is the motion of a single hole in a disordered Mott insulator. This issue has attracted a lot of interest especially after the discovery of high-temperature superconductivity, cf. section 2.2.1 for an introduction to fundamental issues and an instructive overview of possible theoretical approaches.

In principle, the crucial difficulty in describing hole motions in disordered spin backgrounds is the difference between classical and quantum mechanical processes. Depending on the specific spin background or the topology of the lattice, different paths of the hole through the lattice can interfere with each other to different degrees, making it difficult to formulate universal solutions [30]. In general, the charge carrier dynamics in the Mott-Hubbard regime can only be described satisfactorily with theoretical methods in few and special cases. For instance, theoretical statements are feasible for one-dimensional [66], very large or even infinite-dimensional systems [202–204]. Moreover, systems can be approximated, e.g. by means of variational approaches for specific initial spin orientations [205] or by self-consistent perturbation theory [206]. Despite this undeniable progress, there is still no method to obtain generally accurate predictions for arbitrary

---

[1] Authorship statement: The results shown in this chapter are based on the work of several contributors. The author is responsible for the complete implementation and provision of all CET results shown. Furthermore, the author co-supervised Dag-Björn Hering's master's thesis on iEoM. Dag-Björn Hering is responsible for all iEoM results shown. Timo Gräßer is responsible for all results on spinDMFT.

systems. Considering the significant experimental progress in the field of ultracold atoms, e.g. by means of quantum gas microscopy [207, 208], the motion of holes in paradigmatic models such as the FHM or the t–J model is no longer a gedankenexperiment. Thus, the need for reliable theoretical approaches is more urgent than ever.

But even if the motion of charges is completely suppressed, serious problems remain. Although the resulting system then consists exclusively of stationary spins, the mutual interaction of the spins can render the determination of the dynamics highly difficult. This is especially a problem in situations where many nearly equal energy scales are involved and the partitioning of a larger system into a small subsystem and a very weakly coupled bath is no longer an option. Such systems are often referred to as *dense* ensembles and are described in more detail in section 6.3.1. Due to many equal constituents governing the dynamics, theories for weakly coupled open quantum systems are no longer applicable. But how do the spin orientations evolve in time for such and similar systems after they have been aligned in a given initial position? Questions of this kind have a very practical relevance, be it in the context of nuclear magnetic resonance [209] or diamonds with nitrogen vacancies (NVs), cf. Refs. [210, 211]. Especially when systems are being considered as possible candidates for the persistent storage of quantum information, it is essential to predict their decoherence, i.e. the loss of information over time [212].

This chapter consists of two major parts. In section 6.2, we address the dynamics of a hole in the complete t–J model with its full charge and spin degrees of freedom. We outline how an effective generalised t–J model can be derived by means of a CUT and discuss two relevant parameter regimes for disordered spin backgrounds. For these regimes, we calculate the corresponding Green's functions and spectral densities in one and two dimensions using CET. These results are compared to approximate results of an iEoM calculation. In section 6.3, we freeze the charge degrees of freedom and exclusively focus on the spin dynamics in dense systems. For this, we exploit the Heisenberg model on topologies with comparatively high coordination numbers. Then, we compute the quantum mechanical autocorrelation of the system with a numerically exact method and compare it to the results of a novel dynamical mean-field theory. In this way, we demonstrate that the full quantum mechanical dynamics can also be derived in a noticeably easier way, i.e. with classical random fields around each individual spin.

6.2 Charge dynamics

The aim of this section is to study the hole motion in one and two dimensions, i.e. along a chain and on a square lattice. The former case serves both as a benchmark and, due to its lower coordination number, as a system in which a larger number of processes with a larger local spread is numerically accessible than in higher-dimensional lattices. This facilitates an in-depth spectral analysis and, in particular, the analysis of the edges of the excitation spectrum, which are typically noticeably difficult to access. The latter case of a two-dimensional square lattice actually represents the most interesting case in view of experimental realisations in solid state systems or in ultracold atom setups. In our study, we consider the t–J model, which can be derived from the Hubbard model [72, 213–218].

One possible way of doing this transformation has already been explained in section 2.2.2, another possibility is discussed below. Regardless of the concrete transformation, we stress that the mapping from the Hubbard model to the t–J model is not restricted to the magnetic exchange couplings only, but naturally extends to the charge degrees of freedom, i.e. to hopping terms, hole-hole interactions and even correlated hopping processes. This applies to both the one-dimensional chain [59] and to the two-dimensional square lattice [72, 219] at half-filling and in its direct vicinity, i.e. for finite doping [220].

Henceforth, we choose a notation that is slightly different from previous chapters to keep it in line with the current literature on the topic. Consequently, the parameter t denotes the time, indexed quantities or quantities with (double) prime symbols describe hopping processes of different order and J denotes the magnetic interaction strength.

For the analysis, two different approaches are used: a numeric approach using CET, cf. section 3.3, and a semi-analytic approach by means of iEoM, cf. section 3.4. The latter approach by means of iEoM relies on the Heisenberg picture and a set of operators which is enlarged iteratively by repeated commutations with the Hamiltonian. Using the Frobenius scalar product (3.68) a Hermitian, oscillatory dynamics is guaranteed [42, 116]. Moreover, results of the application of the Liouville superoperator are projected such that no double occupancies are created or annihilated. This procedure prevents the emergence of non-physical processes. Thus, the iEoM approach is a systematic expansion in the parameter

$$x := t_0/U. \tag{6.1}$$

For further information on the operator basis used, the accuracy of the method or the derivation of a spectral density in the reduced operator subspace, we refer the interested reader to Ref. [46]. In the following, we will not go into further detail regarding iEoM.

Whereas the first approach using CET is numerically exact, but limited to finite systems, the second approach considers processes up to a certain order only, but in the infinite thermodynamic system. This makes the first technique more reliable for determining the exact dynamics of a given system. Nevertheless, it bears the risk of being unable to access the thermodynamic behaviour due to finite-size effects. The necessary steps of a CET have already been discussed in detail for the FHM in section 3.1. In section 6.2.2, we turn to the required adjustments and simplifications for the t–J model as well as the derivation of the spectral density from the time-dependent Green's function.

For both methods, we proceed in three separate steps. First, we consider a large interaction strength U, i.e. we omit all terms of the order x^2U and, thus, only keep terms of the order U and t_0. Second, we include all hopping terms of the order x^2U which contain uncorrelated as well as correlated spin-dependent hopping. In the last step, we turn on the magnetic interaction J to study to which extent it induces changes in the spectral densities and its band edges. Generally, such changes are expected. For instance, the critical strength U_c, at which the Mott insulator becomes unstable, deviates from the bandwidth W in the quantitative estimate

$$U_\mathrm{c} \approx 1.10W \tag{6.2}$$

for the case of the two-dimensional square lattice as given by Reischl et al. [219].

6.2.1 Effective charge model

As discussed in section 2.2.2, the standard procedure in the analysis of the t–J model is to restrict the full second-order perturbation theory (2.18) to the subspace $\mathcal{H}_0$ of no electronic double occupancy (eDO). This leads to the conventional t–J model as given by equation (2.19). Henceforth, we proceed differently in analogy to the considerations of Ref. [219]. The reason for this rewriting is, in particular, a resulting more descriptive and accessible interpretation of the t–J model than its conventional representation would allow for. What is more, the representation chosen here is more universal. Even though the subspaces $\mathcal{H}_n$ of a fixed number n of eDOs are decoupled from each other and the dynamics of a state does not leave the corresponding subspace, thermal expectation values, for instance, are equally dependent on all subspaces of the entire Hilbert space. Consequently, restricting the discussion only to the subspace of vanishing eDOs might be a potential pitfall. In spite of the fact that we exclusively determine dynamical properties of the system in the following, we would like to emphasise once again the higher generality of the representation chosen here compared to the one given by equation (2.19).

In the limit of strong interaction, i.e. $x \ll 1$, the Hubbard model can be mapped to the t–J model by means of an expansion in the small parameter x. We discuss the terms in three steps. First, we consider all terms up to the first order in x. These terms consist of H_{int}, which is linear in U and thus of zeroth order in x, as well as the $xU = t_0$ term H_0, which describes nearest-neighbour (NN) hopping and which is of first order in x. In the second step, we take into account all terms of up to second order in x but without any spin degrees of freedom and, thus, without the magnetic exchange interaction

$$J = 4x^2U. \tag{6.3}$$

In the last step, we also include J in the analysis. Consequently, we consider solely charge dynamics in the first and second step and both charge and spin dynamics in the third step. Contributions of order x^3U are neglected at any point. A systematic approach to derive such an effective model is to resort to a CUT, cf. especially Refs. [218–224].

For the sake of completeness, we will briefly recall the general concepts as presented in Ref. [219]. For a CUT, one conventionally starts with the flow equation [221] given by

$$\frac{d}{d\ell}H(\ell) = [\eta(\ell), H(\ell)]. \tag{6.4}$$

Here, one has to choose a suitable antihermitian generator $\eta(\ell)$. Similar to the perturbative reasoning [213–217], the key idea is to eliminate all processes which could *change* the total number of DOs in the system. One possible choice of a generator for the CUT is

$$\eta(\ell) = \left[\hat{D}, H(\ell)\right] \tag{6.5}$$

since it preserves the overall number of DOs [219]. In this context, the Hermitian operator

$$\hat{D} := \sum_i \left[\widehat{n}_{i\uparrow}\widehat{n}_{i\downarrow} + (1 - \widehat{n}_{i\uparrow})(1 - \widehat{n}_{i\downarrow})\right] \tag{6.6}$$

counts the number of DOs, i.e. all sites which are either occupied by zero or two electrons. We stress that the resulting generator is proportional to the ones with *sign* functions [219, 222, 223] due to the simplicity of $\hat{D}$. The flow equation (6.4) governs a transformation from the initial Hamiltonian $H(0) = H$ to an effective one according to

$$H_{\text{eff}} = \lim_{\ell \to \infty} H(\ell). \tag{6.7}$$

One is interested in this effective Hamiltonian. Obviously, it is necessary to restrict the number of contributing operator terms generated by the flow equation in a suitable manner. One possibility, which is employed in Refs. [219, 220], is to define a proper measure of locality. The idea is to discard all operator terms which are not sufficiently local. Since the non-locality of the Hubbard model stems from its hopping processes, this approach corresponds to a systematic expansion in the parameter x. By means of this approach it is feasible to derive a generalised t–J model both at strict half-filling [219] and even for moderate doping [220]. This generalised t–J model [219] reads

$$H_{\text{eff}} = H_{0,\text{eff}} + H_J. \tag{6.8}$$

Besides the contributions listed in equation (6.8), there are additional contributions that arise in the course of the CUT. These terms characterise any interactions of two or more DOs with each other. Since we want to study the dynamics of *one* hole in the half-filled model only, interactions of DOs do not play a role. Note that with respect to the half-filled model as the reference state an empty site equals exactly one hole. Consequently, the corresponding contributions for more than one DO can be ignored.

It is instructive to note that the results for the leading order at half-filling can be determined by analytical approaches as well [59, 60, 72]. Basically, the generalised t–J model consists of the charge degrees of freedom as given by the different hopping terms

$$H_{0,\text{eff}} = T_0 + T_0' + T_{s,0}' + T_0'' + T_{s,0}'' + \text{h.c.} \tag{6.9}$$

and the spin dynamics. The second contribution in equation (6.8) is called Heisenberg term, cf. especially equation (2.22), depends on the magnetic interaction (6.3) and reads

$$H_J = J \sum_{\langle i,j \rangle} \mathbf{S}_i \mathbf{S}_j = \frac{J}{2} \sum_{\langle i,j \rangle} \left(P_{ij} - \frac{1}{2} \right). \tag{6.10}$$

The alternative representation by means of permutation operators P_{ij} arising here is explained in detail in the context of section 2.3 and especially before equation (2.28).

It should be noted that the term *generalised* t–J model used in this work takes into account the fact that besides the pure NN hopping T_0 further, partly spin-dependent and thus correlated hopping processes are being considered. The t–J model discussed in the present literature, however, often only consists of the contributions

$$H_{t-J}^{(0)} = T_0 + H_J \tag{6.11}$$

and is not consistent with an expansion in x. For the sake of brevity, we use the term t–J model in the following to denote the generalised t–J model (6.8). In each case, we indicate which contributions of the model are included in the calculation of the dynamics.

The elements in equation (6.9) have a slightly different physical meaning for one and two dimensions. In the following, we start with the more general case of two dimensions and then discuss the adjustments for the special case of one dimension. The term T_0 describes NN hopping from site i to j and vice-versa subjected to the restraint that DOs neither are added nor removed. Thus, it corresponds to a special case of H_0 and leads to

$$T_0 \;=\; t_0 \sum_{\langle i,j\rangle,\,\sigma} \Big[(1-\widehat{n}_{i\sigma}) f^{\dagger}_{i\overline{\sigma}} f_{j\overline{\sigma}} (1-\widehat{n}_{j\sigma}) + \widehat{n}_{i\sigma} f^{\dagger}_{i\overline{\sigma}} f_{j\overline{\sigma}} \widehat{n}_{j\sigma}\Big]. \tag{6.12}$$

The notation below the sums denotes a one-time counting of each bond between the lattice sites i and j while $\overline{\sigma}$ means the opposite of the orientation σ. The generalisation of such hopping to next-nearest neighbour (NNN) hopping processes, i.e. all processes between sites on the square lattice which lie on adjacent diagonal positions, read

$$T'_0 \;=\; t' \sum_{\langle\langle i,j\rangle\rangle,\,\sigma} \Big[(1-\widehat{n}_{i\sigma}) f^{\dagger}_{i\overline{\sigma}} f_{j\overline{\sigma}} (1-\widehat{n}_{j\sigma}) - \widehat{n}_{i\sigma} f^{\dagger}_{i\overline{\sigma}} f_{j\overline{\sigma}} \widehat{n}_{j\sigma}\Big]. \tag{6.13}$$

Likewise, hopping processes between third-nearest neighbour (3NN) sites, i.e. sites that lie in-line on one of the axes and are separated by two links, are described by the term

$$T''_0 \;=\; t'' \sum_{\langle\langle\langle i,j\rangle\rangle\rangle,\,\sigma} \Big[(1-\widehat{n}_{i\sigma}) f^{\dagger}_{i\overline{\sigma}} f_{j\overline{\sigma}} (1-\widehat{n}_{j\sigma}) - \widehat{n}_{i\sigma} f^{\dagger}_{i\overline{\sigma}} f_{j\overline{\sigma}} \widehat{n}_{j\sigma}\Big]. \tag{6.14}$$

Apart from these hopping processes, further *spin-dependent* hops occur in the effective two-dimensional model. Whenever a charge carrier hops from one site to another, e.g. from i to j with a NN site k in between, a spin-dependent hop occured. They read

$$T'_{s,0} = t'_s \sum_{\substack{\langle i,k,j\rangle \\ \alpha,\beta}} \Big\{ \big[(1-\widehat{n}_{i\alpha}) f^{\dagger}_{i\overline{\alpha}} \boldsymbol{\sigma}_{\overline{\alpha},\overline{\beta}} f_{j\overline{\beta}} (1-\widehat{n}_{j\beta})\big]\mathbf{S}_k + \big[\widehat{n}_{i\alpha} f^{\dagger}_{i\overline{\alpha}} \boldsymbol{\sigma}_{\overline{\alpha},\overline{\beta}} f_{j\overline{\beta}} \widehat{n}_{j\beta}\big]\mathbf{S}_k \Big\} \tag{6.15a}$$

$$T''_{s,0} = t''_s \sum_{\substack{\langle\langle i,k,j\rangle\rangle \\ \alpha,\beta}} \Big\{ \big[(1-\widehat{n}_{i\alpha}) f^{\dagger}_{i\overline{\alpha}} \boldsymbol{\sigma}_{\overline{\alpha},\overline{\beta}} f_{j\overline{\beta}} (1-\widehat{n}_{j\beta})\big]\mathbf{S}_k + \big[\widehat{n}_{i\alpha} f^{\dagger}_{i\overline{\alpha}} \boldsymbol{\sigma}_{\overline{\alpha},\overline{\beta}} f_{j\overline{\beta}} \widehat{n}_{j\beta}\big]\mathbf{S}_k \Big\}. \tag{6.15b}$$

The processes (6.15) do not only involve the hopping of a charge over a NN site, but also its interaction with the spin of this NN site. For instance, the spin of the hopping charge may swap with the spin of the charge which is located at the NN site. Again, the spin-dependent processes (6.15) do not change the total number of DOs in the system.

The adaptation of the contributions (6.12), (6.13), (6.14) and (6.15) of the effective two-dimensional model to the case of one dimension is straightforward. Without the second spatial direction, certain processes can no longer be present. Clearly, only the contributions T_0 and T''_0 can exist in one dimension since there are no diagonals. Thus, the double-prime processes represent NNN hopping and all prime hopping processes vanish completely. Unfortunately, this makes the nomenclature NN, NNN and 3NN highly ambiguous if both one and two dimensions are considered. As a remedy, we use the terms *prime* and *double-prime* hopping instead. We stress again that both exist in two dimensions whereas only the double-prime processes are present in one dimension.

The leading orders of the above contributions, i.e. their hopping strengths, may be determined analytically via perturbation-theoretical approaches [59, 72] or numerically by means of the above-discussed CUT [219]. In the following, we make use of the values which have been derived analytically for one dimension in Ref. [59]. They read

$$t'' = -\frac{t_0^2}{2U} \tag{6.16a}$$

$$t''_s = \frac{t_0^2}{U}. \tag{6.16b}$$

A generalisation of these contributions to the additional processes arising in two dimensions is easily possible. In two dimensions, there is exactly one shortest route from a site i to a site j that can generate a t'' contribution. In the case of a diagonal hopping, i.e. for t', there are two shortest routes since a diagonal step on a square lattice can happen via a horizontal step and then a vertical step or vice-versa. For spin-independent diagonal hopping, both routes contribute equally. We account for this by a factor of two such that

$$t' = -\frac{t_0^2}{U}. \tag{6.17}$$

For all spin-dependent processes the involved intermediate lattice site k distinguishes the two routes. Therefore, no doubling is needed and the hopping strength reads

$$t'_s = \frac{t_0^2}{U}. \tag{6.18}$$

The leading contributions in equations (6.17) and (6.18), which we generalised for two dimensions, are fully consistent with the numerically determined contributions t' and t'_s of comparable studies, cf. especially Ref. [219]. Furthermore, they agree with the results for the two-dimensional system that is analysed in Ref. [72].

Evidently, there are two different energy scales in the effective t–J model (6.8). The energy scale J of the spin degrees of freedom and the bandwidth $W = 2zt_0$ governing the charge degrees of freedom. As before, the coordination number of the lattice is denoted by z. For all subsequent considerations, we always choose the physical regime

$$0 < J \ll T \ll W \tag{6.19}$$

where the temperature T is much larger than the typical magnetic coupling strength J but smaller than the bandwidth W. Hence, we consider a completely disordered spin background. The charge carriers, however, behave as if the system was essentially at vanishing absolute temperature, i.e. $T \approx 0$. Such regimes, in which the bandwidth W

lies clearly above the magnetic strength J, are no longer pure gedankenexperiments, but can indeed be measured experimentally on ultracold atoms [208]. To analyse this regime in detail, we especially focus on the following two parameter sets

$$\mathcal{A}\colon \quad J = \frac{t_0}{3} \tag{6.20a}$$

$$\mathcal{B}\colon \quad J = \frac{t_0}{d}. \tag{6.20b}$$

The first set $\mathcal{A}$ is taken from a practical application example. For cuprates, i.e. materials which are relevant for high-temperature superconductivity as discussed in section 2.2.1, the magnetic strength (6.20a) is a representative value. The second parameter set $\mathcal{B}$ is a theoretically motivated one. It roughly represents the boundary value

$$U = W \tag{6.21}$$

up to which the mapping from the FHM to the t–J model is reasonable [219, 220]. For lower values of the interaction, the assumption of a gap between a LHB and an UHB is no longer justified. Moreover, the case $\mathcal{B}$ is of particular interest as it represents the limiting case with the maximum number of second-order terms in the t–J model. For ease of identification, we use the corresponding abbreviations $\mathcal{A}$ and $\mathcal{B}$ below to distinguish between these two parameter sets. We emphasise that in case $\mathcal{B}$ different second-order terms occur depending on the dimension d of the system.

6.2.2 Obtaining Green's functions

While the basic procedure of a CET was already discussed in detail using the example of the FHM in section 3.1, in this section we elaborate on the modifications necessary for the t–J model. Given that we consider the t–J model for half-filling with exactly one additional hole, there are significantly fewer possible states per lattice site than previously in the FHM. Accordingly, it is not reasonable to reuse the original basis of the FHM as presented in section 3.1. After all, the numerical effort involved is significantly larger than what is actually necessary for the t–J model. Hence, we need another suitably chosen complete set of orthonormal states $\{|i\rangle\}$ that forms a basis of the Hilbert space $\mathcal{H}$ for the Hamiltonian (6.8). In order to increase the overall performance we resort to a representation of the basis states by integer numbers. This procedure is completely analogous to the approach taken in equation (3.12). We exemplify this in the following before discussing how to derive Green's functions from the respective Hamiltonian matrix.

Consider a half-filled t–J model doped with a single hole. That is, exactly one hole is inserted into a lattice of N sites with one particle per site. Then, the dimension of the Hilbert space is

$$\dim(\mathcal{H}) = N\,2^{N-1} \tag{6.22}$$

since the hole may occupy one of N sites while on all remaining sites the spins $1/2$ can point upwards or downwards. For notational simplicity, we artificially enlarge the basis size to $d = N\,2^N$ states while keeping in mind that the spin orientation at the site occupied by the hole has no physical meaning. Thus, a real space basis of the form

$$|i\rangle = |i_{N-1} \dots i_0\rangle \, |h_{N-1} \dots h_0\rangle \tag{6.23}$$

can be constructed. In this notation, all spins can be either orientated upwards, i.e. $\uparrow \equiv 0$, or downwards, i.e. $\downarrow \equiv 1$, so that the relation $i_j \in \{0, 1\}$ holds. The hole always occupies exactly one site $h_k = 1$. Consequently, all remaining sites are fully empty such that

$$h_j = 0 \, \forall \, j \neq k \tag{6.24}$$

is ensured. This allows for an easy and concise identification of a specific basis state $|i\rangle$ by means of the integer representation $I \in 0, \dots, N\,2^N - 1$ using

$$I = k\,2^N + \sum_{j=0}^{N-1} i_j 2^j. \tag{6.25}$$

Here, the last sum is equal to the integer value of the binary number given by the binary pattern of the spin orientations. As long as we do *not* consider the magnetic exchange H_J the complete dynamics in the t–J model only takes place in the direct vicinity of the hole position k. This facilitates the numerical task considerably. As before for the FHM, it is possible to construct the respective Hamiltonian matrix either on-the-fly by algorithms linear in the basis size or to keep a highly sparse copy of it. In order to compute spectral densities with the CET, we determine the retarded Green's function which is given by

$$g(t) = -i \, \mathrm{Tr} \left(h_{i\uparrow}(t) h_{i\uparrow}^{\dagger} \rho_0 \right) \theta(t) \tag{6.26}$$

in a first step. Here, we create a hole at the lattice site i with spin orientation σ using

$$h_{i\sigma}^{\dagger} = f_{i\sigma}. \tag{6.27}$$

In realistic cases, the trace in equation (6.26) cannot be calculated exactly, i.e. using an ED, due to the size of the Hilbert space. Hence, we again resort to the concept of the stochastic evaluation of traces, cf. section 4.1.2. Due to the regime given in equation (6.19) we consider a fully disordered spin background. Consequently, we do not deal with a pure state but with a mixed one corresponding to the high-temperature limit of the canonical ensemble $\rho \propto e^{-\beta H}$, i.e. to the disordered system given by the density matrix

$$\rho_0 \propto \mathbb{1}. \tag{6.28}$$

Inserting equation (6.28) into (6.26) while choosing R randomly drawn states $|r\rangle$ to evaluate the trace, the retarded Green's function may be approximated by means of

$$g(t) \approx -\frac{i}{R} \sum_{r=1}^{R} \langle r| e^{iH_{\mathrm{eff}}t} h_{i\uparrow} e^{-iH_{\mathrm{eff}}t} h_{i\uparrow}^{\dagger} |r\rangle \, \theta(t). \tag{6.29}$$

It should be noted that the time-evolutions occurring in (6.29) are all of the general form

$$|\psi(t)\rangle := \exp\left(-iHt\right)|\psi(t{=}0)\rangle\,. \tag{6.30}$$

Hence, we can resort to (3.53) for the evaluation of its time-dependence by means of a CET. As discussed in section 6.2.1, we consider the hole dynamics both in the complete t–J model (6.8) as well as in the hopping-only model (6.9). The last case, in which the magnetic exchange interaction is set to zero such that $J = 0$ holds, allows for a significant simplification of the retarded Green's function (6.29). This simpler version reads

$$g_{0,\mathrm{eff}}(t) \approx -\frac{i}{R}\sum_{r=1}^{R}\langle r|h_{i\uparrow}e^{-iH_{0,\mathrm{eff}}t}h_{i\uparrow}^{\dagger}|r\rangle\,\theta(t). \tag{6.31}$$

Here, we exploited that $e^{iH_{\mathrm{eff}}t}$ has no impact on $\langle r|$ for $J = 0$ because no hopping can take place in $\langle r|$. Consequently, this contribution can be omitted in (6.29). The implication of this simplification is apparent. In the first case (6.29), a hole is inserted into the random state $|r\rangle$ at time $t{=}0$ followed by a simulation of its time-evolution. In parallel, the time-evolution of the state $\langle r|$ is simulated and a hole is inserted at the future point in time $t > 0$. In the second case (6.31), a hole is inserted into both the bra and the ket at time $t{=}0$ whereupon one of the two states is time-evolved. For practical purposes, this means that in the case (6.29) the time-evolution of two states has to be calculated by means of a CET, whereas in the case (6.31) only one state has to be simulated in a CET. In both cases, the Green's functions are calculated for a finite time span $[0; t_{\mathrm{max}}]$ in time steps of $\mathrm{d}t$. Thereafter, a Fourier transform is performed such that

$$g(\omega) \propto \sum_{n} e^{-i\omega t_n} g(t_n)\,\mathrm{d}t \tag{6.32}$$

holds. For the sake of notational brevity, we use the same symbol g both for time- and frequency-dependent quantities. The chosen finite time intervals lead to spurious phenomena in the Fourier transforms (6.32). These can be systematically suppressed by damping the temporal Green's function $g(t)$ by means of multiplying it with a decreasing function. For simplicity, we opt for the approach to damp the Green's function using

$$\widetilde{g}(t) = g(t)\exp\left(-\frac{1}{2}\sigma^2 t^2\right). \tag{6.33}$$

We recall that a multiplication in the time domain, like the one in equation (6.33), equals the convolution of $g(\omega)$ in the frequency domain with the corresponding Gaussian kernel

$$K \propto \exp\left(\frac{-\omega^2}{2\sigma^2}\right). \tag{6.34}$$

Finally, the spectral density of the single hole excitation can be obtained by means of

$$A(\omega) = -\frac{1}{\pi}\,\mathrm{Im}\,\widetilde{g}(\omega). \tag{6.35}$$

6.2.3 Accuracy and finite-size effects

Before turning to an in-depth analysis of the results of hole motion in the t–J model on the basis of the corresponding spectral densities (6.35), it is advisable to compare the two selected approaches in terms of accuracy. Since the native quantity of a CET is the time-dependent Green's function (6.26), we select this very quantity for the following comparison. In particular, we have to answer the questions: Do the results of a CET significantly depend on the lattice size N and do finite-size effects appear for systems that are small? What is the minimum number of fundamental processes that must be considered in an iEoM calculation in order to capture the system with sufficient accuracy?

Since our main interest lies in the thermodynamic system, i.e. the limit $N \to \infty$, both approaches can cause issues. While the CET is exact in the analysis of any finite system with N lattice sites, one may wonder whether the result can be readily applied to infinite systems. In contrast, the iEoM approach considers the thermodynamic system by definition, but does not take into account all processes that may contribute to its dynamics. If processes with a larger spatial extension are not adequately captured but are decisive for the dynamics, this reduces the reliability of the iEoM results.

In addition to the two numerical approaches, an analytical approach for the short-term behaviour of the dynamics suggests itself for comparison. For this analytical estimate, we will slightly modify the former creation operator for a hole $h^\dagger_{i\sigma}$ as given in equation (6.27). In analogy to the procedure we used in Ref. [46], we choose the operator defined by

$$\overline{h}^\dagger_{i\sigma} = f_{i\sigma} f_{i\overline{\sigma}} f^\dagger_{i\overline{\sigma}} \tag{6.36}$$

for creating a hole at site i with spin σ. The operator (6.36) is merely a generalised version of the operator given in equation (6.27). In particular, the operator (6.36) ensures that no particle with spin $\overline{\sigma}$ is located at the site i before it creates a hole of orientation σ there. Moreover, this operator is orthogonal to all other operators of the iEoM basis with respect to the Frobenius scalar product (3.68). We emphasise that the use of (6.36) is motivated by the wish to improve the analytical comparability with the iEoM. This operator is not conceptually different from the operator (6.27) used in the CET. For the practical purposes of a CET simulation, both operators behave in the same way.

The behavior of the retarded Green's function $g(t)$, cf. equation (6.26), of the hole creation operator given in equation (6.36) for times $t \gtrsim 0$ can be estimated analytically by means of an expansion in powers of t. This expansion reads

$$g(t) \approx -\frac{i}{2}\left(1 + \left\langle \left[H, \overline{h}_{i\uparrow}(0)\right] \left[H, \overline{h}^\dagger_{i\uparrow}(0)\right] \right\rangle t^2\right) + \mathcal{O}\left(t^3\right). \tag{6.37}$$

In this context, the translational invariance in time, which can be denoted using

$$g'(t) = g'(-t) = \left\langle \left[H, \overline{h}_{i\uparrow}(0)\right] \overline{h}^\dagger_{i\uparrow}(-t) \right\rangle, \tag{6.38}$$

permits to simplify the expression and to rewrite the second derivative advantageously by

$$g''(t) = \frac{\mathrm{d}g'(-t)}{\mathrm{d}t} = -i \left\langle \left[H, \overline{h}_{i\uparrow}(0)\right] \left[H, \overline{h}^\dagger_{i\uparrow}(0)\right] \right\rangle. \tag{6.39}$$

This way, we are able to avoid a double commutator. Since we perform the comparison of the different methods using the example of the one-dimensional chain, we exemplarily calculate the expansion in powers of t for this case. We emphasise that an analogous procedure using equation (6.37) is also easily possible for the two-dimensional lattice. Due to the additional prime hopping terms and more potential hopping partners in the lattice, more summands occur in this case. The commutators of the chain read

$$\left[T_0, \overline{h}_{i\uparrow}\right] = t_0 \overline{h}_{i\pm1\downarrow}\sigma_i^+ + \frac{1}{2} t_0 \overline{h}_{i\pm1\uparrow}\sigma_i^z + \frac{1}{2} t_0 \overline{h}_{i\pm1\uparrow} \tag{6.40a}$$

$$\left[T_0'', \overline{h}_{i\uparrow}\right] = t'' \overline{h}_{i\pm2\downarrow}\sigma_i^+ + \frac{1}{2} t'' \overline{h}_{i\pm2\uparrow}\sigma_i^z + \frac{1}{2} t'' \overline{h}_{i\pm2\uparrow} \tag{6.40b}$$

$$\left[T_{s,0}'', \overline{h}_{i\uparrow}\right] = \frac{1}{2} t_s'' \overline{h}_{i\pm2\downarrow}\sigma_{i\pm1}^+ + \frac{1}{2} t_s'' \overline{h}_{i\pm2\downarrow}\sigma_{i\pm1}^+\sigma_i^z \tag{6.40c}$$

$$+ t_s'' \overline{h}_{i\pm2\uparrow}\sigma_{i\pm1}^-\sigma_i^+ + \frac{1}{4} t_s'' \overline{h}_{i\pm2\uparrow}\sigma_{i\pm1}^z \tag{6.40d}$$

$$+ \frac{1}{4} t_s'' \overline{h}_{i\pm2\uparrow}\sigma_{i\pm1}^z\sigma_i^z - \frac{1}{2} t_s'' \overline{h}_{i\pm2\downarrow}\sigma_{i\pm1}^z\sigma_i^+ \tag{6.40e}$$

$$\left[H_J, \overline{h}_{i\uparrow}\right] = \frac{1}{4} J \overline{h}_{i\uparrow}\sigma_{i\pm1}^z + \frac{1}{2} \overline{h}_{i\downarrow}\sigma_{i\pm1}^+ . \tag{6.40f}$$

All remaining commutators for the case $\overline{h}_{i\uparrow}^\dagger$ result from equation (6.40) when substituting

$$\overline{h}_{i\uparrow} \to -\overline{h}_{i\uparrow}^\dagger \tag{6.41a}$$

$$\sigma_i^+ \leftrightarrow \sigma_i^- . \tag{6.41b}$$

The expectation values occurring in (6.37) can be calculated straightforwardly since they are needed at time $t = 0$. The trace is computed over states at half-filling without a hole. For instance, the results for the expectation values (6.40f) arising from H_J read

$$\left\langle \overline{h}_{i\uparrow}\sigma_{i\pm1}^z \overline{h}_{i\uparrow}^\dagger \sigma_{i\pm1}^z \right\rangle = 2 \cdot \frac{1}{2} \tag{6.42a}$$

$$\left\langle \overline{h}_{i\downarrow}\sigma_{i\pm1}^+ \overline{h}_{i\downarrow}^\dagger \sigma_{i\pm1}^- \right\rangle = 2 \cdot \frac{1}{4} . \tag{6.42b}$$

One should note that the first factor results from the repeated occurrence of the given expectation value, once for the lattice site $i{+}1$ and once for the site $i{-}1$. The expectation values of the other contributions can be calculated likewise. Then, substituting all expectation values and (6.40) into (6.37) yields the explicit expansion as

$$g(t) = -\frac{i}{2}\left[1 - \left(t_0^2 + t''^2 + \frac{6}{16} t_s''^2 + \frac{3}{32} J^2\right) t^2\right] + \mathcal{O}(t^3). \tag{6.43}$$

In order to perform the actual method comparison we apply the CET to the full one-dimensional t–J model as given by equation (6.8) and compare its results to both the analytical approximation, cf. equation (6.43), and to the corresponding iEoM results.[2]

---

[2] These and all following iEoM results of this chapter were provided as raw data by Dag-Björn Hering, cf. in particular footnote 1 on page 95. The author is responsible for the entire data processing, e.g. by convolution or broadening, data analysis and data comparison. For more details on the calculation of the raw data using iEoM we refer the interested reader to Ref. [46].

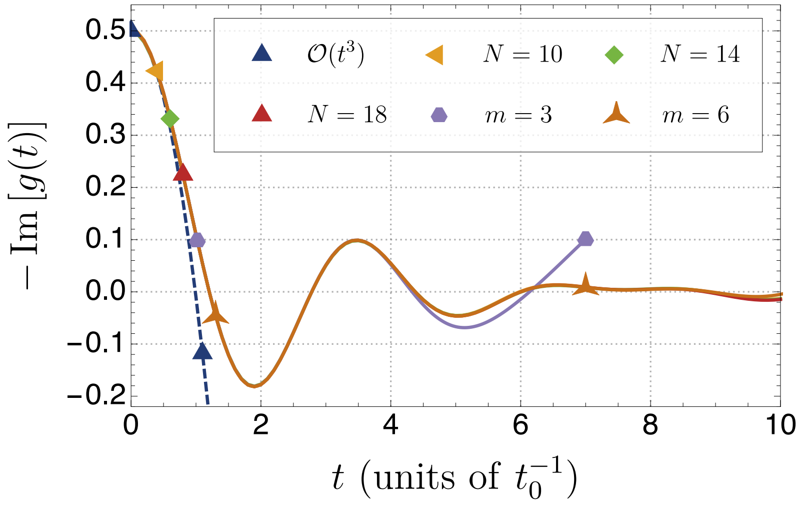

Figure 6.1: Retarded real-time Green's function (6.29) of the one-dimensional chain for the full t–J model with parameters $\mathcal{A}$ as given in equation (6.20a). The results are determined for various lattice sizes N (CET) and loop orders m (iEoM). The parabola of the analytical expansion (6.37) in powers of t up to $\mathcal{O}(t^3)$ is depicted as well (blue triangles). Note that the iEoM result for $m=6$ loops first starts to deviate from the CET results at about $t \geq 9/t_0$ [46].

For this comparison, we resort to the realistic parameter regime $\mathcal{A}$ as given in equation (6.20a). The respective retarded Green's function (6.29) is presented in figure 6.1 for various chain lengths N (CET) and loop orders m (iEoM). Furthermore, the short-time behavior (6.37) is plotted by a dashed line as a reference. Here and henceforth, the hopping element t_0 defines the energy unit and, thus, the time unit according to $[t] = t_0^{-1}$.

Note that the Green's function starts at $g(t\!=\!0) = 0.5$. This is because the creation of a hole can only be performed successfully if an electron with the appropriate spin is present at the respective lattice site. Due to the assumed spin disorder (6.28) this holds in exactly 50 % of the cases. The time-dependence, cf. figure 6.1, resembles a damped oscillation. Nevertheless, we are dealing with a closed quantum system. Therefore, no actual relaxation can occur and merely the superposition of coherent oscillations is possible. As we resort to a large mixture of spin backgrounds it is plausible that no damping but a strong dephasing of very many eigenstates of the hole motion occurs.

The comparison of the different methods shows a high degree of consistency for the times presented. Moreover, no finite-size effects appear in the CET results. Even for longer time intervals up to $t_{\max} = 20$ (not fully shown here) the results for $N = 10$, $N = 14$ and $N = 18$ coincide. Therefore, a further analysis of any finite-size dependence of the CET results is not required in the following. Instead, we use simulations of the largest possible system size $N = 18$ in all subsequent computations by means of CET.

Especially for the highest loop order, i.e. $m = 6$, the iEoM results agree remarkably well with the CET results. For lower loop orders, e.g. $m = 3$, a deviation begins to emerge for times $t \gtrsim 4/t_0$. Albeit it seems that the iEoM results for this smaller loop order diverge more and more from the actual physical result for increasing times $t \to \infty$, the unitarity of the Liouville matrix guarantees that exclusively oscillatory dynamics can occur, cf. equation (3.69) or Refs. [42, 116]. As a result, no contributions to $g(t)$ may decrease or increase exponentially. For all calculations based on iEoM the results which resort to the highest feasible loop order m were provided. This order varies and is strongly dependent on the topology of the lattice as well as on the number of physical processes considered. What is more, the number of processes depends on whether only the first-order contribution T_0, second-order contributions without spin-spin interaction (6.9) or the complete generalised t–J model (6.8) is considered. The numerically most challenging case is given by a large coordination number z in combination with the complete t–J model, i.e. for H_{eff} on a two-dimensional square lattice. For this case, results using the loop order $m = 3$ have been provided.

6.2.4 Results

In this section, we consider the local spectral densities $A(\omega)$ of the t–J model and we compare the spectral densities calculated by CET using equation (6.35) with the raw iEoM data provided. For performance reasons, these iEoM raw data were calculated in reduced Krylov spaces of sufficiently high dimension $f = 200$ so that the corresponding spectral density consists of f discrete peaks. It reads

$$A(\omega) \approx \sum_{n}^{f} a_n \delta\left(\omega - \omega_n\right). \tag{6.44}$$

Here, the a_n denote the weight of the corresponding δ-spike located at frequency ω_n.

The CET data do not exhibit such phenomena and are substantially smoother since they were obtained by means of Fourier transforms for comparatively long time periods. In order to better compare both results, we artificially broaden the δ-spikes of the iEoM results by Gaussians so that the final iEoM spectral densities become

$$A(\omega) = \sum_{n}^{f} \frac{a_n}{\sqrt{2\pi}\sigma} \exp\left(-\frac{(\omega - \omega_n)^2}{2\sigma^2}\right). \tag{6.45}$$

Note that the relevant parameter of this broadening is the second moment of the Gaussian distribution, i.e. the parameter σ^2. This parameter determines how wide the spatial extent of each δ-spike of the spectral density is. This procedure is very similar to the damping of the CET Green's function, cf. equation (6.33) for the influence of σ.

For all subsequent comparisons, we choose the parameter σ as small as possible. A parameter σ that is too large risks erasing physical features of the spectral density and a value of σ that is too small causes large wiggling in the results. In particular, the iEoM results are affected by this wiggling. In cases in which an especially large broadening of the iEoM is required, we show both the slightly broadened CET results on their own as well as a comparison of the results of both methods with a larger broadening.

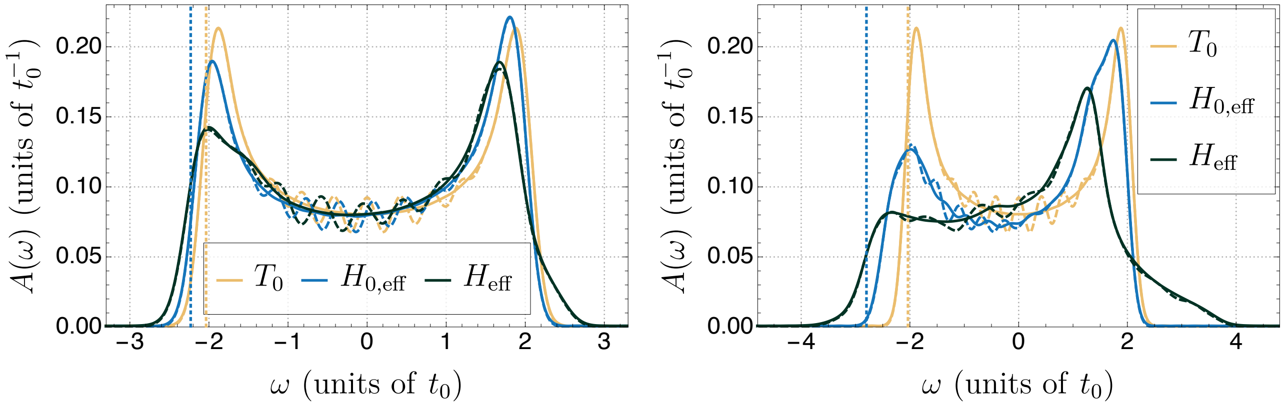

(a) Density for parameter set $\mathcal{A}$

(b) Density for parameter set $\mathcal{B}$

Figure 6.2: Spectral density $A(\omega)$ for a one-dimensional chain and the parameter sets $\mathcal{A}$ and $\mathcal{B}$ of (6.20), respectively. The results are artificially broadened by $\sigma = 0.15t_0$. Solid lines represent CET results, dashed lines denote iEoM results. The iEoM band edges ω_{min} are indicated by vertical dashed lines [46].

Due to its semi-analytical character, the iEoM approach offers a particular advantage over the CET: Band edges of the spectrum, i.e. the smallest occurring frequencies ω_{min}, can be determined in a reliable way. We plot these band edges, determined by iEoM, by vertical dashed lines in the following figures. All cases of H_{eff} in which no band edge is drawn show characteristics of an infinite support. In these cases, the spectral density could possibly extend over the entire real axis with weights which decrease in the outer regions of the spectrum. We explicitly emphasise that all band edges originate from the plain spectrum, i.e. before the artificial broadening was performed. Accordingly, the choice of the parameter σ has no influence on these band edges. For more details on the calculation of the band edges and infinite supports of the spectrum, see Ref. [46].

One-dimensional model

The results of the one-dimensional system are depicted in figure 6.2. Here, the two parameter sets $\mathcal{A}$ and $\mathcal{B}$ are used. Since the results for T_0 do not depend on the specific choice of a parameter set, this curve can serve as a reference in the two figures 6.2a and 6.2b for how much the parameter sets modify the plain NN hopping.

We stress that the results of the different methods agree well in all cases. Note that the results have been broadened by $\sigma = 0.15t_0$. Both the upwards and the downwards flanks of the spectral density as well as the characteristic shape including the peak positions are accurately reproduced by both approaches. The wiggling of the iEoM results around $\omega = 0$ results from a few discrete, Gaussian broadened peaks. A higher loop order m and then possibly a larger Krylov space dimension f could lead to smoother results.

The spectral density $A(\omega)$ for the T_0 part of the t–J model is symmetric around the frequency $\omega = 0$. This is to be expected since NN hopping implies a symmetric local density of states as has been shown rigorously in the one-dimensional case for the limit of infinite interaction, i.e. $U \to \infty$ [59, 60]. Moreover, it explains the frequency

$$\omega_{\text{min}} = -2t_0. \tag{6.46}$$

It is reproduced by the given iEoM results within a relative error of about 2 %.

The pronounced peaks in the outer parts of the densities are van Hove singularities. They are smeared out by finite-size effects (CET) or finite loop orders (iEoM) and the artificial broadening σ. Otherwise, they would show up as $1/\sqrt{\Delta\omega}$ divergences. In fact, the analytical results [47, 59, 60] imply that the spectral density is given by

$$A(\omega) = \frac{1}{2\pi} \frac{1}{\sqrt{\omega^2 - 4t_0^2}}. \tag{6.47}$$

If the spin-dependent and spin-independent hopping is included, i.e. when $H_{0,\text{eff}}$ is considered, the support of the spectrum increases: for the parameter set $\mathcal{A}$ by about 10 % and for the set $\mathcal{B}$ by almost 20 %. Since the density satisfies the sum rule

$$\int_{\mathbb{R}} A(\omega)\,\mathrm{d}\omega = \frac{1}{2}, \tag{6.48}$$

a larger support necessarily translates into a reduced average height. This behaviour is clearly visible. In particular, the black curves show a significantly lower mean height combined with an increased support. In addition, one clearly sees that the spectral density loses its symmetry: the left van Hove peak becomes lower than the right one.

If the magnetic exchange, i.e. the spin-spin interaction H_J, is included as well we consider the dynamics induced by H_{eff}. The corresponding results are shown by the darkest curves in the figures 6.2a and 6.2b. The broadened curves show an even larger asymmetry between the left and the right peak compared to the former results obtained for $H_{0,\text{eff}}$. For the parameter set $\mathcal{B}$, the left peak is reduced to only a shoulder. Furthermore, its seems that the edges have been slightly more shifted and broadened. Nevertheless, a thorough analysis of the minimum frequencies ω_{min} as a function of increasing loop order m with the help of the iEoM approach suggests another conclusion. In this analysis, the minimum frequencies do not asymptotically converge towards a constant value, but continue to increase in their absolute values. This gives rise to the hypothesis that there are *no* minimum frequencies and that the actual physical spectrum of the full t–J model extends over the entire real axis, cf. Ref. [46]. One reason for this observation could be that the number of excitations in the spin sector is not bounded because H_J is an extensive term and that more and more spin excitations can cause an increasing support. Further research on this matter may be appropriate.

Two-dimensional model

Analogous to calculations for the one-dimensional model, i.e. the t–J model along a chain, spectral densities and minimum frequencies can also be determined for the two-dimensional case. We emphasise that such a calculation is not merely an enlargement

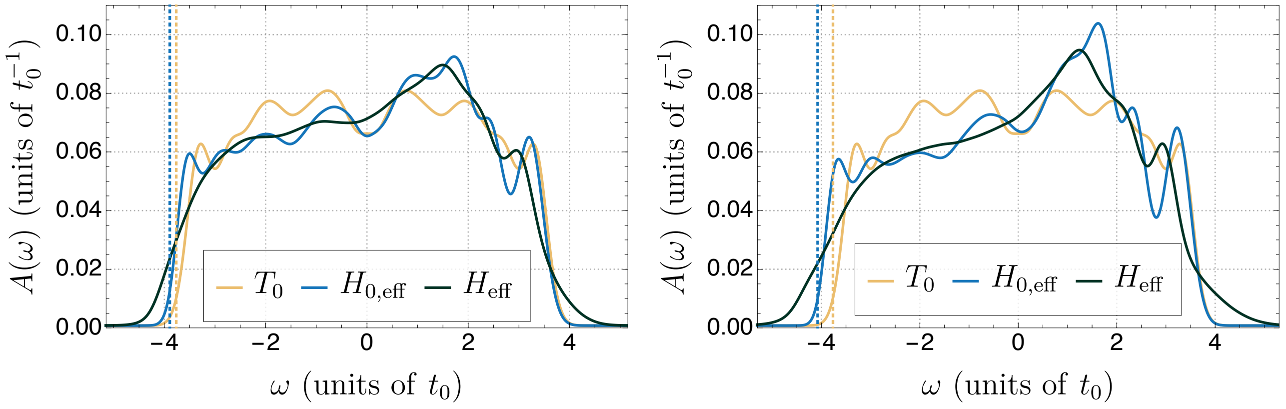

(a) Density for parameter set $\mathcal{A}$

(b) Density for parameter set $\mathcal{B}$

Figure 6.3: Spectral density $A(\omega)$ for a two-dimensional square lattice and the parameter sets $\mathcal{A}$ and $\mathcal{B}$ of (6.20), respectively. The results are artificially broadened by $\sigma = 0.15t_0$. Solid lines represent CET results. The iEoM band edges ω_{min} are indicated by vertical dashed lines [46].

of the dimension but introduces additional physical processes. For instance, there are four NNs on a square lattice instead of two NNs on the chain. This yields a more densely populated Hamiltonian matrix. In parallel, for a constant cluster size N only $\sqrt{N}$ hopping processes for NN hopping and correspondingly fewer for NNN or 3NN hopping are unaffected by wrap-around effects. As a consequence, it becomes significantly more demanding to describe the dynamics without finite-size effects on a square lattice by means of a CET. As a result, the obtained densities are not as smooth as in one dimension and are subject to more wiggling.

In order to achieve a higher number of hopping processes before wrap-around effects set in, we resort to a trick and rotate the studied square cluster by 45°. Then, its edge length is given by $\sqrt{2}n$ according to Pythagoras where n is the number of vertical and horizontal NN steps to pass from one corner of the square cluster to the adjacent one. Consequently, the total number of sites is $N = 2n^2$. For $n = 3$, we have to treat $N = 18$ sites which is still feasible. The advantage is that a wrap-around only occurs after exactly $2n = 6$ NN hops. We emphasise that a naive choice of the square cluster with an equal number of hops for a wrap-around would have required $N = 6^2 = 36$ sites. In this case, the corresponding Hilbert space would be almost $2.6 \cdot 10^5$ times larger than the one our CET has to deal with in the case of the optimised cluster.

Since a significant improvement of the accuracy of the iEoM results would only be realisable with an increase of the loop order m, which is technically extremely difficult to do, the corresponding iEoM results are of low resolution and less detail. For this reason, we show the more finely resolved CET results for the smallest possible broadening $\sigma = 0.15t_0$ in figures 6.3a and 6.3b. Comparable results with a broadening three times as large, i.e. for $\sigma = 0.45t_0$, are shown in figures 6.4a and 6.4b for both methods.

The first feature one notices is that the overall shape of the spectrum is significantly altered compared to the case of a chain. While the one-dimensional model shows strongly pronounced van Hove singularities at the edges as well as the approximate shape (6.47), the spectral density of the two-dimensional model appears more elliptical or even slightly rectangular. The density is symmetric if only T_0 is considered and becomes asymmetric as soon as the Hamiltonian is extended in agreement with what we found in one dimension. Note, however, that the lower band edge for T_0 is *not* given by the naive assumption

$$\omega_{\mathrm{min}} = -4t_0. \tag{6.49}$$

Indeed, the actual iEoM band edge is close to $-4t_0$, see the vertical dashed lines in figures 6.3a and 6.3b. At first glance, one would expect that (6.49) should hold for the simple NN hopping in two dimensions. The motivation for (6.49) is similar to the one-dimensional case where we found (6.46) in accordance with the analytical arguments given in Refs. [59, 60]. The reason for this deviating behaviour in two dimensions is that in one dimension a perfect spin-charge separation occurs for NN hopping and $U \to \infty$. In other words, the sequence of spins is not changed by the hole motion. This does not hold in two dimensions. On a square lattice, loops may occur and merely Trugman paths [57] allow for a hole motion without any changes of the spin order.

It is important to keep in mind that there is a subtle difference between this spin-charge separation and the actual spin-spin interaction H_J. The spin-charge separation also exists for $J = 0$ and stems from the fact that each lattice site is always occupied by a particle of a certain spin orientation. In the one-dimensional model, this spin order is initially predetermined and cannot be changed by a moving hole, as is described by T_0. In two dimensions, there is also an initial orientation of all spins on the square lattice. Yet, this spin orientation can be destroyed by a hopping hole provided that it hops randomly enough through the lattice. Then, the hole will leave a trail of changed spins and the initial spin pattern and the final pattern will no longer be identical.

Furthermore, the iEoM band edges ω_{min} are significantly closer to each other for the two parameter sets displayed than for the one-dimensional case. For the parameter set $\mathcal{A}$, we attribute this to the altered dimensionality. For the parameter set $\mathcal{B}$, this effect is enhanced by the smaller value of the exchange coupling J, i.e. due to

$$J_{\mathrm{1D,B}} = 1 > \frac{1}{2} = J_{\mathrm{2D,B}}. \tag{6.50}$$

We emphasise that our results agree with results of previous research, for instance

$$\omega_c = -4.4t_0 \tag{6.51}$$

for the full t–J model as given in Ref. [219]. The prediction (6.51) resides in the range of the left flanks where the spectral density starts to rise significantly, cf. black curves in figures 6.3a and 6.3b. As previously motivated, an exact determination of the band edge for the complete t–J model for $J \neq 0$ is not possible. We assume this finding not to be an artefact but to reflect that band edges do not exist in this case [46].

Analogous to the one-dimensional case, a broadening of the spectrum upon inclusion of more and more processes is observed for the square lattice. For the parameter set $\mathcal{A}$

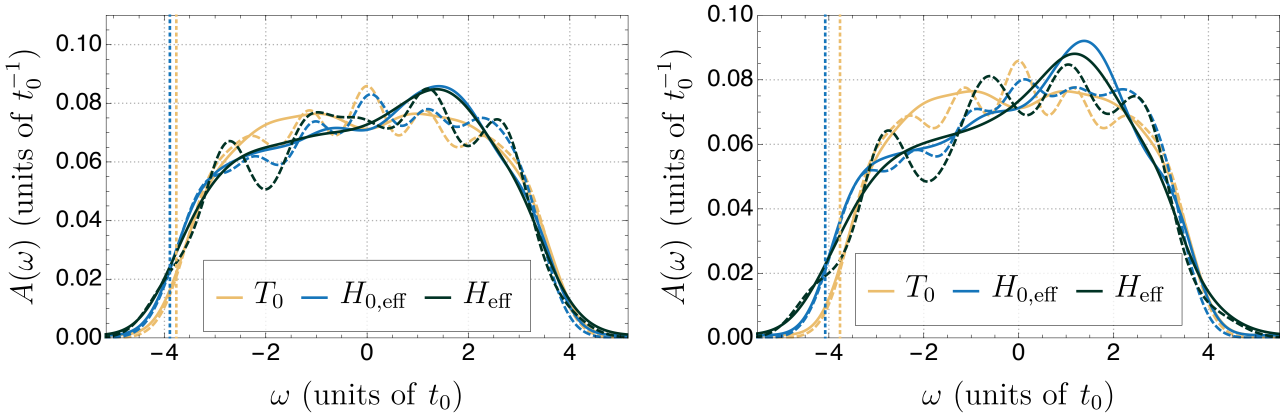

(a) Density for parameter set $\mathcal{A}$ **(b)** Density for parameter set $\mathcal{B}$

Figure 6.4: Spectral density $A(\omega)$ for a two-dimensional square lattice and the parameter sets $\mathcal{A}$ and $\mathcal{B}$ of (6.20), respectively. The results are artificially broadened by $\sigma = 0.45t_0$. Solid lines represent CET results, dashed lines denote iEoM results. The iEoM band edges ω_{min} are indicated by vertical dashed lines [46].

the spectrum broadens from T_0 to the complete t–J model, i.e. H_{eff}, by about 13 %. For the parameter set $\mathcal{B}$, the broadening of the spectrum is near to 25 %. Instead of peaks at the boundaries of the spectral density as in the one-dimensional case one can observe clear knee-like flanks for the square lattice.

6.2.5 Summary

In this section, we studied the dynamics of a single hole in a disordered spin background. For this purpose, we resorted to the full t–J model as it results for the Mott insulating phase of the FHM by an expansion in the small parameter x, cf. equation (6.1), to second order. We systematically extended the NN hopping T_0 by means of spin-dependent and spin-independent NNN and 3NN hopping to all charge degrees of freedom of the t–J model. In a next step, we also included the spin-spin exchange interaction which is given by $\mathbf{S}_i\mathbf{S}_j$. For the one-dimensional chain and the two-dimensional square lattice we computed the lower band edges of the Hubbard bands and the shape of the local spectral density $A(\omega)$ by means of both CET and iEoM.

We found qualitatively different behaviours of $A(\omega)$ depending on the dimension. A thorough comparison with findings of previous studies made these results appear plausible. Moreover, the iEoM indications of an infinitely large support of the spectral density may represent a new finding. This effect has not yet been observed or discussed in the literature to our knowledge. In contrast, a previous analysis of the FHM based on the Bethe ansatz found finite band edges for the hole motion in a disordered spin background [66]. It is unclear whether this difference results from the study of the two different, though related models, i.e. FHM and t–J model, or from differences in the treatment of the magnetic dynamics. This issue surely merits further investigation.

What is more, the substantially higher numerical demand in two dimensions calls for even more efforts to corroborate the advocated scenario further. Analogous studies for other lattices in two dimensions and also in three dimensions to study the influence of lattice topology are conceivable and desirable.

6.3 Spin dynamics

While we dealt with the dynamics of both charge and spin degrees of freedom in section 6.2, we switch off all charge degrees of freedom in the following. In particular, this means that only systems with stationary spins are considered in which exactly one spin $S = 1/2$ particle resides on each lattice site. An illustration of this model can be found in figure 2.5. The corresponding spins interact with each other via the exchange interaction given by equation (2.22). In contrast to the common approach in literature, however, we do not restrict the exchange to NN interactions only, but successively extend the analysis to systems with as many interaction partners as possible.

6.3.1 Dense spin ensembles

The storage of binary information is a common practice nowadays. The characterisation of a system as *binary* means that the information it contains can be clearly assigned to one of two states. Since the mid-1990s, there have been theoretical debates on the algorithmic advantages [225] of storing information in quantum mechanical bits, so-called qubits. These provide the ability to superpose different kinds of information and, thus, are not limited to two distinct states only. At about the same time, one of the first abstract realisation of such qubits via electron spins in quantum dots was proposed in Ref. [226]. Today, there is a multitude of further ideas on how information can be stored in quantum mechanical systems, cf. especially the review in Ref. [212] for an overview. Common to all systems is that they must fulfil a number of prerequisites, first proposed by DiVincenzo [227], for practical usability. In cases where electrons and holes are involved in the storage, the models are roughly divided into two different classes, those with a low connectivity between the constituents and those with a high connectivity.

An archetypal example of the first class, i.e. systems with a low connectivity, is a quantum dot. Here, the spin of an excess electron acts as the information carrier. Decoherence effects arise through the coupling of the electron spin to nuclear spins of the surrounding lattice by means of hyperfine interaction [228, 229]. Such hyperfine interactions are nearly three orders of magnitude larger than the mutual interaction of the nuclear spins with each other [230]. Therefore, all nuclear spins can be regarded as weakly coupled to other spins of the lattice and, thus, are of low connectivity. As a consequence, the interaction of the nuclear spins with each other is often negligible. One theoretical model used to describe this situation is Gaudin's central spin model [231, 232], in which a central spin $\mathbf{S}_0$ is coupled to N bath spins $\mathbf{S}_k$ according to

$$H_{\mathrm{CSM}} = \mathbf{S}_0 \sum_{k=1}^{N} J_k \mathbf{S}_k. \tag{6.52}$$

By now, there are many studies on decoherence in the system described by equation (6.52), e.g. by resorting to correlation functions to probe information conservation. Insights into correlations are of high practical relevance, for example in the context of spin noise spectroscopy [233], and have been obtained by various semi-classical [234, 235] and quantum mechanical approaches [236]. Furthermore, conclusions have been drawn about persistent correlations [237–239], the effect of anisotropies in the model [108] or the influence of nuclear electric quadrupole moments on the long-time dynamics and coherence of the central spin [240, 241].

Recently, a second class of models has received increasing attention, namely systems with a high level of connectivity. Due to the mutual interaction between all of their constituents, these systems no longer permit the use of the same kind of star-shaped topology as in the central spin model (6.52). Instead, all particles interact with all other particles on roughly the same order of magnitude and the system may be thought of as a dense ensemble. In many cases, quantum systems near surfaces exhibit such kind of physical behaviour. A prominent example in which a dense spin ensemble near the surface plays an integral role is the one of single NV centres in diamonds. Here, the NV centres themselves are considered as promising candidates for solid-state qubits [242]. For quite some time, NV centres have been used experimentally in the field of quantum sensing [31], especially for high-precision magnetometry [243] or magnetic resonance microscopy [32]. In this context, one obstacle became apparent early on, which conflicts fundamentally with any practical application: The NV centre has to be close to the surface of the system for an improved sensitivity. The surface itself, however, is a major source of decoherence for the NV centre. A variety of attempts have been made to reduce the surface-generated decoherence of the NV centre, e.g. using a direct physical manipulation of the surface as part of surface-engineering [244], quantum control of the NV centre by dynamical decoupling [245] or coherent driving of the bath spins [246]. Moreover, experimental results suggest that unpaired spins near the surface are one of the primary reasons for this decoherence and that the theoretical description of the phenomenon might be feasible by means of a bath of many identical spins [33].

In the following sections, we use the Heisenberg model with high coordination numbers as an exemplary model for the treatment of these dense spin baths in order to contribute to a detailed understanding and a simplified methodological description of surface dynamics. Being able to easily describe the effects of surfaces is highly desirable for further practical applications of NV centres and an enhancement of their coherence.

6.3.2 Obtaining autocorrelation functions

A key quantity for measuring the coherence in a given spin $S = 1/2$ system is the autocorrelation function. It is formally defined by the expectation value

$$g^{\alpha\beta}(t) = \left\langle S_0^\alpha(0) S_0^\beta(t) \right\rangle . \tag{6.53}$$

Vividly speaking, the function (6.53) characterises to what extent the orientation of the spin component S_0^β at time $t > 0$ differs from the initial orientation S_0^α at time $t = 0$.

Since we turn to the Heisenberg model (2.22) below we can exploit its symmetries. Basically, the model consists of the scalar product $\mathbf{S}_i\mathbf{S}_j$ of two spin operators. Hence, it is invariant under any rotation as well as invariant under time reversal, i.e. the transformation $t \to -t$. Consequently, only the three autocorrelation functions

$$g^{xx}(t) = g^{yy}(t) = g^{zz}(t) \tag{6.54}$$

do not vanish [201]. Without limiting the generality, we choose $\alpha = \beta = z$ henceforth. The orientation of a spin can be used as a persistent information storage, e.g. as a system to realise a qubit [212]. Then, the information would be completely preserved if the autocorrelation function equaled its initial value given by

$$g^{zz}(t=0) = \frac{1}{4} \tag{6.55}$$

for all times $t > 0$. Analogous to section 6.2.2, the expectation value (6.53) is to be understood as the high-temperature limit of the canonical ensemble. In particular, the density matrix of the system is given by equation (6.28). As before, we approximate the occurring trace by means of (4.15) and rewrite the autocorrelation function as

$$g^{zz}(t) \approx \frac{1}{R}\sum_{r=1}^{R} \langle r|S_0^z(0)S_0^z(t)|r\rangle \tag{6.56a}$$

$$= \frac{1}{R}\sum_{r=1}^{R} \langle r|S_0^z e^{iHt} S_0^z e^{-iHt}|r\rangle\,. \tag{6.56b}$$

Here, each randomly drawn state $|r\rangle$ has the dimension $d = 2^N$. Furthermore, each basis state $|i\rangle$ of the Hilbert space has to carry information about the spin orientation at each lattice site by means of the binary pattern

$$|i\rangle = |i_{N-1}\dots i_0\rangle \tag{6.57}$$

with $i_j \in \{0,1\}$. This basis choice is similar to the one of the t–J model, cf. equation (6.23), except for the fact that we do not need to keep track of the position of a hole. According to section 4.1.2, it is sufficient to choose a small number of $R \ll d$ randomly drawn states when calculating the approximated autocorrelation function (6.56).

For computational simplicity, we do not work with the spin operator representation given in equation (2.22) but use the Hamiltonian provided in equation (2.28) for $c = -1/2$. As it was already the case for the t–J model with $J \neq 0$, cf. equation (6.29), two different states have to be evolved in time by means of a CET in order to obtain equation (6.56). These two states read

$$\langle\psi_S(t)| = \langle r|\, S_0^z e^{iHt} \tag{6.58a}$$

$$|\psi(t)\rangle = e^{-iHt}\,|r\rangle\,. \tag{6.58b}$$

The reason for this lies in the fact that, on the one hand, a time-evolution of the random state $|r\rangle$ is necessary and, on the other hand, a time-evolution of the state $\langle r|\, S_0^z$ is required, i.e. after an application of the spin operator S_0^z. A possible misconception is that the application of the operator S_0^z does not change a state in the chosen basis. Nevertheless, this is only the case for the corresponding eigenstates (6.57). For general states $|r\rangle$ of the form (4.16), an application of S_0^z to the state changes the associated coefficients ξ_{ri}. In this process, the operator S_0^z measures the least significant bit i_0 of the basis state $|i\rangle$ associated with ξ_{ri} and modifies the coefficients according to

$$\xi_{ri} \to \frac{1}{2}\begin{cases} +\xi_{ri} & \text{if } i_0 = 0 \\ -\xi_{ri} & \text{otherwise.} \end{cases} \tag{6.59}$$

As before, we stick to the convention established in the context of section 6.2.2 for the identification of physical spin orientations by bits, i.e. we use $\uparrow \equiv 0$ as well as $\downarrow \equiv 1$.

Eventually, the autocorrelation can be obtained from all R pairs of states (6.58) by

$$g^{zz}(t) = \frac{1}{R}\sum_{r=1}^{R} \langle \psi_S(t)|S_0^z|\psi(t)\rangle\,. \tag{6.60}$$

Due to the initial value of the autocorrelation function given by equation (6.55), we choose to plot the quantity $4g^{zz}(t)$ in the following section for easier readability.

6.3.3 Results

The aim of this section is to improve the understanding of decoherence in dense spin systems. Especially in physically realistic systems, where each spin has a high average number of identical or similar interaction partners, numerically exact methods such as the CET are severely limited by the large connectivity and size of the relevant Hilbert spaces. In contrast, approximate methods are often able to provide predictions significantly easier because irrelevant aspects of the full quantum mechanical dynamics are heavily simplified. A typical phenomenon in physics is the remarkable property of single constituents and their individual dynamics to become less important as the number of interacting partners increases. In such situations, mean-field approaches are justified and useful alternatives to the computation of the exact system dynamics.

The mean-field theory for dense spin ensembles, which we will denote by spinDMFT in the following, was proposed by Timo Gräßer and Götz S. Uhrig, cf. especially Ref. [201], and incorporates this fundamental idea. Essentially, the quantum mechanical environment of each individual spin is replaced by a classical, dynamical random field. The classical moments of this field are self-consistently linked to the quantum mechanical moments. Furthermore, since the correlation of two spins is suppressed with the coordination number $z \to \infty$, the mean-field is Gaussian according to the central limit theorem. Due to the fact that a Gaussian distribution is characterised by only two moments, the underlying self-consistency problem is also restricted to just two moments and the use of the spinDMFT is a particularly efficient alternative to numerically exact approaches.

Nevertheless, approximate methods such as the spinDMFT have to prove their validity and correctness in comparison with exact methods such as a CET or an ED. In the following, we use particularly the more efficient CET approach for this comparison. To do so, we proceed in three steps. First, we compare our CET results to the reference results of an ED [247] for one-dimensional PBC chains. On the one hand, this helps us to gain insight into the spin dynamics for a system of comparably small coordination number $z = 2$ and, on the other hand, it enables us to verify the validity of the CET implementation. In the second step, we increase the coordination number to $z = 4$ and consider two-dimensional PBC lattices. In the last step, we extend the CET consideration to infinite-range clusters G_c, cf. especially figure 5.6 for an example. These clusters represent finite systems with maximum possible connectivity because every site is connected to every other site. By using these clusters, a study of the $N \to \infty$ and, thus, also the $z \to \infty$ limit is possible. It is instructive to note that the results of this extrapolation are comparable to the physical situation described by the spinDMFT.

For comparative reasons, we additionally present results of an iEoM approach alongside the spinDMFT results. While both methods are approximate by design and consider the thermodynamic limit, the coordination number z has a significant impact on the performance in the case of the iEoM method. For this reason, the number of processes considered, i.e. the loop order m, is limited for the iEoM as the dimension and connectivity of the system increases. Especially, the dynamics in infinite-range clusters G_c is difficult to realise by means of the iEoM approach. Hence, only iEoM results that have been derived for one- and two-dimensional systems can be contrasted to the CET results.

In agreement with our work in Ref. [201], we choose the global energy unit $\mathcal{J}$ for all following measurements. As a result, the times t can be measured in units of $[t] = \mathcal{J}^{-1}$. For the one- and two-dimensional system (2.22) this energy unit is defined by using

$$\mathcal{J} = \sqrt{z} \cdot \widetilde{J} \tag{6.61}$$

where z denotes the coordination number of the system, e.g. $z = 2$ in one dimension.

In infinite-range clusters G_c, as specified by equation (5.36), we have to proceed slightly differently because these kinds of systems typically have a high degree of symmetry, cf. the in-depth explanations concerning complete graphs in section 5.3.1. These symmetries lead to a severe limitation of the dynamics. As a result, the highly symmetric models are not easily comparable to physically realistic $z \to \infty$ scenarios. To obtain a more generic setting we opt for a randomised approach. Therefore, we choose many different couplings J_{ij} instead of one coupling $\widetilde{J}$ only and draw these couplings from a Gaussian probability distribution. Then, the couplings are normalised, i.e. multiplied by a suitable constant λ_j, in a way that the relation

$$\mathcal{J}^2 = \sum_i J_{ij}^2 \tag{6.62}$$

holds for all sites j. In order to avoid any further unwanted accidental symmetries, we choose 100 sets of random couplings for each cluster size N. Eventually, the corresponding results are averaged to yield a representative generic system.

Results for the one-dimensional system are displayed in figure 6.5. We find that the results of our CET are identical to the reference results of an ED [247] within the error

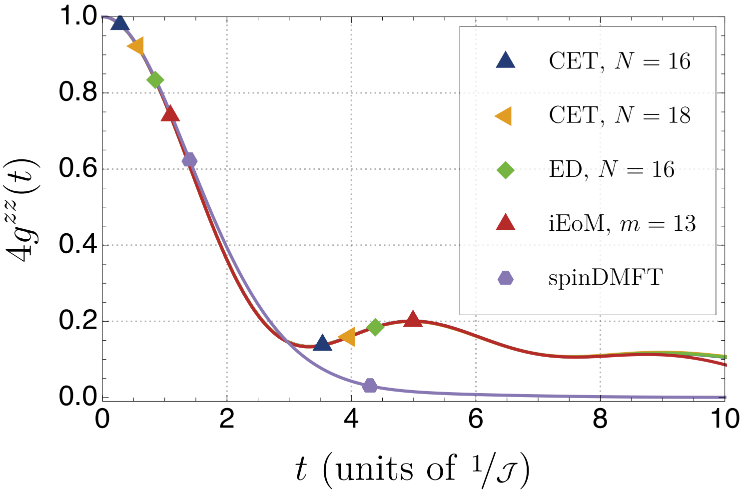

Figure 6.5: Autocorrelation (6.60) of the isotropic Heisenberg model (2.22) on a one-dimensional chain. Both ED [247] and CET results use PBC and finite lattice sizes N. The iEoM approach deals with the thermodynamic limit and physical processes up to m loops. The spinDMFT considers highly dense systems, i.e. systems of large coordination numbers $z \to \infty$. A correlation decrease is visible for denser systems (spinDMFT). Figure adapted and reprinted from Ref. [201].

tolerance $\epsilon = 10^{-3}$ assumed for the CET, cf. equation (3.56). Furthermore, the CET results for the lattice sizes $N = 16$ and $N = 18$ are identical. Clearly, this indicates that finite-size effects do not play a role for the considered time periods $t < 10/\mathcal{J}$. A comparison with the iEoM approach for $m = 13$ loops reveals a high agreement of the initial dynamics up to about $t \approx 9/\mathcal{J}$. After this time, a slight deviation of the iEoM results from the CET and ED simulations can be identified. Since the accuracy of an iEoM calculation is directly dependent on the loop order m, a higher order m should necessarily be chosen for longer observation periods. While the results of CET, ED and iEoM are practically identical, the spinDMFT simulation shows a considerable deviation. Solely the initial dynamics, i.e. the fast decrease of the autocorrelation up to about $t \approx 3/\mathcal{J}$, is approximately captured by the spinDMFT for the one-dimensional system. We emphasise that the one-dimensional system being used is a highly difficult case for the spinDMFT. While the spinDMFT makes assumptions that are justified in the limit $z \to \infty$, the system under consideration here actually has a coordination number which equals $z = 2$ only. The difference concerning the dynamics is evident: The spinDMFT predicts a fast and almost complete decoherence of the system whereas the actual results of the other methods suggest that the decoherence takes place substantially slower. Moreover, the actual results show weak revivals of coherence around $t \approx 5/\mathcal{J}$ and $t \approx 9/\mathcal{J}$. These results are in no way surprising, considering that the one-dimensional system is integrable, cf. section 2.1.1 as well as Ref. [14]. Given that in integrable systems there is only a strongly restricted Hilbert space available for the dynamics, no self-averaging as strong as predicted by the spinDMFT for $z \to \infty$ can occur.

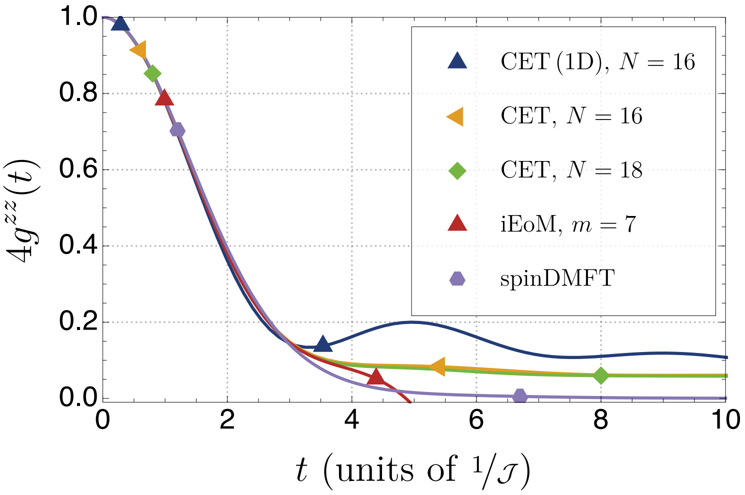

Figure 6.6: Autocorrelation (6.60) of the isotropic Heisenberg model (2.22) on a two-dimensional square lattice. The one-dimensional result (1D) is provided as a reference. See caption of figure 6.5 for further details on the notation. For increasing dimension and, thus, coordination number z the results are consistent with the spinDMFT prediction. Figure adapted and reprinted from Ref. [201].

In the following second step, we expand the dimension of the system under consideration and, thus, also the coordination number z. In the case of the two-dimensional system with exactly four NNs around each lattice site, the coordination number is $z = 4$ and, as a consequence, already twice as large as for the one-dimensional case. The results of the two-dimensional system are presented in figure 6.6. As a visual orientation and to allow for a simplified comparison with systems of lower coordination numbers, we additionally include the CET results for the one-dimensional PBC chain, cf. figure 6.5. We denote these results by the addition (1D) in the legend of figure 6.6.

Focusing on the CET simulations only, it is noteworthy that the results for the two-dimensional lattices of sizes $N = 16$ and $N = 18$ are almost identical and that no relevant finite-size effects seem to occur. Furthermore, in comparison with the one-dimensional results, it turns out that a significantly faster decoherence occurs in the system with higher connectivity. While the one-dimensional system shows a higher average autocorrelation as well as recurrent revivals of coherence, the two-dimensional system shows a strictly monotonically decreasing autocorrelation. The resulting average autocorrelation is significantly lower than in the one-dimensional case.

Interestingly, the agreement of the two-dimensional system with the spinDMFT prediction is significantly improved compared to the one-dimensional case. The explanation for this phenomenon is analogous to the observations in the context of equilibration and thermalisation for the full FHM in section 5.3: The more interaction partners exist for a given particle, the faster the propagation of information across a cluster or lattice can occur. The convergence of the results of systems with increasing finite coordination numbers, i.e. systems with $z = 2$ and $z = 4$, to the ones of a system with maximum density and connectivity, as considered by spinDMFT for $z \to \infty$, supports this hypothesis. Therefore, already for the physically realistic case of two dimensions, the spinDMFT is able to make fairly reliable predictions in an efficient way within bounded error tolerances.

The iEoM results for $m = 7$ loops display a good agreement with the CET results up to about $t \approx 3.5/\mathcal{J}$. From this point onwards, the low loop order becomes noticeable. Vividly speaking, this results from the fact that processes become important for the dynamics which do not take place in the considered iEoM operator subspace. Accordingly, for an improved representation of the dynamics, significantly larger iEoM loop orders would be necessary. This, in turn, would lead to a much higher computational effort.

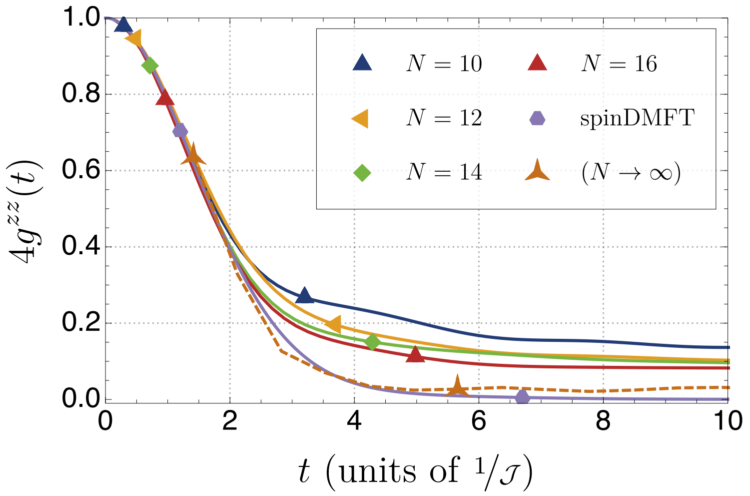

Figure 6.7: Autocorrelation (6.60) of the isotropic Heisenberg model (2.22) on infinite-range clusters G_c as depicted in figure 5.6 (CET). These clusters are a possible systematic approximation of the $z \to \infty$ limiting case (spinDMFT). An $N \to \infty$ extrapolation of the CET results agrees well with the results of the spinDMFT. Figure adapted and reprinted from Ref. [201].

In the last step, we turn to complete graphs G_c, i.e. systems that have the maximum possible connectivity for a given number of sites N. This situation is very similar to the scenario considered by the spinDMFT. We present the corresponding results in figure 6.7. Note that each curve belonging to a finite lattice size N actually represents the average of 100 different randomly generated infinite-range graphs G_c. Each occurring cluster G_c has interaction elements J_{ij} that have been drawn from a standard normal distribution. To ensure that clusters of different sizes N have the same mean energy, each adjacency matrix of such a cluster is normalised according to equation (6.62). The resulting slightly different couplings J_{ij} of the many neighbouring spins can be regarded as a realistic representation of many different distances between spins in the total ensemble.

Evidently, the decoherence increases with increasing lattice size N. This finding is in agreement with the observations for the one- and two-dimensional systems, cf. figures 6.5 and 6.6. As a result, our main objective is to systematically determine the thermodynamic limit $N \to \infty$. In view of the energy scale (6.62) and the associated scaling

$$J_{ij} \propto \frac{1}{\sqrt{N}}, \tag{6.63}$$

it is reasonable to use power law extrapolations for each data point at a fixed time t by

$$4g^{zz}(x) = ax^{p/2} + b \tag{6.64}$$

with $x = {}^{1}\!/_{N}$ and the two fit parameters $a, b \in \mathbb{R}$ to extrapolate the data for finite clusters by means of $x \to 0$. In our analysis of different extrapolations with various values of $p \in \mathbb{N}$ (not shown here), the most robust choice turned out to be $p = 3$. Accordingly, we use this scaling behaviour in the subsequent extrapolation. The corresponding extrapolated data points are denoted by $N \to \infty$ in figure 6.7. The high agreement of the extrapolated data with the spinDMFT predictions is a strong indication for the correct description of the dynamics of dense systems by the spinDMFT. Since systems with increasing connectivity lead to significantly denser Hamiltonians, the effort for a CET calculation increases accordingly. Therefore, infinite-range graphs G_c with even higher lattice sizes are notoriously difficult to realise, but could be used in the future to substantiate the agreement of the extrapolated CET data and the results obtained by means of the spinDMFT approach even further.

6.3.4 Summary

In section 6.3, we reviewed the local autocorrelation function (6.60) of dense spin systems as a measure of the occurrence of decoherence and information loss, respectively. Being able to predict the decoherence of a system is a central ingredient for the effective storage of quantum information or to enable improved forms of quantum sensing, e.g. by means of NV centres. As an archetypal model for a dense spin system, the Heisenberg model on topologies with increasing coordination numbers z was considered. In contrast to the typical approach in literature with the treatment of comparatively low coordination numbers, we studied the strict limit $z \to \infty$ to describe systems of high connectivity. We found clear indications that the one-dimensional model plays a special role due to its integrability and that the decoherence increases with increasing coordination number. A systematic extrapolation of the numerically exact CET results by a power law fit showed a good agreement with the predictions of the spinDMFT, i.e. a dynamical mean-field theory for spin systems in the limit $z \to \infty$. Consequently, we substantiated that highly efficient approximations via classical random fields are a viable alternative to full-fledged quantum mechanical approaches as the number of interacting partners increases.

This finding potentially facilitates the future study of much larger and physically relevant systems, e.g. in the context of nuclear magnetic resonance, diamonds with NV centres or spin diffusion in solids, with a reasonable amount of computational effort.

7 Dynamics in the single impurity Anderson model

Henceforth, our main goal is the theoretical description of a technique to obtain the one-particle Green's function of a system by means of the iEoM approach. We exemplify this approach using the Green's function of the impurity electrons of the SIAM, i.e. of those particles which are located at the central site. For this purpose, we resort to the respective retarded Green's function. Formally, it is defined by

$$G^{\text{ret}}_{f_\sigma f_\sigma^\dagger}(t) = -i \left\langle \left\{ f_\sigma(t), f_\sigma^\dagger \right\} \right\rangle \theta(t). \tag{7.1}$$

Simplified, equation (7.1) describes the dynamics of an impurity electron that is added to the system at time $t = 0$ and removed at time $t > 0$. In order to calculate this expression, we will resort to the iEoM framework presented in section 3.4 and adapt it accordingly. In section 7.1, we outline the general steps involved in calculating arbitrary Green's functions with the aid of the iEoM, in section 7.2, we motivate the methodology using the SIAM as an example. We conclude the chapter with a theoretical description of a potential algorithmic implementation of the concepts presented here in section 7.3.

7.1 Green's functions in the iEoM framework

Throughout the associated analysis of (7.1), we will discover that we do not only need to calculate the Green's function (7.1) that we are actually looking for, but that we may also need other Green's functions as auxiliary quantities. Therefore, we leave aside the concrete form (7.1) for a moment and discuss a Green's function for two entirely general observables $A^\dagger$ and B by means of

$$G^{\text{ret}}_{A^\dagger B}(t) = -i \left\langle \left\{ A^\dagger(t), B \right\} \right\rangle \theta(t). \tag{7.2}$$

In order to avoid any confusion between the iEoM operator basis, cf. equation (3.61), and the actual operator $A^\dagger$, we denote all operators of the operator basis by means of x_i in the following. Consequently, the corresponding column vector $\mathbf{x}$ is given by

$$\mathbf{x}^T := \begin{pmatrix} x_1, & x_2, & x_3, & \dots, & x_m \end{pmatrix} \tag{7.3}$$

and may be used as a shorthand notation to refer to all m basis operators at once.

Note that the Hermitian conjugate in (7.2) is swapped compared to (7.1). This results from the fact that we will subsequently write all operators of the actual iEoM operator basis, i.e. all operators contained in (7.3), *without* Hermitian conjugation. Hereby, we proceed analogously to the notation in (3.61). Since the actual operator basis is always constructed starting from its first basis operator, e.g. $x_1 \propto f_\sigma^\dagger$, the symbolic operator B does not carry a dagger, whereas the concrete operator, say x_1, may have one.

For any given observable, we can use (7.3) to formally express the time-dependence as

$$C(t) = \mathbf{x}^T \mathbf{h}(t). \tag{7.4}$$

Given that only the vector $\mathbf{h}(t)$ is time-dependent, we need to determine its time-dependence first. Its dynamics is governed by (3.64) and the formal solution reads

$$\mathbf{h}(t) = e^{iMt}\mathbf{h}(0). \tag{7.5}$$

In a next step, we insert equation (7.5) into (7.4) which leads us to the general time-dependence of an observable and its Hermitian conjugate given by

$$C(t) = \mathbf{x}^T e^{iMt}\mathbf{e}_c \tag{7.6a}$$

$$C^\dagger(t) = \mathbf{e}_c^T e^{-iMt}\mathbf{x}^\dagger. \tag{7.6b}$$

Here, the column vector $\mathbf{x}^\dagger$ consists of all Hermitian conjugates and is defined using

$$\mathbf{x}^\dagger := \left(x_1^\dagger, \quad x_2^\dagger, \quad x_3^\dagger, \quad \ldots, \quad x_m^\dagger\right)^T. \tag{7.7}$$

Moreover, we used an abbreviation in equation (7.6) to denote the initial conditions of the system. Since the Heisenberg operator $C(t)$ equals the Schrödinger operator C at the time $t = 0$ we can use the unit vector into the corresponding direction as initial condition

$$\mathbf{h}(0) = \mathbf{e}_c. \tag{7.8}$$

Thus, the vector $\mathbf{e}_c$ carries zeros everywhere except for the entry at the index of the basis operator C. Then, the retarded Green's function in the time domain can be determined by inserting equation (7.6) into (7.2). Eventually, this results in

$$G^{\text{ret}}_{A^\dagger B}(t) = -i\mathbf{e}_A^T e^{-iMt}\left\langle\left\{\mathbf{x}^\dagger, B\right\}\right\rangle. \tag{7.9}$$

Far more often than in the time-dependent Green's function (7.9), however, one is interested in the frequency-dependent Green's function. We take this into account and Fourier transform (7.9) accordingly. Finally, this leads to

$$G^{\text{ret}}_{A^\dagger B}(\omega) = -i\int_0^\infty \mathbf{e}_A^T e^{-i(M-\omega-i0^+)t}\left\langle\left\{\mathbf{x}^\dagger, B\right\}\right\rangle \mathrm{d}t \tag{7.10a}$$

$$= \mathbf{e}_A^T R\left\langle\left\{\mathbf{x}^\dagger, B\right\}\right\rangle. \tag{7.10b}$$

Note that we introduced a mathematically necessary convergence generating summand here with the substitution $\omega \to \omega + i0^+$. This summand represents an analytic continuation of the retarded Green's function on the upper half-plane of the complex numbers $\mathbb{C}$ and is a shorthand for the limit

$$\omega + i0^+ := \lim_{\delta\to 0^+} \omega + i\delta. \tag{7.11}$$

To avoid a potentially cumbersome notation in the following, from now on we exclusively refer to ω, but implicitly always mean a frequency with an additional infinitesimally small but finite positive imaginary part δ in the context of a Green's function.

The matrix R that occurs in (7.10b) is called the resolvent of the system and reads

$$R := \frac{1}{\omega - M}. \tag{7.12}$$

In addition, a vector of expectation values appears both in (7.9) and (7.10). For this, the operator B is anticommuted with the entire Hermitian conjugate of the basis, i.e. $\mathbf{x}^\dagger$. Henceforth, we will refer to this vector by means of the abbreviation

$$\mathbf{p}_B := \left\langle \left\{ \mathbf{x}^\dagger, B \right\} \right\rangle. \tag{7.13}$$

Depending on the size and design of the operator basis, the occurrence of the vector given in equation (7.13) may lead to a self-consistency problem. What is the cause of this? In fact, expectation values and Green's functions are always related. For in-depth details, we refer in particular to Ref. [248]. For the sake of brevity, we recapitulate the most important relations without further derivation in the following.

For each Green's function there is a spectral density $\overline{A}_{A^\dagger B}\left(\omega\right)$. In the case of the retarded one, it is directly proportional to the corresponding imaginary part and given by

$$\overline{A}_{A^\dagger B}\left(\omega\right) = -\frac{1}{\pi} \operatorname{Im}\left[G^{\text{ret}}_{A^\dagger B}(\omega)\right]. \tag{7.14}$$

The inverse route is also feasible. For instance, the retarded Green's function reads

$$G^{\text{ret}}_{A^\dagger B}(\omega) = \int_{\mathbb{R}} \frac{\overline{A}_{A^\dagger B}\left(x\right)}{\omega - x}\, \mathrm{d}x \tag{7.15}$$

in terms of the spectral density. Thus, according to (7.14) and (7.15), the calculation of the Green's function and its spectral density are equivalent. Furthermore, it can be shown that any expectation value of any interacting system can be derived directly from the spectral density and the associated distribution, i.e. the Fermi-Dirac distribution in the case of the SIAM. The respective relation [248] reads

$$\left\langle BA^\dagger \right\rangle = \int_{\mathbb{R}} \frac{\overline{A}_{A^\dagger B}\left(\omega\right)}{\exp\left(\beta\omega\right) + 1}\, \mathrm{d}\omega\,. \tag{7.16}$$

Given this advantage as well as the fact that typically the spectral density allows for a more intuitive access to the underlying physics, we will focus exclusively on the calculation of the spectral density in the following sections.

A minor downside of this approach is that each expectation value depends on the spectral density according to equation (7.16), which in turn depends on the Green's function according to equation (7.14). The Green's function, however, requires all of the expectation values comprised in (7.13) due to (7.10b). The resulting self-consistency problem can therefore only be solved iteratively in the great majority of cases. Typically, more than only one expectation value is needed in the process. For an expectation value vector $\langle \mathbf{s} \rangle$ to be determined one starts from sensibly chosen initial values $\langle \mathbf{s} \rangle^{(0)}$ and alternately calculates the associated set of spectral densities $A_k^{(i)}$ and the resulting expectation values $\langle \mathbf{s} \rangle^{(i+1)}$. We denote this process by means of the iterative scheme

$$\langle \mathbf{s} \rangle^{(0)} \to A_k^{(1)} \to \langle \mathbf{s} \rangle^{(1)} \to \ldots \to \langle \mathbf{s} \rangle^{(f)} . \tag{7.17}$$

The terminating condition after the f-th step is fulfilled if the deviation of the last two iterative steps is below a chosen error tolerance ϵ. For this purpose, one can choose any metrics. For instance, one may opt for the Euclidean norm leading to

$$\left\| \langle \mathbf{s} \rangle^{(f)} - \langle \mathbf{s} \rangle^{(f-1)} \right\|_2 < \epsilon. \tag{7.18}$$

7.2 Application to the SIAM

Following the advocated approach of section 7.1, we now turn to the actual goal, the theoretical description of the single-particle Green's function and the corresponding spectral density of the impurity electrons, respectively. The necessary steps consist of the construction of a problem-adapted, orthonormal operator basis, the determination of the resolvent of the system as well as the identification of all necessary expectation value vectors $\mathbf{p}_i$ and their individual components. We carry out these three steps in the following sections 7.2.1 to 7.2.3 and propose an algorithmic implementation in section 7.3.

7.2.1 Operator basis

In order to construct a suitable operator basis, one usually starts from equation (3.60). One begins with the operator one is interested in and commutates it and all contributions arising in the course of the repeated commutations repetitively with the complete Hamiltonian of the system. In our case this is the Hamiltonian described by (2.33). Since we are interested in the single-particle Green's function (7.1), it suggests itself to choose $f_\sigma^\dagger$ as the starting operator for the iteration.

Nevertheless, the standard approach of repeated commutations of the basis with H_{SIAM} is tedious and error-prone. Instead, we propose a different, more intuitive approach. Therefore, we illustrate the effect that a commutation of a given operator with certain contributions of the Hamiltonian can have. In this context, it is noteworthy that only the contributions H_{Imp} and H_{Hyb} possess parts that are not diagonal in the given basis. They either punish DOs at the impurity site by an additional energy U or favour a hopping between the impurity site and the bath sites which is proportional to the transition amplitude V_k. The actual effect of a commutation with these two contributions can be depicted illustratively by two elementary processes. It can be noticed that

(1) $U\widehat{n}_\uparrow\widehat{n}_\downarrow$ extends the operator basis by means of $f_\sigma^\dagger \to f_\sigma^\dagger\widehat{n}_{\overline{\sigma}}$ and $f_\sigma \to -f_\sigma\widehat{n}_{\overline{\sigma}}$,

(2) H_{Hyb} exchanges one impurity and one bath electron via $f_\sigma^{(\dagger)} \leftrightarrow c_\sigma^{(\dagger)}$.

All other parts of the Hamiltonian do not have any relevant influence on the design of an operator basis and will therefore not be considered below. Starting from the first operator of the basis, the creation operator $f^\dagger_\sigma$ at the site of the impurity electron, we iteratively apply the above two processes. Given that the two elementary processes specify the action of the Hamiltonian on *one* operator in a potentially larger product, it is mandatory in such cases to apply the product rule to each of the operators.

As an example for the suggested approach, we carry out the basis creation explicitly in the following. The first commutation is decomposed into both processes and yields

$$f^\dagger_\sigma \xrightarrow{(1)} f^\dagger_\sigma f^\dagger_{\overline{\sigma}} f_{\overline{\sigma}} \tag{7.19a}$$

$$f^\dagger_\sigma \xrightarrow{(2)} c^\dagger_{k\sigma}. \tag{7.19b}$$

Note that the prefactors that may arise during a commutation, i.e. in the context of an application of the processes (1) and (2) in (7.19), are ignored in this representation entirely because they are of no further relevance to the actual basis operators.

In a second commutation, we only need to consider the operator derived in (7.19a) since the operator $c^\dagger_{k\sigma}$ is closed under repeated application of the two elementary processes. Even for the operator (7.19a), merely the process (2) has a non-vanishing effect with respect to newly created basis operators. All resulting new operators read

$$f^\dagger_\sigma f^\dagger_{\overline{\sigma}} f_{\overline{\sigma}} \xrightarrow{(2)} c^\dagger_{k\sigma} \widehat{n}_{\overline{\sigma}} \tag{7.20a}$$

$$\xrightarrow{(2)} f^\dagger_\sigma c^\dagger_{k\overline{\sigma}} f_{\overline{\sigma}} \tag{7.20b}$$

$$\xrightarrow{(2)} f^\dagger_\sigma f^\dagger_{\overline{\sigma}} c_{k\overline{\sigma}}. \tag{7.20c}$$

The operators created as part of (7.20) are closed under repeated application of the process (1) and only the process (2) needs to be executed. For the sake of brevity, we refrain from carrying out all further commutations at this point. Completely analogous to the previous steps (7.19) and (7.20), one more step is performed. Hence, we construct the resulting basis of order $\mathcal{O}(V^3)$ in such a way that it is closed under repeated applications of process (1). In other words, the resulting basis is exact in U excluding $\mathcal{O}(V^3)$ terms.

In fact, however, we are not yet finished by performing the mere commutation. In accordance with (3.66) we orthonormalise all the basis operators with respect to the Frobenius scalar product. The resulting twelve families of basis operators are stated below. At the level of (7.19) and (7.20), i.e. up to the order $\mathcal{O}(V^2)$, we obtain the following six families

$$W_1 = \sqrt{2} f^\dagger_\sigma \tag{7.21a}$$

$$W_2 = \left(\sqrt{2}\right)^3 f^\dagger_\sigma \left(\widehat{n}_{\overline{\sigma}} - \frac{1}{2}\right) \tag{7.21b}$$

$$W_3(k) = \sqrt{2} c^\dagger_{k\sigma} \tag{7.21c}$$

$$W_4(k) = \left(\sqrt{2}\right)^3 c^\dagger_{k\sigma} \left(\widehat{n}_{\overline{\sigma}} - \frac{1}{2}\right) \tag{7.21d}$$

$$W_5(k) = \left(\sqrt{2}\right)^3 f^\dagger_\sigma c^\dagger_{k\overline{\sigma}} f_{\overline{\sigma}} \tag{7.21e}$$

$$W_6(k) = \left(\sqrt{2}\right)^3 f^\dagger_\sigma f^\dagger_{\overline{\sigma}} c_{k\overline{\sigma}}. \tag{7.21f}$$

Another commutation of the basis (7.21) yields six more families. Note that these new families now possess an increased local support. While at most one bath operator has occurred in (7.21) so far, the following families include effects on up to two bath sites

$$W_7(k,l) = \left(\sqrt{2}\right)^3 c^\dagger_{k\sigma} c^\dagger_{l\overline{\sigma}} f_{\overline{\sigma}} \tag{7.22a}$$

$$W_8(k,l) = \left(\sqrt{2}\right)^3 c^\dagger_{k\sigma} f^\dagger_{\overline{\sigma}} c_{l\overline{\sigma}} \tag{7.22b}$$

$$W_9(k,l) = \left(\sqrt{2}\right)^3 f^\dagger_\sigma \left(c^\dagger_{k\overline{\sigma}} c_{l\overline{\sigma}} - \frac{1}{2}\delta_{kl}\right) \tag{7.22c}$$

$$W_{10}(k,l) = \left(\sqrt{2}\right)^5 c^\dagger_{k\sigma} c^\dagger_{l\overline{\sigma}} f_{\overline{\sigma}} \left(\widehat{n}_\sigma - \frac{1}{2}\right) \tag{7.22d}$$

$$W_{11}(k,l) = \left(\sqrt{2}\right)^5 c^\dagger_{k\sigma} c_{l\overline{\sigma}} f^\dagger_{\overline{\sigma}} \left(\widehat{n}_\sigma - \frac{1}{2}\right) \tag{7.22e}$$

$$W_{12}(k,l) = \left(\sqrt{2}\right)^5 \left(c^\dagger_{k\overline{\sigma}} c_{l\overline{\sigma}} - \frac{1}{2}\delta_{kl}\right) f^\dagger_\sigma \left(\widehat{n}_{\overline{\sigma}} - \frac{1}{2}\right). \tag{7.22f}$$

Throughout the notation of (7.21) and (7.22), the functional dependence on the indices represents the up to two bath sites on which the corresponding operator has an effect. Note that the overall basis size for a bath of N sites is $6N^2 + 4N + 2 \in \mathcal{O}(N^2)$. It is instructive to contrast this basis with the one for the full FHM presented in section 5.4.3.

7.2.2 Obtaining the resolvent

The resolvent R of the system is essentially constructed by an inversion of the Liouville matrix, cf. equation (7.12). Consequently, the main task is to work out the corresponding matrix elements M_{ij} of the Liouville matrix. Due to the symmetry (3.69), only those matrix elements belonging to the upper or lower triangular matrix of M have to be determined. For the operator basis given in equations (7.21) and (7.22), there is a total of 78 potential matrix elements to be calculated. For the sake of brevity, we refrain from reproducing the extensive calculations here and only provide the actual results, which are to be presented in appendix C.1.

Nevertheless, it might be an instructive example for understanding the necessary procedure to take a closer look at the first scalar product. Prior to the calculation, it is helpful to recall a central concept: If A_1 and A_2 are bounded operators and act on separable Hilbert spaces $\mathcal{H}_1$ and $\mathcal{H}_2$ a trace in $\mathcal{H} = \mathcal{H}_1 \otimes \mathcal{H}_2$ can be split according to

$$\mathrm{Tr}\left(A_1 A_2\right) = \mathrm{Tr}_1\left(A_1\right) \mathrm{Tr}_2\left(A_2\right). \tag{7.23}$$

Here, $\mathrm{Tr}_m(.)$ denotes a trace over the partial Hilbert space $\mathcal{H}_m$. The equivalence (7.23) implies that we can always decompose a trace of a product of operators that act on different sites. We will make use of this below.

According to (3.67) the scalar product, which is to be evaluated in the following, reads

$$M_{11} = (W_1|\mathcal{L}(W_1))\,. \tag{7.24}$$

Naturally, the commutation with the Hamiltonian of the system that occurs here generates operators that may have an overlap with W_1, but do not necessarily have to possess one. Consequently, we examine the part of the dynamics of W_1 that resides in the corresponding, reduced subspace. The result of the commutation is

$$\begin{aligned} \mathcal{L}(W_1) &= [H_{\mathrm{SIAM}}, W_1] && (7.25\mathrm{a}) \\ &= \sqrt{2}\varepsilon_0 f_\sigma^\dagger + \sqrt{2}U f_\sigma^\dagger \widehat{n}_{\overline{\sigma}} + \sqrt{2}\sum_k V_k c_{k\sigma}^\dagger . && (7.25\mathrm{b}) \end{aligned}$$

In a next step, we are now going to evaluate the actual scalar product. Possible pairings are indicated by square brackets above the operators. Note that scalar products of operators that act on separate partial Hilbert spaces can be decomposed according to equation (7.23). Here, the entire scalar product is zero if at least one of its factors vanishes. Eventually, we obtain for the respective matrix element M_{11} the result

$$\begin{aligned} M_{11} &= 2\varepsilon_0\mathcal{N}\,\mathrm{Tr}\left(\overbracket{f_\sigma f_\sigma^\dagger}\right) + 2U\mathcal{N}\,\mathrm{Tr}\left(\overbracket{f_\sigma f_\sigma^\dagger}\overbracket{f_{\overline{\sigma}}^\dagger f_{\overline{\sigma}}}\right) + 2\mathcal{N}\sum_k V_k\,\mathrm{Tr}\left(f_\sigma c_{k\sigma}^\dagger\right) && (7.26\mathrm{a}) \\ &= \varepsilon_0 + \frac{U}{2} + \underbrace{2\mathcal{N}\sum_k V_k\,\mathrm{Tr}\left(f_\sigma\right)\mathrm{Tr}\left(c_{k\sigma}^\dagger\right)}_{=0} && (7.26\mathrm{b}) \\ &= \varepsilon_0 + \frac{U}{2}. && (7.26\mathrm{c}) \end{aligned}$$

Here, the shorthand $\mathcal{N}$ is used to refer to the normalisation in accordance with (3.68). Completely analogous to the above calculation, every appearing scalar product can be determined. In some cases, scalar products arise that are only different from zero under certain conditions, for example in the case of the scalar product (C.3a). Clearly, this is due to the fact that operators at different bath sites have no influence on each other.

7.2.3 Self-consistency of expectation values

According to equation (7.1) and (7.9), the first expectation value vector to be calculated is the one that couples the entire Hermitian conjugate of the operator basis $\mathbf{x}^\dagger$ to the creation operator $f_\sigma^\dagger$ of the impurity electron. For consistency, we will use operators of the basis only, i.e. we choose W_1 as the rescaled equivalent of $f_\sigma^\dagger$. This leads to the expectation value vector

$$\mathbf{p}_1 := \left\langle\left\{\mathbf{x}^\dagger, W_1\right\}\right\rangle . \tag{7.27}$$

For reasons of brevity, we provide the respective entries of this vector in appendix C.2. The next step would be the self-consistent calculation of all expectation values occurring in (7.27). In order to achieve this, it is necessary to decompose each of the expectation values according to (7.16) into a product of two operators, a basis operator B and the Hermitian conjugate of a basis operator, i.e. $A^\dagger$. The order of the operators in all expectation values in appendix C.2 is chosen such that the first elementary fermionic creation operator represents the operator B, and the subsequent operators form the operator $A^\dagger$. Using the example of the expectation value (C.15f), this means

$$\mathbf{p}_{1,10} = -8\left\langle f^\dagger_\sigma f^\dagger_{\bar\sigma} c_{l\bar\sigma} c_{k\sigma}\right\rangle \tag{7.28a}$$

$$= -2\left\langle W_1 W_7^\dagger(k,l)\right\rangle. \tag{7.28b}$$

In this case, we identify $B = W_1$ and $A^\dagger = W_7^\dagger(k,l)$. Due to (7.13) and (7.27), this expectation value consequently does not generate a new vector $\mathbf{p}$. The situation is different with regard to the expectation value (C.15e). Indeed, this expectation value imposes the self-consistent computation of a new expectation value vector by

$$\mathbf{p}_{1,9} = 4\left\langle c^\dagger_{l\sigma} c_{k\sigma}\right\rangle - 2\delta_{kl} \tag{7.29a}$$

$$= 2\left\langle W_3(l) W_3^\dagger(k)\right\rangle - 2\delta_{kl}. \tag{7.29b}$$

Again, the entries of this new vector are provided in appendix C.2. They are defined by

$$\mathbf{p}_3 := \left\langle \left\{ \mathbf{x}^\dagger, W_3(r) \right\} \right\rangle. \tag{7.30}$$

Note that, thus, nearly all expectation values can be composed of the expectation values

$$\left\langle W_1 W_1^\dagger \right\rangle, \left\langle W_3(l) W_3^\dagger(k) \right\rangle \tag{7.31}$$

as well as of the following expectation values and their Hermitian conjugates, respectively,

$$\left\langle W_1 W_3^\dagger(k)\right\rangle, \left\langle W_1 W_5^\dagger(l)\right\rangle, \left\langle W_1 W_6^\dagger(l)\right\rangle, \left\langle W_1 W_7^\dagger(k,l)\right\rangle, \left\langle W_1 W_8^\dagger(k,l)\right\rangle. \tag{7.32}$$

The only exception to this is (C.15i) due to its spin orientation, which is identical for all operators. Since no operator of the basis has exclusively the same spin orientation, no $A^\dagger$ can be chosen in this case. Thus, the calculation of the expectation value (C.15i) has to be done by means of a Wick decomposition into smaller expectation values [249, 250].

7.3 Proposals for an algorithmic implementation

From a purely theoretical perspective, the task of calculating the spectral density (7.14) has been completely solved by the procedure presented in the former section 7.2 and the results given in appendix C. We conclude this chapter with an outlook concerning a possible future practical implementation of our theoretical results. For this purpose, we use existing ideas such as the logarithmic discretisation of the NRG, propose reasonable starting conditions for the iteration and develop a complete iterative scheme for the determination of expectation values of the desired vector $\mathbf{p}_B$.

7.3.1 Logarithmic discretisation

A major problem in the numerical analysis of the SIAM and its spectral density is to achieve a sufficiently high energy resolution while keeping the numerical effort as low as possible. On the one hand, some highly fine energetic structures like the Kondo peak have to be resolved, on the other hand, there are the energetically rather broad Hubbard satellites. In particular, this means that an adaptive energy discretisation is necessary that represents a variety of energy scales using only a small finite number of actual levels.

This problem is by no means new. Already in the mid-1970s, Wilson proposed to incorporate as many energy scales as possible into the problem in the scope of his NRG theory [251]. This is possible in particular by selecting a logarithmic discretisation for the bath electrons instead of equidistant energy levels. Analogously, we suggest to resort to this fundamental concept for any actual numerical implementation. The following motivation of the corresponding logarithmic discretisation is based on Ref. [83].

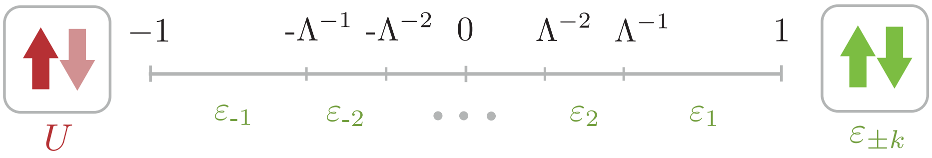

Figure 7.1: A logarithmic discretisation of the bath energies ε_k as given by (7.34) for an arbitrary $|\Lambda| > 1$. The intervals become smaller towards the middle, so that a greater emergence of bath energies around $\varepsilon = 0$ is guaranteed. This is particularly advantageous for the resolution of fine energetic structures, cf. Ref. [83].

Assume that the spectral function has the support $\mathcal{D} = [-D; D]$, cf. figure 7.1 for the normalised case $D = 1$. Note that any arbitrary spectral function on a different support can be mapped to $\mathcal{D}$ by a linear transformation. A similar procedure has been carried out in section 3.3.2 for Hamiltonians. Then, the challenge is to divide the interval $\mathcal{D}$ into a set of non-overlapping subintervals such that as many energy scales as possible are represented. Hence, we choose a parameter $|\Lambda| > 1$ and the logarithmic sequence

$$c_{\pm n} = \pm D\Lambda^{-n} \text{ with } n \in \mathbb{N}_0. \tag{7.33}$$

Arranged in ascending order, the elements (7.33) define the interval boundaries of all subintervals. In each of these subintervals we choose exactly one representative energy level ε_k of the bath. For this, we pick the midpoint of the respective interval by using

$$\varepsilon_{\pm k} = \pm D\frac{\Lambda^{-k} + \Lambda^{-(k-1)}}{2} \text{ with } \Lambda^{-N/2} = 0 \text{ and } k = 1, 2, \ldots, N/2. \tag{7.34}$$

Here, we assume a finite bath of N sites which we need to account for by introducing a manual cut-off around zero. This is necessary to obtain well-defined interval boundaries for the two innermost intervals. Furthermore, note that (7.34) implies the symmetry

$$\varepsilon_k = -\varepsilon_{-k}. \tag{7.35}$$

We choose the transition amplitudes V_k in such a way that the limit of an infinite support, i.e. the so-called wide-band limit $|D| \to \infty$, is still meaningful. Therefore, we resort to

$$V_{\pm k} = \frac{V}{\sqrt{2}} \left| \Lambda^{-(k-1)} - \Lambda^{-k} \right|^{\frac{1}{2}}. \tag{7.36}$$

Thus, it is ensured that the resonance width of the impurity electrons remains finite for vanishing interactions, i.e. for $U = 0$. A physical motivation may be found in Ref. [252].

7.3.2 Initial conditions

For starting the iterative process (7.17), it is necessary to choose an initial vector $\langle \mathbf{s} \rangle^{(0)}$. In principle, it is possible to choose any vector, but for reasons of convergence it is advisable to start close to the expected numerical values. For this reason, one can use the so-called *atomic* picture, in which the isolated interacting impurity electron is chosen as the starting point and the hybridisation by surrounding bath electrons is switched on gradually [252]. Accordingly, we calculate the required expectation values analytically for the boundary case $V_k = 0$. Using n as the filling of the system we obtain

$$\left\langle f_\sigma^\dagger f_\sigma \right\rangle = n \tag{7.37a}$$

$$\left\langle c_{k\sigma}^\dagger c_{j\sigma} \right\rangle = \begin{cases} \delta_{kj} & \text{if } k \leq k_\mathrm{F} \\ 0 & \text{otherwise} \end{cases} \tag{7.37b}$$

$$\left\langle f_\sigma^\dagger c_{k\sigma} \right\rangle = 0. \tag{7.37c}$$

In particular, equation (7.37c) reflects the fact that for $V_k = 0$ there can be no correlation at all between the impurity site and the bath. Similarly, all initial expectation values of quadrilinear order in appendix C.2 have to vanish. Furthermore, all bilinear expectation values whose operators have opposite spin orientations disappear.

7.3.3 Iterative scheme

The actual iterative scheme can be significantly speeded up in advance by means of analytical simplifications. For this purpose, we rewrite the main part of the iteration (7.16) in a smart way and assume that a diagonalisation of the Liouville matrix M has taken place such that the relation

$$M\mathbf{k} = m_k \mathbf{k} \tag{7.38}$$

holds. We recall that all frequencies $\omega = \xi + i\delta$ of the resolvent R have an infinitesimally small but finite positive imaginary part according to (7.11). Hence, the resolvent (7.12) as denoted in the eigenbasis of the Liouville matrix (7.38) reads

$$R = \lim_{\delta \to 0^+} \sum_k \frac{1}{\xi + i\delta - m_k} \mathbf{k}\mathbf{k}^\dagger. \tag{7.39}$$

In order to execute the limit arising in equation (7.39) we resort to the Dirac identity

$$\lim_{\delta\to 0^+} \frac{1}{x+i\delta} = \mathcal{P}\left[\frac{1}{x}\right] - i\pi\delta(x) \tag{7.40}$$

and identify $x := \xi - m_k$. Thus, the resolvent (7.39) may be rewritten and split into a real and an imaginary part of which only the latter one is needed due to (7.14). It reads

$$\operatorname{Im} R = -\pi \sum_k \delta(\xi - m_k)\mathbf{k}\mathbf{k}^\dagger. \tag{7.41}$$

By means of inserting (7.41) into equation (7.10b), we obtain the spectral density as

$$\overline{A}_{A^\dagger B}(\xi) = \sum_k \delta(\xi - m_k)\mathbf{e}_A^T\mathbf{k}\mathbf{k}^\dagger\mathbf{p}_B. \tag{7.42}$$

Due to the fact that all matrix elements of the Hamiltonian (2.33) are real-valued and that a time reversal invariance is present, all expectation values contained in the expectation value vector (7.13) have to be real as well. Eventually, we can insert equation (7.10b), (7.14) and (7.41) into equation (7.16) in order to obtain the final iteration scheme

$$\left\langle BA^\dagger \right\rangle = \sum_k \int_{\mathbb{R}} \frac{\mathbf{e}_A^T\mathbf{k}\mathbf{k}^\dagger\mathbf{p}_B}{\exp(\beta\xi)+1}\delta(\xi - m_k)\,\mathrm{d}\xi \tag{7.43a}$$

$$= \sum_k \underbrace{\frac{\mathbf{e}_A^T\mathbf{k}}{\exp(\beta m_k)+1}}_{=:\, w_{Ak}} \mathbf{k}^\dagger\mathbf{p}_B. \tag{7.43b}$$

Note that the first part of (7.43b) represents the rescaled Fermi-Dirac weight w_{Ak} for the operator $A^\dagger$ and the energy eigenvalue m_k. These weights only have to be evaluated once per iteration and can be reused in each step given by the iteration scheme

$$\boxed{\left\langle BA^\dagger \right\rangle = \sum_k w_{Ak}\,\mathbf{k}^\dagger\mathbf{p}_B.} \tag{7.44}$$

By means of the iterative algorithm which is given by equation (7.44) it is possible to gradually determine approximations to the expectation value vector $\mathbf{p}_B$. As soon as a sufficiently good approximation for $\mathbf{p}_B$ is achieved, the actually wanted one-particle Green's function, cf. equation (7.10b), can be reliably determined numerically.

We are confident that a forthcoming practical implementation of the theoretical concepts proposed in this chapter can serve as a novel methodological approach and semi-analytical complement to existing numerical methods such as NRG. The main strengths of this iEoM approach lie in its polynomially instead of exponentially increasing numerical effort as well as in the possibility to adapt operator bases to the physical regimes to be considered. This will not only help to analyse the dynamics of the SIAM but also to describe the behaviour of a variety of strongly-correlated systems.

8 Summary

If one wanted to summarise the content of this work with just one word, it would probably be *interaction*. Nothing poses as great a challenge to current research on solids as even the smallest interactions and the resulting correlations of the constituents. If particles no longer move undisturbedly and independently of each other, but constantly and drastically influence each other, remarkable collective phenomena arise. Describing the underlying dynamics caused by the mutual influences adequately is highly non-trivial.

As one of the simplest strongly-correlated models of solid state theory, the FHM is still far from being understood a good sixty years after its first mention in the early 1960s. For instance, many theoretical models like the t–J model, the Heisenberg model or the SIAM, which determine the ongoing discourse in highly relevant topics such as Mott metal-insulator transitions, high-temperature superconductivity, quantum dots or nanoelectronics, are limiting cases of the FHM. We examined and discussed some particularly intriguing facets of the FHM and its related models in this work.

Conceptually, we resorted to well-known and widely accepted methods such as ED and CET to compute the dynamics of observables and we made use of comparatively newer ones like KPM and TPQS to describe the thermal behaviour of systems. We implemented these approaches with state-of-the-art techniques on high-performance cluster systems. For the lesser-common method of iEoM, we additionally proposed methodological improvements and novel concepts with respect to operator unitarity and outlined the rigorous derivation of Green's functions in approximated operator subspaces. The recourse to so many different methodological approaches was primarily due to the variety of physical topics and technical requirements in the scope of the present work.

Besides the efficient implementation as well as the methodological enhancement of methods, this work essentially consists of three thematic sections. In the first major section we considered quenches, in particular the abrupt change of global system parameters. For this purpose, we used the FHM on one-dimensional periodic chains, on arbitrary topologies in the form of finite clusters and on infinite-range graphs. By comparing the equilibrated systems and the thermal predictions for the systems, we were able to make substantial contributions to the understanding of the dynamics of a system after sudden external excitations. In particular, by choosing an initial non-product state and thus deliberately violating assumptions made in previous studies on equilibration, we were able to show that equilibration is an even more generic property of excited quantum systems than previously predicted. Moreover, we found strong indications that the intensity of fluctuations decreases with the connectivity of a system, i.e. the number of connected constituents. While this paradigm is widely accepted in equilibrium physics, we were also able to provide evidence for its validity in non-equilibrium regimes by using infinite-range graphs. By studying thermalisation in integrable and non-integrable systems, we contributed to another highly debated topic in non-equilibrium physics. In this way, we confirmed that even in closed quantum systems the amount of integrals of motion present has a significant influence on its dynamics. In our studies, this became evident in the fact that integrable systems showed no signs of thermalisation, whereas generic, non-integrable systems evolved towards thermal equilibrium.

For the quenched one-dimensional FHM with periodic boundary conditions, we succeeded in achieving longer simulation times than they were possible in previous studies thanks to an improvement of the methodological approach. We achieved this by improving the iEoM in terms of their unitarity-preserving dynamics. With the help of a new scalar product and a problem-adapted operator basis, we could describe processes on up to three lattice sites in an exact manner and achieve excellent agreement with highly accurate reference results, especially for strong quenches. Due to these longer simulation times, we were able to partially falsify previous assumptions, especially on a formerly presumed dynamical phase transition for the jump at the Fermi surface. Previous studies assumed that there was a sharp change in the behaviour of the jump depending on the interaction strength of the quench [113, 117, 164, 165]: for weak quenches, weak wiggling should occur, for strong quenches, collapse-and-revival behaviour should be present. Contrary to these assumptions, we found signs of a smooth crossover instead of a dynamical phase transition between the regimes of weak and strong quenches. The spectral features lose or gain weight, but no sharp cut in the frequency spectrum is to be observed.

In the second major part of the work, we dealt with the FHM in the limiting case of strong interactions. This situation, also called t–J model in the literature, is of particular importance in the current research on high-temperature superconductivity and on ultra-cold atoms. For the systematic description of the charge and spin degrees of freedom in the t–J model, we used a perturbative model up to second order in the parameter t_0/U in which spin-dependent and spin-independent hopping and spin-spin interactions are separated from each other. This model was derived in the literature with a CUT [219]. Using CET, we analysed the spectral densities of single hole excitations as the fundamental quantities for understanding the dynamics. Our own analytical estimates as well as the comparison with externally provided iEoM results revealed a high accuracy of the chosen approach. We could demonstrate that the spectral densities for one-dimensional chains and two-dimensional square lattices differ significantly from each other. In the first case, strong influences of the individual processes and of the spin-charge separation on the spectrum are evident, thus indicating a significant change of the underlying dynamics once more processes are turned on. Expected van Hove singularities appear in the outer regions of the spectrum. In the two-dimensional case, however, no spin-charge separation is present and the spectrum is clearly less influenced by the different processes, has an almost elliptical or constant structure and is featureless. Both spectra have in common that the local support increases with the addition of further dynamical processes. The externally provided iEoM results even hint at an unbounded local support as soon as spin-spin interactions are included in the dynamics.

If one excludes all charge degrees of freedom in the half-filled t–J model and only permits spin-spin interactions, one obtains the Heisenberg model. For a better understanding of information loss and, thus, decoherence between the individual spins in the system, we simulated the Heisenberg model on different topologies, with an increasing coordination number in each case. Since for an incrementing amount of interacting spins the importance of each spin becomes successively smaller, it is reasonable to assume that the effect of many spins can be described by a single mean field without significant loss of accuracy. This is the basic idea of the self-consistent spinDMFT, which we could corroborate by numerically exact CET reference results and extrapolations. While pronounced autocorrelations and a correlation revival were detectable for one-dimensional chains even on medium time scales, the amount of correlations decreased gradually with increasing coordination number. Already on two-dimensional lattices, less intense autocorrelations were observed. By systematically extrapolating the results from infinite-range clusters, i.e. finite clusters with the maximum possible coordination number, it was feasible to capture maximally dense spin systems. The agreement with the externally provided results of the spinDMFT was remarkably good and renders the spinDMFT an option for capturing the dynamics of unordered spin systems with large coordination numbers.

The third section was mainly of methodological nature. We described a novel method for the self-consistent computation of Green's functions in approximate operator subspaces. For this purpose, we employed basic ideas of the unitarity-preserving iEoM approach and motivated that the relevant spectral densities in interacting systems can be determined iteratively starting from arbitrary initial values of all expectation values associated with them. We illustrated the procedure using the example of the SIAM. To this end, we derived an operator basis that is exact for all processes on up to two bath sites, calculated the resolvent and described the operator structure of the associated expectation value vectors. Our expectation is that the presented technique can serve as an efficient and easier-to-implement semi-analytical complement to existing numerical methods such as NRG and that already small iEoM operator bases are sufficient to describe physical phenomena such as the Kondo physics, which is an integral part of the SIAM.

Even though we addressed many relevant questions of the FHM and contributed to their clarification, each solved question raises new ones: How many integrals of motion are necessary to prevent thermalisation under realistic circumstances? What are the time scales on which equilibration and thermalisation take place? What determines them? How can the phenomenologically large differences between the one- and two-dimensional t–J model be explained, apart from spin-charge separation and potential integrability? What is the cause of a possibly unbounded local support as soon as spin-spin interaction is added? Moreover, there remains potential for methodological improvement. For example, it would be desirable to recognise all symmetries of a cluster in order to facilitate CET calculations for even larger systems. Furthermore, it would be helpful to enhance the process of creating an iEoM basis and to define metrics that exclude irrelevant operators from consideration. This would allow for using more relevant and accurate operator bases, which would enable longer simulation times and treating more subtle effects.

The outlook given above highlights only a handful of particularly interesting follow-up questions and does not even claim to be comprehensive. Rather, it is intended to inspire future work and to emphasise: Research on the FHM is a constant source of fascination.

A Implementations

A.1 Computational improvements

In the numerical treatment of the FHM, the effective storage of the Hamiltonian matrix is of particular importance. In this, two aspects are involved which are especially relevant.

First, the storage scheme of the Hamiltonian can be optimised. This is due to the fact that while the dimension of the Hamiltonian matrix itself grows exponentially fast the number of non-zero elements in each row and column grows noticeably slower due to the generally small number of available hopping processes. For example, in the case of a one-dimensional lattice with nearest-neighbour hopping, the number of non-zero elements grows linearly with the number of lattice sites N. This implies a high sparsity of the matrix making a sparse storage format a sensible choice.

Second, the matrix does not need to be saved as a whole [253]. Since particles with spin σ and the opposite spin $\overline{\sigma}$ are independent of each other the hopping part H_0 as given by (2.1a) can be decomposed into the two matrices H_σ, $\sigma \in \{\downarrow, \uparrow\}$, by

$$H_0 = (H_\downarrow \otimes \mathbb{1}_\uparrow) \oplus (\mathbb{1}_\downarrow \otimes H_\uparrow) \, . \tag{A.1}$$

For each H_σ, only the upper triangular matrix needs to be stored due to symmetry. Moreover, the interaction matrix H_{int} is diagonal in real space according to (2.1b). Consequently, only its main diagonal needs to be stored, e.g. by means of a one-dimensional array. Applying H_{int} to a state is a mere vector-vector multiplication then.

Unfortunately, with this approach calculating the effect of H_σ on a state is no matrix-vector multiplication anymore. Let $m_\sigma := \dim(\mathcal{H}_\sigma)$ be the dimension of the Hilbert space of spin σ particles in accordance with equation (3.8). Then, each state $|s\rangle \in \mathcal{H}$ given by its coefficient vector $\mathbf{s}$ has the structure

$$\mathbf{s} = \begin{pmatrix} \mathbf{s}_0 \\ \dots \\ \mathbf{s}_{m_\downarrow - 1} \end{pmatrix} \text{ with the components } \mathbf{s}_i := \begin{pmatrix} x_0 \\ \dots \\ x_{m_\uparrow - 1} \end{pmatrix} . \tag{A.2}$$

The application of H_0 to this state is performed according to (A.1) and, thus, becomes

$$H_0 \cdot \mathbf{s} = H_\downarrow \begin{pmatrix} \mathbf{s}_0 \\ \dots \\ \mathbf{s}_{m_\downarrow - 1} \end{pmatrix} + \begin{pmatrix} H_\uparrow \cdot \mathbf{s}_0 \\ \dots \\ H_\uparrow \cdot \mathbf{s}_{m_\downarrow - 1} \end{pmatrix} . \tag{A.3}$$

A.2 Constructing the Fermi sea

As discussed in section 5.2.1, it may be necessary to determine the Fermi sea $|\text{FS}\rangle$, as the initial state of the system, in a real space basis rather than in the eigenbasis of H_0

when performing a global parameter quench. This is especially appropriate when the observables under consideration are themselves easier to treat in real space. We turn to this problem below, briefly recapitulating the most important basics from section 5.2.1 and extending them to real space. Finally, we give a practical example for a concrete application to a toy model.

Since the hopping part consists of interaction-free particles, it is an effective one-particle problem $h_0 := -A(G)$ where $A(G)$ denotes the adjacency matrix of the undirected graph G describing the site topology. Hence, we can restrict all further considerations to states consisting of only one particle and construct the full Fermi sea from the corresponding results. Let $|i\sigma\rangle$ be the eigenstates of the occupation number operator according to

$$\widehat{n}_{i\sigma} |i\sigma\rangle = n_{i\sigma} |i\sigma\rangle \ \text{ with } \ |i\sigma\rangle := f_{i\sigma}^{\dagger} |0\rangle \tag{A.4}$$

where $|0\rangle$ denotes the vacuum and let $|\nu\sigma\rangle$ be the eigenstates of h_0 with the respective energies ϵ_ν. Consequently, these states obey the eigenvalue equation

$$h_0 |\nu\sigma\rangle = \epsilon_\nu |\nu\sigma\rangle \,. \tag{A.5}$$

Therefore, in both states (A.4) and (A.5) exactly one particle with spin σ resides on lattice site i and in state ν, respectively. The Fermi sea (5.7) can be constructed by gradually filling the eigenstates of h_0 in increasing order of the ϵ_ν leading to the definition

$$|\mathrm{FS}\rangle := \prod_{(\nu,\sigma)\,\in\, I} f_{\nu\sigma}^{\dagger} |0\rangle = \prod_{(\nu,\sigma)\,\in\, I} \left(\sum_i \langle i\sigma|\nu\sigma\rangle \, f_{i\sigma}^{\dagger} \right) |0\rangle \,. \tag{A.6}$$

Here, the part in brackets describes the basis change which is necessary since all states which are worked with are eigenstates of the occupation number operator in real space. The index set I is chosen such that the condition $\epsilon_\nu < \epsilon_{\mathrm{F}}$ with ϵ_{F} being the Fermi energy is fulfilled. This means that all states with energies below the energy threshold of the Fermi energy are occupied with particles and all remaining states are unoccupied.

It is worthwhile to keep in mind that each state of a fixed number of n particles is an element of the Hilbert space $\mathcal{H}_n$. Consequently, this means that the new state, after $f_{i\sigma}^{\dagger}$ has been applied, cannot be an element of the former Hilbert space anymore but has to be an element of $\mathcal{H}_{n+1}$ or the vacuum state instead. The space of a variable total particle number is defined as the Fock space according to

$$\mathcal{F} = \mathcal{H}_0 \oplus \mathcal{H}_1 \oplus \mathcal{H}_2 \oplus \ldots \tag{A.7}$$

for which the complete orthonormal basis set is given by the many-particle eigenstates

$$|\{n_\alpha\}\rangle := |n_1, n_2, \ldots\rangle \tag{A.8}$$

defined in equation (3.9). Each of these states represents a system state in which $n_i \in \{0, 1\}$ fermions are in the i-th one-particle state $|\alpha_i\rangle$. In our practical application, cf. equation (A.6), this means that we start from the vacuum state $|0\rangle$ of $\mathcal{H}_0$ and end up with the resulting Fermi sea $|\mathrm{FS}\rangle \in \mathcal{H}_m$ for a total number of m particles. On a finite lattice of N sites, the number of basis states with a fixed number of N_σ particles of spin σ in each intermediate Hilbert space $\mathcal{H}_j$ with $j = N_\downarrow + N_\uparrow$ equals

$$\dim(\mathcal{H}_j) = \binom{N}{N_\downarrow} \cdot \binom{N}{N_\uparrow} \tag{A.9}$$

which is the direct combinatorical result of distributing the two independent kinds of particles over all lattice sites as described by equation (3.8) in section 3.1.1.

Example

In order to see the practical implications of equation (A.6) we resort to a toy model of a one-dimensional lattice without periodic boundary conditions, $N = 3$ sites and a constant hopping strength of $J = 1$. In the occupation number basis the Hamiltonian H_0 can be easily derived by negating the corresponding adjacency matrix of the graph representing the lattice which means

$$H_0 = -\begin{pmatrix} 0 & 1 & 0 \\ 1 & 0 & 1 \\ 0 & 1 & 0 \end{pmatrix}. \tag{A.10}$$

Constructing the Fermi sea can be performed independently for the two spin species which then can be combined by means of a Kronecker product using

$$|\mathrm{FS}\rangle = |\mathrm{FS}\rangle_\downarrow \otimes |\mathrm{FS}\rangle_\uparrow . \tag{A.11}$$

For this reason, we will drop the subscript σ from now on and exemplarily construct the Fermi sea for one arbitrary spin orientation with a filling of $^2/_3$. For this, we have to identify which states are to be filled and in which order. This requires a full diagonalisation of the hopping matrix (A.10) resulting in the eigenenergies

$$\epsilon_1 = -\sqrt{2}, \quad \epsilon_2 = 0, \quad \epsilon_3 = \sqrt{2} \tag{A.12}$$

with their individual corresponding eigenvectors given by

$$\mathbf{v}_1 = \left(1, \sqrt{2}, 1\right)^T, \quad \mathbf{v}_2 = (-1, 0, 1)^T, \quad \mathbf{v}_3 = \left(1, -\sqrt{2}, 1\right)^T. \tag{A.13}$$

For clarity and to be able to differentiate between both bases $|\nu\rangle$ and $|i\rangle$, we will use

$$d_\nu^\dagger := \sum_i \mathbf{v}_{\nu,i} f_i^\dagger \tag{A.14}$$

to denote a creation operator in the eigenbasis of H_0. Hence, the first intermediate state with one particle can be constructed[1] as the linear combination

$$|I\rangle = d_1^\dagger\,|0\rangle = 1\cdot|001\rangle + \sqrt{2}\cdot|010\rangle + 1\cdot|100\rangle\,. \tag{A.15}$$

To obtain the desired filling a second particle has to be inserted into the system in state $|\nu = 2\rangle$ by applying the respective creation operator $d_2^\dagger$ which leads to

$$\begin{aligned}
|\mathrm{FS}\rangle_\sigma = d_2^\dagger\,|I\rangle &= (-1 f_1^\dagger + f_3^\dagger)\,\Big(|001\rangle + \sqrt{2}\,|010\rangle + |100\rangle\Big) && \text{(A.16a)}\\
&= \sqrt{2}\,|011\rangle + |101\rangle + |101\rangle + \sqrt{2}\,|110\rangle && \text{(A.16b)}\\
&= \sqrt{2}\,|011\rangle + 2\,|101\rangle + \sqrt{2}\,|110\rangle\,. && \text{(A.16c)}
\end{aligned}$$

Note that the signs have to be adjusted whenever a particle hops over an already occupied state to comply with the fermionic algebra. For didactic purposes, the states are not normalised in the process of repeated particle creations. In real applications, however, this normalisation has to be performed leading to the Fermi sea coefficient vector with respect to the basis states of $\mathcal{H}_2$ given in (A.16c) as

$$\mathbf{v}_{\mathrm{FS}} = ({}^1\!/\!_2, {}^1\!/\!_{\sqrt{2}}, {}^1\!/\!_2)^T\,. \tag{A.17}$$

The energy of this state is the sum of the one-particle energies of the occupied levels

$$E = \sum_{\epsilon_i < \epsilon_{\mathrm{F}}} \epsilon_i \tag{A.18}$$

which equals $\epsilon_1 + \epsilon_2 = -\sqrt{2}$ in the above case of the toy model example. Obviously, this result could have been obtained as well by calculating the expectation value of the kinetic Hamiltonian $H_0^{(2)}$ in the two-particle subspace with respect to $\mathbf{v}_{\mathrm{FS}}$

$$\langle\mathrm{FS}|H_0^{(2)}|\mathrm{FS}\rangle = -\mathbf{v}_{\mathrm{FS}}^\dagger \begin{pmatrix} 0 & 1 & 0 \\ 1 & 0 & 1 \\ 0 & 1 & 0 \end{pmatrix} \mathbf{v}_{\mathrm{FS}} = -\sqrt{2}. \tag{A.19}$$

In the possible case of a degeneracy at the level of the Fermi energy all combinatorically possible results $\{|\mathrm{FS}\rangle\}$ have to be computed and simulated individually. The final physical outcome can be obtained by averaging over all simulation results.

---

[1] A possibility to implement this process in a fast way for the binary basis described in section 3.1.1 is by using bitmasks. For a creation operator in real space $f_i^\dagger$, two masks are created with the first being the operator itself as $C_i = \underbrace{0\dots0}_{N-i}1\underbrace{0\dots0}_{i-1}$ and the second being the mask $M_i = \underbrace{1\dots1}_{N-i}\underbrace{0\dots0}_{i}$ to obtain the global sign of the final state. Applying $f_i^\dagger$ to a state S equals the following process: if $C_i \wedge S = \varnothing$, the site i is unoccupied and a particle can be created. It can be created using $C_i \vee S$ and the global sign $(-1)^p$ can be deduced by applying $M_i \wedge S =: P$ with $p = \mathrm{popcount}(P)$, i.e. the total number of bits set to 1 in P.

B Generic clusters

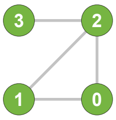

(a)

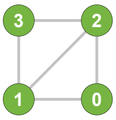

(b)

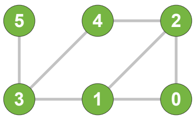

(c)

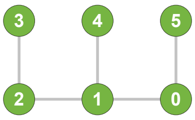

(d)

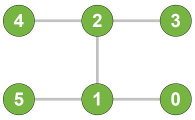

(e)

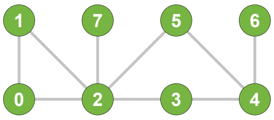

(f)

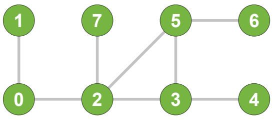

(g)

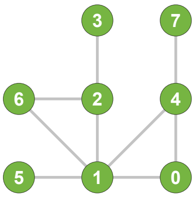

(h)

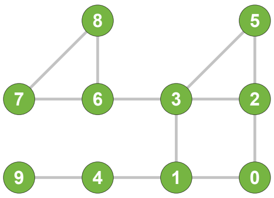

(i)

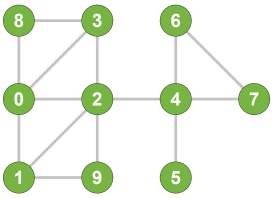

(j)

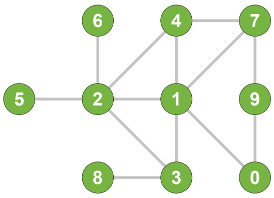

(k)

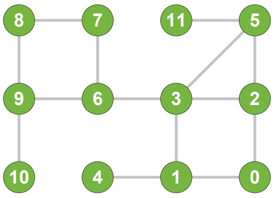

(l)

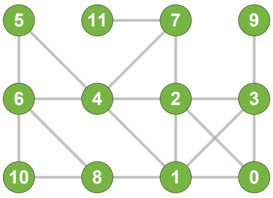

(m)

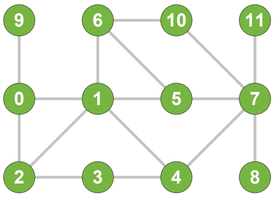

(n)

C SIAM

C.1 Scalar products

The scalar products listed below correspond to all possible non-vanishing combinations of the operators (7.21) and (7.22). Since the Liouville matrix is Hermitian, cf. equations (3.67) and (3.69), not all of these combinations have to be considered and

$$(A_j|\mathcal{L}(A_i)) = (A_i|\mathcal{L}(A_j))^* \tag{C.0}$$

holds. As a consequence, only about half of all possible scalar products are specified here. The indices of an operator denote the bath sites on which it acts. Eventually, we obtain

W_1

$$(W_1\,|\,\mathcal{L}(W_1)) = \varepsilon_0 + \frac{U}{2} \tag{C.1a}$$

$$(W_2\,|\,\mathcal{L}(W_1)) = \frac{U}{2} \tag{C.1b}$$

$$(W_3(c)\,|\,\mathcal{L}(W_1)) = V_c \tag{C.1c}$$

W_2

$$(W_2\,|\,\mathcal{L}(W_2)) = \varepsilon_0 + \frac{U}{2} \tag{C.2a}$$

$$\big(W_{4/5}(c)\,\big|\,\mathcal{L}(W_2)\big) = V_c \tag{C.2b}$$

$$(W_6(c)\,|\,\mathcal{L}(W_2)) = -V_c \tag{C.2c}$$

$W_3(k)$

$$(W_3(c)\,|\,\mathcal{L}(W_3(k))) = \varepsilon_k\,\delta_{ck} \tag{C.3a}$$

$W_4(k)$

$$(W_4(c)\,|\,\mathcal{L}(W_4(k))) = \varepsilon_k\,\delta_{ck} \tag{C.4a}$$

$$(W_7(c,d)\,|\,\mathcal{L}(W_4(k))) = V_d\,\delta_{ck} \tag{C.4b}$$

$$(W_8(c,d)\,|\,\mathcal{L}(W_4(k))) = -V_d\,\delta_{ck} \tag{C.4c}$$

$W_5(k)$

$$(W_5(c)\,|\,\mathcal{L}(W_5(k))) = \varepsilon_k\,\delta_{ck} \tag{C.5a}$$

$$(W_7(c,d)\,|\,\mathcal{L}(W_5(k))) = V_c\,\delta_{dk} \tag{C.5b}$$

$$(W_9(c,d)\,|\,\mathcal{L}(W_5(k))) = -V_d\,\delta_{ck} \tag{C.5c}$$

$W_6(k)$

$$(W_6(c)\,|\,\mathcal{L}(W_6(k))) = (2\varepsilon_0 - \varepsilon_k + U)\;\delta_{ck} \tag{C.6a}$$

$$\big(W_{8/9}(c,d)\,\big|\,\mathcal{L}(W_6(k))\big) = V_c\,\delta_{dk} \tag{C.6b}$$

$$W_7(k,l) \qquad (W_7(c,d)\,|\,\mathcal{L}(W_7(k,l))) = \left(-\varepsilon_0 + \varepsilon_k + \varepsilon_l - \frac{U}{2}\right) \delta_{ck}\, \delta_{dl} \tag{C.7a}$$

$$(W_{10}(c,d)\,|\,\mathcal{L}(W_7(k,l))) = -\frac{U}{2}\, \delta_{ck}\, \delta_{dl} \tag{C.7b}$$

$$W_8(k,l) \qquad (W_8(c,d)\,|\,\mathcal{L}(W_8(k,l))) = \left(\varepsilon_0 + \varepsilon_k - \varepsilon_l + \frac{U}{2}\right) \delta_{ck}\, \delta_{dl} \tag{C.8a}$$

$$(W_{11}(c,d)\,|\,\mathcal{L}(W_8(k,l))) = -\frac{U}{2}\, \delta_{ck}\, \delta_{dl} \tag{C.8b}$$

$$W_9(k,l) \qquad (W_9(c,d)\,|\,\mathcal{L}(W_9(k,l))) = \left(\varepsilon_0 + \varepsilon_k - \varepsilon_l + \frac{U}{2}\right) \delta_{ck}\, \delta_{dl} \tag{C.9a}$$

$$(W_{12}(c,d)\,|\,\mathcal{L}(W_9(k,l))) = \frac{U}{2}\, \delta_{ck}\, \delta_{dl} \tag{C.9b}$$

$$W_{10}(k,l) \qquad (W_{10}(c,d)\,|\,\mathcal{L}(W_{10}(k,l))) = \left(-\varepsilon_0 + \varepsilon_k + \varepsilon_l - \frac{U}{2}\right) \delta_{ck}\, \delta_{dl} \tag{C.10a}$$

$$W_{11}(k,l) \qquad (W_{11}(c,d)\,|\,\mathcal{L}(W_{11}(k,l))) = \left(\varepsilon_0 + \varepsilon_k - \varepsilon_l + \frac{U}{2}\right) \delta_{ck}\, \delta_{dl} \tag{C.11a}$$

$$W_{12}(k,l) \qquad (W_{12}(c,d)\,|\,\mathcal{L}(W_{12}(k,l))) = \left(\varepsilon_0 + \varepsilon_k - \varepsilon_l + \frac{U}{2}\right) \delta_{ck}\, \delta_{dl}. \tag{C.12a}$$

C.2 Expectation values

The expectation value vectors motivated in section 7.2.3, which occur in the context of the operator basis (7.21) and (7.22), are listed below. The actual calculation reveals that it is not mandatory to compute all twelve conceivable expectation value vectors

$$\mathbf{p}_q := \left\langle \left\{ \mathbf{x}^\dagger(k,l), W_q(r,s) \right\} \right\rangle . \tag{C.13}$$

In many cases, the operator $W_q(r,s)$ can be chosen in a smart way and, thus, the calculation be reduced to already existing expectation value vectors. In practice, only the two vectors for $q = 1$ and $q = 3$ are sufficient.

Here and in the following, we use $\mathbf{p}_{q,j}$ to denote the entry for $W_j^\dagger(k,l)$ of the expectation value vector $\mathbf{p}_q$ and the index pairs k, l and r, s to describe the possible site-dependence of an operator family. Occasionally, the emerging expectation values involve operators that are not part of the basis (7.21) and (7.22) due to different spin orientations. Since the SIAM is invariant under the change of the spin orientation, i.e. the transformation

$$\overline{\sigma} \to \sigma, \tag{C.14}$$

we can always rewrite the respective operators into basis operators by using (C.14). If needed, we denote the usage of this transformation by an asterisk.

For brevity, we again only specify non-vanishing elements of the vectors. This means that $\mathbf{p}_{q,j} = 0$ holds if not stated otherwise in the following. Eventually, we obtain the two necessary expectation value vectors $\mathbf{p}_1$ and $\mathbf{p}_3$ as defined in (7.27) and (7.30) by

$\mathbf{p}_1$

$$\mathbf{p}_{1,1} = 2 \tag{C.15a}$$

$$\mathbf{p}_{1,2} = 4\left\langle \widehat{n}_{\overline{\sigma}} \right\rangle - 2 \overset{(*)}{=} 4\left\langle f^\dagger_\sigma f_\sigma \right\rangle - 2 \tag{C.15b}$$

$$\mathbf{p}_{1,5} = 4\left\langle f^\dagger_{\overline{\sigma}} c_{k\overline{\sigma}} \right\rangle \overset{(*)}{=} 4\left\langle f^\dagger_\sigma c_{k\sigma} \right\rangle \tag{C.15c}$$

$$\mathbf{p}_{1,6} = 4\left\langle c^\dagger_{k\overline{\sigma}} f_{\overline{\sigma}} \right\rangle = 4\left\langle c^\dagger_{k\sigma} f_\sigma \right\rangle \tag{C.15d}$$

$$\mathbf{p}_{1,9} = 4\left\langle c^\dagger_{l\overline{\sigma}} c_{k\overline{\sigma}} \right\rangle - 2\delta_{kl} \overset{(*)}{=} 4\left\langle c^\dagger_{l\sigma} c_{k\sigma} \right\rangle - 2\delta_{kl} \tag{C.15e}$$

$$\mathbf{p}_{1,10} = -8\left\langle f^\dagger_\sigma f^\dagger_{\overline{\sigma}} c_{l\overline{\sigma}} c_{k\sigma} \right\rangle \tag{C.15f}$$

$$\mathbf{p}_{1,11} = 8\left\langle f^\dagger_\sigma c^\dagger_{l\overline{\sigma}} f_{\overline{\sigma}} c_{k\sigma} \right\rangle \tag{C.15g}$$

$$\mathbf{p}_{1,12} = -4\left\langle c^\dagger_{l\overline{\sigma}} c_{k\overline{\sigma}} \right\rangle - 4\left\langle \widehat{n}_{\overline{\sigma}} \right\rangle \delta_{kl} + 2\delta_{kl} - 8\left\langle c^\dagger_{l\overline{\sigma}} f^\dagger_{\overline{\sigma}} c_{k\overline{\sigma}} f_{\overline{\sigma}} \right\rangle \tag{C.15h}$$

$$\overset{(*)}{=} -4\left\langle c^\dagger_{l\sigma} c_{k\sigma} \right\rangle - 4\left\langle f^\dagger_\sigma f_\sigma \right\rangle \delta_{kl} + 2\delta_{kl} - 8\left\langle c^\dagger_{l\sigma} f^\dagger_\sigma c_{k\sigma} f_\sigma \right\rangle \tag{C.15i}$$

$$\approx -4\left\langle c^\dagger_{l\sigma} c_{k\sigma} \right\rangle - 4\left\langle f^\dagger_\sigma f_\sigma \right\rangle \delta_{kl} + 2\delta_{kl} \tag{C.15j}$$

$$+ 8\left\langle c^\dagger_{l\sigma} c_{k\sigma} \right\rangle \left\langle f^\dagger_\sigma f_\sigma \right\rangle - 8\left\langle c^\dagger_{l\sigma} f_\sigma \right\rangle \left\langle f^\dagger_\sigma c_{k\sigma} \right\rangle \tag{C.15k}$$

$\mathbf{p}_3$

$$\mathbf{p}_{3,3} = 2\delta_{kr} \tag{C.16a}$$

$$\mathbf{p}_{3,4} = 2\delta_{kr}\left(2\left\langle \widehat{n}_{\overline{\sigma}} \right\rangle - 1\right) \overset{(*)}{=} 2\delta_{kr}\left(2\left\langle f^\dagger_\sigma f_\sigma \right\rangle - 1\right) \tag{C.16b}$$

$$\mathbf{p}_{3,7} = 4\delta_{kr}\left\langle f^\dagger_{\overline{\sigma}} c_{l\overline{\sigma}} \right\rangle \overset{(*)}{=} 4\delta_{kr}\left\langle f^\dagger_\sigma c_{l\sigma} \right\rangle \tag{C.16c}$$

$$\mathbf{p}_{3,8} = 4\delta_{kr}\left\langle c^\dagger_{l\overline{\sigma}} f_{\overline{\sigma}} \right\rangle \overset{(*)}{=} 4\delta_{kr}\left\langle c^\dagger_{l\sigma} f_\sigma \right\rangle \tag{C.16d}$$

$$\mathbf{p}_{3,10} = -4\delta_{kr}\left\langle f^\dagger_{\overline{\sigma}} c_{l\overline{\sigma}} \right\rangle + 8\delta_{kr}\left\langle f^\dagger_\sigma f^\dagger_{\overline{\sigma}} c_{l\overline{\sigma}} f_\sigma \right\rangle \tag{C.16e}$$

$$\overset{(*)}{=} -4\delta_{kr}\left\langle f^\dagger_\sigma c_{l\sigma} \right\rangle + 8\delta_{kr}\left\langle f^\dagger_\sigma f^\dagger_{\overline{\sigma}} c_{l\overline{\sigma}} f_\sigma \right\rangle \tag{C.16f}$$

$$\mathbf{p}_{3,11} = 4\delta_{kr}\left\langle c^\dagger_{l\overline{\sigma}} f_{\overline{\sigma}} \right\rangle - 8\delta_{kr}\left\langle f^\dagger_\sigma c^\dagger_{l\overline{\sigma}} f_{\overline{\sigma}} f_\sigma \right\rangle \tag{C.16g}$$

$$\overset{(*)}{=} 4\delta_{kr}\left\langle c^\dagger_{l\sigma} f_\sigma \right\rangle - 8\delta_{kr}\left\langle f^\dagger_\sigma c^\dagger_{l\overline{\sigma}} f_{\overline{\sigma}} f_\sigma \right\rangle . \tag{C.16h}$$

Bibliography

[1] N. F. Mott, “The Basis of the Electron Theory of Metals, with Special Reference to the Transition Metals”, Proc. Phys. Soc. A **62**, 416–422 (1949).

[2] N. F. Mott, “Metal-Insulator Transition”, Rev. Mod. Phys. **40**, 677–683 (1968).

[3] J. De Nobel and P. Lindenfeld, “The Discovery of Superconductivity”, Phys. Today **49**, 40–42 (1996).

[4] F. J. Morin, “Oxides Which Show a Metal-to-Insulator Transition at the Néel Temperature”, Phys. Rev. Lett. **3**, 34–36 (1959).

[5] J. Bardeen, L. N. Cooper, and J. R. Schrieffer, “Theory of Superconductivity”, Phys. Rev. **108**, 1175–1204 (1957).

[6] C. N. Berglund and H. J. Guggenheim, “Electronic Properties of VO_2 near the Semiconductor-Metal Transition”, Phys. Rev. **185**, 1022–1033 (1969).

[7] J. G. Bednorz and K. A. Müller, “Possible High T_c Superconductivity in the BaLaCuO System”, Zeitschrift für Phys. B Condens. Matter **64**, 189–193 (1986).

[8] J. D. Budai et al., “Metallization of vanadium dioxide driven by large phonon entropy”, Nature **515**, 535–539 (2014).

[9] G. Czycholl, *Theoretische Festkörperphysik* (Springer, Berlin, 2008).

[10] J. Hubbard, “Electron Correlations in Narrow Energy Bands”, Proc. R. Soc. Lond. A. Math. Phys. Sci. **276**, 238–257 (1963).

[11] J. Kanamori, “Electron Correlation and Ferromagnetism of Transition Metals”, Prog. Theor. Phys. **30**, 275–289 (1963).

[12] M. C. Gutzwiller, “Effect of Correlation on the Ferromagnetism of Transition Metals”, Phys. Rev. Lett. **10**, 159–162 (1963).

[13] F. Gebhard, *The Mott Metal-Insulator Transition*, Vol. 137, Springer Tracts in Modern Physics (Springer, Berlin/Heidelberg, 1997).

[14] F. H. L. Essler et al., *The One-Dimensional Hubbard Model* (Cambridge University Press, Cambridge, 2005).

[15] D. Jaksch et al., “Cold Bosonic Atoms in Optical Lattices”, Phys. Rev. Lett. **81**, 3108–3111 (1998).

[16] I. Bloch, J. Dalibard, and W. Zwerger, “Many-body physics with ultracold gases”, Rev. Mod. Phys. **80**, 885–964 (2008).

[17] L. Anderegg et al., “Laser Cooling of Optically Trapped Molecules”, Nat. Phys. **14**, 890–893 (2018).

[18] M. Modugno, J. Ibañez-Azpiroz, and G. Pettini, “Tight-binding models for ultracold atoms in optical lattices: general formulation and applications”, Sci. China Physics, Mech. Astron. **59**, 660001 (2016).

[19] L. M. Duan, E. Demler, and M. D. Lukin, “Controlling Spin Exchange Interactions of Ultracold Atoms in Optical Lattices”, Phys. Rev. Lett. **91**, 090402 (2003).

[20] M. Greiner et al., “Quantum phase transition from a superfluid to a Mott insulator in a gas of ultracold atoms”, Nature **415**, 39–44 (2002).

[21] F. Schäfer et al., “Tools for quantum simulation with ultracold atoms in optical lattices”, Nat. Rev. Phys. **2**, 411–425 (2020).

[22] U. Schneider et al., “Fermionic transport and out-of-equilibrium dynamics in a homogeneous Hubbard model with ultracold atoms”, Nat. Phys. **8**, 213–218 (2012).

[23] S. Kaiser et al., “Optically induced coherent transport far above T_c in underdoped $\mathrm{YBa_2Cu_3O_{6+x}}$”, Phys. Rev. B **89**, 184516 (2014).

[24] W. Hu et al., “Optically enhanced coherent transport in $\mathrm{YBa_2Cu_3O_{6.5}}$ by ultrafast redistribution of interlayer coupling”, Nat. Mater. **13**, 705–711 (2014).

[25] C. R. Hunt et al., “Two distinct kinetic regimes for the relaxation of light-induced superconductivity in $\mathrm{La_{1.675}Eu_{0.2}Sr_{0.125}CuO_4}$”, Phys. Rev. B **91**, 020505 (2015).

[26] M. Mitrano et al., “Possible light-induced superconductivity in $\mathrm{K_3C_{60}}$ at high temperature”, Nature **530**, 461–464 (2016).

[27] J. Eisert, M. Friesdorf, and C. Gogolin, “Quantum many-body systems out of equilibrium”, Nat. Phys. **11**, 124–130 (2015).

[28] Y. Aharonov, L. Davidovich, and N. Zagury, “Quantum random walks”, Phys. Rev. A **48**, 1687–1690 (1993).

[29] N. V. Prokof’ev and P. C. Stamp, “Decoherence and quantum walks: Anomalous diffusion and ballistic tails”, Phys. Rev. A **74**, 020102 (2006).

[30] J. Carlström, N. Prokof’ev, and B. Svistunov, “Quantum Walk in Degenerate Spin Environments”, Phys. Rev. Lett. **116**, 247202 (2016).

[31] C. L. Degen, F. Reinhard, and P. Cappellaro, “Quantum sensing”, Rev. Mod. Phys. **89**, 035002 (2017).

[32] S. Steinert et al., “Magnetic spin imaging under ambient conditions with sub-cellular resolution”, Nat. Commun. **4**, 1607 (2013).

[33] Y. Romach et al., “Spectroscopy of Surface-Induced Noise Using Shallow Spins in Diamond”, Phys. Rev. Lett. **114**, 017601 (2015).

[34] R. Pariser and R. G. Parr, “A Semi-Empirical Theory of the Electronic Spectra and Electronic Structure of Complex Unsaturated Molecules. I.”, J. Chem. Phys. **21**, 466–471 (1953).

[35] J. A. Pople, “Electron interaction in unsaturated hydrocarbons”, Trans. Faraday Soc. **49**, 1375–1385 (1953).

[36] J. A. Vergés et al., “Fit of Pariser-Parr-Pople and Hubbard model Hamiltonians to charge and spin states of polycyclic aromatic hydrocarbons”, Phys. Rev. B **81**, 085120 (2010).

[37] G. H. Wannier, “The Structure of Electronic Excitation Levels in Insulating Crystals”, Phys. Rev. **52**, 191–197 (1937).

[38] C. N. Yang, “Some Exact Results for the Many-Body Problem in One Dimension with Repulsive Delta-Function Interaction”, Phys. Rev. Lett. **19**, 1312–1315 (1967).

[39] R. J. Baxter, *Exactly Solved Model in Statistical Mechanics* (Academic Press, London, 1989).

[40] E. H. Lieb and F. Y. Wu, “Absence of Mott Transition in an Exact Solution of the Short-Range, One-Band Model in One Dimension”, Phys. Rev. Lett. **20**, 1445–1448 (1968).

[41] G. Kotliar and D. Vollhardt, “Strongly Correlated Materials: Insights From Dynamical Mean-Field Theory”, Phys. Today **57**, 53–59 (2004).

[42] P. Bleicker and G. S. Uhrig, “Strong quenches in the one-dimensional Fermi-Hubbard model”, Phys. Rev. A **98**, 033602 (2018).

[43] P. Bleicker, “Stationary states after interaction quenches in the Fermi-Hubbard model”, Master’s thesis (Technische Universität, Dortmund, 2017).

[44] F. Bloch, “Über die Quantenmechanik der Elektronen in Kristallgittern”, Zeitschrift für Phys. **52**, 555–600 (1929).

[45] A. Mielke, *The Hubbard Model and its Properties*, Many Body Physics: From Kondo to Hubbard (Verlag des Forschungszentrums Jülich, 2015).

[46] P. Bleicker, D.-B. Hering, and G. S. Uhrig, "Charge dynamics in magnetically disordered Mott insulators", arXiv:2104.10158 (2021).

[47] W. F. Brinkman and T. M. Rice, "Single-Particle Excitations in Magnetic Insulators", Phys. Rev. B **2**, 1324–1338 (1970).

[48] E. Snider et al., "Room-temperature superconductivity in a carbonaceous sulfur hydride", Nature **586**, 373–377 (2020).

[49] A. Schilling et al., "Superconductivity above 130 K in the HgBaCaCuO system", Nature **363**, 56–58 (1993).

[50] Y. A. Izyumov, "Strongly correlated electrons: the $t-J$ model", Physics-Uspekhi **40**, 445–476 (1997).

[51] S. Schmitt-Rink, C. M. Varma, and A. E. Ruckenstein, "Spectral Function of Holes in a Quantum Antiferromagnet", Phys. Rev. Lett. **60**, 2793–2796 (1988).

[52] P. Prelovšek, I. Sega, and J. Bonča, "Cumulant-expansion study of holes in quantum antiferromagnets", Phys. Rev. B **42**, 10706–10713 (1990).

[53] S. Sachdev, "Hole motion in a quantum Néel state", Phys. Rev. B **39**, 12232–12247 (1989).

[54] C. L. Kane, P. A. Lee, and N. Read, "Motion of a single hole in a quantum antiferromagnet", Phys. Rev. B **39**, 6880–6897 (1989).

[55] J. Bonča, S. Maekawa, and T. Tohyama, "Numerical approach to the low-doping regime of the $t-J$ model", Phys. Rev. B **76**, 035121 (2007).

[56] M. Mierzejewski et al., "Nonequilibrium Quantum Dynamics of a Charge Carrier Doped into a Mott Insulator", Phys. Rev. Lett. **106**, 196401 (2011).

[57] S. A. Trugman, "Interaction of holes in a Hubbard antiferromagnet and high-temperature superconductivity", Phys. Rev. B **37**, 1597–1603 (1988).

[58] E. Dagotto, "Correlated electrons in high-temperature superconductors", Rev. Mod. Phys. **66**, 763–840 (1994).

[59] A. Mielke, "The One-Dimensional Hubbard Model for Large or Infinite U", J. Stat. Phys. **62**, 509–528 (1991).

[60] B. Kumar, "Exact solution of the infinite-U Hubbard problem and other models in one dimension", Phys. Rev. B **79**, 155121 (2009).

[61] A. Nocera, F. H. Essler, and A. E. Feiguin, "Finite-temperature dynamics of the Mott insulating Hubbard chain", Phys. Rev. B **97**, 045146 (2018).

[62] R. Bulla, T. A. Costi, and D. Vollhardt, "Finite-temperature numerical renormalization group study of the Mott transition", Phys. Rev. B **64**, 045103 (2001).

[63] S. Nishimoto, F. Gebhard, and E. Jeckelmann, "Dynamical density-matrix renormalization group for the Mott-Hubbard insulator in high dimensions", J. Phys. Condens. Matter **16**, 7063–7081 (2004).

[64] N. Blümer and E. Kalinowski, "Mott insulator: Tenth-order perturbation theory extended to infinite order using a quantum Monte Carlo scheme", Phys. Rev. B **71**, 195102 (2005).

[65] M. Karski, C. Raas, and G. S. Uhrig, "Single-particle dynamics in the vicinity of the Mott-Hubbard metal-to-insulator transition", Phys. Rev. B **77**, 075116 (2008).

[66] S. Ejima, F. H. Essler, and F. Gebhard, "Thermodynamics of the one-dimensional half-filled Hubbard model in the spin-disordered regime", J. Phys. A. Math. Gen. **39**, 4845–4857 (2006).

[67] K. A. Chao, J. Spałek, and A. M. Oleś, "Canonical perturbation expansion of the Hubbard model", Phys. Rev. B **18**, 3453–3464 (1978).

[68] C. Gros, R. Joynt, and T. M. Rice, "Antiferromagnetic correlations in almost-localized Fermi liquids", Phys. Rev. B **36**, 381–393 (1987).

[69] A. Auerbach, *Interacting Electrons and Quantum Magnetism*, Graduate Texts in Contemporary Physics (Springer, New York, 1994).

[70] P. Fulde, *Electron Correlations in Molecules and Solids*, Springer Series in Solid-State Sciences (Springer, Berlin/Heidelberg, 1995).

[71] C. Cohen-Tannoudji et al., *Quantenmechanik*, 4th Ed. (De Gruyter, Berlin, 2010).

[72] H. Eskes et al., "Spectral properties of the Hubbard bands", Phys. Rev. B **50**, 17980–18002 (1994).

[73] W. Heisenberg, "Zur Theorie des Ferromagnetismus", Zeitschrift für Phys. **49**, 619–636 (1928).

[74] P. W. Anderson, "Theory of Localized Magnetic States in Metals", J. Appl. Phys. **37**, 1194 (1966).

[75] Y. Meir, N. S. Wingreen, and P. A. Lee, “Transport through a Strongly Interacting Electron System: Theory of Periodic Conductance Oscillations”, Phys. Rev. Lett. **66**, 3048–3051 (1991).

[76] Y. Meir, N. S. Wingreen, and P. A. Lee, “Low-Temperature Transport Through a Quantum Dot: The Anderson Model Out of Equilibrium”, Phys. Rev. Lett. **70**, 2601–2604 (1993).

[77] R. Hanson et al., “Spins in few-electron quantum dots”, Rev. Mod. Phys. **79**, 1217–1265 (2007).

[78] W. Metzner and D. Vollhardt, “Correlated Lattice Fermions in $d = \infty$ Dimensions”, Phys. Rev. Lett. **62**, 324–327 (1989).

[79] D. Vollhardt, “Dynamical mean-field theory for correlated electrons”, Ann. der Phys. **524**, 1–19 (2012).

[80] R. D. Mattuck, *A guide to Feynman diagrams in the many-body problem* (Dover Publications, New York, 1976).

[81] E. Müller-Hartmann, “Correlated fermions on a lattice in high dimensions”, Zeitschrift für Phys. B Condens. Matter **74**, 507–512 (1989).

[82] A. Georges and G. Kotliar, “Hubbard model in infinite dimensions”, Phys. Rev. B **45**, 6479–6483 (1992).

[83] R. Bulla, T. A. Costi, and T. Pruschke, “Numerical renormalization group method for quantum impurity systems”, Rev. Mod. Phys. **80**, 395–450 (2008).

[84] M. Caffarel and W. Krauth, “Exact Diagonalization Approach to Correlated Fermions in Infinite Dimensions: Mott Transition and Superconductivity”, Phys. Rev. Lett. **72**, 1545–1548 (1994).

[85] R. Peters, “Spectral functions for single- and multi-impurity models using density matrix renormalization group”, Phys. Rev. B **84**, 075139 (2011).

[86] P. Schlottmann, “Bethe-Ansatz Solution of the Anderson Model of a Magnetic Impurity with Orbital Degeneracy”, Phys. Rev. Lett. **50**, 1697–1700 (1983).

[87] J. E. Hirsch and R. M. Fye, “Monte Carlo Method for Magnetic Impurities in Metals”, Phys. Rev. Lett. **56**, 2521–2524 (1986).

[88] W. C. Oliveira and L. N. Oliveira, “Generalized numerical renormalization-group method to calculate the thermodynamical properties of impurities in metals”, Phys. Rev. B **49**, 11986–11994 (1994).

[89] S. Nishimoto and E. Jeckelmann, “Density-matrix renormalization group approach to quantum impurity problems”, J. Phys. Condens. Matter **16**, 613–625 (2004).

[90] C. Raas, G. S. Uhrig, and F. B. Anders, "High-energy dynamics of the single-impurity Anderson model", Phys. Rev. B **69**, 041102 (2004).

[91] F. B. Anders and A. Schiller, "Real-Time Dynamics in Quantum-Impurity Systems: A Time-Dependent Numerical Renormalization-Group Approach", Phys. Rev. Lett. **95**, 196801 (2005).

[92] F. B. Anders and A. Schiller, "Spin precession and real-time dynamics in the Kondo model: Time-dependent numerical renormalization-group study", Phys. Rev. B **74**, 245113 (2006).

[93] H. Lin et al., "Exact Diagonalization Methods for Quantum Systems", Comput. Phys. **7**, 400 (1993).

[94] A. Dolfen, "Massively parallel exact diagonalization of strongly correlated systems", Diploma thesis (Rheinisch-Westfälische Technische Hochschule, Aachen, 2006).

[95] S. A. Jafari, "Introduction to Hubbard Model and Exact Diagonalization", Iran. J. Phys. Res. **8**, 113–120 (2008).

[96] J. M. Zhang and R. X. Dong, "Exact diagonalization: The Bose-Hubbard model as an example", Eur. J. Phys. **31**, 591–602 (2010).

[97] H. Fehske, R. Schneider, and A. Weiße, eds., *Computational Many-Particle Physics*, Lecture Notes in Physics (Springer, Berlin/Heidelberg, 2008).

[98] J. Hackmann, "Spin Dynamics in Doped Semiconductor Quantum Dots", PhD thesis (Technische Universität, Dortmund, 2015).

[99] H. Tal-Ezer and R. Kosloff, "An accurate and efficient scheme for propagating the time dependent Schrödinger equation", J. Chem. Phys. **81**, 3967–3971 (1984).

[100] I. N. Bronstein et al., *Taschenbuch der Mathematik* (Wissenschaftlicher Verlag Harri Deutsch, Frankfurt am Main, 2012).

[101] H. O. Beća, "An orthogonal set based on Bessel functions of the first kind", Publ. Elektroteh. Fak. Ser. Mat. i Fiz. **695**, 85–90 (1980).

[102] J. Kuczyński and H. Woźniakowski, "Estimating the Largest Eigenvalue by the Power and Lanczos Algorithms with a Random Start", SIAM J. Matrix Anal. Appl. **13**, 1094–1122 (1992).

[103] W. E. Arnoldi, "The principle of minimized iteration in the solution of the matrix eigenvalue problem", Q. Appl. Math. **9**, 17–29 (1951).

[104] C. Lanczos, "An Iteration Method for the Solution of the Eigenvalue Problem of Linear Differential and Integral Operators", J. Res. Natl. Bur. Stand. **45**, 255–282 (1950).

[105] A. Pieper et al., "High-performance implementation of Chebyshev filter diagonalization for interior eigenvalue computations", J. Comput. Phys. **325**, 226–243 (2016).

[106] R. Baer and M. Head-Gordon, "Chebyshev expansion methods for electronic structure calculations on large molecular systems", J. Chem. Phys. **107**, 10003–10013 (1997).

[107] M. Ganahl et al., "Chebyshev expansion for impurity models using matrix product states", Phys. Rev. B **90**, 045144 (2014).

[108] J. Hackmann and F. B. Anders, "Spin noise in the anisotropic central spin model", Phys. Rev. B **89**, 045317 (2014).

[109] H. Fehske et al., "Quantum lattice dynamical effects on single-particle excitations in one-dimensional Mott and Peierls insulators", Phys. Rev. B **69**, 165115 (2004).

[110] R. Rausch and M. Potthoff, "Multiplons in the two-hole excitation spectra of the one-dimensional Hubbard model", New J. Phys. **18**, 023033 (2016).

[111] F. W. J. Olver et al., eds., *NIST Digital Library of Mathematical Functions* (June 2019), Release 1.0.23.

[112] G. S. Uhrig, "Interaction quenches of Fermi gases", Phys. Rev. A **80**, 061602 (2009).

[113] S. A. Hamerla and G. S. Uhrig, "Dynamical transition in interaction quenches of the one-dimensional Hubbard model", Phys. Rev. B **87**, 064304 (2013).

[114] S. A. Hamerla and G. S. Uhrig, "One-dimensional fermionic systems after interaction quenches and their description by bosonic field theories", New J. Phys. **15**, 073012 (2013).

[115] S. A. Hamerla and G. S. Uhrig, "Interaction quenches in the two-dimensional fermionic Hubbard model", Phys. Rev. B **89**, 104301 (2014).

[116] M. Kalthoff et al., "Comparison of the iterated equation of motion approach and the density matrix formalism for the quantum Rabi model", Eur. Phys. J. B **90**, 97 (2017).

[117] M. Eckstein, M. Kollar, and P. Werner, "Thermalization after an Interaction Quench in the Hubbard Model", Phys. Rev. Lett. **103**, 056403 (2009).

[118] A. Weiße et al., "The kernel polynomial method", Rev. Mod. Phys. **78**, 275–306 (2006).

[119] D. Jackson, "Über die Genauigkeit der Annäherung stetiger Funktionen durch ganze rationale Funktionen gegebenen Grades und trigonometrische Summen gegebener Ordnung", PhD thesis (Georg-August-Universität, Göttingen, 1911).

[120] D. Jackson, “On the Degree of Convergence of the Development of a Continuous Function According to Legendre’s Polynomials”, Trans. Am. Math. Soc. **13**, 305–318 (1912).

[121] A. Weiße, “Chebyshev expansion approach to the AC conductivity of the Anderson model”, Eur. Phys. J. B **40**, 125–128 (2004).

[122] J. Skilling, *The Eigenvalues of Mega-Dimensional Matrices*, Maximum Entropy and Bayesian Methods (Springer, Dordrecht, 1988), pp. 455–466.

[123] R. Silver and H. Röder, “Densities of states of mega-dimensional Hamiltonian matrices”, Int. J. Mod. Phys. C **5**, 735–753 (1994).

[124] D. A. Drabold and O. F. Sankey, “Maximum Entropy Approach for Linear Scaling in the Electronic Structure Problem”, Phys. Rev. Lett. **70**, 3631–3634 (1993).

[125] S. Popescu, A. J. Short, and A. Winter, “Entanglement and the foundations of statistical mechanics”, Nat. Phys. **2**, 754–758 (2006).

[126] S. R. White, “Minimally Entangled Typical Quantum States at Finite Temperature”, Phys. Rev. Lett. **102**, 190601 (2009).

[127] S. Sugiura and A. Shimizu, “Canonical Thermal Pure Quantum State”, Phys. Rev. Lett. **111**, 010401 (2013).

[128] R. Steinigeweg, J. Gemmer, and W. Brenig, “Spin-Current Autocorrelations from Single Pure-State Propagation”, Phys. Rev. Lett. **112**, 120601 (2013).

[129] T. Heitmann et al., “Selected applications of typicality to real-time dynamics of quantum many-body systems”, Zeitschrift für Naturforsch. A **75**, 421–432 (2020).

[130] A. Wietek et al., “Thermodynamic properties of the Shastry-Sutherland model throughout the dimer-product phase”, Phys. Rev. Res. **1**, 033038 (2019).

[131] J. M. Deutsch, “Quantum statistical mechanics in a closed system”, Phys. Rev. A **43**, 2046–2049 (1991).

[132] P. Arbenz, “Numerical Methods for Solving Large Scale Eigenvalue Problems”, Lecture Notes (Eidgenössische Technische Hochschule, Zürich, 2016), pp. 173–194.

[133] P. Bleicker, J. Stolze, and G. S. Uhrig, “Probing thermalization in quenched integrable and nonintegrable Fermi-Hubbard models”, Phys. Rev. A **102**, 013321 (2020).

[134] P. W. Leung and P. E. Oppenheimer, “Implementation of the Lanczos algorithm for the Hubbard model on the Connection Machine system”, Comput. Phys. **6**, 603–609 (1992).

[135] B. P. Anderson,
"Macroscopic Quantum Interference from Atomic Tunnel Arrays",
Science **282**, 1686–1689 (1998).

[136] I. Bloch, "Ultracold quantum gases in optical lattices", Nat. Phys. **1**, 23–30 (2005).

[137] S. Trotzky et al., "Probing the relaxation towards equilibrium in an isolated strongly correlated one-dimensional Bose gas", Nat. Phys. **8**, 325–330 (2012).

[138] N. Goldman, J. C. Budich, and P. Zoller,
"Topological quantum matter with ultracold gases in optical lattices",
Nat. Phys. **12**, 639–645 (2016).

[139] V. M. Axt and T. Kuhn, "Femtosecond spectroscopy in semiconductors: A key to coherences, correlations and quantum kinetics", Reports Prog. Phys. **67**, 433–512 (2004).

[140] K. Morawetz, ed., *Nonequilibrium Physics at Short Time Scales*
(Springer, Berlin/Heidelberg, 2004).

[141] L. Perfetti et al., "Time Evolution of the Electronic Structure of $1T$-TaS$_2$ through the Insulator-Metal Transition", Phys. Rev. Lett. **97**, 067402 (2006).

[142] T. Stöferle et al.,
"Transition from a Strongly Interacting 1D Superfluid to a Mott Insulator",
Phys. Rev. Lett. **92**, 130403 (2004).

[143] J. F. Sherson et al.,
"Single-atom-resolved fluorescence imaging of an atomic Mott insulator",
Nature **467**, 68–72 (2010).

[144] S. N. Sanders, F. Mintert, and E. J. Heller,
"Matter-Wave Scattering from Ultracold Atoms in an Optical Lattice",
Phys. Rev. Lett. **105**, 035301 (2010).

[145] K. Mayer, A. Rodriguez, and A. Buchleitner,
"Matter-wave scattering from interacting bosons in an optical lattice",
Phys. Rev. A **90**, 023629 (2014).

[146] I. B. Mekhov, C. Maschler, and H. Ritsch,
"Probing quantum phases of ultracold atoms in optical lattices by transmission spectra in cavity quantum electrodynamics", Nat. Phys. **3**, 319–323 (2007).

[147] N. ten Brinke and R. Schützhold, "Dicke superradiance as a nondestructive probe for quantum quenches in optical lattices", Phys. Rev. A **92**, 013617 (2015).

[148] A. M. Läuchli and C. Kollath, "Spreading of correlations and entanglement after a quench in the one-dimensional Bose–Hubbard model", J. Stat. Mech., P05018 (2008).

[149] D. Chen et al., "Quantum Quench of an Atomic Mott Insulator",
Phys. Rev. Lett. **106**, 235304 (2011).

[150] T. Langen et al., “Local emergence of thermal correlations in an isolated quantum many-body system”, Nat. Phys. **9**, 640–643 (2013).

[151] J. Z. Imbrie, V. Ros, and A. Scardicchio, “Local integrals of motion in many-body localized systems”, Ann. Phys. **529**, 1600278 (2017).

[152] D. A. Abanin et al., “Colloquium: Many-body localization, thermalization, and entanglement”, Rev. Mod. Phys. **91**, 021001 (2019).

[153] N. Strohmaier et al., “Observation of Elastic Doublon Decay in the Fermi-Hubbard Model”, Phys. Rev. Lett. **104**, 080401 (2010).

[154] P. Calabrese, F. H. L. Essler, and M. Fagotti, “Quantum Quench in the Transverse-Field Ising Chain”, Phys. Rev. Lett. **106**, 227203 (2011).

[155] P. Calabrese, F. H. L. Essler, and M. Fagotti, “Quantum quenches in the transverse field Ising chain: II. Stationary state properties”, J. Stat. Mech., P07022 (2012).

[156] J.-S. Caux and F. H. L. Essler, “Time Evolution of Local Observables After Quenching to an Integrable Model”, Phys. Rev. Lett. **110**, 257203 (2013).

[157] M. Rigol, “Quantum quenches and thermalization in one-dimensional fermionic systems”, Phys. Rev. A **80**, 053607 (2009).

[158] H. Aoki et al., “Nonequilibrium dynamical mean-field theory and its applications”, Rev. Mod. Phys. **86**, 779–837 (2014).

[159] P. Navez and R. Schützhold, “Emergence of coherence in the Mott-insulator–superfluid quench of the Bose-Hubbard model”, Phys. Rev. A **82**, 063603 (2010).

[160] K. V. Krutitsky et al., “Propagation of quantum correlations after a quench in the Mott-insulator regime of the Bose-Hubbard model”, EPJ Quantum Technol. **1**, 12 (2014).

[161] A. J. Daley et al., “Time-dependent density-matrix renormalization-group using adaptive effective Hilbert spaces”, J. Stat. Mech., P04005 (2004).

[162] G. G. Batrouni et al., “Dynamic response of trapped ultracold bosons on optical lattices”, Phys. Rev. A **72**, 031601 (2005).

[163] F. Goth and F. F. Assaad, “Time and spatially resolved quench of the fermionic Hubbard model showing restricted equilibration”, Phys. Rev. B **85**, 085129 (2012).

[164] M. Schiró and M. Fabrizio, "Time-Dependent Mean Field Theory for Quench Dynamics in Correlated Electron Systems", Phys. Rev. Lett. **105**, 076401 (2010).

[165] M. Schiró and M. Fabrizio, "Quantum quenches in the Hubbard model: Time-dependent mean-field theory and the role of quantum fluctuations", Phys. Rev. B **83**, 165105 (2011).

[166] K. Ido, T. Ohgoe, and M. Imada, "Time-dependent many-variable variational Monte Carlo method for nonequilibrium strongly correlated electron systems", Phys. Rev. B **92**, 245106 (2015).

[167] M. Moeckel and S. Kehrein, "Interaction Quench in the Hubbard Model", Phys. Rev. Lett. **100**, 175702 (2008).

[168] M. Moeckel and S. Kehrein, "Real-time evolution for weak interaction quenches in quantum systems", Ann. Phys. **324**, 2146–2178 (2009).

[169] J. Sabio and S. Kehrein, "Sudden interaction quench in the quantum sine-Gordon model", New J. Phys. **12**, 055008 (2010).

[170] S. R. Manmana et al., "Time evolution of correlations in strongly interacting fermions after a quantum quench", Phys. Rev. B **79**, 155104 (2009).

[171] P. Barmettler et al., "Relaxation of Antiferromagnetic Order in Spin-$\frac{1}{2}$ Chains Following a Quantum Quench", Phys. Rev. Lett. **102**, 130603 (2009).

[172] J. Mossel, G. Palacios, and J.-S. Caux, "Geometric quenches in quantum integrable systems", J. Stat. Mech., L09001 (2010).

[173] P. Calabrese and J. Cardy, "Entanglement and correlation functions following a local quench: a conformal field theory approach", J. Stat. Mech., P10004 (2007).

[174] V. Alba and F. Heidrich-Meisner, "Entanglement spreading after a geometric quench in quantum spin chains", Phys. Rev. B **90**, 075144 (2014).

[175] P. Reimann, "Foundation of Statistical Mechanics under Experimentally Realistic Conditions", Phys. Rev. Lett. **101**, 190403 (2008).

[176] A. J. Short, "Equilibration of quantum systems and subsystems", New J. Phys. **13**, 053009 (2011).

[177] H. Wilming et al., "Entanglement-Ergodic Quantum Systems Equilibrate Exponentially Well", Phys. Rev. Lett. **123**, 200604 (2019).

[178] K. Ptaszyński and M. Esposito, "Entropy Production in Open Systems: The Predominant Role of Intraenvironment Correlations", Phys. Rev. Lett. **123**, 200603 (2019).

[179] N. Linden et al., "Quantum mechanical evolution towards thermal equilibrium", Phys. Rev. E **79**, 061103 (2009).

[180] N. Linden et al., "On the speed of fluctuations around thermodynamic equilibrium", New J. Phys. **12**, 055021 (2010).

[181] A. J. Short and T. C. Farrelly, "Quantum equilibration in finite time", New J. Phys. **14**, 013063 (2012).

[182] H. Hinrichsen, C. Gogolin, and P. Janotta, "Non-equilibrium Dynamics, Thermalization and Entropy Production", J. Phys. Conf. Ser. **297**, 012011 (2011).

[183] C. Kollath, A. M. Läuchli, and E. Altman, "Quench Dynamics and Nonequilibrium Phase Diagram of the Bose-Hubbard Model", Phys. Rev. Lett. **98**, 180601 (2007).

[184] M. Rigol, V. Dunjko, and M. Olshanii, "Thermalization and its mechanism for generic isolated quantum systems", Nature **452**, 854–858 (2008).

[185] M. Rigol, "Breakdown of Thermalization in Finite One-Dimensional Systems", Phys. Rev. Lett. **103**, 100403 (2009).

[186] B. S. Shastry, "Exact Integrability of the One-Dimensional Hubbard Model", Phys. Rev. Lett. **56**, 2453–2455 (1986).

[187] H. Grosse, "The Symmetry of the Hubbard model", Lett. Math. Phys. **18**, 151–156 (1989).

[188] M. Rigol et al., "Relaxation in a Completely Integrable Many-Body Quantum System: An Ab Initio Study of the Dynamics of the Highly Excited States of 1D Lattice Hard-Core Bosons", Phys. Rev. Lett. **98**, 050405 (2007).

[189] N. Yunger Halpern et al., "Microcanonical and resource-theoretic derivations of the thermal state of a quantum system with noncommuting charges", Nat. Commun. **7**, 12051 (2016).

[190] N. Yunger Halpern, M. E. Beverland, and A. Kalev, "Noncommuting conserved charges in quantum many-body thermalization", Phys. Rev. E **101**, 042117 (2020).

[191] R. Nandkishore and D. A. Huse, "Many-Body Localization and Thermalization in Quantum Statistical Mechanics", Annu. Rev. Condens. Matter Phys. **6**, 15–38 (2015).

[192] W. F. Tsai et al., "Optimal inhomogeneity for superconductivity: Finite-size studies", Phys. Rev. B **77**, 214502 (2008).

[193] A. Wietek and A. M. Läuchli, "Sublattice coding algorithm and distributed memory parallelization for large-scale exact diagonalizations of quantum many-body systems", Phys. Rev. E **98**, 033309 (2018).

[194] T. Kinoshita, T. Wenger, and D. S. Weiss, "A quantum Newton's cradle", Nature **440**, 900–903 (2006).

[195] T. Barthel and U. Schollwöck, "Dephasing and the Steady State in Quantum Many-Particle Systems", Phys. Rev. Lett. **100**, 100601 (2008).

[196] M. Kollar and M. Eckstein, "Relaxation of a one-dimensional Mott insulator after an interaction quench", Phys. Rev. A **78**, 013626 (2008).

[197] M. Eckstein and M. Kollar, "Nonthermal Steady States after an Interaction Quench in the Falicov-Kimball Model", Phys. Rev. Lett. **100**, 120404 (2008).

[198] Y. Tang et al., "Thermalization near Integrability in a Dipolar Quantum Newton's Cradle", Phys. Rev. X **8**, 021030 (2018).

[199] M. Eckstein, M. Kollar, and P. Werner, "Interaction quench in the Hubbard model: Relaxation of the spectral function and the optical conductivity", Phys. Rev. B **81**, 115131 (2010).

[200] S. A. Hamerla, "Dynamics of Fermionic Hubbard Models after Interaction Quenches in One and Two Dimensions", PhD thesis (Technische Universität, Dortmund, 2013).

[201] T. Gräßer et al., "Dynamic mean-field theory for dense spin systems at infinite temperature", arXiv:2107.07821 (2021).

[202] W. Metzner, P. Schmit, and D. Vollhardt, "Hole dynamics in a spin background: A sum-rule-conserving theory with exact limits", Phys. Rev. B **45**, 2237–2251 (1992).

[203] K. A. Hallberg, E. Müller-Hartmann, and C. A. Balseiro, "Hole dynamics in generalized spin backgrounds in infinite dimensions", Phys. Rev. B **52**, 4396–4401 (1995).

[204] M. P. Eastwood et al., "Analytical and numerical treatment of the Mott-Hubbard insulator in infinite dimensions", Eur. Phys. J. B **35**, 155–175 (2003).

[205] M. Vojta and K. W. Becker, "Hole motion in an arbitrary spin background: Beyond the minimal spin-polaron approximation", Phys. Rev. B **57**, 3099–3107 (1998).

[206] Z. Liu and E. Manousakis, "Dynamical properties of a hole in a Heisenberg antiferromagnet", Phys. Rev. B **45**, 2425–2437 (1992).

[207] C. S. Chiu et al., “String patterns in the doped Hubbard model”, Science **365**, 251–256 (2019).

[208] J. Vijayan et al., “Time-resolved observation of spin-charge deconfinement in fermionic Hubbard chains”, Science **367**, 186–189 (2020).

[209] B. Reif et al., “Solid-state NMR spectroscopy”, Nat. Rev. Methods Prim. **1**, 2 (2021).

[210] F. Jelezko and J. Wrachtrup, “Single defect centres in diamond: A review”, Phys. Status Solidi A **203**, 3207–3225 (2006).

[211] F. Dolde et al., “Electric-field sensing using single diamond spins”, Nat. Phys. **7**, 459–463 (2011).

[212] T. D. Ladd et al., “Quantum computers”, Nature **464**, 45–53 (2010).

[213] P. W. Anderson, “New Approach to the Theory of Superexchange Interactions”, Phys. Rev. **115**, 2–13 (1959).

[214] A. B. Harris and R. V. Lange, “Single-Particle Excitations in Narrow Energy Bands”, Phys. Rev. **157**, 295–314 (1967).

[215] D. J. Klein and W. A. Seitz, “Perturbation Expansion of the Linear Hubbard Model”, Phys. Rev. B **8**, 2236–2247 (1973).

[216] M. Takahashi, “Half-filled Hubbard model at low temperature”, J. Phys. C Solid State Phys. **10**, 1289–1301 (1977).

[217] A. H. MacDonald, S. M. Girvin, and D. Yoshioka, “t/U expansion for the Hubbard model”, Phys. Rev. B **37**, 9753–9756 (1988).

[218] J. Stein, “Flow Equations and the Strong-Coupling Expansion for the Hubbard Model”, J. Stat. Phys. **88**, 487–511 (1997).

[219] A. Reischl, E. Müller-Hartmann, and G. S. Uhrig, “Systematic mapping of the Hubbard model to the generalized $t-J$ model”, Phys. Rev. B **70**, 245124 (2004).

[220] S. A. Hamerla, S. Duffe, and G. S. Uhrig, “Derivation of the $t-J$ model for finite doping”, Phys. Rev. B **82**, 235117 (2010).

[221] F. Wegner, “Flow-equations for Hamiltonians”, Ann. Phys. **506**, 77–91 (1994).

[222] A. Mielke, “Flow equations for band-matrices”, Eur. Phys. J. B **5**, 605–611 (1998).

[223] C. Knetter and G. S. Uhrig, “Perturbation theory by flow equations: Dimerized and frustrated $S = \frac{1}{2}$ chain”, Eur. Phys. J. B **13**, 209–225 (2000).

[224] S. Kehrein, *The Flow Equation Approach to Many-Particle Systems*, Vol. 217, Springer Tracts in Modern Physics (Springer, Berlin/Heidelberg, 2006).

[225] P. W. Shor, "Polynomial-Time Algorithms for Prime Factorization and Discrete Logarithms on a Quantum Computer", SIAM J. Comput. **26**, 1484–1509 (1997).

[226] D. Loss and D. P. DiVincenzo, "Quantum computation with quantum dots", Phys. Rev. A **57**, 120–126 (1998).

[227] D. P. DiVincenzo, "The Physical Implementation of Quantum Computation", Fortschritte der Phys. **48**, 771–783 (2000).

[228] I. A. Merkulov, A. L. Efros, and M. Rosen, "Electron spin relaxation by nuclei in semiconductor quantum dots", Phys. Rev. B **65**, 205309 (2002).

[229] A. V. Khaetskii, D. Loss, and L. Glazman, "Electron Spin Decoherence in Quantum Dots due to Interaction with Nuclei", Phys. Rev. Lett. **88**, 186802 (2002).

[230] R. B. Liu, W. Yao, and L. J. Sham, "Quantum computing by optical control of electron spins", Adv. Phys. **59**, 703–802 (2010).

[231] M. Gaudin, "Diagonalisation d'une classe d'hamiltoniens de spin", J. Phys. **37**, 1087–1098 (1976).

[232] M. Gaudin, *La fonction d'onde de Bethe* (Masson, Paris, 1983).

[233] N. A. Sinitsyn and Y. V. Pershin, "The theory of spin noise spectroscopy: a review", Reports Prog. Phys. **79**, 106501 (2016).

[234] D. Stanek, C. Raas, and G. S. Uhrig, "Dynamics and decoherence in the central spin model in the low-field limit", Phys. Rev. B **88**, 155305 (2013).

[235] B. Fauseweh et al., "Efficient algorithms for the dynamics of large and infinite classical central spin models", Phys. Rev. B **96**, 054415 (2017).

[236] R. Röhrig et al., "Quantum mechanical treatment of large spin baths", Phys. Rev. B **97**, 165431 (2018).

[237] A. Faribault and D. Schuricht, "Spin decoherence due to a randomly fluctuating spin bath", Phys. Rev. B **88**, 085323 (2013).

[238] G. S. Uhrig et al., "Conservation laws protect dynamic spin correlations from decay: Limited role of integrability in the central spin model", Phys. Rev. B **90**, 060301 (2014).

[239] U. Seifert et al., "Persisting correlations of a central spin coupled to large spin baths", Phys. Rev. B **94**, 094308 (2016).

[240] J. Hackmann et al., "Influence of the Nuclear Electric Quadrupolar Interaction on the Coherence Time of Hole and Electron Spins Confined in Semiconductor Quantum Dots", Phys. Rev. Lett. **115**, 207401 (2015).

[241] N. Fröhling and F. B. Anders, "Long-time coherence in fourth-order spin correlation functions", Phys. Rev. B **96**, 045441 (2017).

[242] M. W. Doherty et al., "The nitrogen-vacancy colour centre in diamond", Phys. Rep. **528**, 1–45 (2013).

[243] J. M. Taylor et al., "High-sensitivity diamond magnetometer with nanoscale resolution", Nat. Phys. **4**, 810–816 (2008).

[244] F. Alghannam and P. Hemmer, "Engineering of Shallow Layers of Nitrogen Vacancy Colour Centres in Diamond Using Plasma Immersion Ion Implantation", Sci. Rep. **9**, 5870 (2019).

[245] J. Bylander et al., "Noise spectroscopy through dynamical decoupling with a superconducting flux qubit", Nat. Phys. **7**, 565–570 (2011).

[246] D. Bluvstein et al., "Extending the Quantum Coherence of a Near-Surface Qubit by Coherently Driving the Paramagnetic Surface Environment", Phys. Rev. Lett. **123**, 146804 (2019).

[247] K. Fabricius and U. Löw, "Dynamic correlations of antiferromagnetic spin-XXZ chains at arbitrary temperature from complete diagonalization", Phys. Rev. B **55**, 5833–5846 (1997).

[248] G. Rickayzen, *Green's Functions and Condensed Matter* (Dover Publications, New York, 2013).

[249] F. Wegner, "Expectation Values, Wick's Theorem and Normal Ordering", Lecture Notes (Ruprecht-Karls-Universität, Heidelberg, 2000).

[250] G. C. Wick, "The Evaluation of the Collision Matrix", Phys. Rev. **80**, 268–272 (1950).

[251] K. G. Wilson, "The renormalization group: Critical phenomena and the Kondo problem", Rev. Mod. Phys. **47**, 773–840 (1975).

[252] P. Coleman, "Heavy Fermions: Electrons at the Edge of Magnetism", Handb. Magn. Adv. Magn. Mater., edited by H. Kronmüller et al. (2007).

[253] T. Siro and A. Harju, "Exact diagonalization of the Hubbard model on graphics processing units", Comput. Phys. Commun. **183**, 1884–1889 (2012).

Abbreviations

3NN Third-nearest neighbour

BCS Superconductivity theory by Bardeen, Cooper and Schrieffer

CET Chebyshev expansion technique

CUT Continuous unitary transformations

DMFT Dynamical mean-field theory

DMRG Density matrix renormalisation group

DO Double occupancy

ED Exact diagonalisation

eDO Double occupancy by two electrons

FHM Fermi-Hubbard model

iEoM Iterated equations of motion

KPM Kernel polynomial method

LHB Lower Hubbard band

NN Nearest neighbour

NNN Next-nearest neighbour

NRG Numerical renormalisation group

NV Nitrogen vacancy

ONOB Orthonormal operator basis

PBC Periodic boundary conditions

QMC Quantum Monte Carlo

SIAM Single impurity Anderson model

spinDMFT Dynamical mean-field theory for dense spin ensembles

TPQS Thermal pure quantum states

UHB Upper Hubbard band

Danksagungen

Sind Sie über das omnipräsente *we* beim Lesen dieser Arbeit gestolpert? Ursprünglich lediglich ein *pluralis modestiae*, wurde mir mit der Zeit klar, dass noch ein anderer, ein viel schönerer Sinn in diesem Plural steckt. Denn kein Mensch ist eine Insel. Eine Arbeit wie die vorliegende entsteht niemals allein. Sowohl auf fachlicher als auch auf persönlicher Ebene hat mich eine Vielzahl von Menschen dabei unterstützt, diese Dissertationsschrift zu dem zu machen, was sie ist. Genug von mir, diese Seite gehört Euch:

Ich danke meinen Betreuern bei sowie dem gesamten Team der Konrad-Adenauer-Stiftung für die umfangreiche mir zuteil gewordene Unterstützung in finanzieller und ideeller Hinsicht, große persönliche Freiheiten und vielfältige Impulse.

Für die Themenvergabe, diverse hilfreiche Ideen zum inhaltlichen und methodischen Vorgehen sowie seine Tätigkeit als geduldiger Betreuer dieser Arbeit danke ich Herrn Prof. Dr. Götz S. Uhrig. Ich danke Herrn Prof. Dr. Kai P. Schmidt für die Übernahme des Zweitgutachtens dieser Arbeit. Herrn Prof. Dr. Joachim Stolze danke ich für ein stets offenes Ohr und hilfreiche, mitunter persönliche Ratschläge.

Ich danke Herrn Dr. Philipp Schering. Deine kritischen Kommentare zu ausgesuchten Kapiteln sowie hilfreiche Erläuterungen zur Spin-Dynamik waren fachlich wertvoll, Deine Begleitung bei so manchem Workshop das unbestrittene Tageshighlight.

Ich danke Frau Dr. Leanna B. Müller. Unsere Gespräche und Diskussionen der letzten Jahre waren mal humorvoll, mal ernst, dabei aber immerzu bereichernd. Mit Dir, Leanna, habe ich weit mehr als nur eine fachkundige, aufmerksame Lektorin – ich habe eine gute Freundin gewonnen.

Ich danke Herrn Matthias Gianfelice. Ein Studium gemeinsam zu verleben, schweißt bereits zusammen, die Dissertationszeit zu teilen, verbindet unauflöslich. Ich danke Dir, Matthias, für unzählige Ratschläge, ein allzeit offenes Ohr und – unvergessen – viele digitale Stunden in Bolivien.

Ich danke meinen Eltern. Mama und Papa, Ihr seid nicht einfach nur diejenigen beiden Menschen, die seit meiner Geburt mit Engelsgeduld sowie unendlich viel Liebe und Wärme jede meiner Launen ertragen haben, Ihr seid tagein und tagaus meine Stütze in schwierigen Situationen, mein Korrektiv bei dummen Ideen und der stete Anker in einem unüberblickbaren Meer von Orientierungslosigkeit.
Mein größtes Glück, Papa und Mama, ich habe Euch lieb.

Eidesstattliche Versicherung

Ich versichere hiermit an Eides statt, dass ich die vorliegende Dissertation mit dem Titel *The Fermi-Hubbard model and its limiting cases as a testbed for techniques and phenomena* selbstständig und ohne unzulässige fremde Hilfe erbracht habe. Ich habe keine anderen als die angegebenen Quellen und Hilfsmittel benutzt sowie wörtliche und sinngemäße Zitate kenntlich gemacht. Die Arbeit hat in gleicher oder ähnlicher Form noch keiner Prüfungsbehörde vorgelegen.

Dortmund, den 15.11.2021	Philip Bleicker
Ort, Datum	Unterschrift

Belehrung

Wer vorsätzlich gegen eine die Täuschung über Prüfungsleistungen betreffende Regelung einer Hochschulprüfungsordnung verstößt, handelt ordnungswidrig. Die Ordnungswidrigkeit kann mit einer Geldbuße von bis zu 50 000 € geahndet werden. Zuständige Verwaltungsbehörde für die Verfolgung und Ahndung von Ordnungswidrigkeiten ist der Kanzler/die Kanzlerin der Technischen Universität Dortmund. Im Falle eines mehrfachen oder sonstigen schwerwiegenden Täuschungsversuches kann der Prüfling zudem exmatrikuliert werden (§ 63 Abs. 5 Hochschulgesetz –HG–).

Die Abgabe einer falschen Versicherung an Eides statt wird mit Freiheitsstrafe bis zu drei Jahren oder mit Geldstrafe bestraft.

Die Technische Universität Dortmund wird ggf. elektronische Vergleichswerkzeuge (wie z. B. die Software *turnitin*) zur Überprüfung von Ordnungswidrigkeiten in Prüfungsverfahren nutzen.

Die oben stehende Belehrung habe ich zur Kenntnis genommen.

Dortmund, den 15.11.2021	Philip Bleicker
Ort, Datum	Unterschrift